Politecnico di Milano
Department of Aerospace Science and Technology
Doctoral Programme In Aerospace Engineering

A Mid-Fidelity Aeroelastic Environment for Tiltrotor Analysis and Design

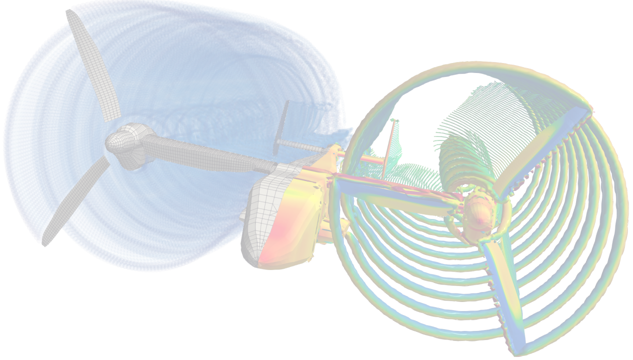

Doctoral Dissertation of:
Alberto Savino

Supervisor:
Prof. Vincenzo Muscarello

Tutor:
Prof. Franco Auteri

The Chair of the Doctoral Program:
Prof. Pierangelo Masarati

Academic Year 2021 – 2022

Doctoral Cycle XXXV

It is not because things are difficult that we do not dare,

it is because we do not dare that things are difficult.

– Seneca

. . . al mio nonno.

Abstract

ROTARY-WING vehicles like tiltrotors pose a significant challenge for engineers and scientists. To develop new aircraft designs, it is crucial to conduct complete aeroelastic simulations that account for the interaction between the aerodynamics of the rotating wings and the structural dynamics of the vehicle. Additionally, in order to gain deeper insights into the vehicle's performance and guide the design process effectively, it is important to have a thorough understanding of the airflow around the aircraft.

The purpose of the research work presented in the thesis is to build and obtain a numerical environment for aeroelastic simulations suitable for complex vehicles such as tiltrotors. The tool aims to position itself among various branches already widely established and explored by the research and aviation sector in general, such as the aerodynamic, aeroelastic, aeromechanical, and design fields. The underlying idea is to provide an environment in which different analyses can be carried out at the same time, thus allowing a complete understanding of the machine's behavior already in the preliminary design phase.

To achieve this, a mid-fidelity aerodynamic solver based on the vortex particle method for wake modeling, DUST, is coupled through the partitioned multi-physics coupling library preCICE to a multibody dynamics code, MBDyn. By utilizing a multibody structural model in combination with mid-fidelity numerical software, the method allowed for accurate assessment of aerodynamic interaction effects inherent in rotary-wing aircraft while maintaining a cost-effective approach when compared to traditional

and more sophisticated CSD/CFD tools. All of this was done with an open-source approach in order to provide the research community with an accessible and usable tool that can be developed in the future to enhance its capabilities for upcoming studies.

The new developed numeric tool has been implemented and validated by comparing their results considering a classic aeroelastic benchmark of wing. Validation tests revealed that providing a more precise explanation of aerodynamics is crucial for replicating the dynamic performance of a wedged wing during flutter state with detail. Particular attention has been dedicated to the solution of the aerodynamic part in order to demonstrate its abilities and limitations in typical configurations of the interactional aerodynamics present in tiltrotors and in VTOL vehicles, through comparisons with numerical and experimental literature data. In general, the results of DUST simulations showed the capability to obtain a degree of accuracy, respecting the limits of the theory on which the code is based, similar to the high-fidelity CFD approach, but at a much lower computational cost. Furthermore, the strength of the DUST approach based on the description of the free wake, has been demonstrated to be the ability to capture the physics of the flow field around the aircraft, a fundamental factor for understanding and investigating different designs in the preliminary phase. This result further highlighted the potential of the implemented approach for the design and investigation of rotorcraft configurations.

To demonstrate the modeling flexibility and the type of results that can be achieved, a complete aeroservoelastic tiltrotor model has been implemented. Thanks to the large amount of public data, the XV-15 tiltrotor aircraft equipped with Advanced Technology Blade (ATB) is chosen. In order to highlight the advantages of a more complete and realistic modeling, different hybrid models with different levels of complexity were used.

Globally, a good correlation was reached in the analysis for the entire system with literature data. The transient roll maneuver of a complete tiltrotor aircraft is performed, to show the capability of the coupled solver to analyze the aeroelasticity of complex rotorcraft configurations. Simulation results show the importance of the accurate representation of rotary wing aerodynamics provided by the vortex particle method for loads evaluation, aeroelastic stability assessment and analysis of transient maneuvers of aircraft configurations.

This work represents a significant advancement in the scientific and industrial community by introducing a novel perspective on coupled simulations utilizing a mid-fidelity aerodynamic solver. The results of this study demonstrate that this approach can yield highly accurate results while

utilizing substantially less computational effort than conventional, higher-fidelity CSD tools. The numerical environment that was developed has broad applications across various branches of aeronautical projects and beyond, such as in wind energy and turbomachinery applications.

Sommario

IL design di velivoli ad ala rotante complessi come i convertiplani rappresenta una sfida per ingegneri e ricercatori. Poter eseguire simulazioni aeroelastiche complete considerando l'interazione dell'aerodinamica del rotore con la dinamica strutturale della macchina è essenziale per lo sviluppo di nuove configurazioni di aeromobili. Inoltre, al fine di comprendere al meglio il comportamento del velivolo e guidare il design verso la direzione ottimale, è necessario avere una rappresentazione della fisica del campo di moto intorno all'aeromobile.

Lo scopo del lavoro di ricerca presentato nella tesi è di costruire e ottenere un ambiente numerico per simulazioni aeroelastiche adatto a veicoli complessi come i convertiplani. Lo strumento mira a posizionarsi tra diverse branche già ampiamente consolidate ed esplorate dal settore della ricerca e dell'aviazione in generale, come l'aerodinamica, l'aeroelasticità, la meccanica del volo e il design. L'idea alla base è fornire un ambiente in cui diverse analisi possano essere effettuate contemporaneamente, consentendo così una comprensione completa del comportamento della macchina già nella fase di design preliminare.

Per raggiungere questo obiettivo, è stato accoppiato, attraverso la libreria preCICE, un software aerodinamico a media fedeltà basato sul metodo delle particelle vorticose per la modellizzazione della scia, DUST, ad un codice di dinamica multicorpo, MBDyn. Utilizzando un modello strutturale multicorpo in combinazione con software aerodniamico a media fedeltà, il metodo permette una valutazione accurata degli effetti di interazione aerodinamica tipici dei convertiplani, mantenendo un approccio economico

rispetto agli strumenti CSD/CFD tradizionali e più sofisticati. Tutto ciò è stato fatto con un'approccio open-source al fine di fornire alla comunità scientifica uno strumento accessibile e utilizzabile che possa essere sviluppato in futuro per migliorare le sue funzionalità per studi successivi.

Il nuovo ambiente numerico sviluppato è stato implementato e validato confrontando i risultati ottenuti con quelli di un caso di riferimento aeroelastico classico di un'ala. I test di validazione hanno evidenziato che avere un modello più preciso dell'aerodinamica è fondamentale per replicare le prestazioni dinamiche di un'ala a basso allungamento alare e predire l'instabilità aeroelastica del flutter con dettaglio. Particolare attenzione è stata dedicata al solutore aerodinamico al fine di dimostrare le sue capacità e limitazioni nelle configurazioni tipiche dell'aerodinamica interazionale presenti nei convertiplani e nei velivoli VTOL, attraverso il confronto con dati numerici e sperimentali della letteratura. In generale, i risultati delle simulazioni DUST hanno dimostrato la capacità di ottenere un livello di precisione simile all'approccio CFD ad alta fedeltà, ma con un costo computazionale molto inferiore, entro i limiti della teoria su cui si basa il codice. Inoltre, la forza dell'approccio DUST basato sulla descrizione ed evoluzione della scia libera, ha dimostrato di essere in grado di catturare la fisica del campo di moto intorno all'aeromobile, un elemento fondamentale per la comprensione e l'indagine di diverse configurazioni nella fase preliminare. Questo risultato ha ulteriormente evidenziato il potenziale dell'approccio implementato per la progettazione e l'indagine di configurazioni di velivoli ad ala rotante.

Per dimostrare la flessibilità di modellizzazione e i tipi di risultati che possono essere ottenuti, è stato costruito un modello completo aeroelastico di convertiplano. Grazie alla grande quantità di dati pubblici, è stato scelto il convertiplano XV-15 dotato di Advanced Technology Blade (ATB). Al fine di evidenziare i vantaggi di una modellizzazione più completa e realistica, sono stati utilizzati diversi modelli ibridi con diversi livelli di complessità.

Globalmente, è stata raggiunta una buona correlazione con i dati della letteratura per l'intero sistema. Per mostrare la capacità del codice accoppiato di analizzare l'aeroelasticità di configurazioni di velivoli complesse, si è simulata una manovra di rollio instazionaria dell'intero convertiplano. I risultati della simulazione mostrano l'importanza di rappresentare in maniera accurata l'aerodinamica del velivolo attraverso DUST per la valutazione dei carichi, la valutazione della stabilità aeroelastica e l'analisi delle manovre transitorie di aeromobili.

Questo lavoro rappresenta un significativo progresso nella comunità scien-

tifica e industriale introducendo una nuova prospettiva sulle simulazioni accoppiate utilizzando un solutore aerodinamico a media fedeltà. I risultati di questo studio dimostrano che questo approccio può produrre risultati altamente precisi utilizzando un notevole minor sforzo computazionale rispetto agli strumenti CSD convenzionali a maggiore fedeltà. L'ambiente numerico sviluppato ha ampie applicazioni in vari rami di progetti aeronautici e oltre, come nell'energia eolica e nelle applicazioni di turbomacchine.

Acknowledgements

I would like to express my gratitude to my supervisor, Prof. Vincenzo Muscarello, whose mentorship and insights have been pivotal in shaping the trajectory of my research. Your unwavering support has been instrumental in every step of this journey.

I am deeply thankful to Prof. Alex Zanotti for his consistent presence and invaluable contributions to my research. Your input and discussions have added depth and perspective to my work.

I would like to express my appreciation to my colleagues and friends at the office, Alessandro Cocco and Andrea Colli, for their collaborative spirit, thought-provoking discussions, and the sense of camaraderie that has made this academic pursuit a rewarding experience. We will always be the DUST team. To the members of the wind tunnel team, Donato and Luca, who I look forward to joining as future colleagues, I am grateful for our interactions, and the shared enthusiasm for our field of study. A general thanksgiving to the Politecnico di Milano, for all that it has been and for all that it will be.

I want to acknowledge Ing. Matteo Pecoraro from Leonardo Helicopters for generously sharing his expertise in tiltrotor technology, which significantly enriched the technical aspects of my research.

My gratitude knows no bounds when it comes to my family. Your unwavering support, belief in my abilities, and freedom to make choices have been the bedrock of my journey. A special mention goes to my wife, Roberta, and our little D. Your love and understanding have been a constant source of inspiration and strength.

This dissertation has been founded by the Clean Sky 2—H2020 Framework Program, under grant agreement N. 885 971 (the FORMOSA project).

Contents

Introduction

TILTROTORS are a type of aircraft that have been developed to overcome the limitations of conventional helicopters, which have limited speed and range capabilities. These aircraft combine the vertical takeoff and landing ability of helicopters with the range and speed of fixed-wing planes, making them widely applicable for various missions. In terms of their design, tiltrotors have rotors that are oriented so that the plane of rotation is horizontal, providing lift in the same manner as a typical helicopter rotor. As the aircraft gains speed, the rotors gradually tilt forward until they become vertically oriented. By functioning as a propeller, the rotors enable flight and the fixed wing's airfoil generates uplift, enabling the airplane to operate in a typical manner. Tiltrotors offer several benefits compared to traditional helicopters. They can vertically land and take off in cramped and hard-to-reach areas and can achieve high speeds, enabling them to serve a diverse range of missions. However, they have many moving components, making them costly to maintain and operate. Furthermore, their hovering ability could be compromised in extreme temperature and high-altitude locations, limiting their efficiency in specific missions. In general, tiltrotors hold great promise as a technology that stands to transform aviation in numerous ways. With ongoing research and development, they are expected to become more adaptable and effective, thereby expanding the horizons of military, commercial, and civilian applications.

Historical background

Tiltrotors have been in development for over 70 years, starting from the late 1940s. Despite several attempts and various prototypes, it took until the 1980s for the first successful tiltrotor, the V-22 Osprey [90], to take flight. The Osprey is a versatile aircraft suitable for both military and commercial purposes. It has been the result of over three decades of technological advancements and prototypes, including the Bell XV-3 tilt rotor and the Boeing Vertol VZ-2 tilt wing, both from the 1950s. However, it was the Bell XV-15, which started testing in the late 1970s, that successfully demonstrated the mature and advanced tiltrotor technology that led to the development of the Osprey.

Back in 1951, the US Army and US Air Force established a joint program to construct innovative aircraft that could perform vertical takeoff and landing (VTOL) operations. To achieve this goal, they issued a Request for Proposal for convertible aircraft, and Bell Aircraft Corporation promptly replied with its Model 200 tilt-rotor, later called XV-3 (Fig. 1). The development process was intense, culminating in the combined efforts of research and development led by two brilliant minds, Larry Bell and Robert Lichten. To put this innovative model to the test, the XV-3 underwent extensive ground testing before its inaugural hover trial in August 1955. The aircraft began by demonstrating satisfactory characteristics during the early stages of the flight, but high vibrations during the hovering stage emerged, resulting from the proprotor-pylon assembly's dynamic instability observed in subsequent test flights. Things reached a fever pitch in October 1956 when the XV-3 experienced a near-fatal crash, forcing Bell engineers to ground the aircraft immediately. Rather than throw in the towel, the Bell engineers hunkered down and got to work. They embarked on an extended research initiative that included an array of tiedown experiments that would help them to unravel the mystery behind the instability problems plaguing the XV-3. Ultimately, this deep dive into the issues that caused the crash allowed the team to come up with groundbreaking solutions that would later inform the development of the successful tilt-rotor concept that achieved early flight in the V-22 Osprey.

During the development of the XV-3 program, analysis capabilities were limited, leaving dynamicists to rely on physical testing to understand the causes of the dynamic instability that plagued the aircraft. Despite these setbacks, the program persisted and achieved full tiltrotor conversion in December 1958, marking a significant milestone in the feasibility of the tilt-rotor concept. However, evaluations conducted at Bell and military

Figure 1: *Bell XV-3 tiltrotor in airplane mode.*

facilities revealed several significant shortcomings in the XV-3's performance. The aircraft was underpowered, with poor handling qualities and structural stability deficiencies that impacted hover and high-speed flight. Despite these issues, the XV-3 program's achievement in safely performing in-flight conversion between airplane and helicopter modes paved the way for the development of tilt-rotor aircraft. While interest in tilt-wing aircraft waned, the success of the XV-3 program convinced the aeronautical community of the unique potential of tilt-rotor technology. The design's ability to combine the vertical takeoff and landing capabilities of a helicopter with the range and speed of a fixed-wing aircraft offered immense potential for both military and commercial applications. The groundwork laid by the XV-3 program continues to influence the development of tilt-rotor aircraft and may ultimately transform the future of air mobility.

Bell initiated the development of the tiltrotor model 300 in the 1960s and later altered the design to create the model 301, also known as the XV-15 [64], Fig. 2, in response to an RFP from NASA and the Army for the Tiltrotor Research Aircraft Program. The XV-15 successfully incorporated the crucial aeromechanical characteristics learned from the XV-3, making it possible for the aircraft to transition smoothly and stably to high-speed forward flight. In the late 1970s, the Navy expressed a significant interest in tiltrotor technology and provided substantial funding for the XV-15 project. This support set the stage for the Navy's JVX requirement, which ultimately turned into the Bell-Boeing partnership to develop the V-22 throughout the 1980s and 1990s [40]. Thanks to the success of the XV-15, the development of tiltrotor aircraft had a clear path forward. The

V-22 Osprey, a product of the Bell-Boeing collaboration, became the first tiltrotor aircraft to achieve fully operational military status. Currently, the V-22 is the only aircraft of its kind to be in active service.

Figure 2: *Bell XV-15 tiltrotor aircraft in airplane mode.*

To meet the increasing demand for aircraft with vertical lift, speed, and range, the Department of Defense launched the Joint-Service Vertical Take-Off/Landing Experimental (JVX) program in 1981. Operating jointly with Boeing Vertol, Bell responded to the call for proposals by submitting an expanded version of the XV-15, which resulted in the production of the Bell Boeing V-22 Osprey (shown in Fig. 3). The V-22 Osprey became the first tiltrotor aircraft to enter operational service and be mass-produced [17]. Its development also led to numerous experimental and numerical investigations, with results that shed light on various physical phenomena related to the aerodynamic interaction between the wing and rotor [72, 109]. One significant discovery was the "download effect" in hover, where the wing experiences a vertical force opposite to the rotor thrust when the rotor wake strikes it. Further experimentation also uncovered the "fountain effect," where rotor-rotor interaction at the aircraft's symmetry plane hurts its performance. Numerical computations on a half-model applying symmetry requirements showed that this effect was consistent with actual flight conditions [85]. Overall, the development and continual refinement of the V-22 Osprey has contributed significantly to advancements in tiltrotor technology and related aeronautical research.

Tiltrotors have been further advanced and enhanced following the success of the V-22 Osprey. Among the prominent examples are the Leonardo AW609 (refer to Fig. 4) wich caters to civilian purposes and the Bell V-280 Valor, a successor of the Osprey that is currently under development for the

Figure 3: *Bell-Boeing V22 Osprey, first production tiltrotor aircraft in hover.*

United States Army's Future Vertical Lift (FVL) initiative.

The Leonardo AW609 had its first flight in March 2003, as a result of the collaboration between Bell Helicopter and AgustaWestland. An article published by the American Institute of Aeronautics and Astronautics highlights the advanced design features of the Leonardo AW609 [59] that allow it to achieve high speeds and maneuverability, while maintaining efficiency and stability. The technical paper also outlines the aircraft's modern avionics, fly-by-wire flight controls, and cutting-edge safety features, which make it an attractive option for use in various applications. Even though the project received significant financial and engineering investment, the Leonardo AW609 remains incomplete. The rotorcraft is particularly noteworthy for being the first pressurized helicopter to seek certification since 1946, presenting complex implications for the project. This factor is just one of many reasons why the Leonardo AW609 has not yet become fully operational.

There are several future developments of tiltrotors in the US that are currently in progress or planned. One of the most notable is the Future Vertical Lift (FVL) program, which aims to replace aging military helicopters with next-generation aircraft. The FVL program includes the development of a new tiltrotor aircraft, the V-280 Valor, by Bell and Lockheed-Martin. The V-280 has completed several successful flight tests and is currently undergoing further testing and evaluation, it is an evolution of the V22 Osprey and it is intended to replace the Sikorsky UH-60 Black Hawk.

The Clean Sky 2 Joint Undertaking (CSJU) was formed in Europe in 2014 to achieve environmental performance goals through a partnership between the European Commission and the European aeronautics industry.

Figure 4: *Leonardo AW609 in conversion phase.*

The EU has extended funding for two high-speed rotorcraft projects as part of the Clean Sky 2 Fast Rotorcraft Innovative Aircraft Demonstrator Platform (IADP): the Airbus RACER compound helicopter (Fig. 6) and the Leonardo Next-Generation Civil Tiltrotor (NGCTR) (Fig. 5).

Figure 5: *Leonardo Next-Generation Civil Tiltrotor in conversion phase.*

The advancement of tiltrotor technology has opened up new possibilities for its use beyond traditional military and tactical purposes. Small businesses are now considering the application of tiltrotors in urban air mobility, a growing area of interest as global cities seek more eco-friendly and efficient transportation alternatives. By combining the strengths of helicopters' vertical takeoff and landing with the speed and efficiency of fixed-wing aircraft, tiltrotors can significantly improve urban transportation, particularly

Figure 6: *Airbus RACER.*

in congested areas where traditional modes are slow and sub-optimal. Furthermore, tiltrotors can operate in a greater range of environments due to their minimized runway space requirement. Despite such potential, challenges remain in the development and certification of tiltrotors for urban air mobility. Key concerns include noise pollution, safety, and regulatory approvals. Nonetheless, engaging in continued research and development in this arena is promising to yield exciting new advances toward sustainable and advanced urban transportation systems.

Figure 7: *Archer midnight eVTOL.*

One possible evolution of the tiltrotor concept is that which has led to the development of more generic aircraft with multiple rotors. The emergence of electric vertical takeoff and landing (eVTOL) aircraft presents a promising new category of aerial vehicles. These aircraft feature multiple rotors powered by electric batteries, allowing for vertical takeoff and landing and reduced reliance on traditional infrastructure like runways. Consequently, eVTOLs are poised to transform urban and regional air mobility and become a major transportation mode in the future [2]. This innovative aircraft category is projected to fuel a 1.5 $ trillion urban air mobility industry by 2040 [6]. Archer's model depicted in Fig. 7 is an example of these latest developed machines.

Tiltrotor challenges

When considering the design of a tiltrotor, it is necessary to identify the critical issues that this type of configuration presents compared to more conventional aircraft. Current limitations and challenges for tiltrotors and in general for VTOL configurations include:

1. **Costs**: tiltrotor and general VTOL are complex aircraft with a large number of moving parts, which can make them expensive to operate and maintain. This can be a significant barrier to overcome, particularly for commercial applications where cost-effectiveness is a key consideration.

2. **Noise**: Considering the helicopter mode flight phase, typical during takeoff and landing, it must be taken into account that, compared to a helicopter, the tiltrotor has dual rotors. This inherently implies that from an aerodynamic noise perspective, the impact is considerably greater. In the case of more general VTOL configurations, where multiple rotors are present, because of the high rotational speed, the aircraft generates a lot of noise, which might be a significant issue for urban air transportation. In heavily crowded locations, noise may restrict their use.

3. **Regulations**: Although the concept of tiltrotor is not new, it is not easy to establish general guidelines from a regulatory point of view. This problem is even more critical for newer VTOL aircraft. Governments and aviation authorities must set VTOL aircraft safety standards, certification processes, and air traffic control systems.

4. **Safety**: Tiltrotors are still relatively new, and there are concerns about their safety. Several accidents have involved these aircraft in recent years, such as the case of the V-22 crash on June 2022 or the AW609 [1].

In general, tiltrotors and VTOL have the capacity to transform aviation in multiple ways. However, before they can be extensively utilized for commercial and military purposes, certain obstacles and constraints need to be resolved. With additional research and development, it is probable that these difficulties will be tackled, ultimately paving the path for broader utilization of this potential technology. The aim of this research effort is to create a numerical environment for the study and design of these complex aircraft, capable of capturing the key phenomena with a reasonable computational cost to facilitate multiple analyses.

Interest in Mid-Fidelity Aeroelastic numerical environment

The design of complex rotary-wing vehicles such as tiltrotors and eVTOLs represents a challenge for engineers and scientists and is driven by mission and safety requirements. However, the aerodynamics of these configurations are dominated by intricate rotor-rotor, wing-rotor, and rotor-wing-airframe interactions that are difficult to simulate and predict. To address this challenge, mid-fidelity tools have emerged as an optimal trade-off between computational cost and desired accuracy, particularly in the early stages of design. While computational fluid dynamics (CFD) methods can analyze these unsteady interactions, the resolution of wake dynamics in conventional CFD tools requires high-order numerical schemes and computationally expensive mesh resolutions, making them unsuitable for design space exploration. Several research groups have been focused on accurately computing unsteady aerodynamic loads for rotary-wing vehicles. To achieve this, they have developed high-fidelity Computational Fluid Dynamics (CFD) codes that utilize advanced Navier-Stokes equations solvers. To name a few examples, ONERA, University of Glasgow, DLR and Airbus Helicopters Deutschland and Politecnico di Milano developed respectively elsA [25], HBM3 [20], FLOWer [55] and ROSITA [19], high-fidelity CFD codes based on the block-structured grid, finite volume and Chimera approach for the simulation of rotating bodies. These tools were purposely developed in Europe for rotorcraft and tiltrotor application studies [32,34,51]. Similarly, considerable research effort was dedicated in the USA to the numerical study of rotorcraft, particularly to tiltrotor aerodynamics, as shown for instance by the works by Meakin [73], Potsdam and Strawn [86], and Wissink et al. [108], where hover configurations were simulated using different implementations of the Navier-Stokes equations, and by the recent works of Lim, Tran et al. [60, 99–101] that investigated the aerodynamic interaction between rotors and wing of the XV-15 tiltrotor aircraft. Time-accurate RANS simulations of eVTOL aircraft are still computationally demanding and require significant resources. Therefore, high-fidelity CFD tools are often limited to a small number of detailed analyses and are unsuitable for use in designing new eVTOL aircraft due to the large number of required aerodynamic simulations. As a result, a mid-fidelity numerical approach that combines different models is the preferred choice for designers of novel eVTOL aircraft.

Academia and industry have therefore turned their attention to mid-fidelity codes to predict complex aerodynamic interactions. In recent years, considerable effort was dedicated by several research groups to the development of mid-fidelity aerodynamic solvers based on the use of the vortex particle method (VPM) [29, 107] for wake modeling. This numerical methodology showed a quite accurate representation of the aerodynamic interactions among several bodies typical of complex rotorcraft configurations and limited computational time concerning URANS CFD simulations. To cite a few examples, Lu et al. [62] developed an optimization methodology for a helicopter design based on a viscous VPM model combined with an unsteady panel hybrid method. Alvarez and Ning developed a VPM-based code [8] for the investigation of multi-rotor configurations. Tan et al. [97] used a vortex-based approach coupled with a viscous boundary model to study rotor-to-rotor interactional problems occurring during shipboard operations [97]. Recently, Politecnico di Milano developed a novel, flexible mid-fidelity computational tool, called DUST (`https://public.gitlab.polimi.it/DAER/dust`) aimed at representing a fast and reliable asset for the simulation of the aerodynamics of complex rotorcraft configurations, such as the electrical Vertical Take Off and Landing (eVTOL) aircraft. DUST is an open-source code, released under MIT license, integrating different aerodynamic models for solid bodies, such as thick surface panels, thin vortex lattice elements and lifting lines elements. Moreover, a VPM method was implemented for wake modeling providing a stable Lagrangian description of free-vorticity flow field, which is suitable for numerical simulations of configurations characterized by strong aerodynamic interactions. DUST was thoroughly validated by comparison with both high-fidelity CFD simulations results and experimental data over complex rotorcraft configurations, such as eVTOLs [102] and tiltrotors [115]. Consequently, this novel open-source tool is reaching maturity for the simulation of the aerodynamics of complex rotorcraft configurations accurately reproducing the interaction between rotors and wings.

It is crucial to be able to conduct comprehensive aeroelastic simulations that consider the interplay between the aerodynamics of rotary-wing aircraft and the structural dynamics of the vehicle. This capability is vital for the advancement of new aircraft designs [12]. Advanced numerical techniques have been developed to aid in the examination of various flight conditions commonly encountered by VTOL vehicles. These tools provide a higher level of accuracy and precision as the level of detail increases. Indeed, a substantial effort was spent in the past years to develop sophisticated structural dynamics codes (CSD) that were effectively used for rotorcraft applications (e.g. [16, 52, 111]). In detail, the structural dynamics of rotary-wing vehicles was typically investigated using the multibody approach [43, 87], which takes into account the nonlinear dynamics of the interconnected rigid and flexible bodies representing the aircraft components during transients. The multibody approach is commonly utilized to study aeroelastic phenomena, particularly in the case of airplane mode flight. This approach is helpful in examining whirl-flutter instabilities that may arise. [71]. A particular effort in this research field was spent at Politecnico di Milano, where starting in the 1990s a free general-purpose multibody software called MBDyn (`https://public.gitlab.polimi.it/DAER/mbdyn`) was developed, with the aim of gaining autonomous modeling capabilities of generic problems related to the dynamics of complex aeroelastic systems, specifically rotorcraft and tiltrotors [69]. In simpler terms, a tiltrotor flight mission involves taking off and landing vertically like a helicopter, and then flying horizontally like an airplane. The transition between these flight conditions is done by tilting the proprotor-nacelle system. To accurately analyze the dynamics of these vehicles and the loads they experience during these transitions, it is important to use a model that considers the unsteady loads that occur. However, most multibody solvers, like MBDyn, use simplified aerodynamics models based on Blade Element/Momentum Theory (BE/MT). These models do not account for the aerodynamic interactions between rotors and the actual geometry of lifting surfaces. This can result in an inaccurate representation of the aerodynamic loads and a loss of information related to periodic actions. To overcome this limitation, a more accurate and detailed aerodynamics model should be used, one that takes into account the interference between rotors and the actual geometry of lifting surfaces. By using such a model, a correct analysis of the complex dynamics of tiltrotor vehicles can be achieved.

Coupling of CSD codes with high fidelity CFD solvers was successfully investigated and implemented in the last two decades years for aeroelastic simulation of rotorcraft applications [7, 31, 54, 95, 96, 110]. The coupled CSD/CFD numerical approach was successfully validated against experimental results, e.g. for the flutter calculations of a vertical tail model [45] and for the analysis of rotor blade structural loads of a complete helicopter model tested in a transonic wind tunnel [70]. Nevertheless, despite continuous advances in the field of high-performance computing, coupled simulations of CSD and time-accurate URANS simulations of complete rotorcraft configurations still require a robust computational effort, not suitable for the preliminary design stage of novel VTOL aircraft configurations as tiltrotors, which requires a great number of simulations to reproduce the different flight conditions that characterize their mission.

The present research work proposes the combination of a multibody dynamics solver with a mid-fidelity aerodynamic tool aims at representing an ideal trade-off between speed of execution and accuracy of the solution, devoted to the preliminary design phase of novel rotary-wing aircraft configurations. A novel open-access aeroelastic tool is obtained by coupling MBDyn with DUST. The coupling of the two codes relies on the partitioned multi-physics coupling library preCICE [23], a very useful and robust tool for managing communication between different solvers. An interesting novelty proposed by this tool is the capability of modeling the deflection of a control surface, representing an essential aspect in the simulation of aircraft maneuvers. One of the strengths of the tool aims to be the flexibility in modeling complex configurations both from a structural and aerodynamic perspective, with the possibility of obtaining parametric and easily modifiable models in order to test numerous configurations during the preliminary design phase. An additional crucial aspect lies in the fact that all components of the code are both freely accessible and open source. This approach not only aims to deliver a functional tool for conducting aeroservoelastic analyses but also serves as a cornerstone for upcoming advancements and the integration of multiple disciplines. This, in turn, can effectively tackle the challenges linked to VTOL aircraft, as outlined earlier.

Thesis objective and outline

The purpose of the research work presented in the thesis is to build and obtain a numerical environment for aeroelastic simulations suitable for complex vehicles such as tiltrotors. The tool aims to position itself among various branches already widely established and explored by the research and aviation sector in general, such as the aerodynamic, aeroelastic, aeromechanical, and design fields. The underlying idea is to provide an environment in which different analyses can be carried out at the same time, thus allowing a complete understanding of the machine's behavior already in the preliminary design phase.

In order to demonstrate the capability of the mid-fidelity approach, a thorough validation of the aerodynamic part of the tool was presented using various test cases characterizing the interactional aerodynamics present in the tiltrotor, and in general in VTOL aircraft. Subsequently, in order to demonstrate the modeling and simulation capabilities of the aeroelastic tool, a complete numerical model of an aeroservoelastic tiltrotor was implemented. Thanks to the large amount of public data [3,18,24,36,39] the XV-15 tiltrotor aircraft equipped with Advanced Technology Blade (ATB) is chosen as the base model.

The work is organized as follows.

- *Chapter 1*: This chapter offers a theoretical perspective on the software tools that were both utilized and created. The MBDyn code is briefly covered, while the DUST code is examined in detail. Additionally, significant attention is given to the intricate connection between the two codes. Specifically, the interpolation scheme needed to properly alter the aerodynamic mesh and transmit the aerodynamic loads to the structure is thoroughly discussed.

- *Chapter 2*: In this chapter, the focus is on DUST's capability to capture different types of aerodynamic interactions, one of the strengths of the developed coupled code. To this end, four cases are considered:
  - Isolated Rotor:
    proprotor of the XV-15 tiltrotor equipped with metal blades in various flight conditions, namely hover, forward flight in helicopter mode, and airplane mode. The results are compared to high-fidelity numerical simulations and experimental data gathered during the available test campaigns.
  - Propeller-propeller:
    propeller aerodynamics considering the aerodynamic interaction between multiple propellers configurations based on an experimental activity performed at the *S. De Ponte* wind tunnel of Politecnico di Milano. This application wants to assess DUST capability to capture the effect of aerodynamic interactions on propeller performance by means of loads measurements and interacting flow mechanisms for tandem propellers configurations.
  - Wing-propeller:
    wing/propeller model widely investigated in literature both by experiments and high-fidelity CFD simulations and representing

  a classical benchmark case for the aerodynamic study of tiltrotors and electrical distributed propulsion aircraft configurations. This case aims to show the capabilities of DUST to capture the aerodynamic interactional effects of the installed propeller on the wing by a direct comparison of wing pressure coefficient distributions and propeller airloads with both experimental data and high-fidelity CFD simulations.

  - Tiltrotor full aircraft configuration:
    a full XV-15 tiltrotor model, equipped with metal blades proprotors, is considered. DUST simulations of the complete flight envelope, i.e. hover, conversion, and cruise phases, are compared to the high-fidelity numerical results available in the literature.

- *Chapter 3*: In this chapter, the aeroelastic numerical model of the XV-15 tiltrotor equipped with Advanced Technology Blades (ATB) is presented. The presented model is made with the new numerical DUST-MBDyn environment presented in *Chapter 1*. The model description is divided into two parts: the rotor component and the airframe model, which includes the wing, nacelles, and tail. The rotor component is validated structurally and aerodynamically against literature data, while the airframe model is constructed using a parallel high-fidelity aerodynamic model due to the lack of detailed literature data.

- *Chapter 4*: This chapter discusses the analyses conducted on the tiltrotor model constructed and explained in *Chapter 3*. Two types of analysis are shown in the trim of the complete machine and the machine's response to an aileron maneuver. In order to highlight the innovative aspects of the developed aeroelastic code, different levels of accuracy of the model are used. The purpose of this different modeling will be to emphasize the importance of having a comprehensive aeroservoelastic model that allows the interactions between the different parts to be included even at a preliminary design stage, especially when dealing with a complex aircraft such as a tiltrotor or, more generally, a multi-rotor configuration.

- *Chapter 5*: In this final chapter is presented one application of the coupled DUST-MBDyn tool. In the context of the EU-funded FORMOSA project (`https://cordis.europa.eu/project/id/885971`), the code is employed for the preliminary design and optimization of the flaperon control surface of the NGCTR, aiming at developing innovative wing control surfaces concepts. An optimization procedure, based on a Design of Experiment (DoE) approach, is exploited to define the best configuration to improve the roll performance, trying to reduce the complexity of the actuation system.

- *Conclusions*: In this chapter, the conclusions and further development are discussed.

In the context of this study, we address three pivotal questions that underpin the research objectives:

1. Understanding Applicability Limits of the Proposed Approach:
   The first question revolves around comprehending the boundaries within which the proposed approach, based on a mid-fidelity description of aerodynamics, remains effective. This exploration involves elucidating the scenarios where this methodology proves most relevant, while balancing precision and computational resources.
2. Exploring Modeling Flexibility and Complexity:
   The second inquiry centers on assessing the actual modeling flexibility of the system. This involves utilizing a complex case, representative of VTOL aircraft challenges, to verify the feasibility of conducting diverse analyses and optimizations within reasonable timeframes and with limited computational resources. This evaluation is crucial to ascertain the practicality of our approach in handling real-world scenarios.
3. Examining the Impact of Enhanced Modeling on Preliminary Design:
   The third question delves into the repercussions of employing more accurate modeling during the preliminary design phase. This entails unraveling how heightened precision in aerodynamics modeling could influence initial design decisions and potentially streamline the overall design process.

These three fundamental questions serve as the guiding pillars of the presented research, enabling to establish a comprehensive understanding of the proposed approach's potential and its implications for the design of VTOL aircraft.

CHAPTER 1

Aeroelastic numerical environment

THE aim of developing a new tool that combines a multibody dynamics solver with a mid-fidelity aerodynamic tool is to strike a balance between speed and accuracy for designing rotary-wing aircraft configurations. This new open-access tool is designed to be used during the preliminary stages of aircraft design. It tightly couples the multibody code MBDyn with the mid-fidelity aerodynamic code DUST, using the partitioned multiphysics coupling library preCICE [23]. This library allows for seamless communication between the two solvers, ensuring that the coupling is robust and efficient. To explain this in more detail, the chapter first provides a brief overview of multibody dynamics and then delves into the theory behind mid-fidelity aerodynamics solvers, which have been updated in the latest release. The chapter then describes the methodology used to couple the two codes, which is a key aspect of the tool's design. One of the most interesting features of this tool is its ability to model the deflection of a control surface, which is crucial for simulating aircraft maneuvers. It is worth noting that this chapter is an extension of the work published in [94]. The new tool represents a significant improvement over the previous one, and the results obtained from its use are expected to be more accurate and reliable. Overall, the development of this new tool represents a significant contribution to the field of aircraft design, and its open-access nature makes it accessible to a wide range of users, including researchers, engineers, and students.

1.1 MBDyn

MBDyn is a general-purpose multibody solver, developed at the Department of Aerospace Science and Technology of Politecnico di Milano and distributed as free and open-source software, available at `https://public.gitlab.polimi.it/DAER/mbdyn`. MBDyn is a software tool that takes care of writing and solving the equations of motion for a system. This system consists of various entities, each of which has its own degrees of freedom or nodes. These entities are connected together through algebraic constraints. The system is also subjected to both internal and external loads. MBDyn specifically considers the constraint equations and uses a redundant coordinate set approach to handle them. This means that the equations are explicitly accounted for and taken into consideration as part of the overall system dynamics. By automating the process of writing and solving the equations, MBDyn simplifies the task of analyzing and understanding the behavior of complex systems. Thus, the resulting system of Differential-Algebraic Equations (DAE) takes the form

$$\mathbf{M}(\mathbf{x}, t)\dot{\mathbf{x}} = \mathbf{p} \tag{1.1a}$$

$$\dot{\mathbf{p}} = \boldsymbol{\phi}_{/\mathbf{x}}^{T}\boldsymbol{\lambda} + \mathbf{f}_i(\dot{\mathbf{x}}, \mathbf{x}, t) + \mathbf{f}_e(\dot{\mathbf{x}}, \mathbf{x}, t) \tag{1.1b}$$

$$\mathbf{0} = \boldsymbol{\phi}(\mathbf{x}) \tag{1.1c}$$

where $\mathbf{x}$ is the vector of the kinematic unknowns, $\mathbf{p}$ that of the momentum unknowns, $\boldsymbol{\lambda}$ that of the algebraic Lagrangian multipliers, $\mathbf{M}$ is a configuration- and time-dependent inertia matrix, $\mathbf{f}_i$, $\mathbf{f}_e$ are arbitrary internal and external forces, $\boldsymbol{\phi}(\mathbf{x})$ is the vector of the (usually nonlinear) algebraic equations that express kinematic (holonomic) constraints, and $\boldsymbol{\phi}_{/\mathbf{x}}$ is the Jacobian matrix of the constraints concerning the kinematic unknowns.

Every node creates the necessary balance equations according to its properties, as mentioned in equation 1.1b. However, only nodes with inertia properties will incorporate the definitions of related momenta mentioned in equation 1.1a. If there are additional scalar fields like hydraulic pressure, temperature, or electric potential, separate sets of nodes can be used to consider them. These dedicated sets of nodes will also have their corresponding balance equations.

Elements are responsible for contributions to the balance equations through (visco) elastic, internal forces $\mathbf{f}_i$, possibly state-dependent external force fields $\mathbf{f}_e$ (e.g. aerodynamic forces) and reaction forces $\mathbf{f}_c = \boldsymbol{\phi}^T_{/\mathbf{x}}\boldsymbol{\lambda}$, introduced using Lagrange multipliers $\boldsymbol{\lambda}$ and the Jacobian matrix of algebraic constraint equations in Eq. (1.1).

The connections between the nodes in the structural problem can be of two types: elastic/viscoelastic internal forces or kinematic constraints. The elastic/viscoelastic internal forces are represented by lumped structural components [66], beams [15, 42], shells, or Component Mode Synthesis (CMS) elements [30]. These forces are denoted as $\mathbf{f}_i$ and can have different viscoelastic constitutive laws. On the other hand, the kinematic constraints are formulated in Equation (1.1). These constraints restrict the motion between the nodes. For modeling simple aerodynamics, there are built-in elements available. These elements utilize the 2D strip theory model and use look-up tables to store the aerodynamic coefficients. Additionally, classical rotor inflow models based on momentum theory can be used. Overall, the nodes in the structural problem can be connected by internal forces or kinematic constraints, while aerodynamics can be modeled using built-in elements and rotor inflow models.

The DAE system can be solved using various integration methods that are both stable and accurate. One such method is a unique multistep approach that includes a tunable algorithmic dissipation. This method has been specifically developed to handle problems typically encountered in the field of Multibody Dynamics.

The process of integrating an external solver into the code is achieved by using an external force element. This element is responsible for facilitating communication with the external solver. It does this by transmitting the model's kinematics to the solver and receiving the corresponding loads in return.

There are two types of coupling that can be used: loose coupling and tight coupling. Loose coupling, also known as an explicit scheme, involves a straightforward and direct interaction between the code and the external solver. The code calculates the kinematics and passes them to the solver, which then computes the loads and sends them back. Tight coupling, the one adopted in this work, on the other hand, is an implicit scheme. It involves a more complex and iterative process. The code and the external solver exchange information multiple times until convergence is achieved. This allows for a more accurate and detailed analysis, but it also requires more computational resources. For more in-depth information about the different types of coupling with an external solver, I recommend referring to [67]. It provides detailed explanations and insights into this topic.

External forces can be expressed in two ways: either in the absolute frame or in reference to a specific node. If the forces are formulated directly in the absolute frame, the operations to handle them are uncomplicated. However, if the forces are referred to a reference node, the kinematics (motion) of the system are first reported in the reference node's frame. Then, this information is transmitted to the other nodes along with the motion of the reference node. In this case, the other nodes calculate the nodal forces and moments based on the reference frame of the reference node.

1.2 DUST

DUST is an open-source software designed using object-oriented paradigms of the latest FORTRAN standards, available at `https://public.gitlab.polimi.it/DAER/dust`. The code incorporates various classical potential-based elements like lifting lines [41, 84], surface panels [78], linear vortex lattice elements [53], and non-linear vortex lattice elements [27]. Although the code assumes incompressible potential flow, it considers compressibility effects during computations. To calculate steady aerodynamic loads using surface panels and vortex lattice elements, a Prandtl-Glauert correction [58] is applied. On the other hand, lifting lines and non-linear vortex lattice elements inherently account for compressibility and viscous effects. These effects are introduced using Mach-dependent sectional aerodynamic coefficients obtained from experiments or 2D RANS numerical simulations.

Figure 1.1 summarizes the typical workflow needed to build and run a DUST simulation. The geometry of the solid bodies, in form of cgns mesh or parametric directive, must be provided to the preprocessor, which performs preliminary operations and generates a binary geometry file. Such file is provided, alongside the parameters for the simulation and the reference frames, to the solver, which executes the simulation and produces the complete results inside binary files. The produced results contain the complete solution obtained during the simulation, in terms of distribution of singularities on body surfaces and wake. However it is difficult to obtain condensed, meaningful data from such results. For this reason it is possible to specify a variety of different analyses to be performed by the postprocessor, which employs the global results to generate a series of different meaningful results, from visualization and flow fields to loads and loads distribution, in different formats.

The DUST preprocessor is used to generate the geometrical compo-

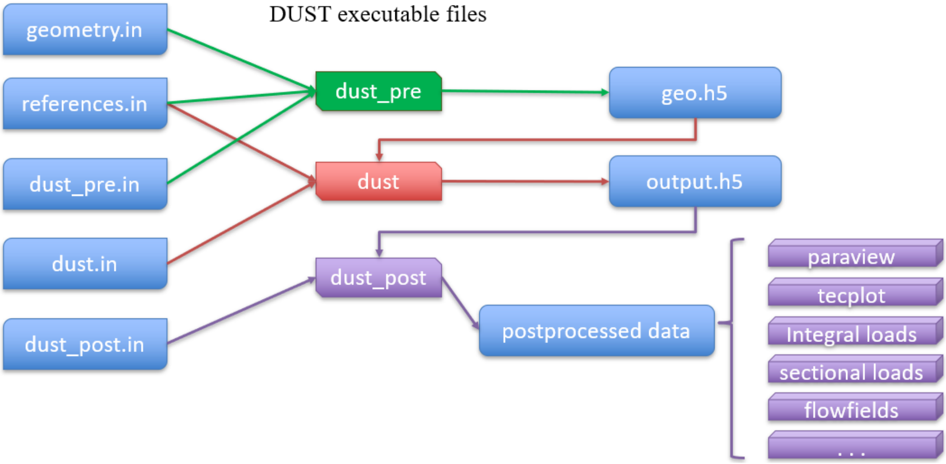

Figure 1.1: *DUST user workflow.*

nents (`geometry.in` file) required to model the surfaces of the analysed body. It gathers the meshes of all the components required for the complete model, process them when necessary and generates all the parametrically specified components. The input file (`dust_pre.in`) containing all the required informations for the execution of the preprocessor must be passed as argument to the command call. The input file of the preprocessor specifies the geometrical components required for the model, their name and the reference system (`references.in` file) to which they will be attached. After running the preprocessor, an output file (`geo.h5`) is output containing all the information about the geometry to be loaded for running the solver. The DUST solver is the main executable of DUST, and its aim is to run the actual simulation and obtain the required full solution to the problem. The solver requires, among other inputs contained in the `dust.in`, the geometry file result of the preprocessor and the definitions of the references. The input file which should be provided to the solver is used to set all the parameters required for the execution of the simulation, from execution options, time parameters to the wake and model settings. When running the solver, a certain number of hdf5 binary files are generated (`output.h5`) containing the solution during the simulation evolution. The DUST postprocessor is used to generate meaningful data from the binary results generated during the execution of the solver. It is also possible to look directly at the content of the hdf5 results, these being based on the singularities intensities on the surface provide little insight on the solution of the solver. The postprocessor takes the specified results and use them to obtain a variety of different processed data easy to use, from visualizations to flowfields and loads, based on the desired input selected in the configuration file `dust_post`.

A DUST model can be made up of multiple components that use different aerodynamic elements, offering varying levels of accuracy in the model. These can range from simple lifting line elements to more complex models using zero-thickness lifting surfaces and surface panels for solid bodies with thickness.

The lifting line (LL) element used in DUST is a one-dimensional model that represents thin, slender lifting bodies. The element considers the sectional aerodynamic coefficients of lift, drag, and pitching moment, denoted as c_l, c_d, and c_m, respectively. These coefficients are calculated based on the local angle of attack α, the local Reynolds number Re, and the local Mach number M. By taking into account the airfoil's camber and thickness, as well as the effects of viscosity and compressibility, the model is able to accurately calculate aerodynamic loads.However, since the problem is stated in explicit form, numerical instability may occur during aerodynamic or aeroelastic analysis. The vortex lattice (VL) method offers a discrete representation of the average surface of thin lifting bodies by modeling them as a sheet of vortex rings with an intensity of Γ. This is equivalent to a piecewise-uniform surface doublet distribution. While the VL method accounts for compressibility effects by applying a Prandtl-Glauert correction to the loads, it cannot capture the non-linear behavior of aerodynamic loads. To ensure numerical stability, the VL element utilizes a fully implicit numerical scheme. The non-linear vortix lattice element (NL-VL) has been implemented in order to try to add the ability of LL to use an aerodynamic database to vortex lattices. In this way, a hybrid element between LL and VL is obtained that allows for an element with viscous correction formulated according to an implicit method and therefore more numerically stable. The surface panels (SP) are formulated as a Morino-like problem [77] in implicit form. This allows the SP element to accurately describe the real shape of the component by applying non-penetration boundary conditions in the physical position. However, the SP element is not able to capture the non-linear effects on aerodynamic loads.

Table 1.1 outlines the main characteristics of the aerodynamic elements used in DUST, while a complete mathematical formulation of the code can be found in [103].

A DUST model needs only surface meshes since the mid-fidelity aerodynamics implemented in the code relies on the vortex particle method (VPM) [29,107]. The VPM is a grid-free Lagrangian approach that models

	Lifting Line (LL)	Vortex Lattice (VL)	Non-Linear VL (NL-VL)	Surface Panel (SP)
3D Unsteady	Yes	Yes	Yes	Yes
Thickness	Yes (Via database)	No	Yes (Via database)	Yes
Camber	Yes (Via database)	Yes	Yes	Yes
Viscous effects	Yes (Via database)	No	Yes (Via database)	No
Compressibility	Yes (Via database)	Yes (Via correction)	Yes (Via database)	Yes (Via correction)
Physical shape	No	No	No	Yes
Numerical scheme	Explicit	Implicit	Implicit	Implicit
Computational cost	Low	Low-Medium	Medium	High

Table 1.1: *DUST elements.*

the free vorticity of wakes, eliminating the need for a volume mesh of the flow surrounding the object being studied. This approach enables a robust representation of the interacting wakes generated by lifting surfaces and bodies, as is typically seen in rotary-wing vehicle applications. In order to decrease the amount of computing resources needed to simulate interactions between vortex particles, in the code is implemented a method known as the Cartesian fast multipole method (FMM). This method, introduced by Lindsay [61], employs a hierarchical approach to divide the simulation domain into clusters of cells, which aids in organizing and simplifying the calculations.

In the subsequent paragraphs, we delve into the theory behind DUST.

1.2.1 Mathematical Formulation

The mathematical formulation of the aerodynamic solver relies on a vorticity-velocity formulation of the aerodynamic problem, which means that it uses two important concepts to describe the behavior of the fluid: vorticity and velocity. Vorticity ω is a measure of the local spinning motion of a fluid. In other words, it describes the tendency of fluid particles to rotate around a specific point. Velocity u, on the other hand, describes the speed and direction of fluid particles as they move through space. The Helmholtz decomposition is a mathematical technique used to break down the velocity field into two components: a curl-free component, which represents the part of the velocity field that is not associated with any spinning motion, and a divergence-free component, which represents the part of the velocity field that is associated with the spinning motion of the fluid. This allows the solver to separate the two important concepts of vorticity and velocity and describe them independently.

The Lagrangian description of the vorticity field is another key concept used in the solver. It is based on the idea of tracking individual fluid particles as they move through space, rather than looking at the fluid as a whole. By doing this, the solver can accurately predict the behavior of the vorticity field and how it interacts with the velocity field. Overall, the vorticity-velocity formulation of the aerodynamic problem, founded on the Helmholtz decomposition of the velocity field and a Lagrangian description of the vorticity field, is a powerful tool for understanding and predicting the behavior of fluids in motion. It allows engineers and scientists to simulate complex fluid dynamics scenarios and design more efficient and effective vehicles, structures, and systems.

The decomposition of the velocity field states that the velocity field $\boldsymbol{u}(\boldsymbol{r}, t)$ can be written as the sum of an irrotational field, the potential velocity, $\boldsymbol{u}_\varphi = \boldsymbol{\nabla}\varphi$, and a soleinoidal field, the rotational velocity, $\boldsymbol{u}_{\boldsymbol{\psi}} = \boldsymbol{\nabla} \times \boldsymbol{\psi}$ as:

$$\boldsymbol{u}(\boldsymbol{r}, t) = \boldsymbol{u}_\varphi(\boldsymbol{r}, t) + \boldsymbol{u}_{\boldsymbol{\psi}}(\boldsymbol{r}, t) \tag{1.2}$$

Since the rotational velocity is a solenoidal vector field, the incompressibility constraint reduces to the Laplace equation for the kinetic potential $\boldsymbol{\varphi}(\boldsymbol{r}, t)$ in the fluid domain Ω. The statement that "the rotational velocity is a solenoidal vector field" means that the vorticity field, which describes the tendency of fluid particles to rotate around a specific point, is a divergence-free vector field. In other words, the divergence of the vorticity field is zero everywhere in the fluid domain Ω.

$$0 = \boldsymbol{\nabla} \cdot \boldsymbol{u} = \boldsymbol{\nabla} \cdot \boldsymbol{u}_\varphi + \underbrace{\boldsymbol{\nabla} \cdot \boldsymbol{u}_{\boldsymbol{\psi}}}_{\boldsymbol{\nabla}\cdot(\boldsymbol{\nabla}\times\boldsymbol{\psi})\equiv 0} \quad \rightarrow \quad \Delta\boldsymbol{\varphi} = 0 \tag{1.3}$$

Since the potential velocity is an irrotational velocity field, the vorticity field $\boldsymbol{\omega}(\boldsymbol{r}, t)$ acts as a volume forcing of the Poisson equation for the vector potential $\boldsymbol{\psi}(\boldsymbol{r}, t)$,

$$\boldsymbol{\omega} = \underbrace{\boldsymbol{\nabla} \times \boldsymbol{u}_\phi}_{\boldsymbol{\nabla}\times\boldsymbol{\nabla}\varphi\equiv 0} + \boldsymbol{\nabla} \times \boldsymbol{u}_{\boldsymbol{\psi}} \quad \rightarrow \quad -\Delta\boldsymbol{\psi} = \boldsymbol{\omega} \tag{1.4}$$

given the vector identity $\Delta\boldsymbol{\psi} = \boldsymbol{\nabla}(\boldsymbol{\nabla} \cdot \boldsymbol{\psi}) - \boldsymbol{\nabla} \times \boldsymbol{\nabla} \times \boldsymbol{\psi}$ and the gauge condition $\boldsymbol{\nabla} \cdot \boldsymbol{\psi} = 0$. Then, the Lagrangian description of the dynamical equation governing the vorticity field $\boldsymbol{\omega}(\boldsymbol{r}, t)$ of an incompressible flow reads:

$$\frac{D\boldsymbol{\omega}}{Dt} = (\boldsymbol{\omega} \cdot \boldsymbol{\nabla})\boldsymbol{u} + \nu\Delta\boldsymbol{\omega} \tag{1.5}$$

where ν indicates the flow kinematic viscosity and the material derivative of the vorticity field $D\boldsymbol{\omega}/Dt$ represents the material derivative of the vorticity related to a material particle. In order to solve differential problems in the fluid domain Ω, we can utilize the Green function method. This method allows us to manipulate these differential equations and derive a grid-free volume formulation for the aerodynamic problem.

Eq. (1.3) is recast as a boundary integral problem, describing the potential velocity field $\boldsymbol{u}_\phi$ as the superposition of the free-stream velocity $\boldsymbol{U}_\infty$ and the fields induced by surface doublet and source distributions with intensity μ and σ respectively, as described in Sec. 1.2.2. To obtain a mixed panel-vortex particle representation of the wake, we condense the wake panels into equivalent vortex particles. These vortex particles induce a rotational velocity field, denoted as $\boldsymbol{u}_\psi$. This velocity field is defined as the curl of the vector potential, denoted as $\boldsymbol{\psi}$. To evaluate this rotational velocity field, we use a vortex particle approximation of the free-volume solution of Equation (1.4). This equation represents the Poisson equation for the vortex particles. The formulation of the problem naturally fits a time-stepping method for time evolution of the aerodynamic field around a model.

1.2.2 Potential Velocity - Body

The aerodynamic problem can be solved by using a boundary element formulation, which involves the potential velocity. This formulation utilizes the superposition principle, combining surface elementary singularities associated with three different aerodynamic elements: surface panels, vortex rings, and lifting lines. Each element type has its own singularity distribution, boundary condition, and load computation, which are used to determine the overall solution for the aerodynamic problem. By considering these factors, we can effectively analyze and understand the behavior and characteristics of the potential velocity in the given system.

Surface panels are used to model solid thick bodies, such as airplanes or cars. These panels represent the outer solid surface of the body S_s and are used to calculate the aerodynamic forces acting on it. The behavior of these panels is determined by a combination of source and doublets, which are mathematical representations of the flow around the body. The boundary condition for the kinetic potential is also considered in this modeling approach. Vortex lattice elements provide a zero-thickness model for the surface S_v of thin lifting bodies with a distribution of vortex rings and non-penetration boundary conditions for the velocity field. Lifting line elements provide a 1-D line vortex model for thin lifting bodies, with tabulated sectional aerodynamic coefficients naturally including the viscous effects. The representation of lifting line elements in modeling involves vortex rings, where their streamwise sides correspond to the trailing vorticity. By utilizing the concept of vortex-doublet equivalence, the solid body modeling is simplified, resulting in a surface distribution of doublets and sources. Furthermore, vortex ring elements are also employed to model the surface S_w of the potential portion within the wake.

Surface panels (SP)

The velocity field's potential component is determined by the Laplace equation (1.3). This equation describes the kinetic potential in the fluid region called Ω_φ, which is enclosed by certain aerodynamic elements. These elements are represented by the surfaces $\partial\Omega_\varphi = S_b \cup S_w = S_s \cup S_v \cup S_l \cup S_w$. We can reframe the problem by introducing two new quantities: the perturbation kinetic potential, denoted as φ, which is defined as the difference between the total kinetic potential ϕ and the infinity kinetic potential ϕ_∞, and the perturbation potential velocity, denoted as $\boldsymbol{u}_\varphi$, which is the gradient of φ concerning position, resulting in the difference between the total potential $\boldsymbol{u}_\phi$ and the infinity velocity field $\boldsymbol{U}_\infty$. This reformulation leads to the Laplace equation for the perturbation kinetic potential

$$\Delta\varphi = 0 \qquad \text{in } \Omega_\varphi \ , \tag{1.6}$$

supplemented with the far-field boundary condition,

$$\varphi \to 0 \qquad |\boldsymbol{r}| \to \infty \ , \tag{1.7}$$

and the Neumann's non-penetration boundary condition, $\hat{\boldsymbol{n}} \cdot \boldsymbol{u} = \hat{\boldsymbol{n}} \cdot \boldsymbol{u}_b$, on the surface S_s of solid bodies modelled with surface panel elements, reading

$$\begin{aligned} \frac{\partial\varphi}{\partial n} &= \hat{\boldsymbol{n}} \cdot \boldsymbol{\nabla}\varphi = \hat{\boldsymbol{n}} \cdot \boldsymbol{u}_\varphi = && \text{on } S_s \\ &= \hat{\boldsymbol{n}} \cdot (\boldsymbol{u}_b - \boldsymbol{U}_\infty - \boldsymbol{u}_\psi) =: \sigma(\boldsymbol{u}_\psi; \boldsymbol{U}_\infty, \boldsymbol{u}_b) \ , \end{aligned} \tag{1.8}$$

and considering the influence of the free-stream condition, the motion of the surface S_s and the rotational component of the velocity field $\boldsymbol{u}_\psi$. Using Green's function approach, the problem is recast as a boundary element problem,

$$\begin{aligned} E(\boldsymbol{r})\varphi(\boldsymbol{r},t) = &+ \oint_{\partial\Omega_\varphi} \hat{\boldsymbol{n}}(\boldsymbol{r_0}) \cdot \boldsymbol{\nabla_0} G(\boldsymbol{r_0},\boldsymbol{r})\, \varphi(\boldsymbol{r_0},t) \\ &- \oint_{S_s} G(\boldsymbol{r_0},\boldsymbol{r})\, \hat{\boldsymbol{n}}(\boldsymbol{r_0},t) \cdot \boldsymbol{\nabla_0}\varphi(\boldsymbol{r_0},t) \ , \end{aligned} \tag{1.9}$$

where $\hat{\boldsymbol{n}}\mathrm{rot}$ is the unit normal vector on the surface $\partial\Omega_\varphi$, pointing outward the solid bodies on S_s, and $G(\boldsymbol{r_0}, \boldsymbol{r}) = 1 / (4\pi|\boldsymbol{r} - \boldsymbol{r_0}|)$ is the Green's function of the Laplace problem in the three-dimensional space and $E(\boldsymbol{r_0})$ is the indicator function of the fluid domain Ω,

$$E(\boldsymbol{r_0}) = \begin{cases} 0 \ , & \boldsymbol{r_0} \in \Omega_\varphi \\ \dfrac{1}{2} \ , & \boldsymbol{r_0} \in \partial\Omega_\varphi \\ 1 \ , & \boldsymbol{r_0} \notin \Omega_\varphi \quad . \end{cases} \tag{1.10}$$

The formulation (1.9) of the problem is interpreted as the superposition principle for the perturbation kinetic potential, identifying the Green's function $G(\boldsymbol{r_0}, \boldsymbol{r})$ and the term $\hat{\boldsymbol{n}}\mathrm{rot} \cdot \boldsymbol{\nabla_0} G(\boldsymbol{r_0}, \boldsymbol{r})$ with the opposite of the kinetic potential induced in $\boldsymbol{r}$ by a unitary source and a unitary doublet singularity located in $\boldsymbol{r_0}$, respectively. A doublet distribution is associated with the whole boundary $\partial\Omega_\varphi$ of the fluid domain for the potential velocity, while S_v, S_l and S_w have no source contribution because of the normal velocity boundary conditions on zero-thickness surfaces.
The problem is solved by a collocation method. The surface of the solid bodies S_b and the potential part of the wake S_w are subdivided into panels. Using a uniform-intensity panel discretization and defining the intensity of the doublets, $\mu_{i_s} = -\varphi_{i_s}$, and the sources, $\sigma_{i_s} = \hat{\boldsymbol{n}}_{i_s} \cdot (\boldsymbol{u}_b - \boldsymbol{U}_\infty - \boldsymbol{u}_\psi)_{i_s}$, the discrete counterpart of the problem reads

$$\begin{aligned} &\sum_{k_s=1}^{N_s} A_{i_s k_s} \mu_{k_s} + \sum_{k_v=1}^{N_v} A_{i_s k_v} \mu_{k_v} + \sum_{k_l=1}^{N_l} A_{i_s k_l} \mu_{k_l} + \\ &\qquad + \sum_{k_s=1}^{N_s} B_{i_s k_s} \sigma_{k_s} + \sum_{k_w=1}^{N_w} A_{i_s k_w} \mu_{k_w} = 0 \ , \quad \forall i_s = 1 : N_s \ , \end{aligned} \tag{1.11}$$

where A_{ik} and B_{ik} represents the induced potential of the k^{th} doublet and source panel at the point $\boldsymbol{r}_i$,

$$\begin{aligned} A_{ik} &= -\int_{S_k} \hat{\boldsymbol{n}}_{k_s} \cdot \boldsymbol{\nabla_0} G(\boldsymbol{r_0}, \boldsymbol{r}_i) \\ B_{ik} &= -\int_{S_k} G(\boldsymbol{r_0}, \boldsymbol{r}_i) \ . \end{aligned} \tag{1.12}$$

except for the self-induction potential AIC of a doublet,

$$A_{i_s i_s} = E(\boldsymbol{r}_{i_s}) - \int_{S_{i_s}} \hat{\boldsymbol{n}}_{i_s} \cdot \boldsymbol{\nabla_0} G(\boldsymbol{r_0}, \boldsymbol{r}_{i_s}) = \frac{1}{2} \ . \tag{1.13}$$

The intensity of the sources at each time step, denoted as σ_{k_s}, is determined by the boundary condition (1.8). It is a function of the velocity of the body surface, $\boldsymbol{u}_b$, and the rotational velocity, $\boldsymbol{u}_\psi$, at the collocation points $\boldsymbol{r}i_s$. On the other hand, the intensity of the wake doublet elements, denoted as μk_w, is known from previous time steps. The boundary element problem (1.11) for modeling solid bodies with surface panels can be represented as a linear system with N_s equations. This linear system involves $N = N_s + N_v + N_l$ unknown doublet intensities, denoted as μ_k, which are associated with surface panels, vortex lattice elements, and lifting line elements. If the model includes vortex lattice or lifting line elements in addition to surface panels, the resulting linear system becomes under-determined.

The system is analyzed using the Eulerian description, and the unsteady Bernoulli theorem is applied to an irrotational flow of an incompressible fluid with a constant density ρ. It is important to note that no volume forces are acting on the system.

$$\frac{\partial \phi}{\partial t} + \frac{|\boldsymbol{U}|^2}{2} + \frac{P}{\rho} = C(t) \tag{1.14}$$

where P is the pressure field, ϕ the kinetic potential, ans $\boldsymbol{U} = \boldsymbol{\nabla}\phi$ the velocity field. The kinetic potential and velocity fields can be decomposed as the sum of the free-stream and perturbation contributions as

$$\phi = \phi_\infty + \varphi \quad \rightarrow \quad \boldsymbol{\nabla}\phi = \boldsymbol{\nabla}\phi_\infty + \boldsymbol{\nabla}\varphi \tag{1.15}$$

so that $\phi_\infty = \boldsymbol{U}_\infty \cdot \boldsymbol{r}$, being $\boldsymbol{r}$ the space variable.

To calculate loads on a moving body using the Bernoulli equation in a panel method, an Arbitrary Lagrangian Eulerian (ALE) description can be utilized. This approach offers several advantages by leveraging the spatial derivatives obtained from the body's surface grid and the temporal derivatives for specific material points on the solid surface. This technique is similar to the one used to compute the wake boundary condition. The time derivative of a physical quantity for a material point $\boldsymbol{r}_b$ (of the solid surface) moving with velocity $\boldsymbol{u}_b = \left.\dfrac{\partial \boldsymbol{x}}{\partial l}\right|_{\boldsymbol{r}_b}$ is expressed as follows.

$$\left.\frac{\partial}{\partial t}\right|_{\boldsymbol{r}_b} = \frac{\partial}{\partial t} + \boldsymbol{u}_b \cdot \boldsymbol{\nabla} \tag{1.16}$$

Therefore, the explanation of the Bernoulli theorem (1.14) in the ALE description can be stated as follows:

$$\left.\frac{\partial \phi}{\partial t}\right|_{\boldsymbol{r}_b} - \boldsymbol{u}_b \cdot \boldsymbol{\nabla}\phi + \frac{|\boldsymbol{U}|^2}{2} + \frac{P}{\rho} = C(t) \tag{1.17}$$

To simplify, the Bernoulli equation (1.17) can be obtained by equating the decomposition (1.15) with the free-stream condition taken as a reference. This equation can be expressed as follows:

$$\left.\frac{\partial(\cancel{\phi_\infty}+\varphi)}{\partial t}\right|_{\boldsymbol{r}_b} - \boldsymbol{u}_b \cdot \boldsymbol{\nabla}(\cancel{\phi_\infty}+\varphi) + \frac{|\boldsymbol{U}|^2}{2} + \frac{P}{\rho} = \tag{1.18}$$

$$= \left.\frac{\partial \cancel{\phi_\infty}}{\partial t}\right|_{\boldsymbol{r}_b} - \boldsymbol{u}_b \cdot \boldsymbol{\nabla}\cancel{\phi_\infty} + \frac{|\boldsymbol{U}_\infty|^2}{2} + \frac{P_\infty}{\rho} \tag{1.19}$$

Therefore, we can calculate the pressure for a single panel in the following way.

$$P_i = P_\infty + \rho\frac{|\boldsymbol{U}_\infty|^2}{2} - \left(\rho\left.\frac{\partial\varphi_i}{\partial t}\right|_{\boldsymbol{r}_b} - \boldsymbol{u}_b\cdot\boldsymbol{\nabla}\varphi + \rho\frac{|\boldsymbol{U}|^2}{2}\right) \tag{1.20}$$

$$P_i^{\mathrm{P-G}} = \frac{P_i}{\sqrt{1-\mathrm{Ma}^2}} \tag{1.21}$$

Once the pressure on each element is known, it is possible to calculate the corresponding force. Note that the Prandtl-Glauert correction for compressibility is applied on the pressure term, Eq. 1.21.

$$\boldsymbol{F}_i = -\left(P_\infty - P_i^{\mathrm{P-G}}\right) dA_i \cdot \hat{\boldsymbol{n}}_i \tag{1.22}$$

Vortex Lattice (VL)

The vortex lattice method is a technique used to represent the aerodynamic characteristics of thin lifting bodies. In this method, the body is modeled as a sheet of vortex rings, where each ring has a specific intensity denoted by Γ_{i_v}. This vortex ring sheet can be equivalently represented by a surface distribution of doublets with the same intensity $\mu_{i_v} = \Gamma_{i_v}$, where i_v ranges from 1 to N_v. The vortex sheet follows the non-penetration boundary condition,

$$\hat{\boldsymbol{n}}\cdot\boldsymbol{u}_\varphi = \hat{\boldsymbol{n}}\cdot(\boldsymbol{u}_b - \boldsymbol{U}_\infty - \boldsymbol{u}_{\boldsymbol{\psi}}) =: \sigma \qquad \text{on } S_v \ , \tag{1.23}$$

The condition that needs to be satisfied at the collocation point $\boldsymbol{r}_{i_v}$ is expressed as

$$\begin{aligned}\sum_{k_s=1}^{N_s} C_{i_v k_s}\mu_{k_s} + \sum_{k_v=1}^{N_v} C_{i_v k_v}\mu_{k_v} + \sum_{k_l=1}^{N_l} C_{i_v k_l}\mu_{k_l} + \\ + \sum_{k_s=1}^{N_s} D_{i_v k_s}\sigma_{k_s} + \sum_{k_w=1}^{N_w} C_{i_v k_w}\mu_{k_w} = \sigma_{i_v} \ , \quad \forall i_v = 1:N_v \ ,\end{aligned} \tag{1.24}$$

where C_{ik} and D_{ik} represents the induced velocity of the k^{th} doublet and source panel at the point $\boldsymbol{r}_i$ respectively, expressed as

$$\begin{aligned} C_{ik} &= -\boldsymbol{\nabla}\int_{S_k} \hat{\boldsymbol{n}}_{k_s} \cdot \boldsymbol{\nabla}_{\mathbf{0}} G(\boldsymbol{r}_{\mathbf{0}}, \boldsymbol{r}_i) \\ D_{ik} &= -\boldsymbol{\nabla}\int_{S_k} G(\boldsymbol{r}_{\mathbf{0}}, \boldsymbol{r}_i)\ . \end{aligned} \tag{1.25}$$

When we have the values of surface variables σ_k, and wake doublet intensities μ_{k_w}, we can use them to establish a set of boundary conditions. These boundary conditions can be represented by a system of linear equations, where the number of equations is denoted by Nv and the number of unknowns (doublet intensities) is denoted by N. Now, in the case of using surface panels or lifting line elements along with vortex lattice elements to create the model, we may end up with an under-determined linear system. This means that we have more unknowns than equations.

To calculate the aerodynamic loads, is employed the unsteady formulation of the Kutta-Joukowsky theorem along with the Prandtl-Glauert compressibility correction. Consider a stripe consisting of n_{str} panels, numbered from $i_{\text{str}} = 1$ to n_{str}, with the leading edge being the starting point. The force acting on the i^{th} panel can be determined as follows:

$$\begin{cases} \boldsymbol{F}_i = \rho_\infty \dfrac{(\boldsymbol{V}_i \times \boldsymbol{d\ell}_i)}{\sqrt{(1-\text{Ma}^2)}} \cdot (\Gamma_i - \Gamma_{i-1}) - \rho dA_i \dfrac{d\Delta\Gamma}{dt} \cdot \hat{\boldsymbol{n}}_i \quad \text{if } i \neq 1 \\ \boldsymbol{F}_i = \rho_\infty \dfrac{(\boldsymbol{V}_i \times \boldsymbol{d\ell}_i)}{\sqrt{(1-\text{Ma}^2)}} \cdot (\Gamma_i) - \rho dA_i \dfrac{d\Gamma}{dt} \cdot \hat{\boldsymbol{n}}_i \quad \text{if } i = 1 \end{cases} \tag{1.26}$$

In this equation, we have several variables: ρ_∞ represents the flow density. $\boldsymbol{V}_i$ represents the induced velocity on the panel caused by all elements. $\boldsymbol{d\ell}_i$ represents the spanwise vector. Ma stands for the local Mach number. $\frac{d\Delta\Gamma}{dt}$ represents the time derivative of the circulation, which is calculated using an explicit Euler method. dA_i represents the area of the panel. $\hat{\boldsymbol{n}}_i$ represents the normal vector of the panel.

Lifting Lines (LL)

A lifting line is a simplified model used to analyze the aerodynamics of thin and slender lifting bodies. It assumes that the body can be represented as a one-dimensional line and considers the aerodynamic coefficients of each section along the line. These coefficients are determined based on the local angle of attack α, the local Reynolds number Re, and the local Mach number M at each section. This allows us to predict the overall lift and drag forces acting on the body.

$$\{c_\ell,\, c_d,\, c_m\}\,(\alpha, Re, M; \boldsymbol{r}) \; . \tag{1.27}$$

The circulation $\Gamma_l(t)$ of the lifting line is calculated by solving a nonlinear problem that relates $\Gamma_l(t)$ to the tabulated aerodynamic coefficients of its lifting sections.

The Γ-method [41] solver is implemented.

The method consists of the equivalence of the semi-empirical expression of the sectional lift and its analytical expression from the Kutta-Joukowski theorem,

$$\frac{1}{2}\rho\,|\boldsymbol{u}_{rel}(\boldsymbol{r},t)|^2 c(\boldsymbol{r})\, c_\ell(\alpha(\boldsymbol{r},t);\boldsymbol{r}) = \\ = -\rho\,|\boldsymbol{u}_{rel}(\boldsymbol{r},t)|\,\Gamma(\boldsymbol{r},t)\;, \tag{1.28}$$

where $c(\boldsymbol{r})$ and $c_\ell(\alpha;\boldsymbol{r})$ represent the chord and the lift curve of the aerodynamic sections of the component, and the local angle of attack α and the relative velocity $\boldsymbol{u}_{rel}$ are functions of the lifting line circulation Γ_l through the induced velocity.

A discrete representation of the components of a lifting line is achieved by combining multiple lifting line elements with uniform circulation. Each lifting line element, represented by a circulation value Γ_{i_l}, forms a vortex ring along with its trailing vortices. The last vortex in the wake is aligned with the spanwise direction. This vortex ring, with an intensity of Γ_{i_l}, can be equivalently represented by a uniform surface doublet, $\mu_{i_l} = \Gamma_{i_l}$.

The Γ-method, Eq. 1.28, which involves the intensity of the surface panel, vortex lattice, potential wake singularities, body motion, and rotational velocity, can be expressed as a fixed point problem in a discrete representation,

$$\mu_{i_l} = f_{i_l}(\mu_{k_s}, \mu_{k_v}, \mu_{k_l}, \sigma_{k_s}, \mu_{k_w}), \quad i_l = 1:N_l\;. \tag{1.29}$$

To calculate the loads for the lifting line, we can follow a similar approach to the vortex lattice method, considering the case with only 1 in the chord. In addition, we have a term related to viscosity, computed through strim theory:

$$\boldsymbol{F}_i^{\text{visc}} = \frac{1}{2}\rho_\infty |\boldsymbol{u}_{rel}(\boldsymbol{r},t)|^2 dA \cdot c_d \left(\sin(\alpha_i)\hat{\boldsymbol{n}} + \cos(\alpha_i)\hat{\boldsymbol{t}}\right) \tag{1.30}$$

Finally, the computed force acting on a single lifting line is:

$$\boldsymbol{F}_i = \rho_\infty(\boldsymbol{V}_i \times \boldsymbol{d\ell}_i)\cdot(\Gamma_i) - \rho dA_i \frac{d\Gamma}{dt} + \boldsymbol{dF}_i^{\text{visc}} \tag{1.31}$$

Non-Linear Vortex Lattice (NL-VL)

To overcome both limitations of the lifting line (due to numerical scheme instabilities that occur when the lifting line is used to evaluate the lift of a short aspect ratio wing) and the vortex lattice (related to the capture of viscous effects), the two elements were joined together, providing a new non-linear vortex lattice element. In the first step, the potential solution of the linear vortex lattice is calculated by solving the linear system that imposes the non-penetration boundary condition on the vortex lattice panel as described in1.2.2. Then, the idea behind the method is to modify the right-hand side term of the complete aerodynamic system to obtain the match between the calculated lift coefficient and the tabulated one. The modification of the right-hand side occurs only on the rows of the linear system that are linked to μ_v^{nl}, which is the unknown intensity of the surface doublet for the i^th non-linear vortex lattice panel. Any modification occurs on the left-hand side of the system, which means that the overall system is factorized only once for each time step.

To address the limitations of both the lifting line and the vortex lattice methods, a non-linear vortex lattice element is created by combining the two approaches. In the first step, the linear vortex lattice solution is calculated by solving a linear system. This system enforces the non-penetration boundary condition on the vortex lattice panel. This step is described in Sec. 1.2.2. The next step is where the *non-linear* part comes into play. The goal is to modify the right-hand side term of the complete aerodynamic system to achieve a match between the calculated lift coefficient and the tabulated (expected) lift coefficient. This modification only affects the rows of the linear system that are connected to μ_v^{nl}, which represents the unknown intensity of the surface doublet for each non-linear vortex lattice panel. It is important to note that the modification occurs only on the right-hand side of the system. This means that the overall system is only factorized once for each time step, and no changes are made to the left-hand side of the system. In summary, the non-linear vortex lattice method combines the lifting line and vortex lattice approaches and introduces modifications to the right-hand side of the linear system to achieve the desired lift coefficient.

Once the solution of the system is calculated, it is possible to compute the angle of attack of each chordwise section in the component in the same way as the lifting line case. The velocity $\boldsymbol{v}_{v_{nl}}(\boldsymbol{r}, t)$ at the control point (center of the element) at time t of each stripe is computed as:

$$\boldsymbol{v}_{v_{nl}}(\boldsymbol{r}, t) = \boldsymbol{U}_\infty - \boldsymbol{u}_{v_{nl},b} + \boldsymbol{u}_{tot\setminus v_{nl}}(\boldsymbol{r}, t) + \boldsymbol{u}_{v_{nl}}(\boldsymbol{r}, t) \tag{1.32}$$

where $\boldsymbol{u}_{v_{nl}}(\boldsymbol{r}, t)$ represents the induced velocity of the considered stripe on the others. The overall stripe intensity is computed with the procedure of the classic vortex lattice.

$$\Gamma_{v_{nl}} = d\Gamma_{v_{nl}^1} + \sum_{i=2}^{N} d\Gamma_{v_{nl}^i} - d\Gamma_{v_{nl}^{i-1}} \tag{1.33}$$

where $d\Gamma_{v_{nl}^i}$ corresppnds to the intensity i^th of the stripe calculated in the previous iteration.

To solve a fixed-point iterative problem, such as the lifting line Γ method, we need to ensure convergence between the lift coefficient obtained from the aerodynamic look-up table and the one calculated from the stripe intensity. In order to increase the stability of the implemented method, two different kinds of relaxation schemes are available:

- Fixed relaxation, where the updated right-hand side of the system is:

  $$\mathbf{RHS}_k = \mathbf{RHS}_{k-1} + \alpha \cdot \mathbf{r} \tag{1.34}$$

  where α represents the relaxation factor. The residual vector is calculated by subtracting the lift coefficient obtained from solving the linear system from the one obtained from the aerodynamic look-up table in iteration k.

- Aitken acceleration [57], where the updated right-hand side of the system is

  $$\alpha_k = -\alpha_{k-1} \frac{\mathbf{r}_{k-1} \cdot \Delta\mathbf{r}_k}{\Delta\mathbf{r}_k \cdot \Delta\mathbf{r}_k} \tag{1.35}$$

  The Aitken relaxation factor for each iteration, denoted as α_k, is determined based on the difference between the residuals of the current and previous iterations, represented as $\Delta\mathbf{r}_k$. The residual vector is denoted as $\mathbf{r}$.

To calculate aerodynamic loads for non-linear vortex lattice elements, we use the unsteady formulation of the Kutta-Joukowsky theorem, similar to the linear case. However, in the non-linear case, there is an additional viscous correction applied to the drag term:

$$\boldsymbol{dF}_{i\in s} = \boldsymbol{dF}_{i\in s}^{sys} + \frac{1}{2}\rho_\infty(\boldsymbol{u}(\boldsymbol{r},t))^2 dA_{i\in s} c_d^s \left(\cos(\alpha)\hat{\boldsymbol{t}} + \sin\alpha\hat{\boldsymbol{n}}\right) \tag{1.36}$$

where the notation $i \in s$ represents a specific panel i that is a part of the stripe s. On the other hand, $\boldsymbol{dF}_{i\in s}^{sys}$ denotes the force that is calculated from the system.

1.2.3 Rotational Velocity - Vortex particle method

The wake shed from the trailing edges of lifting bodies is modeled as a panel wake, which shares the same spatial discretization that is used to model the lifting bodies and the same formulation as vortex lattice elements in terms of geometry and singularity distribution. When advected downstream, the panel wake is converted into vortex particles to obtain a more robust wake formulation that is suitable for the representation of the interactional aerodynamics of both rotorcraft and complex aircraft configurations.

The vortex particles method (VPM) [29, 107] is a Lagrangian grid-free method describing the wake evolution through the rotational component of the velocity field $\boldsymbol{u}_\psi$ by means of the material vortex particles used to obtain the approximated vorticity field namely:

$$\boldsymbol{\omega}_\varepsilon^h(\boldsymbol{r},t) = \sum_{p=1}^{N_p} \boldsymbol{\alpha}^p \zeta_\varepsilon \left(\boldsymbol{r} - \boldsymbol{r}^p(t)\right) \tag{1.37}$$

where $\boldsymbol{r}^p(t)$ denotes the coordinates of the p^{th} vortex particle and the regular *cut-off* function $\zeta_\varepsilon(\boldsymbol{x})$ replaces the Dirac delta of the singular model. By substituting Eq. 1.37 in the equation of the dynamics of vorticity,

$$\frac{D\boldsymbol{\omega}}{Dt} = (\boldsymbol{\omega} \cdot \boldsymbol{\nabla})\boldsymbol{U} + \nu\nabla^2\boldsymbol{\omega} \ , \tag{1.38}$$

the dynamical equations for the intensity $\boldsymbol{\alpha}_p(t)$ and position $\boldsymbol{r}_p(t)$ of all the material vortex particles to be integrated in time can be obtained, as follows:

$$\begin{cases} \dfrac{d\boldsymbol{r}_p(t)}{dt} = \boldsymbol{u}(\boldsymbol{r}_p(t),t) \\[2ex] \dfrac{d\boldsymbol{\alpha}^p}{dt} = (\boldsymbol{\alpha}^p \cdot \boldsymbol{\nabla})\boldsymbol{u}(\boldsymbol{r}_p(t),t) + \nu\nabla^2\boldsymbol{\alpha}^p \end{cases} \tag{1.39}$$

where $\boldsymbol{u} = \boldsymbol{U}_\infty + \boldsymbol{u}_\varphi + \boldsymbol{u}_\psi$ is the complete velocity field and the operator $\nu\nabla^2\boldsymbol{\alpha}^p$ represents the viscous term that acts on the p -th particle:

$$\nu\nabla^2\boldsymbol{\alpha}^p = \nu \int_{V_p} \nabla^2\boldsymbol{\omega} \tag{1.40}$$

The irrotational velocity $\boldsymbol{u}_\varphi$ is the solution to the linear problem, the rotational velocity $\boldsymbol{u}_\psi$ is replaced by its regularized approximation of $\boldsymbol{u}_\varepsilon$. The diffusion term is approximated by means of Particle-Strength Exchange

(PSE) which approximates the Laplacian operator acting on the vorticity field with an integral operator, as reported in [107].

It can be proven that Eq. 1.37 corresponds to the convolution of the singular vorticity field,

$$\boldsymbol{\omega}(\boldsymbol{r}, t) = \sum_{p=1}^{N_p} \boldsymbol{\alpha}^p(t)\delta\left(\boldsymbol{r} - \boldsymbol{r}_p(t)\right) \tag{1.41}$$

where $\boldsymbol{r}^p(t)$ denotes the coordinate of the p^{th} vortex particle, $\boldsymbol{\alpha}^p(t)$ is the intensity vector of the p^{th} vortex particle, and $\delta\left(\boldsymbol{r} - \boldsymbol{r}_p(t)\right)$ is the Dirac delta.

Several regularized Green functions are available in the literature with their respective regular Biot-Savart kernels. In DUST, the Rosenhead kernel is implemented as a regularized version of the Biot-Savart kernel,

$$\boldsymbol{K}_\varepsilon(\boldsymbol{x},\, \boldsymbol{y}) = -\frac{1}{4\pi} \frac{\boldsymbol{x} - \boldsymbol{y}}{\left(|\boldsymbol{x} - \boldsymbol{y}|^2 + \delta^2\right)^{3/2}} \tag{1.42}$$

defined as the gradient of the Plummer potential;

$$\mathcal{G}_\varepsilon(\boldsymbol{x},\, \boldsymbol{y}) = \frac{1}{4\pi(|\boldsymbol{x} - \boldsymbol{y}|^2 + \delta^2)^{1/2}} \tag{1.43}$$

In the previous version of the code, the regularization parameter δ was determined based on a fixed input value, which remained constant for all the wake particles. This approach is illustrated in Figure 1.2(a). However, in the recent updates implemented during this research, a more advanced method has been implemented. Now, the regularization parameter δ is automatically calculated as being proportional to the radius of the vortex particles. Specifically, the radius of the circumscribed circle on the corresponding wake panel is determined, and this value is considered as the radius of the vortex particle. This new approach is depicted in Figure 1.2(b). Under development, there is the possibility to split each particle into multiple subparticles to obtain a wake refinement where the overlap between the particles is always guaranteed and smooth (Fig. 1.2(c)). In this case, since the number of particles increases largely, the computational cost is obviously higher.

1.3 Aeroelastic coupling between MBDyn and DUST

1.3.1 Theorical background

DUST and MBDyn communicate with each other through preCICE, which stands for Precise Code Interaction Coupling Environment. preCICE is a

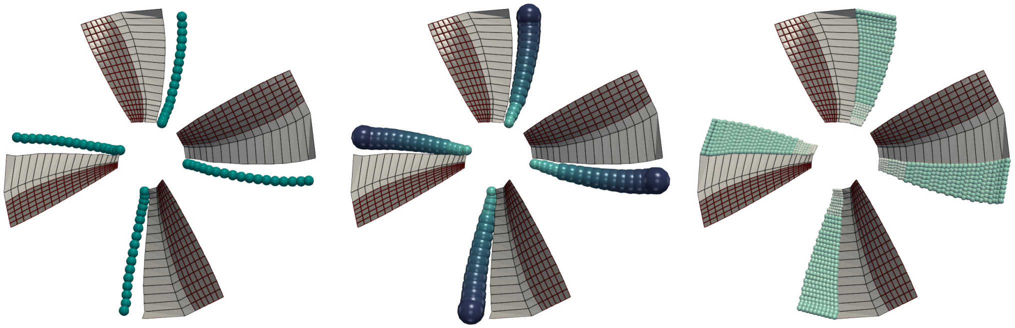

(a) Fixed vortex radius.

(b) Adaptive vortex radius.

(c) Adaptive vortex radius with wake refinement.

Figure 1.2: *Comparison of different vortex radius behaviors.*

library that enables communication between different software programs in partitioned multiphysics simulations. It was initially created for simulations involving fluid-structure interaction and conjugate heat transfer. In simpler terms, preCICE acts as a bridge between DUST and MBDyn, allowing them to exchange information and work together in a coordinated way. It ensures that the simulations run smoothly by handling the communication between the two programs. By using preCICE, DUST and MBDyn can collaborate effectively and achieve accurate and efficient results in their multiphysics simulations.

preCICE is a (`https://github.com/precice/`) is a free software released under the LGPL3 license, designed to facilitate the coupling, or integration, of transient equations. It provides various methods for coupling these equations, as well as communication tools and data mapping schemes. preCICE is primarily written in C++, but it also offers additional bindings for programming languages such as C, Fortran, MATLAB, and Python.

To establish communication between MBDyn and external software in DUST, MBDyn utilizes its own C++, C, Fortran, and Python API. However, in the case of DUST, there was no existing API available. Therefore, to enable coupling with DUST and provide the necessary functionalities for the adapter with preCICE, new Fortran modules were developed. The process involved implementing these Fortran modules to encompass all the essential classes, subroutines, and functions required by the adapter.

A new adapter was implemented to support the communication of all kinematic variables (position, orientation, velocity, and angular velocity), plus the forces and moments that act on the nodes of a model MBDyn exposed through an external structural force element. Figure 1.3 shows the communication and information exchange scheme managed through the adapters for the two solvers.

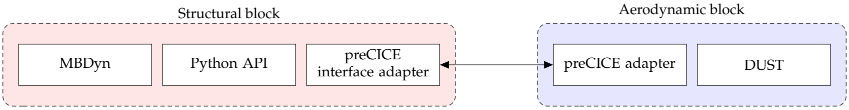

Figure 1.3: *Scheme of the communication managed through adapters for MBDyn and DUST.*

The interface between structural and aerodynamic grids is obtained as a weighted average of the anisotropic distance between the nodes of the two grids and is used for motion interpolation and consistent force and moment reduction. Figure 1.4 shows the q nodes of the structural grid, namely Q_q. The centers and vertices of each aerodynamic mesh are, respectively, P_e and P_p, where e and p are the corresponding indices.

The kinematic variables ϕ_p, of a point p positioned on the aerodynamic surface of a DUST component, are evaluated as the following weighted average:

$$\phi_p = \sum_q w_{pq} \phi_q \tag{1.44}$$

where ϕ_q is the same kinematic variable associated with the qth structural node of the MBDyn model.

The weights denoted as w_{pq} are a collection of real numbers that are greater than or equal to zero and fulfill certain conditions that ensure their total sum is normalized,

$$\sum_q w_{pq} = 1 \qquad \forall p \tag{1.45}$$

The coefficients for the weighted average of the variables linked between the structural nodes q and the aerodynamic nodes p are determined based on the inverse distance of the anisotropic norm of the vectors $|(P_p - Q_q)|$. For instance, let's consider the local coordinates in the reference configuration denoted as $\boldsymbol{r}_{pq}$. We can define the norm of these vectors as

$$\|(P_p - Q_q)\|^2 := \boldsymbol{R}_{pq}^T \, \mathbf{W} \, \boldsymbol{R}_{pq} \tag{1.46}$$

where $\mathbf{W}$ is a positive semidefinite matrix that provides an anisotropy degree of freedom in defining the norm [89]:

$$\mathbf{W} = \begin{bmatrix} 0.001 & 0 & 0 \\ 0 & 1. & 0 \\ 0 & 0 & 0.001 \end{bmatrix} \tag{1.47}$$

The rotation matrix $\boldsymbol{R}_{pq}$ is used to transform the structural coordinates from the MBDyn reference frame to the DUST component reference frame. These weights can be utilized for interpolating rotations by employing the orientation vector parameterization, denoted as $\boldsymbol{\varphi}_{pq}$.

Kinematic and Load Variables

The coordinates of a point P belonging to an aerodynamic surface in the global reference frame g are evaluated as

$$(P_p - O)^g = \sum_{Q \in I_P} w_{pq} \left\{ (Q_q - O)^g + \mathbf{R}_Q^{r \to g} (P_p - Q_q) \right\} \tag{1.48}$$

where a set Q that represents certain structural points Q_q. These points belong to an aerodynamic component called I_p. The expression $(Q_q - O)^g$ represents the distance between each structural point Q_q and the origin. The term $\mathbf{R}_Q^{r \to g}(P_p - Q_q)$ involves rotating the difference between an aerodynamic point P_p and a structural point Q_q using a global coordinate system. Its angular velocity $\boldsymbol{\omega}_P$ and velocity $\boldsymbol{v}_P$, respectively, are

$$\boldsymbol{\omega}_P = \sum_{Q \in I_P} w_{pq} \, \boldsymbol{\omega}_Q \quad \boldsymbol{v}_P = \sum_{Q \in I_P} w_{pq} \left\{ \boldsymbol{v}_Q + \boldsymbol{\omega}_Q \times (P - Q) \right\} \tag{1.49}$$

To evaluate the aerodynamic forces and moments, we use evaluation points, denoted as P_e, located in the center of each panel. These evaluation points help us calculate the forces and moments acting on the aircraft. For the lifting line component, firstly is determined the center of the lifting line, which is positioned at 25% of the chord. At this point, the loads acting on the lifting line are assessed. Next, we transfer these loads from the lifting line to the structural nodes. To achieve this is applied the principles of conservation of forces and moments. This approach allows us to determine the forces and moments at each structural node, as

$$\boldsymbol{f}_Q = \sum_{e \in J_Q} w_{qe} \, \boldsymbol{f}_e \quad \boldsymbol{m}_Q = \sum_{e \in J_Q} w_{qe} \left\{ \boldsymbol{m}_e + (P_e - Q_q) \times \boldsymbol{f}_e \right\} \tag{1.50}$$

where $e \in J_Q$ indicates the subset of evaluation points that belong to each sub-component J_Q, and the weights w_{qe} are calculated using Equations (1.46) and (1.48), by computing the distance between each structural node and the evaluation point.

It can demonstrated that the equations representing the loads are in agreement with the equations representing the kinematic variables. The power exerted by the loads on the structure, denoted as W_s, is the same as the power exerted by the loads on the aerodynamic surface, denoted as W_a. In other words, the virtual work done by the aerodynamic forces is equal to the work done on the structure, expressed as $\delta W_s = \delta W_a$.

$$W_s = \sum_Q \{\boldsymbol{f}_Q \cdot \boldsymbol{v}_Q + \boldsymbol{m}_Q \cdot \boldsymbol{\omega}_Q\} = \tag{1.51}$$

$$= \sum_Q w_{eq} \left\{ \sum_{e \in J_Q} \boldsymbol{f}_e \cdot \boldsymbol{v}_Q + \sum_{e \in J_Q} [\boldsymbol{m}_e + (P_e - Q) \times \boldsymbol{f}_e] \cdot \boldsymbol{\omega}_Q \right\} = \tag{1.52}$$

$$= \sum_Q \sum_{e \in J_Q} w_{eq} \{\boldsymbol{f}_e \cdot \boldsymbol{v}_Q + [\boldsymbol{m}_e + (P_e - Q) \times \boldsymbol{f}_e] \cdot \boldsymbol{\omega}_Q\} = \tag{1.53}$$

$$= \sum_e \sum_{Q \in I_e} w_{eq} \{\boldsymbol{f}_e \cdot \boldsymbol{v}_Q + [\boldsymbol{m}_e + (P_e - Q) \times \boldsymbol{f}_e] \cdot \boldsymbol{\omega}_Q\} = \tag{1.54}$$

$$= \sum_e \left\{ \boldsymbol{f}_e \cdot \sum_{Q \in I_e} w_{eq} [\boldsymbol{v}_Q + \boldsymbol{\omega}_Q \times (P_e - Q)] + \boldsymbol{m}_e \cdot \sum_{Q \in I_e} w_{eq} \boldsymbol{\omega}_Q \right\} = \tag{1.55}$$

$$= \sum_e \{\boldsymbol{f}_e \cdot \boldsymbol{v}_e + \boldsymbol{m}_e \cdot \boldsymbol{\omega}_e\} = W_a \tag{1.56}$$

1.3.2 Implementation

In this coupled simulation between two solvers using an implicit tight serial scheme, the flow of information is shown in Figure 1.5.

First, the object `precice` of class `t_precice` is declared. This object is responsible for handling the coupled simulation through the preCICE library. It manages both data communication and updating of the coupled components in the aerodynamic model. Next, an instance of the DUST solver is created to participate in the coupled simulation. It reads the XML preCICE configuration file. After some preliminary operations, the mesh

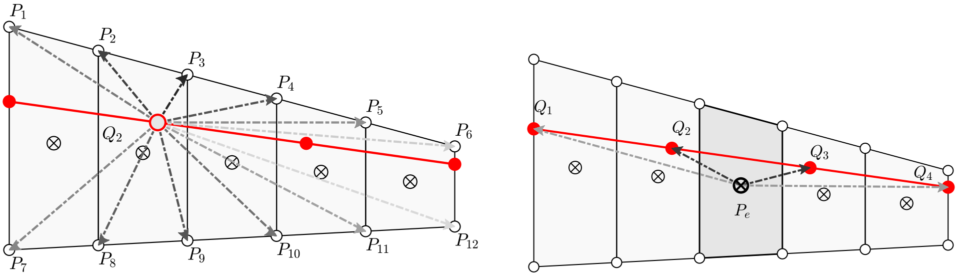

Figure 1.4: *Scheme for motion interpolation (**left**) and force and moment transfer (**right**). Structural points are represented by red dots. Nodes of the aerodynamic mesh and panels centers are represented with plain dot and crosses, respectively.*

used for coupling the codes is defined. This mesh determines how the different components interact with each other. The fields that will be involved in the communication between the solvers are initialized. These fields represent the data that will be exchanged during the simulation. The Fast Multiple Kernels, wake, and linear system are initialized. These are crucial components in the simulation that handle different aspects of the aerodynamic model. Before the time loop starts, communication is established between the coupled codes. This ensures that the solvers are ready to exchange information during the simulation.

The time loop begins with the update of DUST's explicit aerodynamic elements, such as lifting lines and actuator disks. These elements are updated based on the current state of the simulation. A checkpoint of the exchanged fields is stored. This checkpoint will be used during sub-iterations of preCICE's implicit coupling. It allows the solver to reload the previously exchanged data during these sub-iterations. DUST receives the kinematic variables of the structural nodes from MBDyn. These variables are used to update the surfaces of the coupled components and the near-field wake elements. The linear system is then updated and solved. This step calculates the strengths of the vortexes of the surface panels and the vortex lattice elements. Then, The solution of the non-linear vortex lattice and lifting line problems follow.

The aerodynamic forces and moments are calculated and applied to the nodes at the interface between the aerodynamic and structural meshes. These forces and moments are then sent to a software called MBDyn. The kinematics variables are checked for convergence. If they have not converged, the checkpoint fields are reloaded, and a new subiteration starts. If convergence is achieved, the current time step is finalized. The program saves the current status and updates the wake and geometry of the com-

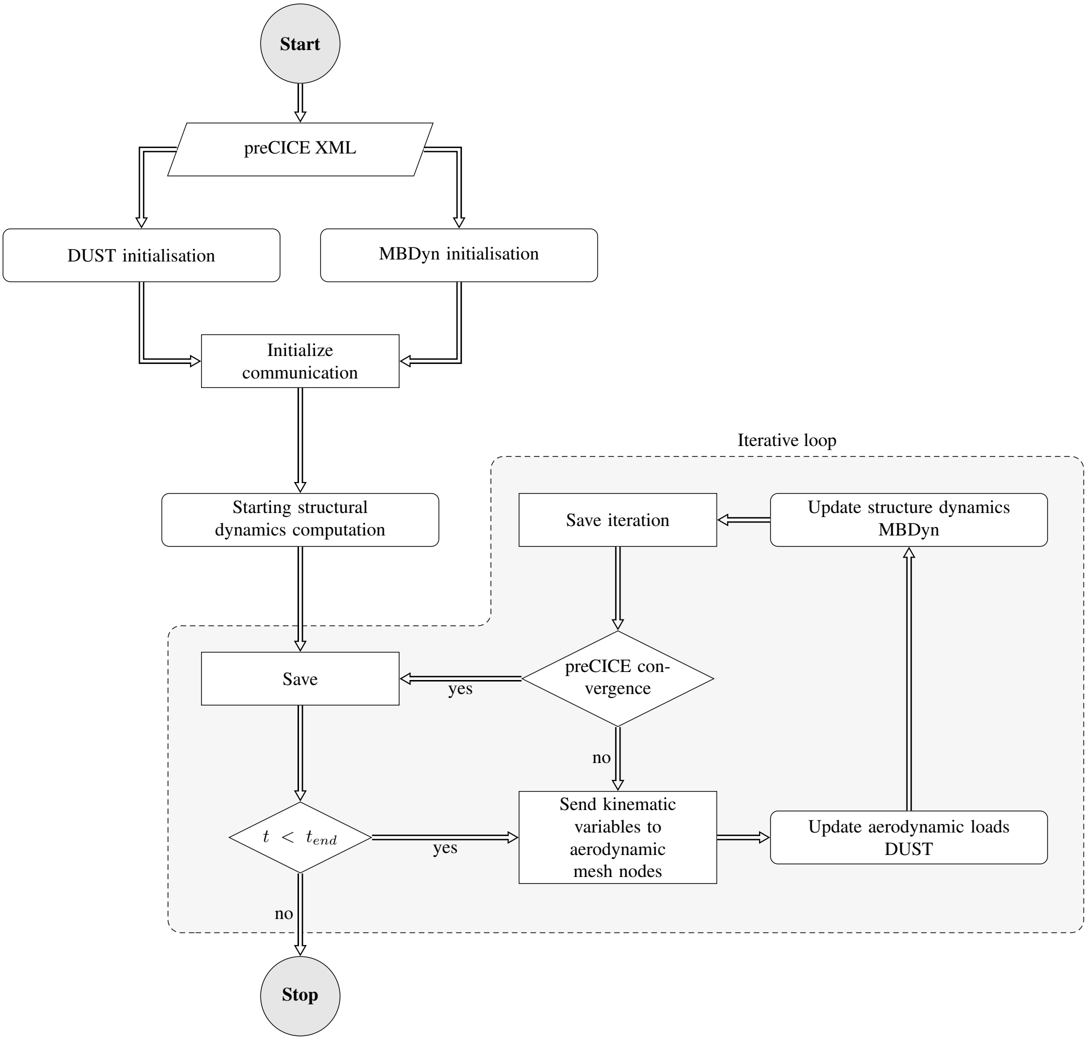

Figure 1.5: *Flowchart of the implicit coupled simulation managed by preCICE between DUST and MBDyn [94].*

ponents that are not coupled for the next time step. During each internal iteration of preCICE (a software for coupling simulations), the location of the trailing edge point is consistently updated. This ensures that the leading edge of the wake is properly positioned and that the released particle is correctly placed.

1.3.3 Hinged surfaces modeling

Modeling the deflection of a control surface is crucial for simulating aircraft maneuvers and achieving proper trimming in a free-free condition. To accomplish this in MBDyn, we can model the deflection of the control surface as a rigid or deformable body, which is appropriately constrained to the fixed part of the vehicle. This constraint ensures that the control surface can only rotate relative to the hinge axis. In DUST, the capability to include a control surface in the aerodynamic mesh has been recently introduced. Let's first discuss the model implemented for hinged surfaces in DUST using a two-dimensional example and then extend it to three-dimensional deformable components.

In Fig. 1.6 (left), is depicted how the control surface is defined in a two-dimensional problem. This is done in the local reference frame of the component. The position of the hinge axis is denoted as H. The direction along the chord of the airfoil is represented by ξ. Additionally, a blending region $[-u, u]$ is introduced to ensure a smooth transition in the mesh as the surface rotates at an angle θ. It is important to note that in this 2D modeling, it is assumed that the rotation axis, denoted as $\hat{\boldsymbol{h}}$, is perpendicular to the plane of the airfoil.

As shown in Fig. 1.6, an orthonormal reference frame for the hinge is defined with the origin in H and the axes $\hat{\boldsymbol{\xi}}$, $\hat{\boldsymbol{\eta}} = \hat{\boldsymbol{h}} \times \hat{\boldsymbol{\xi}}$. The position of a point with respect to this reference frame is as follows.

$$\boldsymbol{r} = \xi \, \hat{\boldsymbol{\xi}} + \eta \, \hat{\boldsymbol{\eta}} + h \, \hat{\boldsymbol{h}} \tag{1.57}$$

Three regions are defined using the coordinates based on this reference frame:

1. $\xi \leq -u$: no influence on control surface rotation;

2. $\xi \geq u$: rigid rotation on the hinge:

$$\Delta \boldsymbol{r} = \sin\theta \hat{\boldsymbol{h}} \times \boldsymbol{r} + (1 - \cos\,\theta) \hat{\boldsymbol{h}} \times \hat{\boldsymbol{h}} \times \boldsymbol{r} \tag{1.58}$$

3. $-u \leq \xi \leq u$: blending region to avoid irregularities, defined as an arc

of a circle whose center is located at point C and whose radius is:

$$\overline{CC'} = \frac{\overline{C'H}}{\tan\dfrac{\theta}{2}} \qquad \text{where} \quad \overline{C'H} = u \tag{1.59}$$

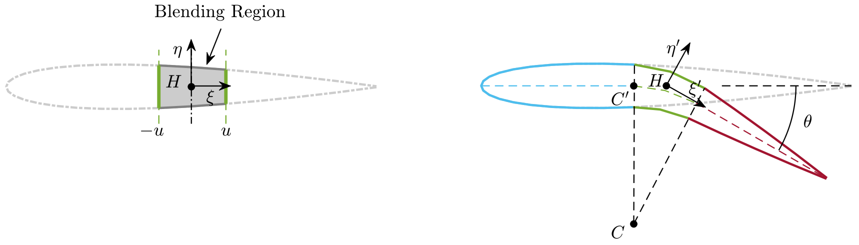

Figure 1.6: *Scheme of the two-dimensional hinged surface configuration.*

In a three-dimensional problem, the reference configuration of a control surface for a generic swept wing is defined in the wind axis reference frame of the component, as shown in Fig. 1.7.

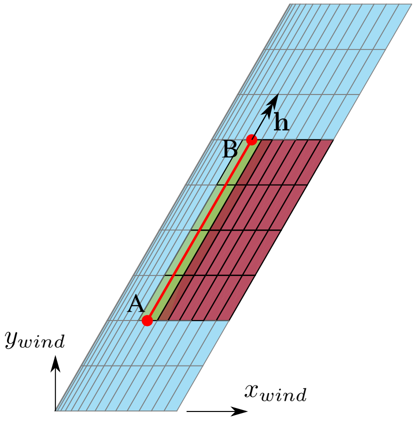

Figure 1.7: *Hinge reference system for a swept wing.*

Therefore, the aerodynamic sections involved in the deflection of the control surface are those that satisfy condition $y(A) < y(P) < y(B)$,

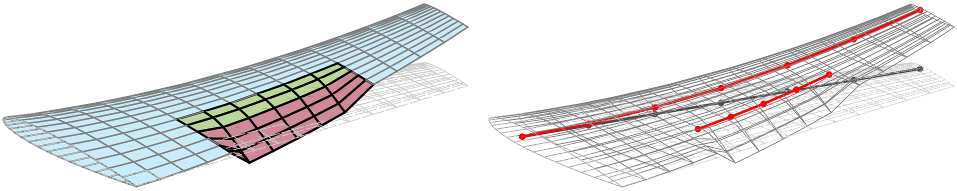

Figure 1.8: *Control surface deflection for a deformable wing.*

where $y(P)$ is the ordinate of the aerodynamic mesh point $P_i - th$ expressed in the wind reference system. As in the 2D case, one can define the three regions for each stripe identified at the previous point. The y coordinate of the origin of the sectional reference frame is determined by linear interpolation between points A and B.

In MBDyn, when the movable surface is connected to a structural component, the orientation of the hinge in the DUST nodes is determined by the orientation of the nodes in the MBDyn model. To calculate the rotation axis, we use the formula: $\hat{\mathbf{h}} = \dfrac{(B - A)}{|B - A|}$. For each point on the movable surface, it is linked to the hinge nodes. The kinematic variables of the hinge nodes are then used to determine the motion of the movable surface. This is done by taking a weighted average of the motion induced by the rotation of the hinge nodes. The weights, denoted as w_{ph}, are calculated based on the h components of the vectors connecting the control surface points to the hinge nodes. These weights, w_{ph}, are combined with the structural interpolation weight, w, to allow for deformation of the structure. This combination of weights enables the rigid deflection of the moving surface. You can refer to Fig. 1.8 for a visual representation of this process.

1.3.4 Coupling Validation

A detailed validation of the implemented coupled code is published in [92]. For brevity, in this work, only the case of aeroelastic validation of the Goland wing is reported. The Goland's wing, a numerical test case that was widely used in literature as a benchmark for flutter predictions. This low aspect ratio wedged wing ($AR \approx 3.33$) is also interesting to highlight the impact on flutter calculations of 2D and 3D aerodynamic models. Figure 1.9 shows the layout of the problem. EA indicates the elastic axis; CG indicates the center of gravity axis. U_∞ is the free-stream velocity. All the relevant geometrical and structural properties are reported in Table 1.2. They have been obtained from [83].

Two different aerodynamic meshes were utilized for the Goland wing.

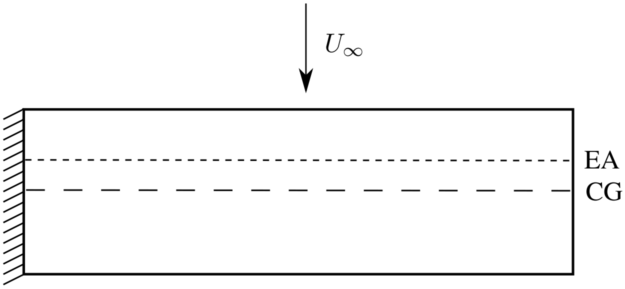

Figure 1.9: *Goland's wing model layout.*

Wing properties			
Half span	6.096 m	Moment of inertia	8.64 $\mathrm{kg\,m^2}$
Chord, c	1.8288 m	Mass/unit span	35.71 $\mathrm{kg\,m^{-1}}$
Elastic axis	$0.33 \cdot$ c	Torsional stiffness	$0.99{\times}10^6$ $\mathrm{N\,m^2}$
Center of gravity	$0.43 \cdot$ c	Bending stiffness	$9.77{\times}10^6$ $\mathrm{N\,m^2}$
Flight conditions			
Air density	1.020 $\mathrm{kg\,m^{-3}}$	AoA Perturbation	0.05 deg

Table 1.2: *Goland's wing properties and flight condition [83].*

The first mesh involved modeling the wing as a flat plate using vortex lattice (VL) elements, while the second mesh used surface panels (SP) to reproduce the wing's geometrical shape and thickness. The computed aerodynamic loads were subjected to a convergence analysis, which revealed that both models required 30 spanwise elements for proper spatial discretization. For the VL flat mesh, 30 uniform divisions were needed in the chordwise direction. In contrast, the SP model required 30 divisions for the lower and upper side of the wing, with a half-cosine refined distribution at the leading edge. The structural model created in MBDyn consisted of four beams that were discretized using a C^0 beam discretization based on the finite volume concept proposed in [42]. To ensure an adequate number of beam elements, a convergence requirement on the first four modes of the wing was satisfied. The frequencies of the first four normal vibration modes of the wing, as computed by MBDyn, were compared to those of Goland's work [44] and NASTRAN, and the results are reported in Table 1.3.

The present study utilized tight coupled time-marching simulations, with a time discretization of $0.001\,\mathrm{s}$, and a fourteen-chord long box behind the wing was considered to model the evolution of the wake particles. This resulted in a developed wake composed of approximately three thousand vortex particles. To perform a time-marched coupled simulation with a to-

	Goland [44] Hz	NASTRAN Hz	MBDyn Hz
1^{st} Bending	7.66	7.66	7.66
1^{st} Torsion	15.24	15.24	15.21
2^{nd} Bending	38.80	38.59	38.54
2^{nd} Torsion	55.33	54.84	54.79

Table 1.3: *Comparison of the first four natural frequencies computed for the Goland's wing [44].*

tal duration of one second, a workstation equipped with an Intel® Core™ i9-9980XE processor was used. This processor has a base frequency of 3.00 GHz, 18 physical cores, and 2 threads for each core. The computation time for the vortex lattice (VL) model was approximately 19 minutes, while the surface panels (SP) model took about 29 minutes.

To investigate the flutter instability of the Goland wing, a perturbation in the form of a non-zero angle of attack of $0.05°$ was introduced, which was also employed in [79]. The matrix pencil estimation (MPE) method [49] was utilized to identify the frequency and damping of the response by analyzing the time history of the wing-tip deflection. Figure 1.10 displays the z-displacement of the last structural external node during the flutter onset, as computed with the SP model. The red line represents a stable damped response, whereas the blue line depicts the incipient flutter condition, where a constant amplitude free oscillation is observed. The green line illustrates the unstable response at a speed greater than the flutter speed. Additionally, Fig. 1.10 (left) demonstrates the deformed mesh associated with the bending-torsion instability and the corresponding distribution of the pressure coefficient. These findings demonstrate the accurate capturing of fixed-wing flutter by the coupled simulation.

Table 1.4 presents a comparison of the flutter speed and frequency computed by various independent researchers. The results obtained with the coupled code are in good agreement with those obtained by similar codes that use 3D aerodynamic models [79, 83, 105]. Specifically, the discrepancy with the results obtained using the same MBDyn structural model but with its built-in aerodynamics based on two-dimensional unsteady strip theory highlights the superior capability of the coupled code in investigating aeroelastic problems. Furthermore, the comparison of the results from the literature, which are based on 2D and 3D models, confirms the need for a three-dimensional aerodynamic model for an accurate and realistic flutter analysis of low aspect ratio wings.

Fig. 1.11 showcases the frequency and damping of the first beam tor-

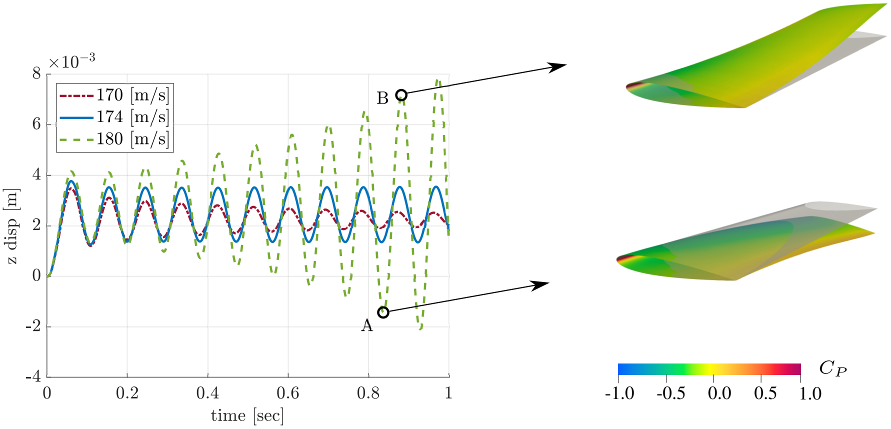

Figure 1.10: *Time history of the Goland's wing-tip deflection evaluated with surface panels aerodynamic mesh at three different wind speeds.*

Author	*Model*	V_f $\mathrm{m\,s^{-1}}$	f_f Hz
Goland [44]	Analytical	137.2	11.25
Patil et al. [83]	Intrinsic beam + strip theory	135.6	11.17
Wang et al. [105]	ZAERO	174.3	-
Wang et al. [105]	Intrinsic beam + UVLM	163.8	-
Murua et al. [79]	SHARP, Displacement beam + UVLM	165	10.98
Present Work	MBDyn's built-in strip theory	135.1	11.07
Present Work	DUST (VL)-MBDyn	168.2	10.84
Present Work	DUST (NL-VL)-MBDyn	173.9	11.01
Present Work	DUST (SP)-MBDyn	174.2	11.06

Table 1.4: *Comparison of flutter speed and frequency computed for Goland's wing (V-g diagram).*

sional mode of the wing as a function of the free-stream velocity, which enables the assessment of the performance of the coupled code using different aerodynamic models. The graph provides insights into the effects of the employed aerodynamic models on the aeroelastic behavior of the wing, which is crucial in evaluating the accuracy of the coupled code. By comparing the performance of the code using different aerodynamic models, researchers can identify the strengths and limitations of each model and choose the most appropriate one for their specific application. As complete frequency/damping-velocity plots have not been found in the literature, the presented data can also serve as a reference for future studies on aeroelasticity, particularly in the context of low aspect ratio wings.

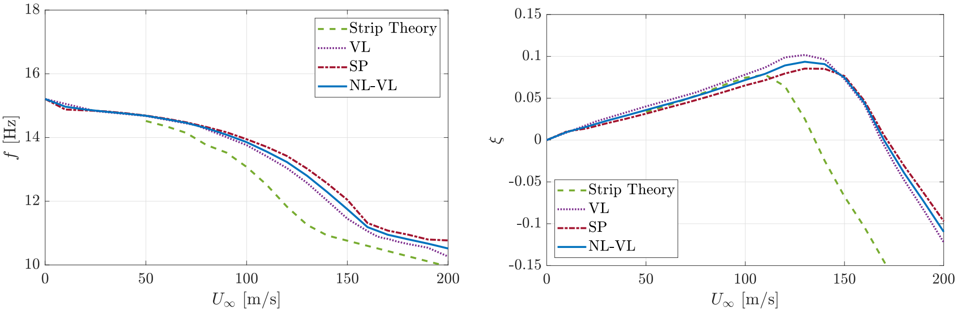

Figure 1.11: *Frequency and damping vs velocity for Goland's wing. Coupled simulations results (VL and SP mesh) and MBDyn results with 2D Strip Theory aerodynamics.*

The numerical findings from the coupled simulations utilizing a surface panel mesh (SP) exhibit a marginally higher aerodynamic damping compared to the ones obtained through vortex lattice (VL). The analysis demonstrates an approximate 3.7% increase in predicted flutter speed (Fig. 1.11 right). When the correction is implemented on the VL, which involves the transition to the NL-VL, the outcomes are remarkably similar to those attained from surface panels (SP). Nevertheless, the minute differences in the results between the various models indicate that for uncomplicated configurations without intricate aerodynamic interactions between the bodies, a vortex lattice mesh is more advantageous than surface panels as it significantly reduces the computational cost.

CHAPTER 2

Interactional aerodynamics assessment

INTERACTIONAL aerodynamics plays a key role when dealing with complex aircraft configurations in which you have several components interacting with each other aerodynamically. In particular, these interactions are relevant when there are rotating lifting surfaces, as in the case of rotors and propellers, whose wake generates a complex three-dimensional field of motion around the aircraft. The interaction between rotors was widely investigated in the literature, with particular effort on helicopter configurations. Indeed, rotorcraft research literature considers several studies of the aerodynamic interaction between tandem, coaxial rotors, and tiltrotors mainly focused on hover flight conditions (see for instance the works from Harris [47] and Ramasamy [88]).

Aerodynamic interaction between rotors represents a key aspect also in the study of tiltorotor and compound helicopter configurations. In particular, very recent literature presents some studies of aerodynamic interactions occurring between the main rotor and propeller wakes for a high-speed compound helicopter such as the Airbus Racer (see for instance [22]). Indeed, for such configuration strong aerodynamic interactions between propellers and main rotor wake occur typically at low speeds, affecting aircraft performance and maneuverability. Considering a machine such as a tiltrotor, the interaction between rotor wake and other lifting surfaces such as the main wing and tailplanes is also important to take into account.

Generally speaking, aerodynamic interaction between multi-propeller-wings configurations represents also an interesting benchmark for the validation of numerical CFD tools. In particular, in recent years, the rotorcraft industry and research dedicated a wide effort to the development of mid-fidelity aerodynamic solvers to be used for the preliminary design of novel innovative VTOL aircraft configurations [102, 112] or to investigate problems related to interactional flow physics typical of complex rotorcraft configurations, as tiltrotors and compounds helicopters [97, 106]. The use of vortex particle methods (VPM) for wake modeling [29, 107], implemented in some of these mid-fidelity solvers, opened a novel scenario for a faster and more accurate evaluation of the aerodynamic performance of complex rotorcraft vehicles. Indeed, these VPM-based mid-fidelity numerical tools showed the capability to accurately evaluate the complex flow mechanisms involved in aerodynamic interactions between rotor wakes and bodies, while keeping low the computational effort required for simulations. Nevertheless, these solvers required a robust validation against experimental data, as done for instance by Alvarez and Ning [9, 10] that reproduced the side-by-side propellers experiment in hover by Zhou et al. [117] through a mid-fidelity VPM aerodynamic code finding a quite promising agreement with numerical results in terms of both performance and flow field representation.

In this chapter, the focus is on DUST's ability to capture different types of aerodynamic interactions, one of the strengths of the developed coupled code. To this end, 4 cases are considered:

- Isolated Rotor
- Propeller-propeller
- Wing-propeller
- Tiltrotor full aircraft configuration

2.1 Isolated Rotor

The initial test case involves simulating the proprotor of the XV-15 tiltrotor in various flight conditions, namely hover, forward flight in helicopter mode, and airplane mode. The aerodynamic profiles and main rotor data are presented in Table 2.1 and Table 2.2. The proprotor is equipped with metal blades. In the current study, the propeller blades were simulated as rigid blades using non-linear vortex lattice elements (NL-VL), and the aerodynamic performance data for the propeller airfoils were obtained from [39]. The simulations were performed using DUST with a propeller revolution length of 10 and a discretization time of 5° for the azimuthal angle of the blade. The computational time required to complete the simulation of the rotor configuration was about 8 minutes using a workstation with a Dual Intel® Xeon Gold 6230R @2.10GHz processor with 52 physical cores and 2 threads for each core. The subsequent section presents a comparison between the results obtained from DUST simulations using the NL-VL approach, the high-fidelity numerical simulations conducted by Jia et al. in [50] using a Detached Eddy Simulation (DES) approach, and the experimental data gathered during the test campaigns described by Felker et al. in [39] and Betzina in [18].

Table 2.1: *XV-15 metallic blade rotor: main data*

Parameter	Value	Unit
Blade	3	
Solidity	0.0891	
Radius (R)	3.81	m
Precone β	2.5	deg
Chord	0.3556	m
Twist	45	deg
Nominal speed (Ω)	589	RPM

Table 2.2: *XV-15 metallic blade rotor: profiles*

Profile	start (r/R)	end (r/R)
NACA 64-935	0.09	0.13
NACA 64-528	0.13	0.34
NACA 64-118	0.34	0.655
NACA 64-(1.5)12	0.655	0.9
NACA 64-208	0.9	1

2.1.1 Hover flight condition

The comparison of rotor thrust coefficient (C_T) and rotor torque coefficient (C_Q) as a function of the collective angle of the blade are shown in Figs. 2.1(a) and 2.1(b). The comparison of rotor figure of merit (FM) is shown in Figure 2.1(c). To calculate these coefficients, the following formulas were used:

$$C_T = \frac{T}{\rho \pi \Omega^2 R^4} \qquad C_Q = \frac{Q}{\rho \pi \Omega^2 R^5} \qquad F_M = \frac{C_T^{3/2}}{C_Q \sqrt{2}} \tag{2.1}$$

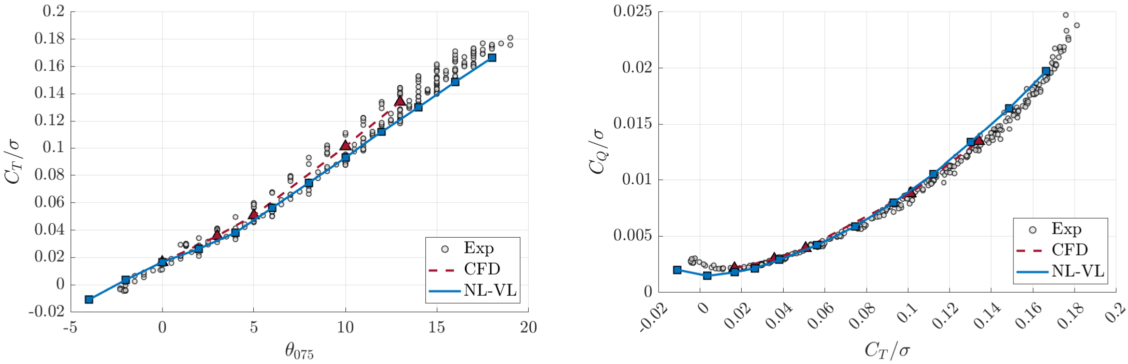

(a) C_T/σ vs collective angle.

(b) C_Q/σ vs C_T/σ.

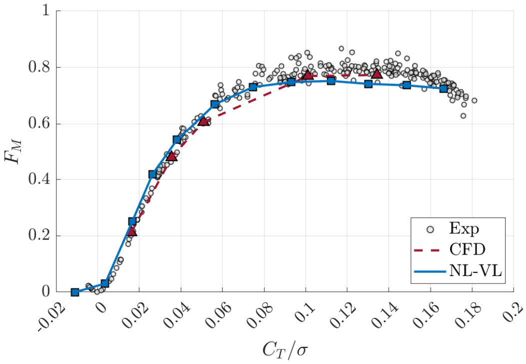

(c) F_M vs C_T/σ.

Figure 2.1: *Comparison of the aerodynamic performances for the XV-15 proprotor in hover. Experimental data taken from [39] (Exp), numerical data from [50] (CFD) and DUST (NL-VL).*

The performance curves obtained from the DUST simulations capture the behavior of the experimental data across the entire range of tested collective blade angles. Additionally, the comparison between the curves shows that the DUST approach is capable of evaluating aerodynamic performance similar to that of a DES approach for this case, but with significantly lower computational requirements. The comparison of the figure of merit in Fig. 2.1(c) indicates excellent agreement between the DUST results and the experimental data for the rotor's overall performance in hover, particularly at low C_T/σ. Furthermore, due to the lower computational cost of the DUST approach, a larger number of simulations could be performed with finer steps in collective angle, covering the entire operational range of the experimental curve.

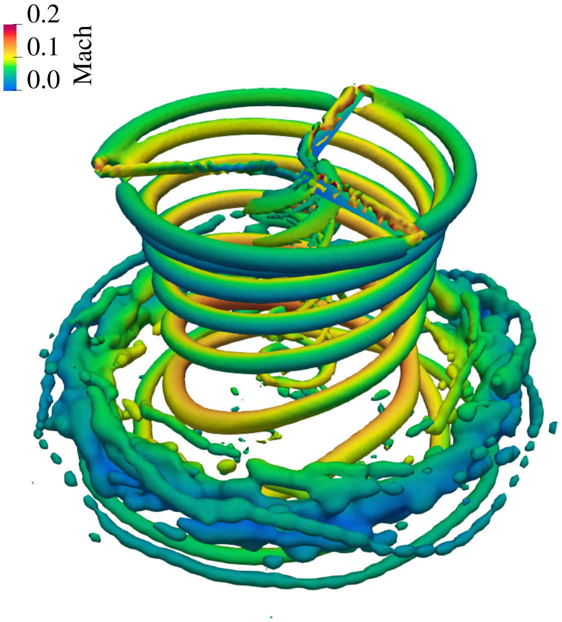

Figure 2.2: *Wake visualization of the XV-15 proprotor in hover by means of isosurfaces of the Q-criterion computed by DUST colored by Mach number.*

Figure 2.2 depicts a visualization of the flow field for the current test scenario, where the proprotor is in a hover configuration. The helical vortices that form in the wake of the proprotor are clearly visible in the image, which was generated using DUST and highlights these vortices through iso-surfaces of Q-criterion.

2.1.2 Forward flight condition

DUST was used to investigate the proprotor of the XV-15 in forward flight conditions, specifically in helicopter mode configurations. Three shaft angle attitudes were considered: α=$-5°$, α=$0°$, and α=$5°$, all at an advance ratio J of 0.17. This choice was made to allow for an investigation of DUST's capabilities in both propulsive and descending forward flight conditions, similar to the approach taken in [50]. Figures 2.3(a) and 2.3(b) show the comparison of the rotor torque coefficient (C_Q) as a function, respectively, of the rotor thrust coefficient(C_T) and of the lift coefficient (C_L). Figures 2.3(a) and 2.3(b) illustrate the comparison of the rotor torque coefficient (C_Q) with the rotor thrust coefficient (C_T) and the lift coefficient (C_L), respectively. All quantities are scaled with respect to the rotor solidity σ.

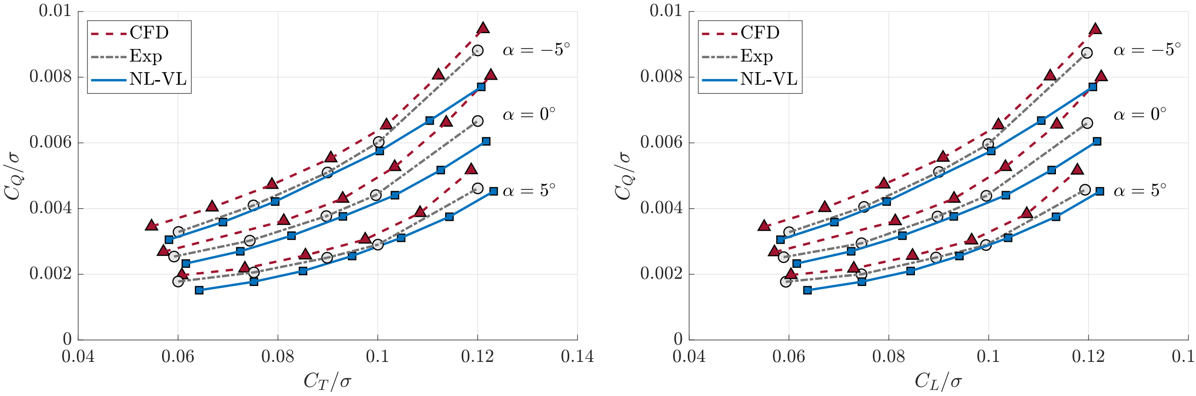

(a) C_Q/σ vs C_T/σ.

(b) C_Q/σ vs C_L/σ.

Figure 2.3: *Comparison of the aerodynamic performances for the XV-15 proprotor in forward flight. Experimental data taken from [18] (Exp), numerical data from [50] (CFD) and DUST (NL-VL).*

The comparison between the DUST simulations and the experimental data for this flight condition reveals that the DUST approach provides a reasonable representation of the proprotor aerodynamic performance. The relatively good agreement found between the DUST results and the experimental data indicates that the NL-VL method is capable of capturing the key physics involved in the proprotor flowfield. However, the observed underestimation of the experimental data by the DUST results in the entire range of collective blade angles suggests that there may be room for improvement in the NL-VL model. It is worth noting that the DUST approach shows a better performance in reproducing the experimental data than the high-fidelity CFD simulations, especially in the lower range of collective angles. This highlights the potential of the DUST approach in providing accurate aerodynamic performance evaluation with significantly reduced computational cost compared to CFD simulations. However, in the higher range of thrust or lift coefficient, larger discrepancies are observed between the DUST results and the experimental data. This behavior is expected as high blade loading conditions are characterized by more significant viscous effects and separated flow regions, which are not accurately captured by the DUST approach. Therefore, while the DUST approach is a promising tool for the proprotor aerodynamic performance evaluation, its limitations should be carefully considered when dealing with high blade loading conditions.

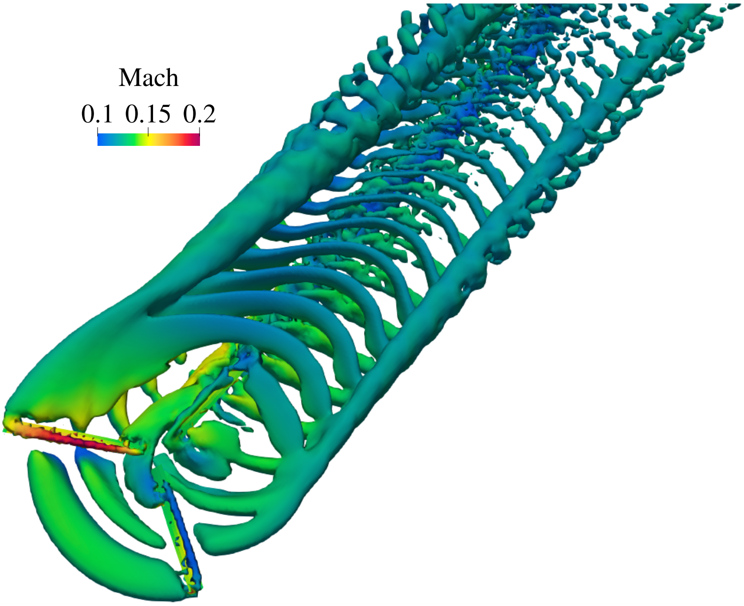

Figure 2.4: *Wake visualization of the XV-15 proprotor in advanced flight at* $5°$ *collective, and* $\alpha = 5°$ *by means of iso-surfaces of Q-criterion computed by DUST colored by Mach number.*

The flight conditions considered in this study are characterized by significant aerodynamic interactional effects, as demonstrated by the flow visualization presented in Fig. 2.4. The figure highlights the interaction of the downstream blades with the tip vortices, indicating the presence of strong flow interactions.

2.1.3 Airplane Mode flight condition

The XV-15 proprotor's aerodynamic performance in aircraft mode configurations is investigated using DUST simulations for various collective blade pitch angles at an advance ratio of 0.337. The aim is to assess DUST's ability to accurately model the proprotor's aerodynamic behavior in this flight condition. The resulting aerodynamic performance is evaluated by comparing the torque coefficient (C_Q) and propulsive efficiency (η) against the thrust coefficient (C_T) for different collective blade pitch angles. Figures 2.5(a) and 2.5(b) show the comparisons, respectively.The propulsive efficiency (η) is calculated as follows:

$$\eta = \frac{C_T V_\infty}{C_Q \Omega R} \tag{2.2}$$

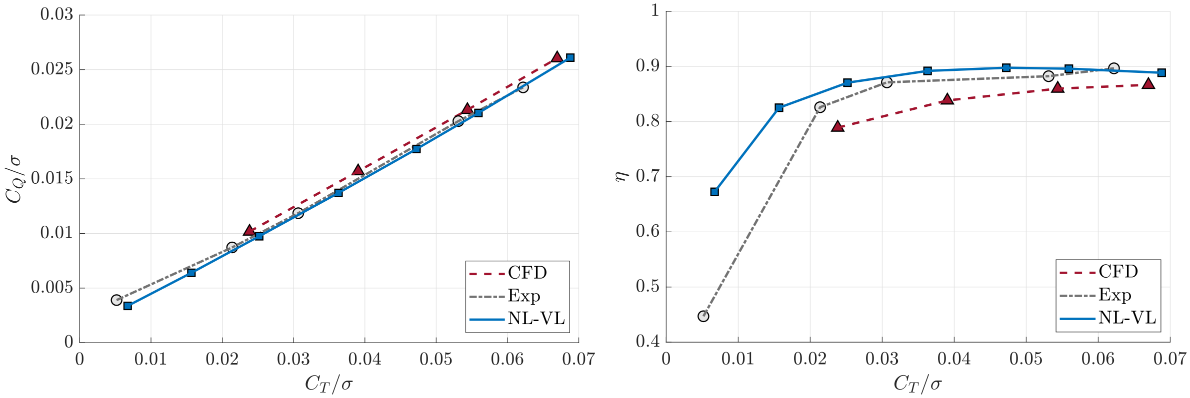

(a) C_Q/σ vs C_T/σ.

(b) C_Q/σ vs C_L/σ.

Figure 2.5: *Comparison of the aerodynamic performances for the XV-15 proprotor in airplane mode flight. Experimental data was taken from [18] (Exp), numerical data from [50] (CFD), and DUST (NL-VL).*

The DUST simulations exhibit a high level of agreement with the experimental data for the considered flight conditions, confirming the effectiveness of the DUST approach in accurately predicting propeller aerodynamic performance. The discrepancies between the DUST simulation results and the experimental data are considerably lower than those observed in high-fidelity CFD simulations. The experimental propulsive efficiency curves are slightly overestimated by the DUST simulations across almost the entire range of rotor thrust conditions tested. However, a larger discrepancy of around 20% is found only for the lowest blade load condition tested. This level of accuracy demonstrates the capability of DUST to accurately evaluate the propulsive efficiency of a rotor under these flight conditions.

The flow field representation of an airplane mode flight condition computed by DUST is presented in Fig. 2.6, where the isosurfaces of the Q-criterion are used to highlight the helical vortical structure of the proprotor wake. Unlike in helicopter mode configurations, this flight condition is characterized by a free-stream velocity dragging effect, which leads to the absence of interactions between the tip vortices and the downstream

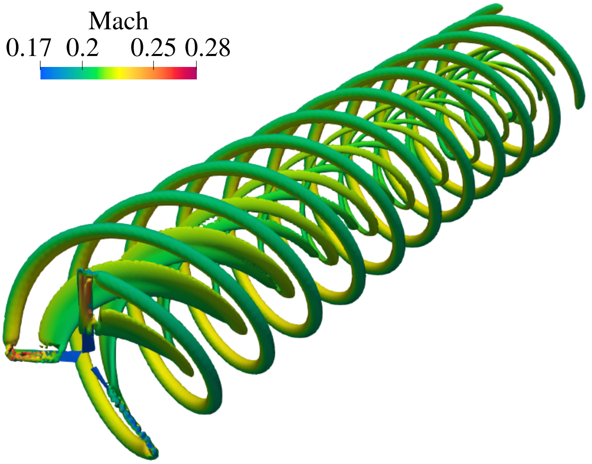

Figure 2.6: *Wake visualization of the XV-15 proprotor in airplane mode by means of isosurfaces of Q-criterion computed by DUST colored by Mach number.*

blades. The isosurfaces show a quite coherent and stable helical structure of the proprotor wake, which is consistent with the expected behavior of a well-designed rotor system in airplane mode flight. The DUST approach is able to accurately capture these complex flow phenomena, providing valuable insights into the aerodynamic performance of the proprotor system in various flight conditions.

2.2 Propeller-propeller

The second application concerns propeller aerodynamics considering the aerodynamic interaction between multiple propellers configurations. In particular, this application wants to analyze the effect of aerodynamic interactions on propeller performance by means of loads measurements and investigated the interacting flow mechanisms for tandem propellers configurations. The available experimental data are based on an experimental activity performed at the *S. De Ponte* wind tunnel of Politecnico di Milano described in [113, 114]. The propeller reported in Fig. 2.7(a) is a three-bladed configuration hub equipped with left-handed VarioProp 12C blades, thus resulting in a propeller disk diameter equal to $300\,\mathrm{mm}$. A $65\,\mathrm{mm}$ diameter aluminum spinner was screwed on the propeller hub and a polycarbonate nacelle with $270\,\mathrm{mm}$ is aimed to shield the driving system and the load cell. The propeller model geometry is available thanks to a 3D scanning of the blades. An internal aluminium frame was designed to support the propeller driving system and a bi-axial strain gauge load cell. One of the propeller models was equipped with a Hall-effect sensor that was mounted on the metallic plate below the motor. The Hall-effect sensor was used during the tests to provide the 1/rev signal for the measurement of propeller rotational speed and to trigger the phase-locked PIV measurements. The experimental campaign was performed on two propeller models in tandem configuration by changing their lateral separation distance at a fixed axial distance. Wind tunnel tests included loads measurements to evaluate, particularly, the effects on rear propeller performance provided by aerodynamic interaction of front propeller slipstream. Moreover, stereo PIV surveys were performed to accurately evaluate insights about interacting flow fields between propeller wakes for a typical cruise flight condition of eVTOL aircraft in an urban environment. A picture of the tandem propeller models set up inside the wind tunnel test section is shown in Fig. 2.7(b).

The axial distance L_x between the propellers disk is set equal to 5 rotor radii while several lateral separation distances L_y between propeller rotation axis were considered, see Fig. 2.8. Wind tunnel test conditions consisted of runs performed with tandem co-rotating clockwise propellers with the rotational speed of both propellers controlled to 7050 RPM. This RPM target value was considered to reproduce a typical tip Mach number, i.e., $M_t = 0.325$, of full-scale eVTOL aircraft propellers in cruise flight conditions.

The blade geometry used to build the numerical model of the propeller was digitally created by means of a 3D scanning of the blade model. In

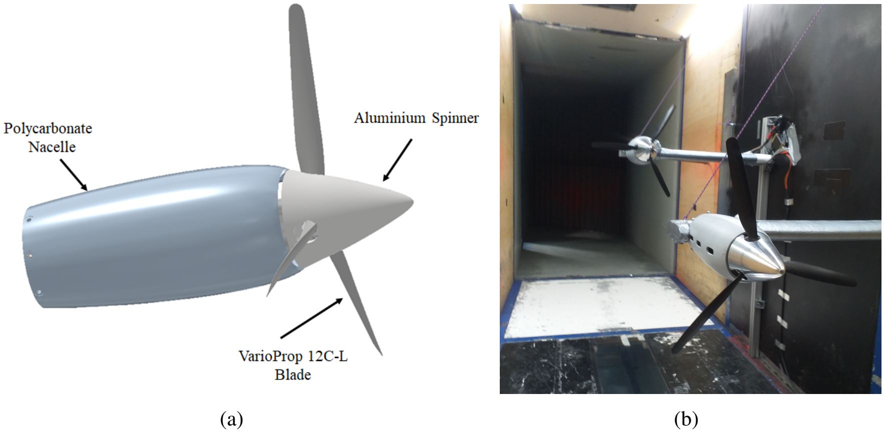

(a) (b)

Figure 2.7: *Layout of the experimental propeller model (a) and of the tandem propellers set up (b) at S. De Ponte wind tunnel of POLIMI.*

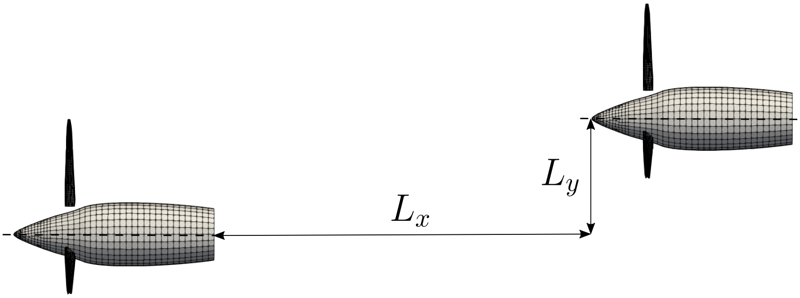

Figure 2.8: *Layout of the tandem propellers model mesh built for DUST simulations.*

particular, CAD software was used to generate the blade geometry from the surfaces provided by the scanning system. The maximum difference between the reconstructed blade CAD geometry and the 3D scanned surfaces was below $0.1\,\mathrm{mm}$.

A total number of 12 were extracted along the span direction. For each section, the airfoil geometry was extracted and the distribution of twist, chord, sweep, and dihedral was derived along the blade radial coordinate (r), as reported in Table 2.3 and illustrated in Fig. 2.9. Known airfoils were identified by identifying those most similar to those derived from the previous procedure.

r/R	chord [m]	twist [deg]	Airfoil
0.24	15.6	24.8	GOE-570
0.32	19.0	15.0	GOE-421
0.39	20.3	9.8	GOE-421
0.47	20.3	6.6	GOE-421
0.55	19.9	4.0	GOE-222
0.62	19.3	2.2	MH-112
0.70	18.5	0.78	GOE-675
0.77	17.5	-0.33	GOE-412
0.85	16.3	-1.07	NACA-4412
0.92	14.9	-1.57	GOE-564
0.97	13.2	-1.40	MH-23
1.00	7.3	-1.24	MH-23

Table 2.3: *Airfoils sections, chord and twist distributions along blade span.*

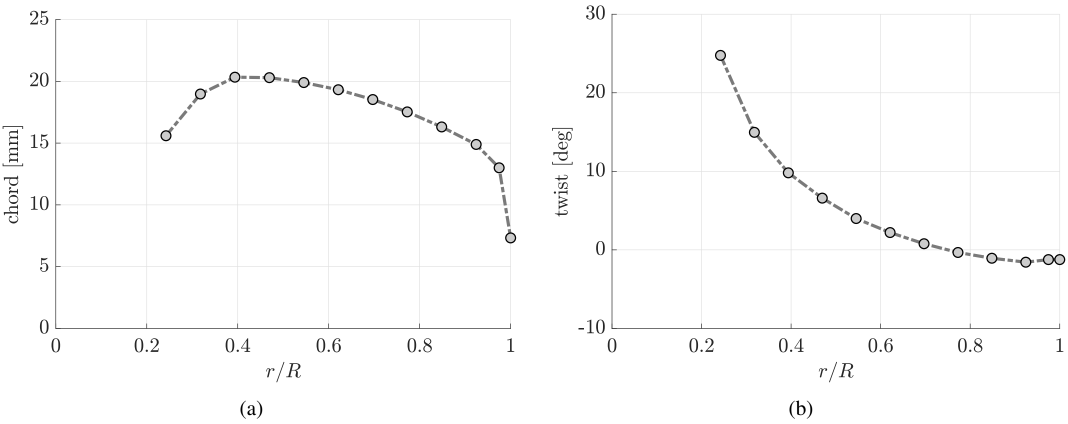

(a)

(b)

Figure 2.9: *Chord (a) and twist (b) distributions of the propeller blade along span-wise radial coordinate considering the 12 sections extracted.*

The numerical model of the propeller in DUST was built using two different elements: in the first, lifting lines (LL) were employed (Fig. 2.10(a)), while in the second, nonlinear vortex lattices (NL-VL) were used (Fig. 2.10(b)). For each of the three blades, both models have a total of 50 elements in a spanwise direction and in the case of NL-VL, the chord is discretized in 5 elements. The sectional tabulated aerodynamic coefficients were calculated by XFOIL simulations [33] in the angle of attack range before stall. The Viterna method [104] was used to calculate the post-stall behavior of the sectional aerodynamic load's coefficients in the range between ±180° of the angle of attack. In order to accurately reproduce the whole experimental propeller model geometry, the spinner-nacelle surface was included in the mesh. In particular, 1212 surface panel elements were used to model the spinner-nacelle geometry. The layout of the propeller mesh built for DUST simulations is shown in Fig. 2.10.

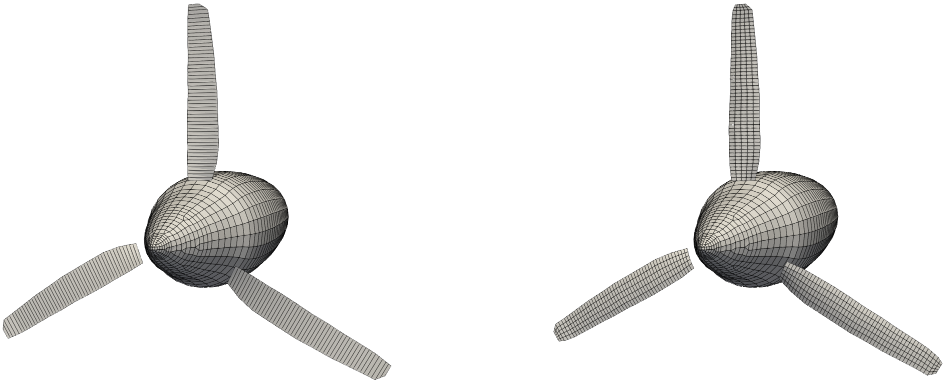

(a) Lifting lines blades.

(b) Vortex lattice blades.

Figure 2.10: *Layout of the propeller model mesh.*

2.2.1 Isolated propeller

The performance of the single propeller, considered as a reference to evaluate the effects of aerodynamic interaction between two overlapping propellers in tandem, is now presented. The thrust and the power coefficient, C_T and C_P, are defined as

$$C_T = \frac{T}{\rho \Omega^2 D^4},$$
$$C_P = \frac{2\pi Q}{\rho \Omega^2 D^5},$$

where S is the propeller diameter, Ω is the rotation speed in revolution per second, ρ is the free-stream density, T and Q are the propeller thrust and torque measured at the hub respectively.

Fig. 2.11 shows the behavior of the thrust coefficient C_T and power coefficient C_P as a function of advance ratio J for the two different DUST models compared to the experimental measurements.

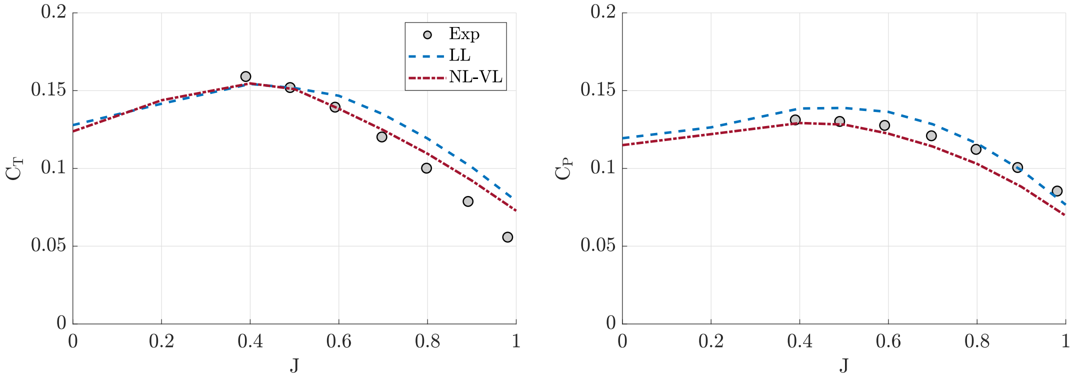

(a)

(b)

Figure 2.11: *Single propeller performance experimental and numerical results,* $M_t = 0.325$.

In general, there is good agreement between numerical and experimental results, especially at low advance ratios. At high J, the DUST model tends to overestimate propeller performance in terms of $\mathrm{C_T}$, especially in the case of the LL model. Numerical analyses showed a strong sensitivity of the numerical model from the viscous aerodynamic tables of the more in-root profiles that have a high thickness and unconventional shape. Greater agreement with experimental results could be achieved by improving the aerodynamic prediction of two-dimensional airfoil characteristics by experimental procedure or accurate high-fidelity numerical simulation. However, since the purpose of the investigation is aimed at the ability of the medium-fidelity solver to capture interactional physics, these results are considered sufficient and satisfactory.

Fig. 2.12 shows the normal load $\mathrm{M^2C_n}$ on the blade along the adimensional radius r/R obtained for the two different LL and NL-VL models. The load distribution is similar for both models, with a slight deviation, where the LL model has higher load values, as highlighted by the overall results of Fig. 2.11.

All DUST simulations were performed considering a length of 10 propeller revolutions with a time discretization of 4° of blade azimuthal angle. The computational time required to complete the simulation of a single propellers configuration was about 10 minutes for the LL mesh and about 20 minutes for the NL-VL using a workstation with a Dual Intel® Xeon Gold 6230R @2.10GHz processor with 52 physical cores and 2 threads for each core.

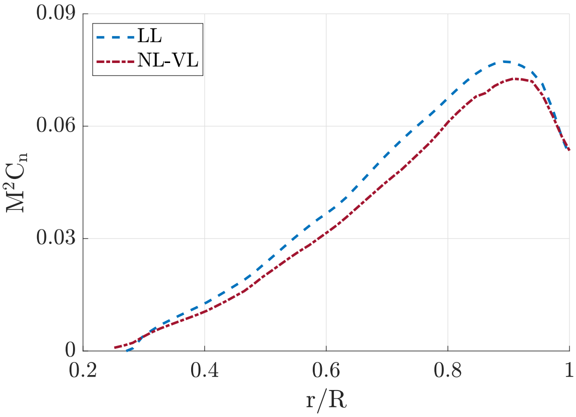

Figure 2.12: *Comparison of the non-dimensional normal force* $\mathrm{M^2C_n}$ *on the isolated propeller blade along the adimensional blade radius* r/R *averaged during the last revolution,* $J = 0.8$, $M_t = 0.325$

From the perspective of the physics of the problem, flowfield comparisons between experimental data obtained from PIV measurements and numerical simulations are reported. Since the differences in performance between the LL and NL-VL models appear minimal, the results presented will be referred to the LL model only.

The suitability of the numerical model in reproducing the aerodynamic characteristics of the propeller was demonstrated by analyzing the averaged flow fields for the single propeller configuration. Good agreement was found between the PIV and simulation results for the overall flow behavior in the wake of the single propeller, as evidenced by the similar freestream (u) and out-of-plane (w) velocity components (refer to Fig. 2.13). To aid comparison between the experimental results and simulations, the boundaries of the PIV fields of view are shown with dashed black lines on the numerical flow fields. Moreover, the numerical results provided a larger field of view, which allowed for the observation of a slight contraction of the core of the helicoidal wake in the axial coordinate X.

The comparison between the adimensional out-of-plane vorticity component obtained by phase-locked PIV measurements and numerical simulations at $\psi = 170°$ for the isolated propeller configuration is illustrated in Fig. 2.14. To visualize the three-dimensional representation of vortex behavior, numerical results show an iso-surface of criterion Q along with the vorticity contours. It is important to note that the experimental data were obtained from the phase average of PIV measurements triggered by the position of the azimuthal angle of the propeller blades when comparing the

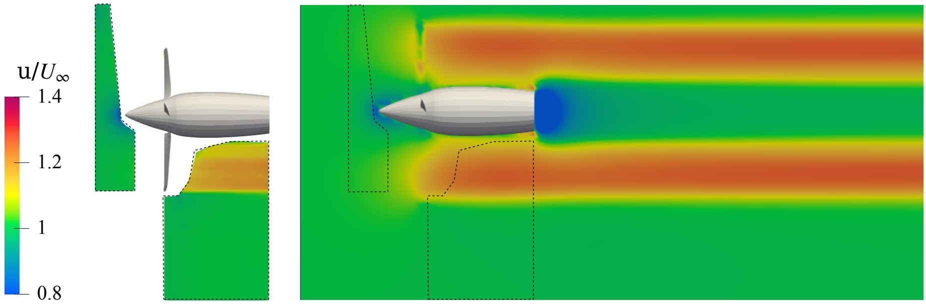

(a) Axial velocity component.

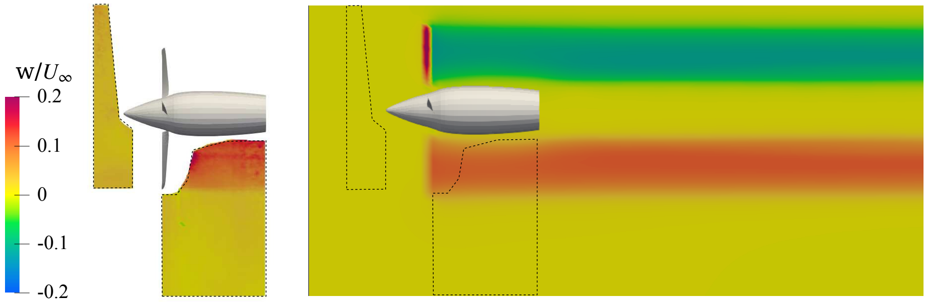

(b) Out-of-plane velocity component.

Figure 2.13: *Comparison of the averaged velocity components for single propeller configurations at* $J = 0.8$*,* $M_t = 0.325$ *between PIV (left) and DUST LL (right).*

instantaneous flow fields.

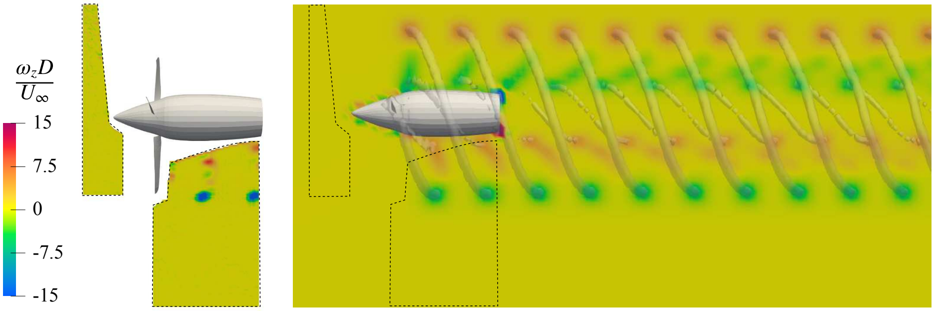

Figure 2.14: *Comparison of the instantaneous out-of-plane vorticity component and iso-surface of Q-criterion for the isolated propeller configuration at* $J = 0.8$, $\psi = 170°$, $M_t = 0.325$, *between PIV (left) and DUST LL (right).*

Using out-of-plane vorticity and Q-criterion iso-surfaces, the instantaneous flow field for a single propeller configuration clearly illustrates the periodic release of the blade's tip and root vortices, which are linked to the shear layers created by the rotating blades. Figure 2.14 demonstrates a reasonably good agreement between phase-averaged PIV data and numerical simulation results with respect to the location and strength of the vortices within the propeller wake.

2.2.2 Tandem propeller

In order to explore the interactional aerodynamics, the study now turns to tandem propellers. To simulate a typical eVTOL cruise flight condition, an advance ratio J of 0.8 is used. The thrust and torque measurements obtained for overlapping tandem propeller configurations, with varying values of L_x and L_y (as illustrated in Fig. 2.8), are discussed below. As the experimental campaign [113] revealed insignificant differences in the performance of the front propeller across all the lateral separation distances L_y and the range of advance ratios examined, its results are omitted here for consistency. Instead, the focus of the investigation is on the changes in performance of the rear propeller caused by the wake of the front propeller in tandem configuration. The computational time required to complete the simulation of a tandem propellers configuration was about 17 minutes for the LL mesh and about 40 minutes for the NL-VL using a workstation with a Dual Intel® Xeon Gold 6230R @2.10GHz processorwith 52 physical cores and 2 threads for each core. In Fig. 2.15, the comparison between the thrust coefficient C_T and power coefficient C_P of the rear propeller in tandem configuration is presented, with results obtained from both experiments and numerical simulations at an advance ratio of $J = 0.8$. The numerical performance coefficients depicted on the graphs represent the average value over the last computed rotor revolutions and have been normalized with respect to the values obtained from the simulations of a single propeller.

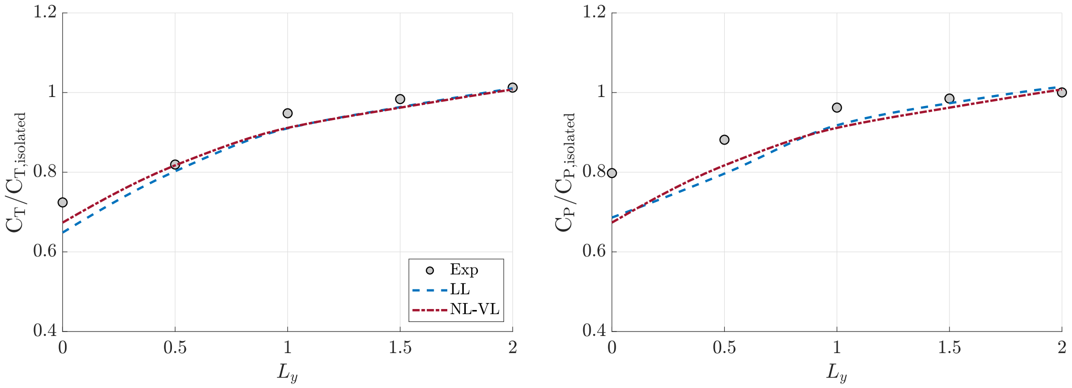

(a)

(b)

Figure 2.15: *Rear propeller performance as function of the lateral distance* L_y *and* $L_X = 5R$, $J = 0.8$, $M_t = 0.325$.

When the lateral separation distance between propellers is set to L_y=2R, the normalized performance coefficients tend to converge towards unity, indicating that aerodynamic interactions have a negligible effect on propeller performance for that configuration. As the degree of overlapping between the propeller disks is increased to $L_y = R$, the experimental results show only minor losses in performance, with the single propeller performance coefficients decreasing by only a few percent. However, the relationship between performance losses and lateral separation distance is not linear. When the lateral distance between propellers decreases below $L_y = R$, the curves' slope increases significantly due to the negative impact of aerodynamic interaction effects on the rear propeller's performance. If the propellers overlap completely, meaning that they are coaxial, the performance of the rear propeller decreases by nearly 30% and 20% for the thrust and power coefficients, respectively.

The comparison of experimental and numerical normalized performance coefficients reveals a high degree of agreement across the entire range of lateral separation distances tested. Both DUST models exhibit similar behavior regarding the impact of aerodynamic interactions on propeller performance. However, the most significant deviation from the experimental data occurs in the case of coaxial propellers ($L_y = 0$). In this configuration, the NL-VL model shows better agreement with experimental results than the LL model, particularly when considering the thrust coefficient C_T. Apart from the analysis of the average propeller performance, another aspect that warrants investigation, particularly regarding dynamics, aeroelasticity, and acoustics, is the evaluation of the effects of aerodynamic interaction on the dynamic behavior of aerodynamic loads acting on the rear propeller in tandem configurations. To this end, the time histories of thrust coefficients computed by DUST simulations for the rear propeller in various tandem configurations at $J = 0.8$ are compared in Fig. 2.16.

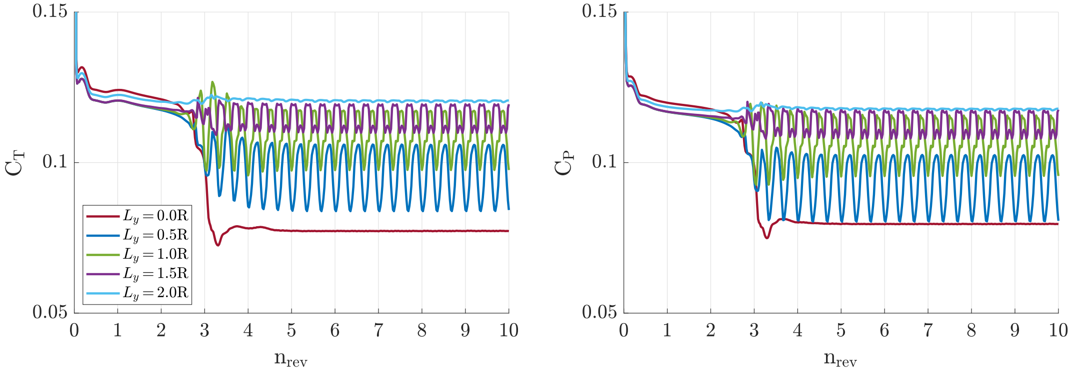

(a) LL

(b) LL

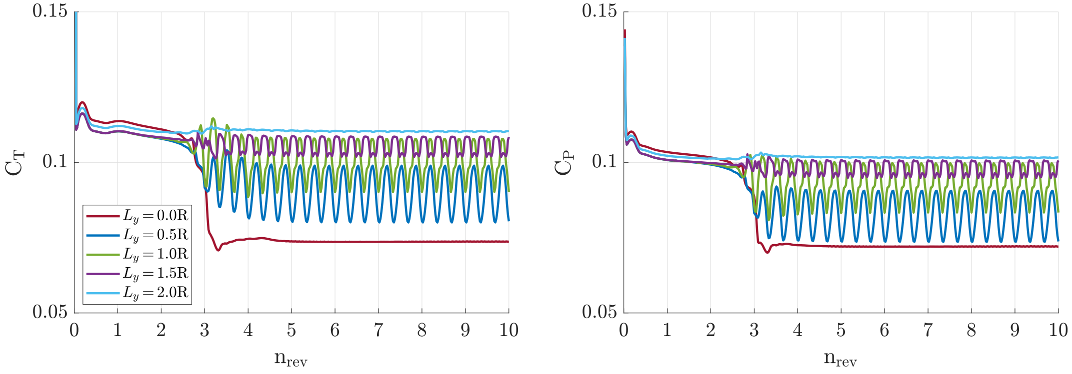

(c) NL-VL

(d) NL-VL

Figure 2.16: *Rear propeller time histories performance computed by DUST simulations as function of the lateral distance L_y and $L_X = 5R$, $J = 0.8$, $M_t = 0.325$.*

The C_T curve computed for the tandem configuration with completely overlapped propeller disks, i.e., L_y=0.8, indicates that the rear propeller experiences negligible thrust fluctuations due to the interaction with the slipstream generated by the front propeller.

Fig. 2.17 shows a comparison of the contours of the blade non-dimensional normal force ($\mathrm{M^2C_n}$) computed over a complete rotor revolution considering both LL and NL-VL model in order to provide detailed insight into the evaluation of the impact of the front propeller wake on the rear one and assess the consistency between the two DUST elements. The complete overlap of the front propeller slipstream with the rear propeller disk leads to an axially symmetrical distribution of aerodynamic loads on the rear propeller blade with respect to the azimuthal phase angle. This is demonstrated by the computed blade sectional lift shown in Figs. 2.17(a) and 2.17(b), and explains the negligible amount of load fluctuations observed in this coaxial tandem configuration. However, as the area of overlap between the propeller disks decreases, the time history of the rear propeller thrust exhibits periodic behavior starting after 3 rotor revolutions, indicating the onset of aerodynamic interaction effects due to ingestion of the front propeller wake. This behavior is observed in all other lateral separation distances considered. The amplitude of the periodic thrust oscillations increases as the degree of overlapping between the propeller disks decreases, with the highest amplitude occurring at $L_Y = 1$R. This is due to the asymmetrical distribution of normal forces along the rear propeller blade airfoils during a rotor revolution caused by the partial ingestion of the front propeller slipstream, as shown in Figs. 2.17(e) and 2.17(f). As the lateral distance between the tandem propellers increases to L_y=1.5R, the amplitude of thrust fluctuations decreases, and becomes almost negligible when the degree of overlapping between propeller disks is zero at L_y=2R.

Both DUST models, LL and NL-VL, provide similar and mutually consistent results. Slightly more load on the disk is shown for the LL case, associated with the performance results of Fig. 2.11 in which the LL curve always remains above the NL-VL curve on both the thrust and power coefficients.

Fig. 2.18 provides a more detailed and quantitative representation of the load trend. The curves shown in the figure correspond to the $\mathrm{M^2C_n}$ load, which is evaluated at the station located at $r/R = 75\%$ throughout the entire azimuth of the last propeller revolution. It is important to note that the load trend is not uniform along the azimuth and varies significantly for different values of L_y. Specifically, for $L_y = 0$ (as illustrated in Fig. 2.18(a)), the load remains constant throughout the rotation. On the other hand, for $L_y = 1$ (as shown in Fig. 2.18(b)), the load varies significantly throughout the revolution. It is worth mentioning that the behavior of the

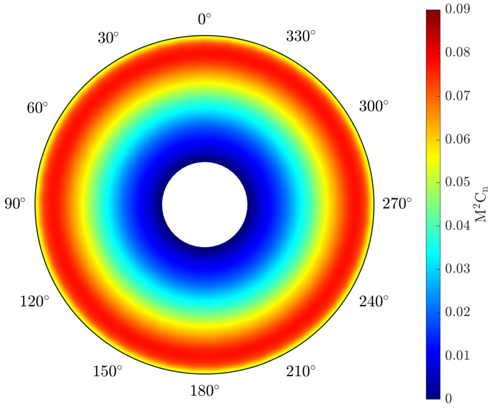

(a) Isolated, LL

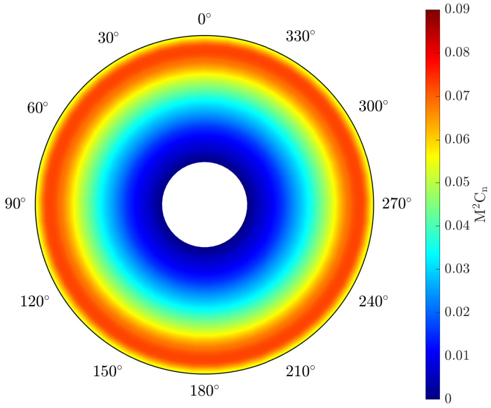

(b) Isolated, NL-VL

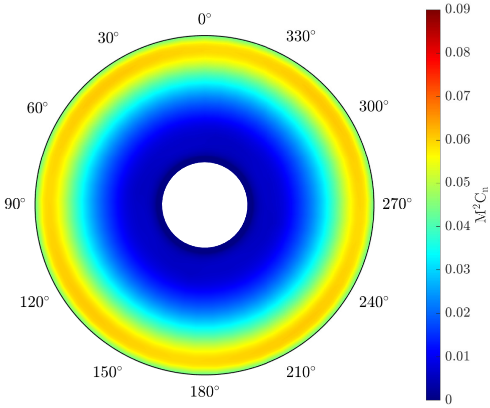

(c) Rear propeller $L_Y = 0$R, LL

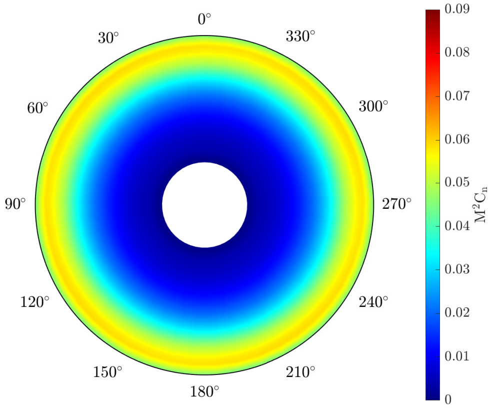

(d) Rear propeller $L_Y = 0$R, NL-VL

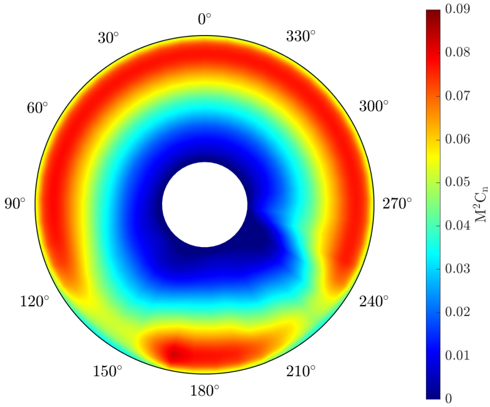

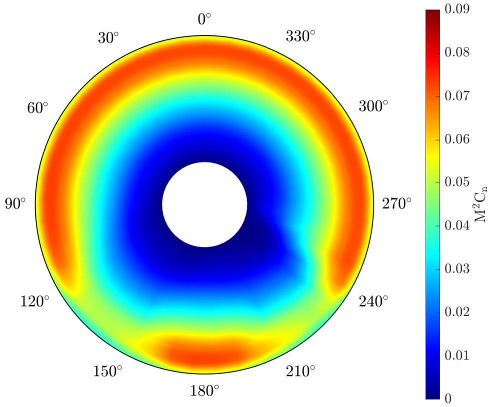

(e) Rear propeller $L_Y = 1$R, LL

(f) Rear propeller $L_Y = 1$R, NL-VL

two elements LL and NL-VL is quite similar, with only a slight deviation in their respective load trends. Therefore, the load characteristics of these two elements can be considered to be almost identical. This information can be crucial for understanding the load distribution in the propeller system and optimizing its design for improved performance.

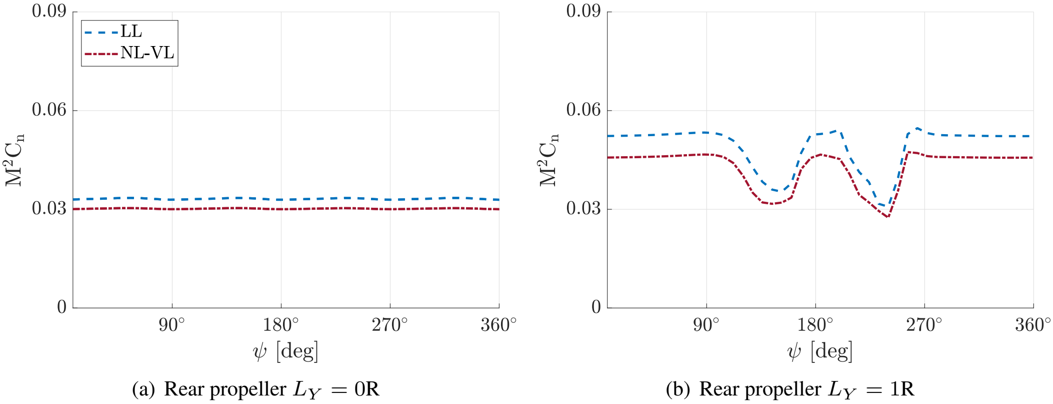

(a) Rear propeller $L_Y = 0\mathrm{R}$ (b) Rear propeller $L_Y = 1\mathrm{R}$

Figure 2.18: *Comparison of the non-dimensional normal force* $\mathrm{M^2C_n}$ *on the propeller blade evaluated at* $r/R = 75\%$ *during the last revolution,* $J = 0.8$, $M_t = 0.325$

The aerodynamic interaction between the tandem propeller configurations can be better understood by analyzing the flow fields obtained from PIV surveys and numerical simulations at $J = 0.8$ for two different lateral distances between the propellers, namely $L_y = 0$ and $L_y = R$. Considering the averaged field, the analysis of the flow fields is based on the comparison of the average freestream (u) and out-of-plane (w) velocity components' contours, which is similar to what was done for the isolated propeller. The PIV results obtained for the co-axial tandem propeller configuration, with $L_y = 0$, reveal that the slipstream generated by the front propeller causes the outer wake region of the rear propeller to accelerate in comparison to the single propeller configuration. Additionally, the ingestion of the front propeller's co-rotating slipstream leads to an increase in the swirl velocity component within the wake of the co-axial rear propeller, as depicted in Fig. 2.19(b). The accelerated and swirled flow regions that pass through the outer areas of the tandem propellers' disks are accurately captured by numerical simulations, which show that the flow field for both velocity components is quite symmetrical in the co-axial configuration.

By increasing the separation distance between the propellers to $L_y = R$, PIV measurements reveal an asymmetrical inflow behavior of the rear propeller, as shown in Fig. 2.20. The upper region of the front propeller slip-

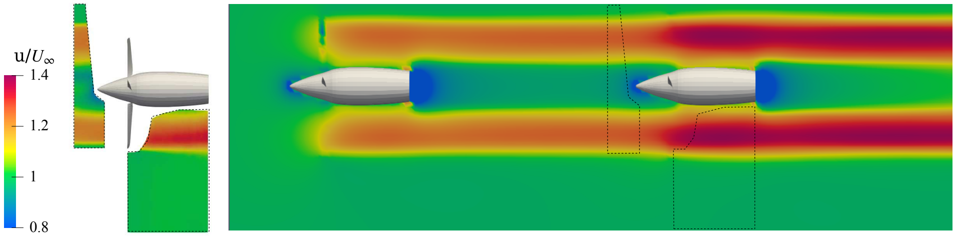

(a) Axial velocity component.

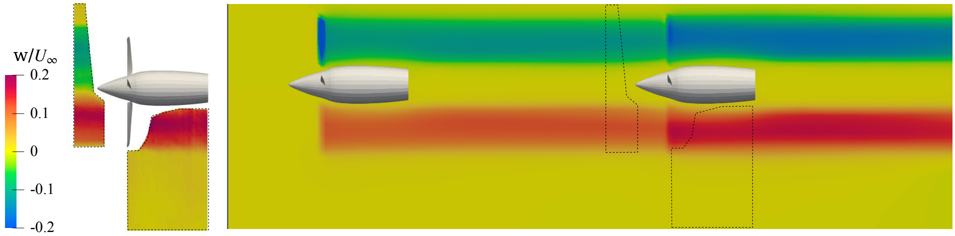

(b) Out-of-plane velocity component.

Figure 2.19: *Comparison of the averaged velocity components for tandem propeller configurations* $L_x = 5R$ *and* $L_y = 0R$ *at* $J = 0.8$ *and* $M_t = 0.325$, *between PIV (left) and DUST LL (right).*

stream is observed to be lifted upward by the rear propeller nacelle curvature, leading to a streamlined accelerated flow region over the nacelle area of the rear propeller wake. This observation is supported by the numerical simulation results presented in Fig. 2.20(a). In addition, this region is also characterized by a slightly increased positive out-of-plane velocity component, as shown in Fig. 2.20(b).

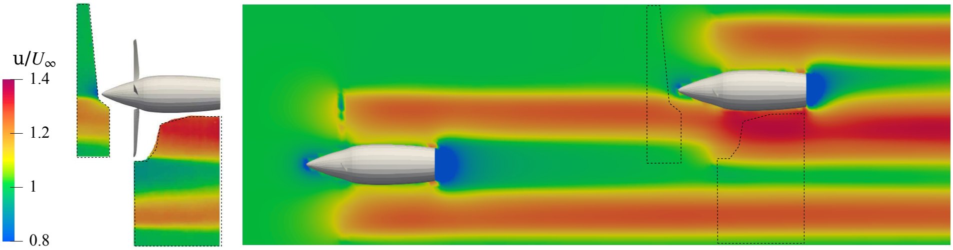

(a) Axial velocity component.

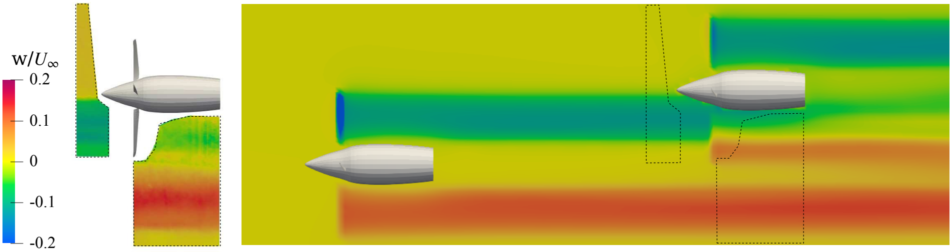

(b) Out-of-plane velocity component.

Figure 2.20: *Comparison of the averaged velocity components for tandem propeller configurations $L_x = 5R$ and $L_y = 0R$ at $J = 0.8$, and $M_t = 0.325$ between PIV (left) and DUST LL (right).*

Comparing the averaged velocity components, it can be seen that there is general concurrence between the PIV and DUST simulations.

To gain a better understanding of the vortex-vortex interactions in the tandem propeller configurations, both phase-locked PIV surveys and numerical simulations are used to analyze instantaneous flow fields. Figure 2.21 compares the instantaneous out-of-plane vorticity component obtained from phase-locked PIV measurements and numerical simulations at ψ=170°, for the lateral distances $L_Y = 0$ and $L_Y = 1$R at J =0.8. However, it should be noted that the experimental data were obtained by phase-averaging PIV measurements data triggered by the rear propeller blade azimuthal angle position, while the numerical results were obtained by synchronizing the blade azimuthal phase of the two tandem propellers. This comparison allows for a detailed investigation of the effects of the front propeller slipstream on the flow field past the rear propeller.

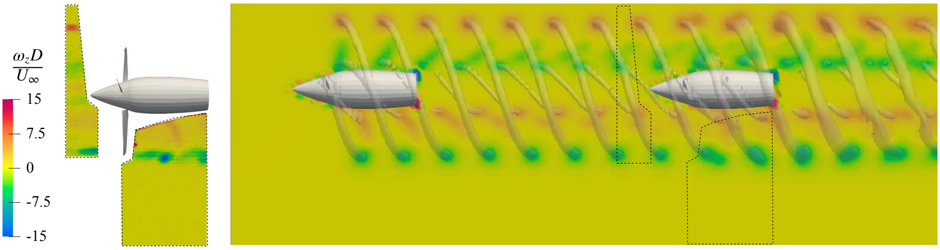

(a) L_X = 5R and L_Y = 0R.

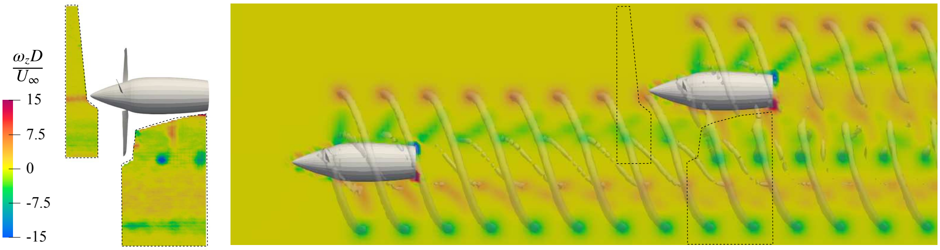

(b) L_X = 5R and L_Y = 1R.

Figure 2.21: *Comparison of the averaged velocity components for tandem propeller configurations at $J = 0.8$ and $M_t = 0.325$ between PIV (left) and DUST LL (right).*

For the co-axial tandem propellers configuration, with L_y =0, PIV results reveal the presence of the blade tip vortices from the front propeller, which are delimited by the slipstream that reaches the rear propeller disk. As a result of this interaction, the rear propeller tip vortex detected in the PIV wake measurement area has lower vorticity compared to the single propeller configuration shown in Fig. 2.14. Specifically, only a faint trace of the second tip vortex is visible at the right edge of the PIV field of view in the wake of the rear propeller. In contrast, numerical results for the co-axial propellers configuration in Fig. 2.21(a) show a double array of tip vortices in the wake of the rear propeller, resulting from the rotation of both propellers. The Q-criterion iso-surface representation highlights that, due to the interaction with the front propeller slipstream, the coherence of the helical structure provided by the rear propeller blades tip vortices is lost earlier than that of the front propeller. As a consequence, there is a higher degree of dissipation observed for the rear propeller blade tip vortices, as

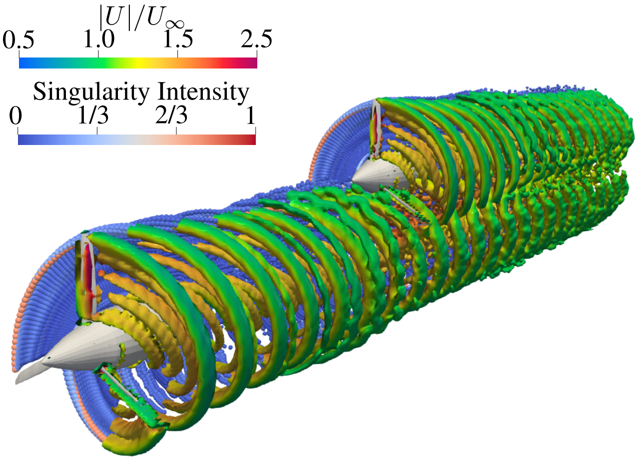

Figure 2.22: *Visualization of the flow field (Q-criterion iso-surface colored by non-dimensional freestream velocity) and particles wake (colored by adimensional singularity intensity) computed by DUST. Tandem propellers configuration,* $L_x = 5R$ *and* $L_y = 1R$.

indicated by the vorticity level evaluated past the rear propeller disk. Similar considerations can be made by analyzing the behavior of the blade root vortices past the rear propeller disk, given the co-axial configuration of the tandem propellers.

PIV results in Fig. 2.21(b) indicate that tandem propellers configuration with a lateral distance of $L_Y = 1$R exhibits a lower degree of dissipation of the rear propeller blade tip vortices in comparison to the previously analyzed configurations. This phenomenon can be attributed to the fact that the lower array of rear propeller blades' tip vortices is situated between the double array of root vortices released by the front propeller blades, as shown by the numerical results. Additionally, a mutual interaction between the upper array of vortices issued by the front propeller blades' root and the lower array of vortices issued by the rear propeller blades' tips is also observed. The Q-criterion iso-surface representation reveals that, in general, only the lower half of the helical structure associated with the rear propeller blades' tip vortices loses coherence due to the front propeller slipstream interaction in this tandem configuration. Figure 2.22 shows the entire flow field in terms of Q-criterion iso-surfaces and the adimensional intensity of wake particles, considering the tandem configuration with case $L_x = 5R$ and $L_y = 1R$.

In general, when propeller disks are fully overlapping in a coaxial configuration, aerodynamic interaction between propellers has the greatest negative impact on rear propeller performance. On the other hand, when the disks only partially overlap, the average aerodynamic performance of the rear propeller improves, but this results in a rather high level of fluctuations in aerodynamic loads, which is disadvantageous for aeroacoustic and dynamic issues, particularly important in the design of vehicles operating in urban areas. DUST's mid-fidelity approach is a valuable tool for investigating these interactional phenomena in terms of both the quality of results and computational cost required.

2.3 Wing-propeller

The present test case is based on a numerical investigation of a wing with an integrated propeller. The wing/propeller model considered in this work, released by the Workshop for Integrated Propeller Prediction (WIPP) [48], was widely investigated in literature both by experiments and high-fidelity CFD simulations and represents a classical benchmark case for the aerodynamic study of tiltrotors and electrical distributed propulsion aircraft configurations. This case aims to show the capabilities of the mid-fidelity aerodynamic approach based on the vortex particle method, such as DUST, to capture the aerodynamic interactional effects of the installed propeller on the wing by a direct comparison of wing pressure coefficient distributions and propeller airloads with both experimental data and high-fidelity CFD simulations.

The WIPP model represents a useful test case for validating aerodynamic codes since an intense experimental campaign was carried out, the results of which constitute a powered wind tunnel test database. The tests took place in the Lockheed Martin Low-Speed Wind Tunnel (LSWT) in Marietta, Georgia, USA as part of the NASA/Armstrong X-57 research program [48]. The model consisted of a 40.5% scale semi-span wing designed for the wind tunnel test campaign to be mounted on the LSWT external balance. The span, from the tunnel floor to the top of the nacelle, is equal to $1.772\,\mathrm{m}$, with a root chord of $0.295\,\mathrm{m}$ and a tip chord of $0.218\,\mathrm{m}$. The wing presents a leading edge sweep of $1.9°$. The model incorporates a nonmetric boundary layer splitter plate $0.163\,\mathrm{m}$ high, which is mounted to the tunnel floor. The model was equipped with an existing C-130 four-blade propeller with a diameter of $0.411\,\mathrm{m}$ and a blade pitch angle of $38°$. The propeller was also used extensively in past activities for testing a 10% scale C-130 aircraft model. The propeller was mounted to a nacelle at the tip of the wing. The nacelle was $0.613\,\mathrm{m}$ long with a maximum diameter of $0.12\,\mathrm{m}$. The accurate geometries, necessary for the construction of the numerical model, were extracted through a digital scan of the wind tunnel model. The latter was equipped with 96 static pressure taps located at six different wing spanwise sections, as shown in Fig. 2.23. The six sections are reported in Table 3.7, together with the distance from the propeller axis. Each section included 10 static pressure taps on the upper surface and 6 static pressure taps on the lower surface.

The DUST numerical model of the WIPP system was built using different aerodynamic elements. Figure 2.24 illustrates the DUST aerodynamic mesh of the WIPP model, while Tab. 5.1 summarizes the details of the aero-

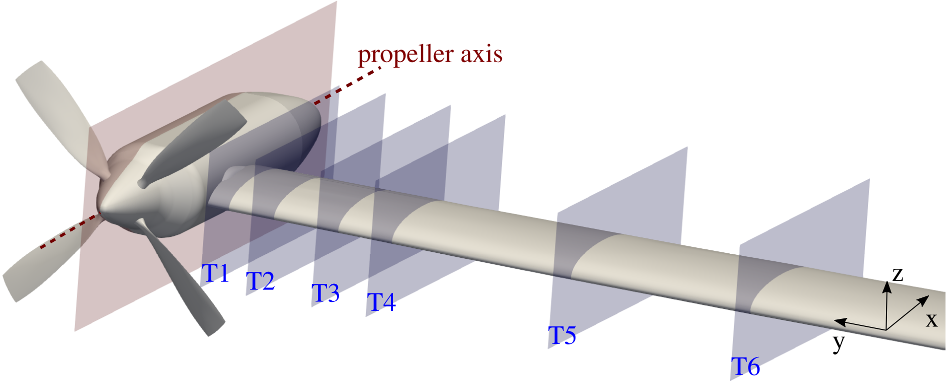

Figure 2.23: *Location of the pressure taps sections on the WIPP model.*

Section	Distance
T1	0.101 m
T2	0.165 m
T3	0.256 m
T4	0.332 m
T5	0.586 m
T6	0.840 m

Table 2.4: *Positions of the pressure probe sections.*

dynamic elements used to mesh the different components of the wing/propeller system.

The wing and the nacelle were modeled as surface panels (SP). Surface panel elements allow to model thick solid bodies, with source and doublet distributions, and following Morino's formulation of the aerodynamic problem a Dirichlet boundary condition for the velocity potential is introduced.

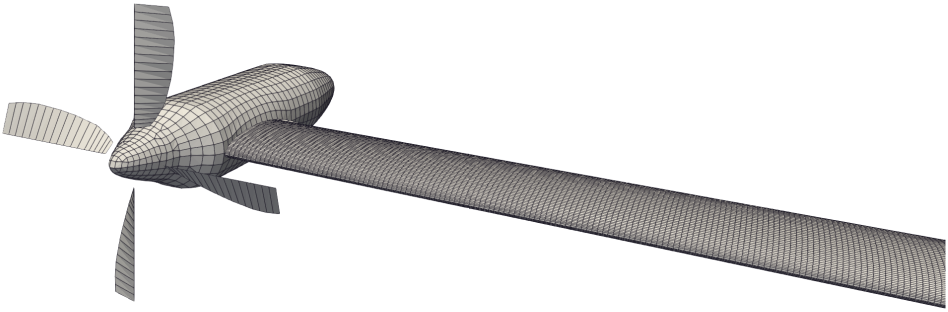

Figure 2.24: *DUST aerodynamic mesh of the WIPP model.*

	Elements	
Component	Type	Number
Blade	LL	17×4
Wing	SP	21500
Nacelle	SP	1167
Total		22735

Table 2.5: *Details of aerodynamic elements used to mesh WIPP model with DUST.*

The propeller blades were modeled as lifting lines (LL). Lifting lines elements should comprise a single vortex line representing the circulation introduced by a lifting surface, whose intensity is obtained from the tabulated aerodynamic data of the airfoil section they should represent. In DUST they are modeled as a single row of vortex lattice panels with uniform doublet distribution. Thanks to the equivalence between doublet surface distribution and vortex ring, the panels describe both the lifting vortex with the leading edge side, and the beginning of the wake with the remaining sides. While the panels used to model the lifting lines are equal to the ones of the vortex lattice components in terms of singularity distribution and hence in the computation of potential, velocity and gradient induction, there are no conditions imposed on the panels, and their intensity is computed with fixed point iterations to solve the nonlinear problem generated by the introduction of the tabulated aerodynamic data [41]. In the context of this work, the tabulated aerodynamic performances of the propeller airfoils were calculated with 2D simulations performed with the RANS SU2 solver [35], assuming the Spalart-Allmaras turbulence model. Each blade has been modeled with eight airfoils; for each one the aerodynamic coefficients between $-20°$ and $20°$ degrees are computed and subsequently extended between $-180°$ and $180°$ with the method proposed in Ref. [14]. DUST simulations were performed considering a length of 10 propeller revolutions with a time discretisation of $5°$ of the azimuthal angle of the blade. The computational time required to complete the simulation of the WIPP model configuration was about 70 minutes using a workstation with a Dual Intel Xeon Gold 6230R @2.10GHz processor of 104 cores.

The results of DUST simulations are compared with experimental data from [48] and high-fidelity CFD simulations performed with SU2 software from [116]. In particular, all the CFD simulations data selected for comparison are obtained by the URANS approach over the finest grid considered in the reference work (i.e., G3 grid, see details of the CFD numerical model in [116]). Moreover, the following figure legends retrieve the wind tunnel run indicated in the experimental reference work [48], corresponding to the experimental data set selected for the comparisons.

Run No	Configuration	AoA°	Mach	C_T
187	Isolated Wing	[-10, 20]	0.11	-
30	Wing-Propeller	0	0.04	-
32	Wing-Propeller	0	0.08	-
33	Wing-Propeller	0	0.11	-
80	Wing-Propeller	0	0.11	0.4

Table 2.6: *Details of the experimental runs considered.*

Table 2.6 shows the test conditions corresponding to the experimental runs used for the comparisons. Hereafter, the thrust coefficient is defined as

$$C_T = \frac{T}{\frac{1}{2}\rho V^2 S},$$

where S is the wing reference area equal to $0.4365\,\mathrm{m}^2$.

2.3.1 Isolated Wing

Firstly, the isolated wing case without the propeller was considered. Figure 2.25 shows the aerodynamic loads of the wings, ie lift coefficient (Fig. 2.25(a)) and polar curves (Fig. 2.25(b)), calculated by DUST and compared with experimental measurements, considering a test condition with Mach equal to 0.11.

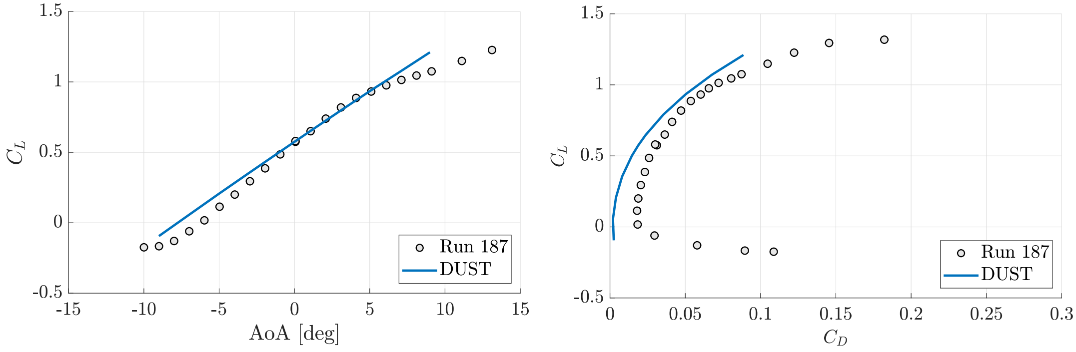

(a) C_L vs AoA.

(b) C_L vs C_D.

Figure 2.25: *Comparison of the aerodynamic performances for the isolated wing configuration, Mach=0.11.*

For small angles of attack, the lift coefficient obtained with DUST shows a good agreement with the experimental data, while close to the stall the nonlinear effects on the lift curve are not captured, as can be expected considering the assumptions of the numerical method. Since the parasite drag is not modeled by the mid-fidelity solver, there is a discrepancy between the polar curves in the region with a zero lift coefficient. On the other hand, since the induced drag generated by the wing tip vortices is almost well represented, coherence between the curves is recovered as lift increases.

Figure 2.26 shows the pressure coefficient distributions calculated with DUST for the isolated wing on four different wing sections, from T1 to T4, compared with the pressure coefficient measurements at two different angles of attack, i.e. AoA=0° and AoA=5°, and Mach number equal to 0.11. The results highlight a very good agreement between the DUST numerical simulations and the experiments, particularly pointing out the suitability of the solver for the wing aerodynamic performance evaluation.

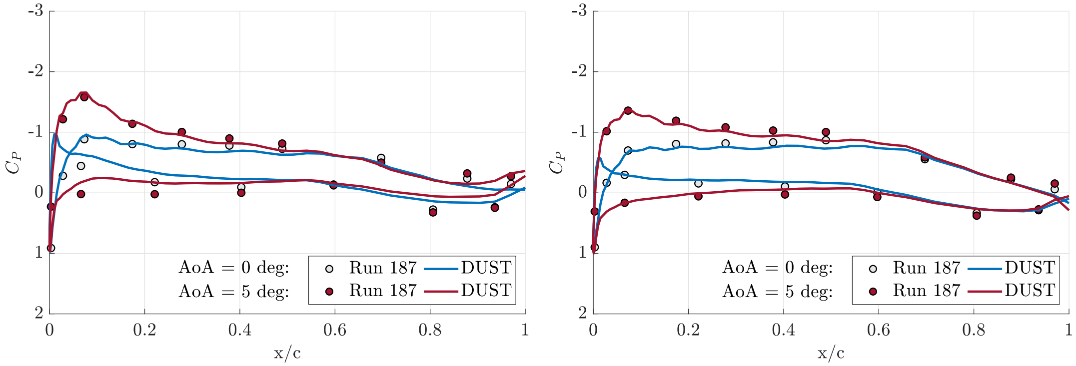

(a) T1.

(b) T2.

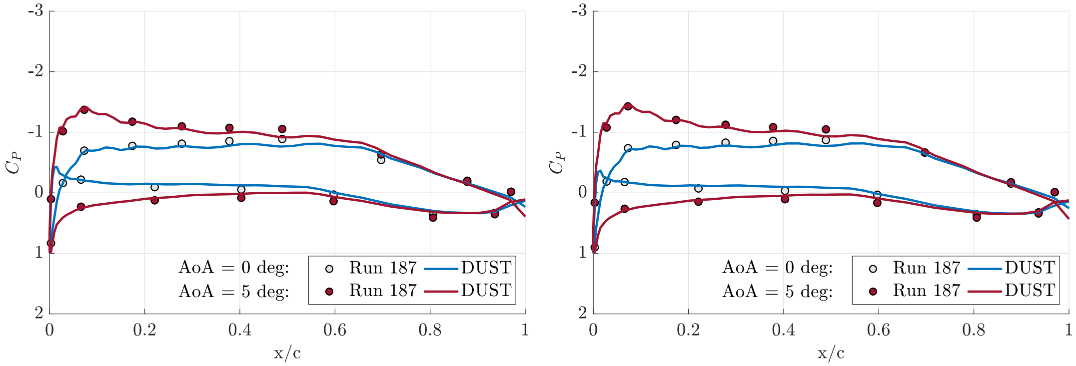

(c) T3.

(d) T4.

Figure 2.26: *Comparison of the pressure coefficient distribution at different span section for the isolated wing, Mach=0.11.*

2.3.2 Wing with Integrated Propeller

The complete model with the installed propeller is now considered. In this phase, the DUST capabilities to capture the aerodynamic interactions linked to the propeller wake are tested, both in terms of total loads and pressure coefficient distributions, particularly in the region nearer to the nacelle. In particular, numerical results were also analyzed to identify the effects of the nacelle and propeller on the local sectional airloads of the wing. Finally, DUST capabilities are evaluated to reproduce the complex aerodynamic flow in general and to capture instantaneous pressure fluctuations on the wing.

Figure 2.27 shows the comparison of the propeller thrust coefficient computed as a function of the RPM for three different conditions of free stream Mach number. In order to evaluate the capabilities of the mid-fidelity solver to capture the interactional effects on propeller loads due to the wing-nacelle, DUST results are presented here for simulations considering both the isolated propeller as well as for the integrated system.

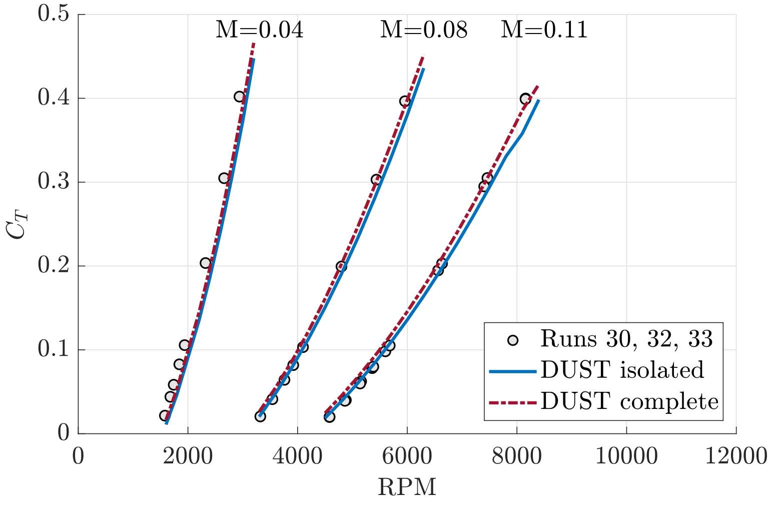

Figure 2.27: *Comparison of the propeller thrust coefficient as a function of angular velocity for different free-stream Mach number.*

Very good agreement with the experimental data was found for all three free-stream Mach numbers considered. In particular, DUST results show that the wing-nacelle system interaction provides a slight additional thrust on the propeller, that is appreciable with the DUST approach and gets numerical results nearer to the experimental ones, particularly at higher RPM.

Figure 2.28 shows the comparison of the pressure coefficient distributions on the wing for the complete model equipped with nacelle and propeller, at the three sections closest to the nacelle, that is, those more affected by the propeller wake, assuming an AoA=0°. Considering the pressure comparison in section T1, i.e. the closest to the propeller, thus highlighting the highest interactional effects on the wing, the CFD data are in quite good agreement with experiments, while the DUST results present some discrepancies. In particular, the suction peak level on the upper surface of the wing is slightly underestimated by DUST, as well as a lower and quite flatter pressure distribution is observed over the lower surface of the wing at this section with respect to the CFD and experimental data. However, in the panel model, the detail on the existing connection between wing and nacelle is not introduced, which may have effects on the results of T1 section. On the other hand, DUST results quite well resume the pressure behavior obtained by both CFD and experiments on sections T2 and T3.

Indeed, on section T2 only a slight underestimation of the pressure coefficient is observed on the wing lower surface, while the agreement on wing upper surface distribution is satisfactory. Similar results are observed at section T3 as well.

The validation against experimental data opened the opportunity to use numerical results obtained with DUST to analyse the effects of the nacelle and propeller on the local aerodynamic performance of the wing. With this aim, Figure 2.29 shows the comparison of the pressure coefficient distributions computed by DUST on three wing sections adding the nacelle and the propeller to the numerical model of the wing. In particular, on section T1 and T2 the effect of the propeller is remarkable. Indeed, the high-velocity air blown by the propeller provides an apparent increase of suction on the wing upper surface, particularly for the sections nearer to the propeller. Furthermore, an increase in pressure coefficient is observed on the lower surface of the wing, close to the trailing edge region, due to the propeller effect. Consequently, the propeller provides a local increase of the lift coefficient in the outer region of the wing.

A similar effect on the upper surface of the wing for sections T1 and T2 can be observed due to the nacelle only. Indeed, the local curvature of the nacelle provides an acceleration of the flow in the outer wing region, thus slightly increasing the suction on the upper surface of the wing. The comparison of pressure coefficient distribution on section T3, further from the propeller, confirms the trend observed for the wing outer sections, but here the effects of the nacelle and of the propeller are, as expected, quite lower.

The analysis of the results follows by evaluating the capabilities of DUST

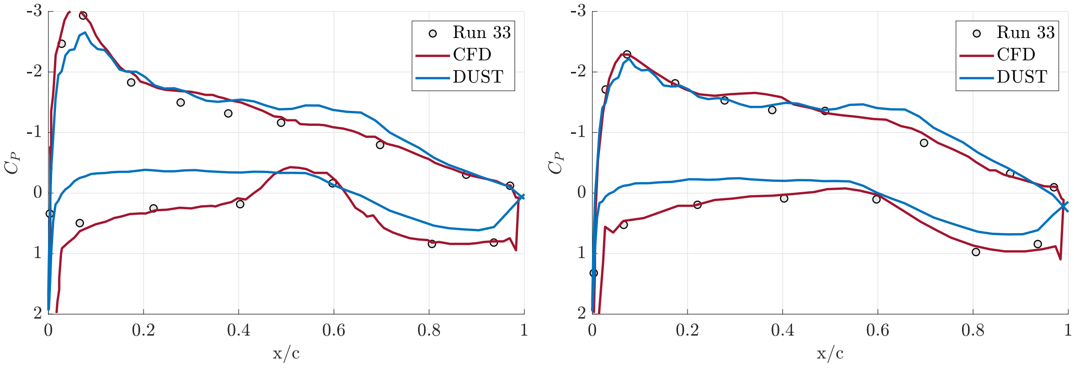

(a) T1.

(b) T2.

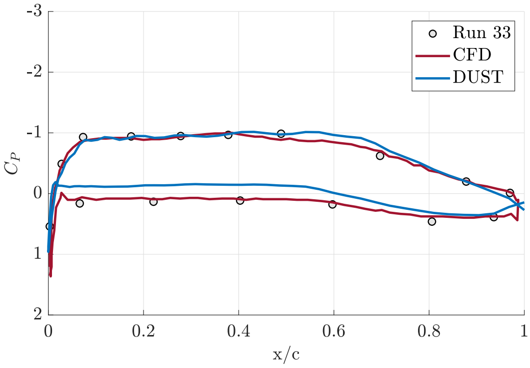

(c) T3.

Figure 2.28: *Comparison of the pressure coefficient distribution at different span section for the installed configuration propeller, AoA=0°, Mach=0.11.*

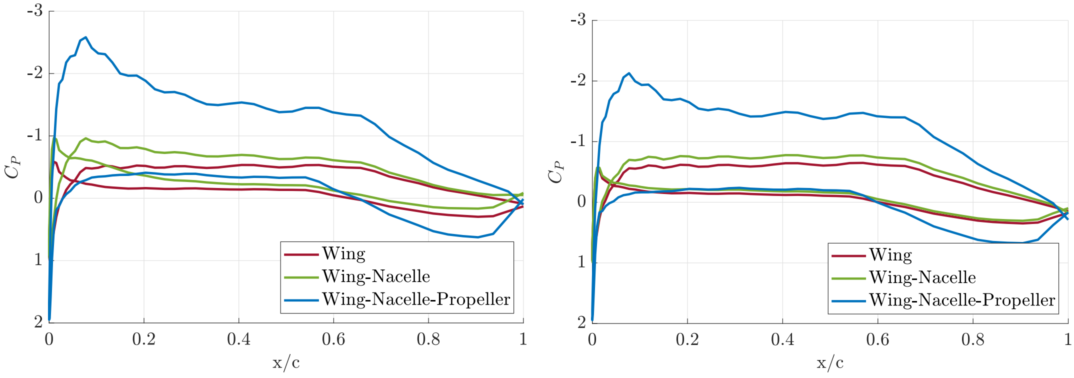

(a) T1.

(b) T2.

Figure 2.29: *Comparison of the pressure coefficient distribution at different span sections for different model configuration, AoA=0°, Mach=0.11.*

to represent the flow field. With this aim, Figure 2.30 shows the comparison of the profiles of the free-stream velocity component U evaluated at five wake stations downstream the propeller. In particular, the experimental wake data are measured at $0.0673\,\mathrm{m}$, $0.1562\,\mathrm{m}$, $0.3594\,\mathrm{m}$, $0.5626\,\mathrm{m}$, and $1.076\,\mathrm{m}$ downstream from the propeller disk [48]. CFD data obtained by URANS simulations were not available for the fifth station [116]. The quantitative comparison of the velocity profiles highlights two main features. The first is that the behavior of the wake profiles computed with DUST quite well resumes the representation obtained by high-fidelity CFD.

The second is that both the mid-fidelity and the high-fidelity numerical approaches evaluate a downward deflection of the velocity deficit in the propeller wake with respect to experimental data. This aspect is, indeed, commonly observed on almost all the wake stations considered for the comparison.

A global visualization of the flow field computed by DUST around the complete WIPP model is provided in Fig. 2.31, showing the Q-criterion isosurface colored by the nondimensional free-stream velocity component and the contours of pressure coefficient on the model surface. The flow representation clearly shows the DUST capability to capture the interaction of the helical structure generated by the propeller blade tip vortices with the wing-nacelle surface. Moreover, DUST numerical solution appreciates also a secondary helical vortical structure generated from blades trailing edge interacting with the nacelle surface. The footprint of these vortical structures on wing-nacelle surface can be observed in Fig. 2.32 showing the contours of the instantaneous pressure fluctuations computed by DUST. In particular, an alternate dotted pressure pattern due to the impinging of the blade tip vortices structure is clearly visible from DUST results on the outboard portion of the wing. Moreover, a streaked pressure pattern can be observed on the nacelle surface as a result of the secondary vortex structure interaction.

These results highlight very similar features with respect to high-fidelity CFD approach [116] and suggest that the DUST numerical model would allow a good identification of the possible noise sources related to the wing-propeller interaction, thus encouraging the use of this mid-fidelity approach to investigate the aeroacoustics of similar configurations. In particular, thanks to the very low computational effort required by DUST simulations, the mid-fidelity approach could be successfully used for the aerodynamic and aeroacoustic optimization of novel wing-propeller configurations.

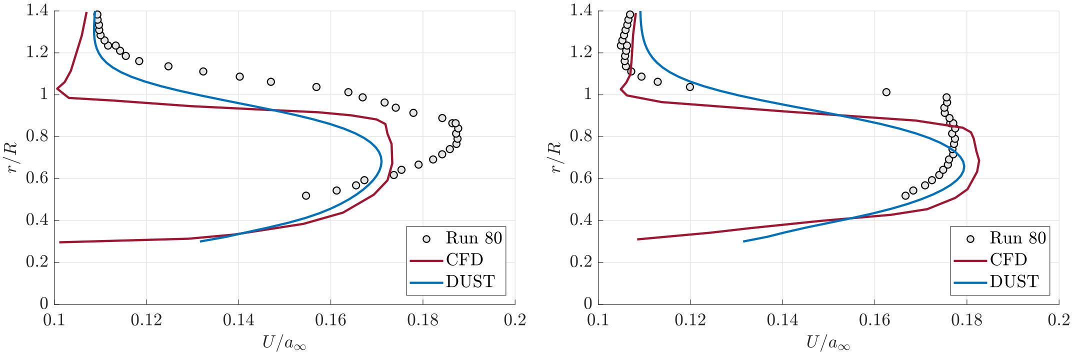

(a) x = 0.0673 m.

(b) x = 0.1562 m.

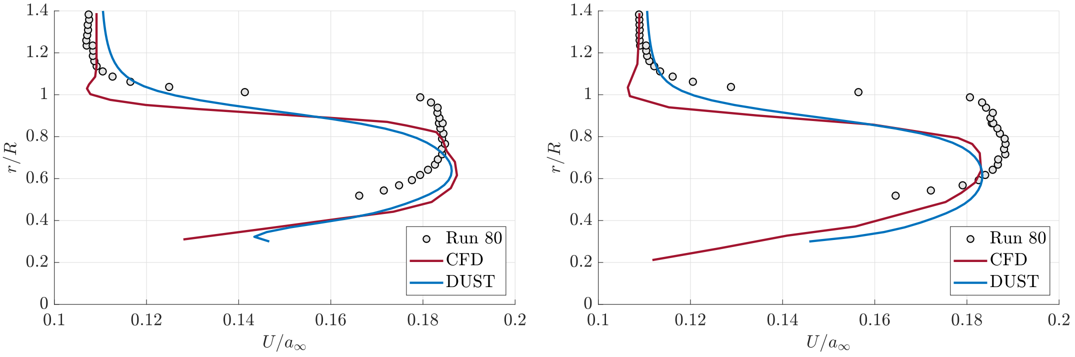

(c) x = 0.3594 m.

(d) x = 0.5626 m.

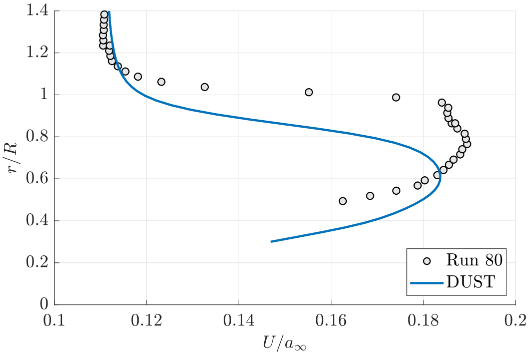

(e) x = 1.076 m.

Figure 2.30: *Comparison of the free-stream velocity component profiles at different distance downstream from the propeller disk, AoA=0°, Mach=0.11.*

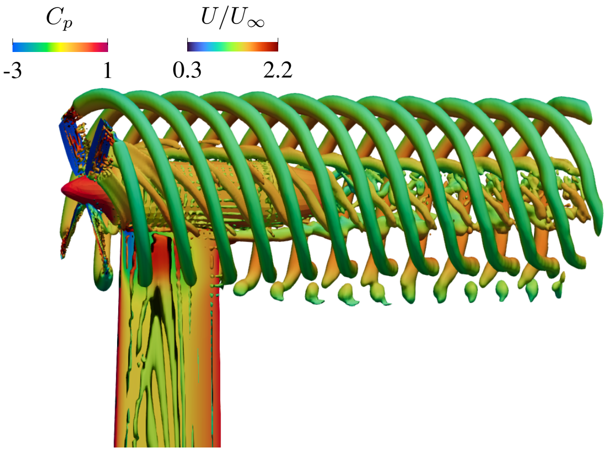

Figure 2.31: *Visualization of the flow field computed by DUST around the complete WIPP model: Q-criterion iso-surface colored by the non-dimensional free-stream velocity component and contours of pressure coefficient on the model surface,* M_∞=*0.11,* C_T=*0.4,* AoA=0°

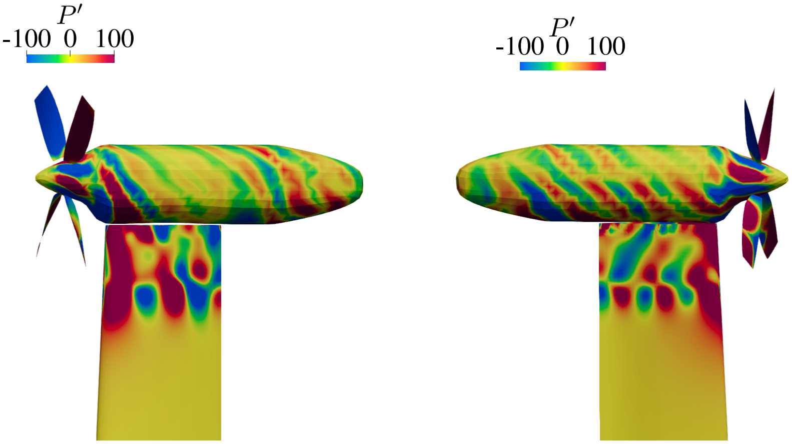

(a) Top view.

(b) Bottom view.

Figure 2.32: *Instantaneous pressure fluctuations computed by DUST (top and reverse bottom views),* M_∞=*0.11,* C_T=*0.4,* AoA=0°.

2.4 Tiltrotor full aircraft configuration

In the context of studying interactional effects, a complete tiltrotor configuration is selected as the final case. This is done with the aim of unifying and integrating the various aspects of the interactional phenomena that were highlighted in the three previous cases. By analyzing a complete tiltrotor configuration, it is possible to gain a more comprehensive understanding of the complex interactions that occur between the various aerodynamic surfaces and components and assess the DUST capability. This can provide valuable insights into the behavior and performance of the aircraft in different flight regimes and operational scenarios.

The aircraft selected for analysis is the XV-15 tiltrotor equipped with metal blades proprotors due to the abundance of available and thorough data in literature. DUST simulations of the complete flight envelope of this tiltrotor aircraft are compared to the high-fidelity numerical results presented in the works by Tran et al. [100, 101]. The numerical analysis, carried out using DUST, was conducted under steady state conditions for the entire XV-15 tiltrotor aircraft during hover, conversion, and cruise phases.

The numerical model of the XV-15 tiltrotor was built considering the full scale dimensions and all the aircraft components. This model encompassed the $14.1\,\mathrm{m}$ fuselage, the horizontal and vertical tailplanes, the wing with control surfaces such as flaps and flaperons, and the two proprotors with nacelles. The mesh layout of the entire aircraft is displayed in Fig. 2.33. The main characteristics of the full vehicle geometry, including the airfoil series used to build the numerical model, are reported in Table 2.7.

	Wing	Horizontal Tail	Vertical Tail
Airfoil	NACA 64A223	NACA 64015	NACA 0009
Span	9.8 m	3.91 m	2.34 m
Mean aerodynamic chord	1.60 m	1.20 m	1.13 m
Sweep ($c/4$)	$-6.5°$	0°	31.6°
Dihedral	2.0°	0°	-
Incidence	3.0°	0°	0°
	Flap	Flaperon	
Span along hinge line	1.30 m	2.40 m	
Chord/Wing chord	0.25	0.25	
Maximum deflection	75°	47°	

Table 2.7: *Geometrical features of the XV-15 tiltrotor numerical model.*

The DUST model of the proprotor is the same as presented in Sec. , except that in this application, the blade is modeled with lifting lines com-

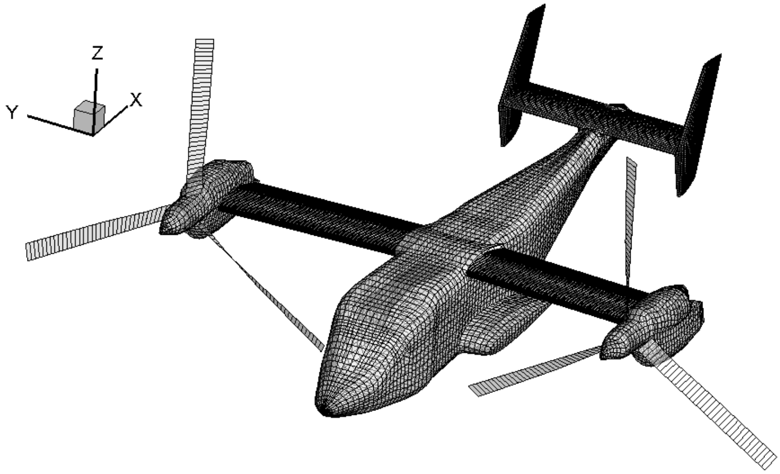

Figure 2.33: *Layout of the mesh for DUST simulations of the full XV-15 tiltrotor.*

ponents. All other components of the vehicle were modeled using surface panels, in particular, a total of 13758 elements were used to model the fuselage and tailplanes, 873 elements were used for each of the two nacelles, and each semi-span wing was modelled using 5400 elements. Further details regarding the aircraft mesh and convergence studies can be found in the complete published work [115].

It should be noted that the CFD models selected as a reference for comparison with the DUST results contain geometry inaccuracies compared to the actual aircraft. Specifically, during flight tests [11], the wing had a Gurney flap, which was reported in the latest work by Tran and Lim [101]. However, this feature was not taken into account in the work by Tran et al. [100] used for the comparison with DUST in hover and cruise conditions. The latest simulations by the same authors [101], which included the Gurney flap, were considered to be more accurate for the comparison in conversion mode. The DUST simulations conducted in this study did not take into account the Gurney flap on the wing that was present during flight tests [11]. As a result of the differences in the way the two CFD models were constructed, the overall lift of the aircraft cannot be accurately assessed and will not be presented in the results discussion. However,the rotation of the vehicle wing control surfaces was correctly reproduced in the DUST simulations tilting the last portion of the wing airfoil for the spanwise region of the flaps and flaperons, as indicated by the real aircraft geometry parameters that are presented in Table 2.7.

The DUST simulations considered the three different flight conditions characteristic of a tiltrotor mission, namely, hover, conversion, and cruise. Specifically, the simulations reproduced the hover and cruise flight parameters used in the high-fidelity CFD simulations performed by Tran et al. [100] and the conversion mode parameters of the CFD simulations conducted by Tran and Lim [101]. A summary of the flight parameters replicated in the DUST simulations is shown in Table 2.8, and their definitions are illustrated in the aircraft sketch presented in Figure 2.34. To ensure a thorough comparison of the results, the blade azimuthal angle definition and the reference system used in this work are the same as those used in the reference works [100, 101].

The DUST simulations were conducted for three distinct flight conditions, namely hover, conversion, and cruise, which are typically encountered during a tiltrotor mission. The simulations were designed to replicate the hover and cruise flight parameters that were utilized in the high-fidelity CFD simulations carried out by Tran et al. [100], as well as the conversion mode parameters of the CFD simulations performed by Tran and Lim [101]. A summary of the flight parameters that were replicated in the DUST simulations can be found in Table 2.8, while their definitions are presented in the aircraft sketch shown in Figure 2.34. To ensure a comprehensive comparison of the results, the blade azimuthal angle definition and reference system used in this study are consistent with those used in the reference works [100, 101].

Flight condition	Speed V_∞	Vehicle pitch α_V	Nacelle θ_N	Rotor speed Ω	Flap angle	Flaperon angle
Hover	0 knots	0°	90°	589 RPM	40°	25°
Conversion	40 knots	8.569°	75°	589 RPM	40°	25°
Cruise	160 knots	4.332°	0°	517 RPM	0°	0°

Table 2.8: *Parameters of the full XV-15 vehicle configurations considered for DUST numerical simulations.*

The testing conditions used in this study were obtained from the flight simulation data of the Generic Tiltrotor (GTR), which was initially provided by Ferguson [38]. To maintain consistency with the methodology employed in the high-fidelity CFD simulations [100, 101], the thrust (T) and lateral force (H) on the proprotors were adjusted by trimming the rotor collective and longitudinal cyclic pitch angles to match the simulator data [38]. This approach was identical to the CFD studies and was adopted

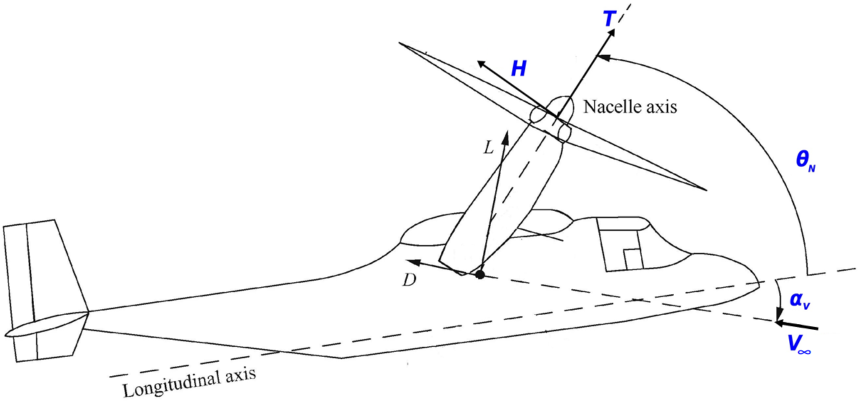

Figure 2.34: *Definition of the main parameters of the full XV-15 tiltrotor configuration.*

to ensure the accuracy and reliability of the results obtained from the DUST simulations.

Figure 2.35 shows a comparison between the trim targets for the thrust and H-force of the single proprotor, obtained from DUST simulations, and the GTR data for all tested flight conditions, as presented in Tran et al.'s CFD work [100]. The comparison of the average proprotor torque computed by DUST in the trimmed conditions to the GTR data and flight test data provides valuable insights into the accuracy of the numerical models used in the simulations. Figure 2.35(c) illustrates this comparison for all flight conditions considered, as well as for the cruise condition alone based on flight test data available in the literature [11]. The results show that the torque behavior predicted by DUST simulations is in good agreement with the GTR data, indicating that the numerical models used are reliable and accurate. This agreement instills confidence in the simulations and suggests that they can be used to predict the torque behavior of the proprotors in different flight conditions with a high degree of accuracy.

The simulations were run considering 40 steps per rotor revolution and conducting the simulation for ten rotor revolutions in total. The wake produced in the full-vehicle simulations varies from around 140 thousands vortex particles during hover to roughly 80 thousands vortex particles in cruise. Using a workstation that included an Intel® Core™ i9-9980XE processor with a base frequency of 3.00 GHz, 18 physical cores, and 2 threads per core, it took approximately 80 minutes to compute a single flight condition for the full vehicle.

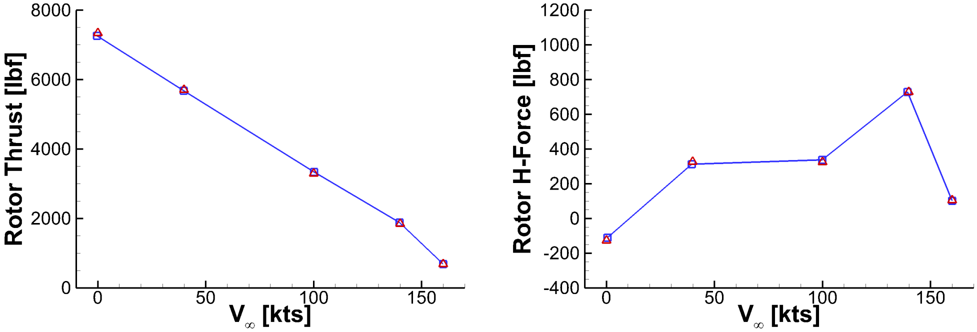

(a) Thrust.

(b) H-force.

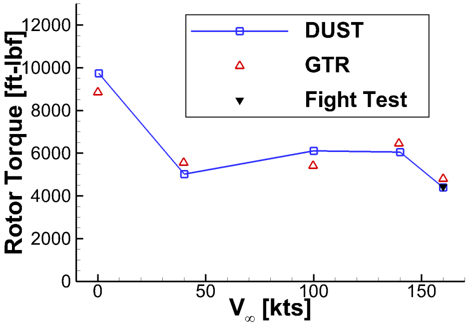

(c) Torque.

Figure 2.35: *Trim targets for the proprotor provided by Generic Tiltrotor (GTR) [38] compared with the results from the trimmed DUST simulations for all the flight conditions considered.*

2.4.1 Hover

The first condition considered is hover. In this condition, the aircraft is in stationary flight without any asymptotic flow velocity. Figure 2.36 shows the comparison of the contours of the instantaneous vertical velocity component around the vehicle computed in hover for blade azimuth $\psi = 270°$ over a Y_Z plane passing through the nacelle axis.

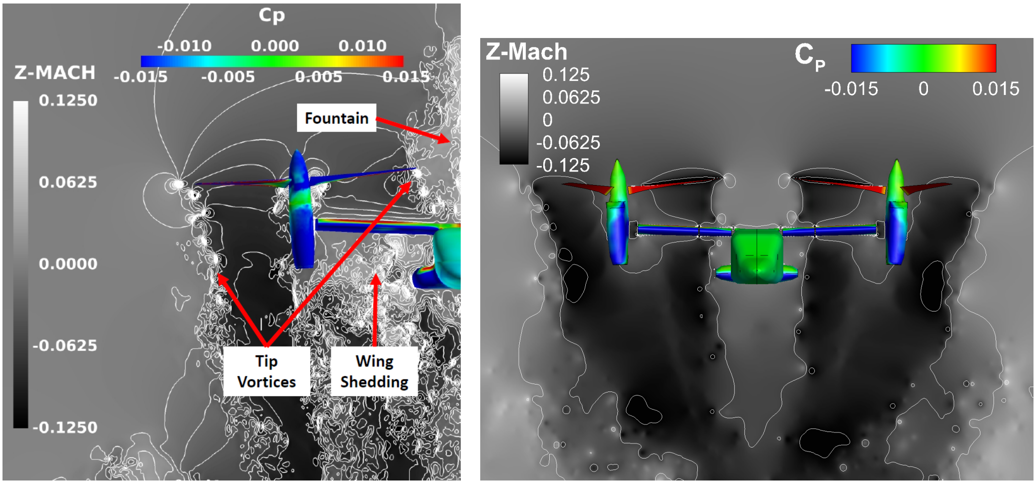

(a) Half-span model- CFD [100].

(b) Complete model - DUST [115].

Figure 2.36: *Comparison of the contours of the vertical velocity component around the vehicle in hover at* $\psi = 270°$, $\theta_N = 90°$, $\Omega = 589$ *RPM.*

The DUST simulations have been successful in replicating the flow field around the aircraft, which closely matches the global behavior predicted by high-fidelity CFD. One interesting flow feature that has been observed in the DUST results is the moderate upwash over the fuselage, which is a typical characteristic of tiltrotor configurations and is known as the fountain flow phenomenon [86]. However, it is worth noting that the size and strength of the fountain flow is greater in half-span CFD models due to the reflection of the flow caused by the symmetry boundary condition [86]. In comparison to high-fidelity CFD results, the DUST simulation shows a slightly weaker upwards velocity region over the fuselage, as shown in Fig. 2.36(a). Nevertheless, the DUST simulation has demonstrated a promising capability to accurately reproduce the complex flow field around the entire vehicle that is typical of this flight condition, while also requiring much less computational time compared to high-fidelity CFD simulations.

In hover and climb flight conditions, the wing's aerodynamic interfer-

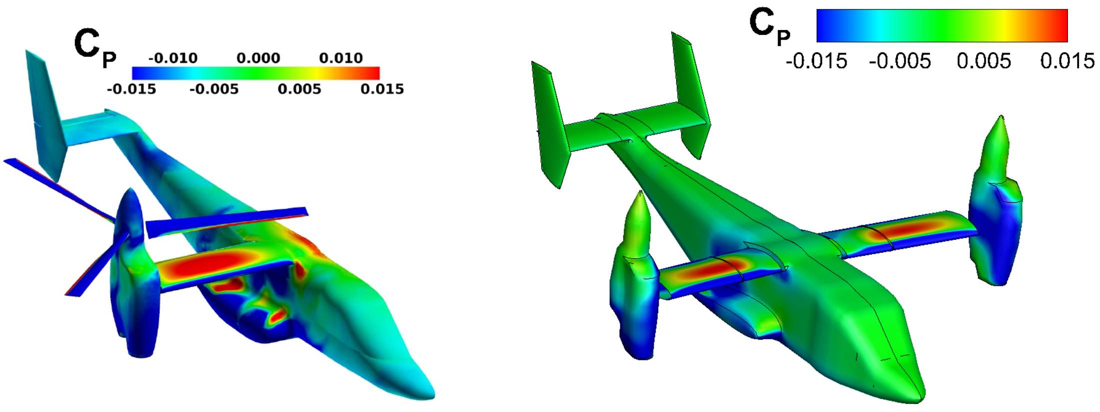

(a) Half-span model- CFD [100].

(b) Complete model - DUST [115].

Figure 2.37: *Comparison of the contours of the pressure coefficient C_p on the vehicle surface in hover at $\psi = 270°$, $\theta_N = 90°$, Ω = 589 RPM.*

ence on the rotor downwash generates a substantial downward force on the vehicle, which must be counteracted. Figure 2.37 illustrates the comparison of the instantaneous surface pressure coefficient C_p on the fuselage, as computed by DUST and high-fidelity CFD at a blade azimuth of $\psi = 270°$ in hover condition.

Due to the rotor wake's impact, there is a vast high-pressure zone that covers almost the entire wing surface. When comparing high-fidelity CFD with DUST, the high-pressure region's extent and positive C_p values are significantly greater. As a result, DUST underestimates the download on the wing in comparison to high-fidelity CFD. Specifically, DUST's wing download only amounts to 3% of the global proprotor thrust, whereas high-fidelity CFD calculates it as 10.3%. The discrepancy is likely caused by an erroneous forecast of the aerodynamic impact on the wing's surface resulting from the proprotor wake. However, it's challenging to model the intricate flow patterns around the wing accurately, as they are marked by areas of intense shedding, low flow velocities, and low Reynolds numbers, making them difficult to simulate using potential methods. Moreover, high-fidelity CFD shows a higher pressure region over the upper surface of the fuselage (see Fig. 2.37(a)) due to an higher strength of fountain flow effect related to the use of an half-span CFD model. Fig. 2.38 depicts an analysis of the aerodynamic performance of the proprotor during hover, with contour plots comparing the non-dimensional normal force (M^2c_n) and pitching moment (M^2c_m) of the blade computed over the last rotor revolution.

The DUST simulation captures the general trends of the high-fidelity CFD polar distributions of normal force and pitching moment. However, the CFD results exhibit sudden fluctuations in both normal force and pitching moment, especially around the azimuthal region near $\psi = 270°$, which are believed to be caused by the blade's passage through the high-pressure region over the wing and the re-ingestion of the fountain flow. Tran et al. [100] attribute these fluctuations to a combination of factors. CFD may overestimate the impulsive loading of the blades due to the larger size and stronger fountain flow related to the half-span model, as discussed in [86]. In contrast, since the fountain size and dynamics are weaker for the full-span vehicle, the DUST simulation results do not exhibit these fluctuations in this azimuthal region, and the overall behavior of the normal force and pitching moment is smoother than that of high-fidelity CFD results.

2.4.2 Conversion mode

The flight condition analyzed in conversion mode is characterized by a high incidence angle of the nacelle ($\theta_N = 75°$) and a low freestream velocity ($V_\infty = 40$ kts), resulting in complex vortex interactions. The vortices produced by the proprotor blades rapidly wrap up into a pair of disk vortices, beginning around $\psi = 90°$ and $\psi = 270°$. High-fidelity CFD results [101] highlight this feature, which is also clearly captured by the DUST simulation results. An instantaneous flow field computed at $\psi = 270°$ is illustrated by the iso-surface of the Q-Criterion in Fig. 2.39(a). At $\psi = 90°$ and $\psi = 270°$, a proprotor blade interacts significantly with the vortices produced by the second and third blades, passing simultaneously over both the upper and lower surfaces of the rotor blade (see Fig. 2.39(b)). The DUST simulation quantitatively captures the flow physics of this interaction when compared to high-fidelity CFD results presented in [101].

The formation of disk vortices results in significant variations of normal force that affect the interactional effects on proprotor blades. These variations are clearly visible in the comparison of the blade M^2c_n computed at $r/R = 0.95$, as shown in Fig. 2.40(a). DUST simulations accurately capture the occurrence and amplitude of the normal force variations around $\psi = 90°$ and $\psi = 270°$ computed by CFD. However, the amplitude of the sudden fluctuations in pitching moment, depicted in Fig. 2.40(a), is not well captured by DUST, even though the mean value along the rotor revolution is quite similar to the CFD results. The inaccurate representation of the peak loading in the pitching moment could also be influenced by the prediction of a chord-wise force component, which is not available for

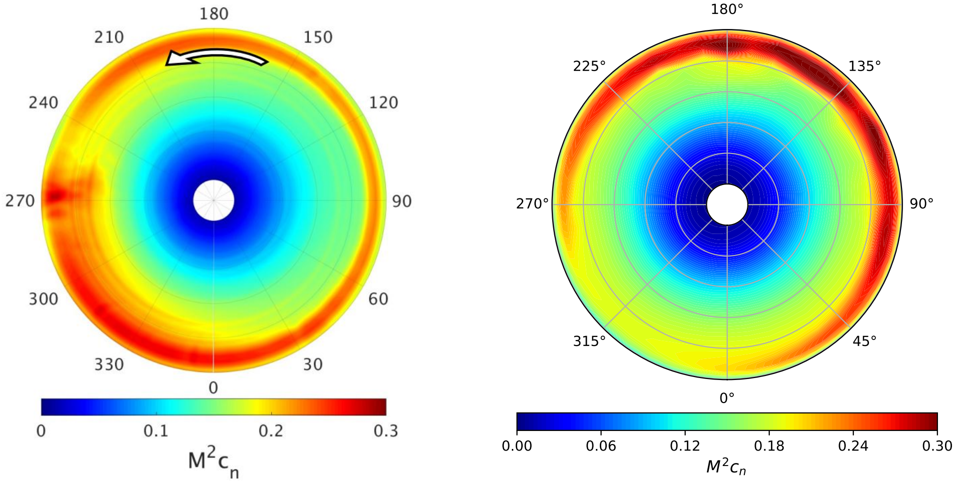

(a) M^2c_n - CFD [100]

(b) M^2c_n - DUST [115]

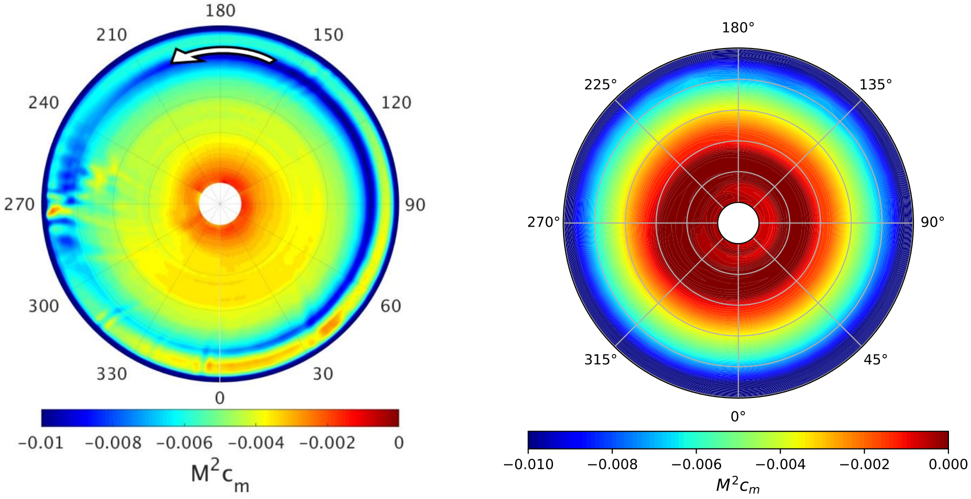

(c) M^2c_m - CFD [100]

(d) M^2c_m - DUST [115]

Figure 2.38: *Comparison of the contours of the non-dimensional normal force* M^2c_n *and pitching moment* M^2c_m *on the proprotor blade in hover,* $\theta_N = 90°$, Ω *= 589 RPM.*

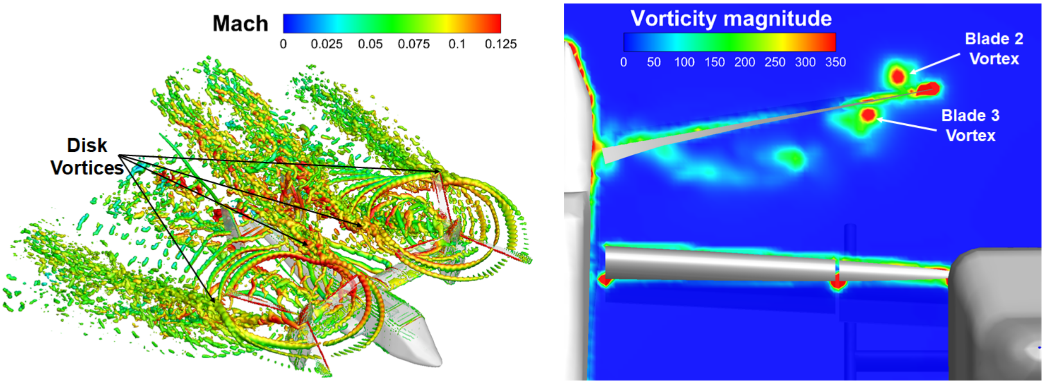

(a) Iso-surface of Q-Criterion.

(b) Iso-contours of vorticity on a slice cutting the nacelle axes

Figure 2.39: *Instantaneous flow field computed by DUST in conversion flight condition at* $\psi = 270°$, $\theta_N = 75°$, V_∞ *= 40 kts,* Ω *= 589 RPM (published in [115]).*

comparison from CFD.

Fig. 2.41 is presented to assess the aerodynamic impact on the flow field caused by the interaction between the proprotor wake and the wing. The comparison of the instantaneous flow field on a slice that cuts the wing longitudinally at midspan is depicted.

The comparison between the high-fidelity CFD and DUST flow field representations shows a fairly good agreement, indicating that the proprotor wake in this flight condition is transported downstream and does not interact with the wing. However, DUST simulations fail to exhibit the restricted separated flow area on the upper surface of the deflected flap.

2.4.3 Cruise

Finally, we consider the advanced flight condition, that is typical of cruise flight. During the cruise condition, the proprotor wake flows downstream, exhibiting a coherent helical structure of the vortices that envelop the wing blade tips. DUST simulations accurately replicate this flow pattern, as evidenced by the Q-criterion iso-surface depicted in Fig. 2.42 at $\psi = 270°$. Additionally, since the wing control surfaces are not deflected and the nacelle axis is aligned with the freestream velocity, the shedding from the nacelle is clearly discernible.

The interaction between the proprotors and the wing has an aerodynamic effect on the blade performance. When in cruise mode, the thick airfoil of the XV-15 tiltrotor configuration creates a blockage effect, resulting in an

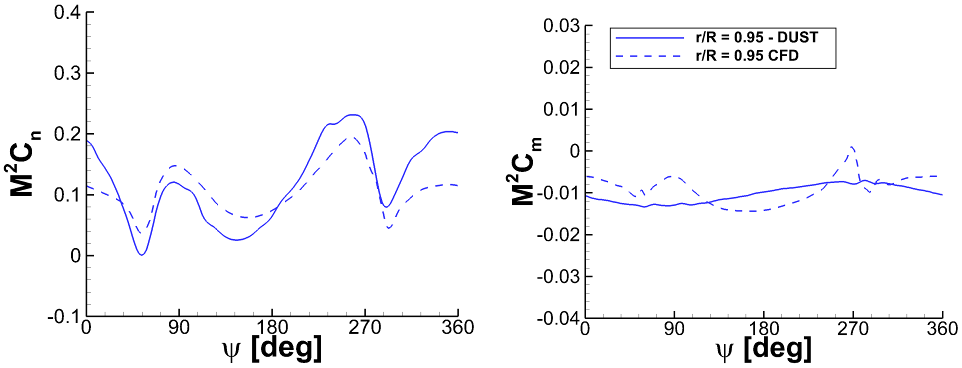

(a) M^2c_n.

(b) M^2c_m.

Figure 2.40: *Comparison of the time histories of the non-dimensional normal force* M^2c_n *and pitching moment* M^2c_m *on the proprotor blade in conversion flight condition at* $r/R = 0.95$, $\theta_N = 75°$, V_∞ *= 40 kts,* Ω *= 589 RPM (published in [115]).*

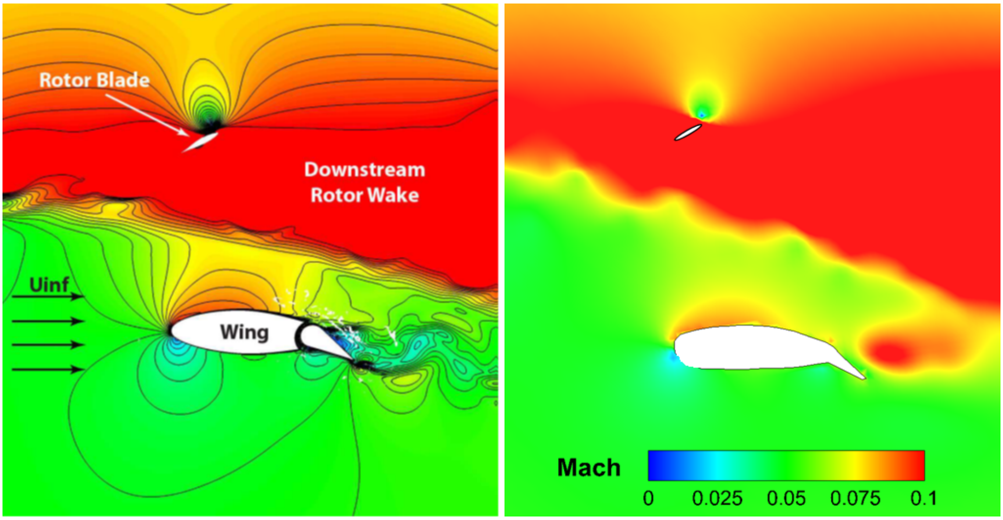

(a) CFD - [101]

(b) DUST - [115]

Figure 2.41: *Comparison of the instantaneous flow field at wing midspan in conversion flight condition at* $\psi = 270°$, $\theta_N = 75°$, V_∞ *= 40 kts,* Ω *= 589 RPM.*

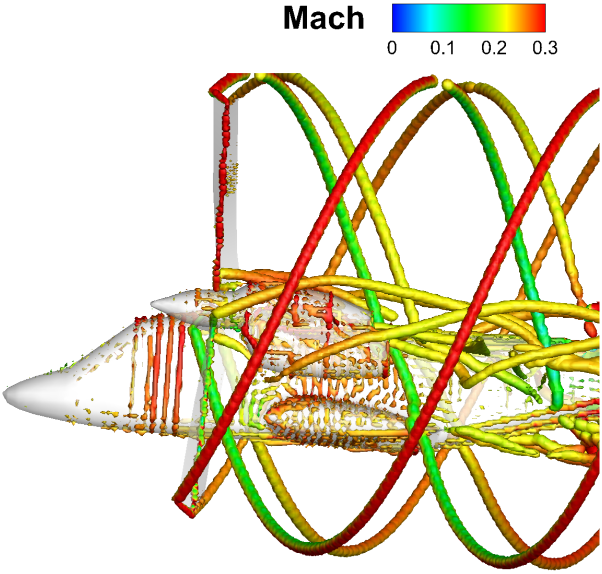

Figure 2.42: *Instantaneous flow field computed by DUST in cruise flight condition at* $\psi = 270°$, $\theta_N = 0°$, V_∞ *= 160 kts,* Ω *= 517 RPM; iso-surface of Q-Criterion (published in [115]).*

upwash when the blade passes over the wing. This produces a positive peak in the normal force of the proprotor, occurring once per revolution on each blade. Additionally, due to the wing's aerodynamic circulation, a doublet wash occurs on the blade's normal velocity, producing an upwash followed by a downwash when the blade passes in front of the wing. This creates a local unsteady doublet of the blade's normal force. The comparison of the blade's non-dimensional normal force and pitching moment contours over the last rotor revolution shows a doublet loading related to the blade's passage in front of the wing, particularly evident for $M^2 c_n$. The loads polar distributions computed by DUST and high-fidelity CFD are in good agreement, with some minor discrepancies observed for the pitching moment only. The outcomes of this comparison confirm the capabilities of the mid-fidelity approach implemented in DUST to reproduce the flow features related to proprotor/wing interactions and to capture the behaviour of the rotor aerodynamic performances also for aircraft cruise condition.

The findings of this study clearly demonstrate the strengths and limitations of mid-fidelity aerodynamic numerical solvers in comparison to URANS solvers when evaluating the aerodynamic performance and interactional flow characteristics of complex VTOL aircraft designs. The favor-

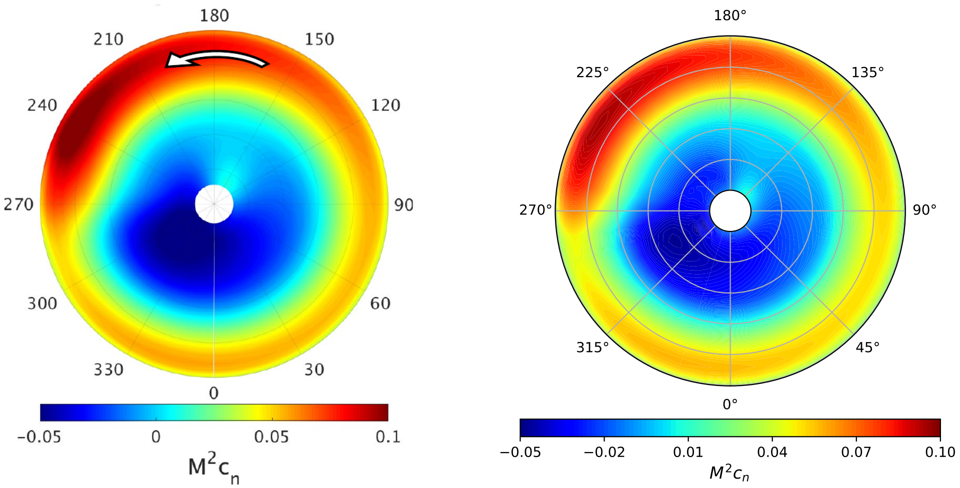

(a) M^2c_n - CFD [100] (b) M^2c_n - DUST [115]

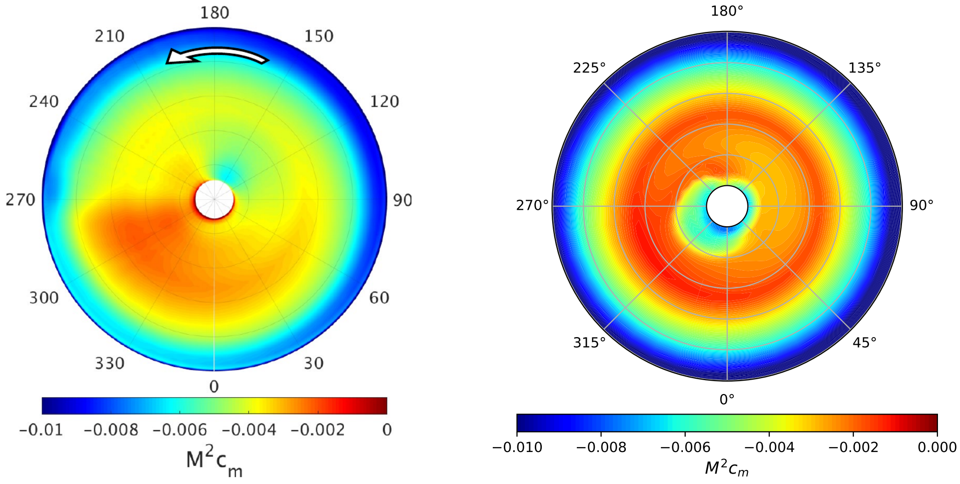

(c) M^2c_m - CFD [100] (d) M^2c_m - DUST [115]

Figure 2.43: *Comparison of the contours of the non-dimensional normal force* M^2c_n *and pitching moment* M^2c_m *on the proprotor blade in cruise,* $\theta_N = 0°$, V_∞ *= 160 kts,* Ω *= 517 RPM.*

able agreement between the mid-fidelity results obtained through physics-based vortex particle methods and the CFD results over the analyzed flight conditions indicates that such solvers are capable of exploring the main interactional flow features unique to tiltrotor aerodynamics. However, it is important to keep in mind that there may still be some limitations to DUST simulations, such as the inability to capture certain flow phenomena with high accuracy, as well as the need for further validation against experimental data. This comprehensive assessment provides a new avenue for the aerospace scientific and industrial communities, representing a valuable tool for engineers and researchers in the field of rotorcraft design. The reduced computational effort required to run mid-fidelity simulations, as evidenced by DUST, suggests that these solvers can be a valuable tool in the preliminary design of novel VTOL aircraft architectures, such as tiltrotors, which necessitate extensive configuration exploration to cover various stages of their flight missions.

CHAPTER 3

XV-15 Tiltrotor aeroeservoelastic model

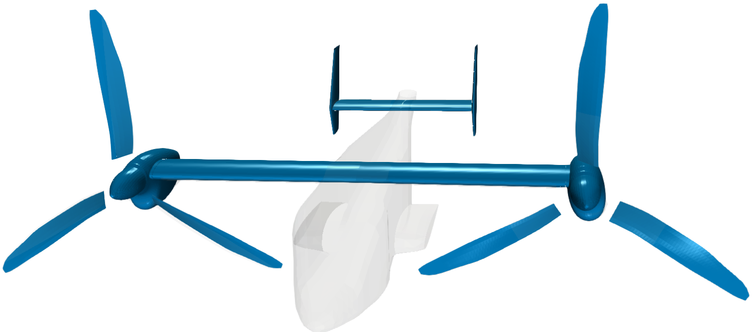

Figure 3.1: *XV-15 tiltrotor model.*

In this chapter, the aeroelastic numerical model of the XV-15 tiltrotor equipped with Advanced Technology Blades (ATB) is presented. The current study utilizes the new numerical DUST-MBDyn environment presented in Chapter 1 to construct a complete XV-15 aeroelastic model of the tiltrotor equipped with Advanced Technology Blades (ATB). The model illustrated in 3.1 is divided into two parts: the rotor component and the airframe model, which includes the wing, nacelles, and tail. The rotor component is validated structurally and aerodynamically against literature data, while the airframe model is constructed using a parallel high-fidelity aerodynamic model due to the lack of detailed literature data. This allows for the demonstration of the accuracy of the aerodynamic results on the wing-nacelle system, and some comparisons are made. The following description and the relative validation of the structural dynamics model was published in the course of the research work in [28].

3.1 Proprotor

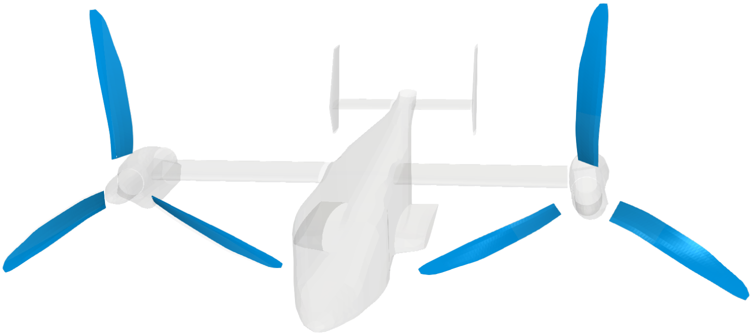

Figure 3.2: *Prop-rotor model.*

The multibody model of the XV-15 proprotor, Fig. 3.2, is made up of ATB blades. The rotor is stiff-in-plane with a gimballed hub. In MBDyn, the universal gimbal joint has been modeled as an ideal homokinetic joint, neglecting the 2/rev components caused by rotor flapping [21]. The proprotor is designed to be stiff-in-plane, which means that it resists bending in the direction of the blade rotation. This stiffness is important for maintaining the structural integrity of the rotor and ensuring that it operates efficiently. The hub of the rotor is gimballed, which allows it to tilt and swivel in response to changes in the aircraft's orientation. In order to simulate the behavior of the proprotor numerically in MBDyn, it is necessary to model the various components of the system. One of the components that must be modeled is the gimbal joint that connects the hub to the blades. In the case of the XV-15 proprotor, this joint has been modeled as an ideal homokinetic joint. An ideal homokinetic joint is a type of universal joint that is designed to transmit motion smoothly and without any loss of power.

However, this type of joint does not take into account the 2/rev components that are caused by rotor flapping [21]. Rotor flapping refers to the up-and-down motion of the blades as they rotate, which can cause additional forces and stresses on the rotor system. While neglecting the 2/rev components caused by rotor flapping may simplify the modeling process, it is important to recognize that this simplification may introduce some inaccuracies in the simulation. As with any modeling technique, it is important to carefully consider the assumptions and limitations of the model in order to ensure that the results are reliable and accurate. The main rotor data taken from the original CAMRAD-JA model presented in [24] are listed in Table 3.1.

Table 3.1: *XV-15 main rotor data [24].*

Rotor data		
Number of blades	3	
Solidity	0.103	
Radius	3.81	m
Precone	2.5	deg
Pitch-flap coupling, δ_3	-15	deg
Sweep	0.8870	deg
Droop	0.4617	deg
Chord	0.41	m
Helicopter speed (HC)	601	RPM
Airplane speed (AP)	480.8	RPM

3.1.1 Control Chain

Based on the information provided by [24], the layout of a dual path control chain representative of that of the XV-15 proprotor shown in Fig. 3.3 was modeled. Figure 3.4 represents a top view of the constructed model, highlighting the characteristic angles of the rotor mechanism.

Each component reported in the built CAD model has a corresponding part in the implemented MBDyn multibody model. The flowchart in Fig. 3.5 details the blade pitch control system implemented in MBDyn with the employed joints. The blade pitch control system, which is an essential component of the proprtor, has been implemented in MBDyn using different joints. The flowchart shown in Figure 3.5 provides a comprehensive overview of the different joints utilized in the MBDyn model to simulate the mechanism. The flowchart illustrates the various stages of the blade pitch control system, starting from the input signals provided by mast and control nodes and moving toward the output given to the blade part. The employed

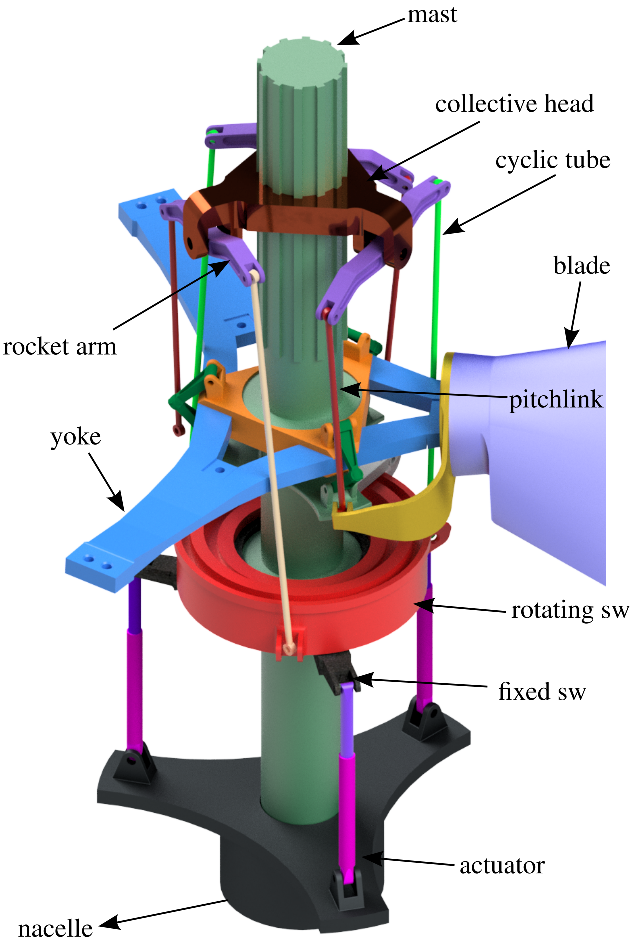

Figure 3.3: *Layout of the XV-15 proprotor control chain.*

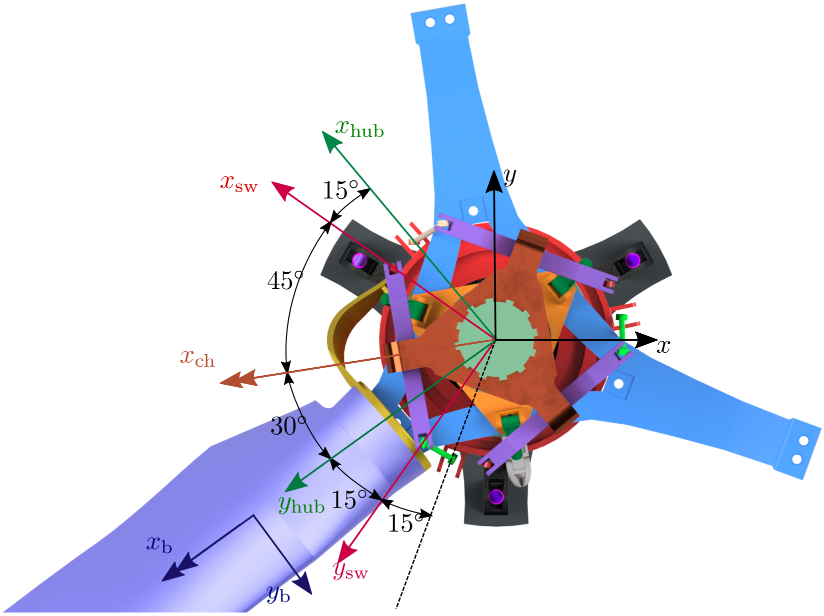

Figure 3.4: *Layout of the XV-15 proprotor control chain angles, top view.*

joints play a crucial role in modeling the motion of different components of the system accurately. By using MBDyn, it becomes possible to simulate the dynamic behavior of the blade pitch control system under varying operating conditions. Overall, the correspondence between the CAD model and the MBDyn model, along with the use of different joints in the MBDyn model, enables a more detailed and accurate simulation of the blade pitch control system in rotors. A brief description of the role of each part of the multibody model is given below:

- `Nacelle`: the node that represents the attachment between the wing and the nacelle;
- `Control`: the node to which collective and cyclic inputs are assigned is defined in a reference system that is rotated about the shaft by an angle of $\psi_{\mathrm{sp}} = \tan^{-1}(x_{\mathrm{sp}}/y_{\mathrm{sp}})$. This is done to separate longitudinal and lateral cyclic inputs. The point where the pitch link is connected to the swashplate determines the in-plane components x_{sp} and y_{sp} used in the calculation of ψ_{sp}. Although the real XV-15 did not employ lateral cyclic command as lateral movements were achieved using differential collective, it was deemed necessary to incorporate both lateral and

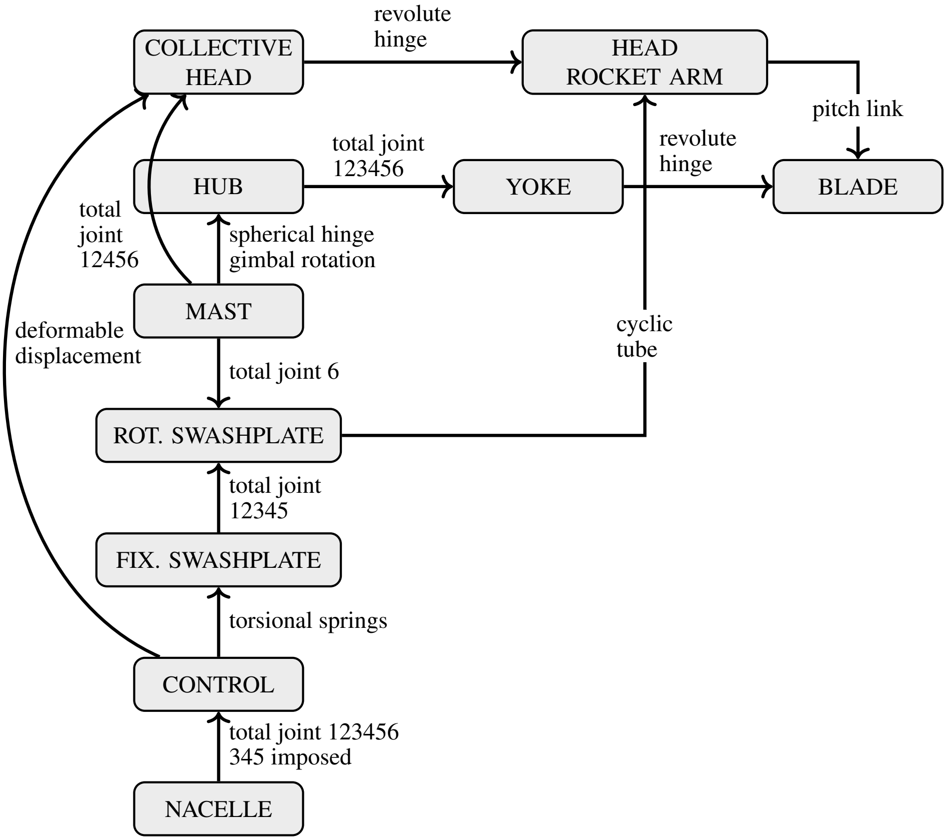

Figure 3.5: *Flowchart of the MBDyn model of the XV-15 proprotor, particularly showing the individual blade pitch control system components and their connections for the dual control path.*

longitudinal cyclic commands in this model;

- `Fixed Swashplate`: the non-rotating part of the swashplate is depicted by this node, and its movements in the in-plane direction as well as rotation around the shaft axis are restricted to the `Control` node. In order to consider the flexibility of the control chain, two torsional springs that have been calibrated to coincide with the pitch mode frequency at 2.89/rev [24] are utilized to connect it to the `Control` node. ;

- `Rotating Swashplate`: a revolute hinge links this node to the `Fixed Swashplate`, while another joint causes it to rotate in unison with the shaft by connecting it to the `Mast` node (which is defined later);

- `Collective Head`: the placement of this node is in the rotating reference system. It is connected to the `Control` node via a deformable spring that runs along the shaft axis, allowing for the flexibility of the collective control pathway to be taken into account;

- `Head Rocket Arm`: this node is linked to the `Collective Head` node by a revolute hinge and to the rotating swashplate using a cyclic tube. The cyclic and collective commands are then conveyed to the blade through the pitch link. Furthermore, the `Mast` node propels the `Hub` (which will be explained later) and the `Rotating Swashplate` nodes. It is connected to the `Nacelle` node through a revolute hinge, with its angular velocity pre-defined.

- `Hub`: this node is restricted to the `Mast` node using a spherical hinge and a gimbal joint [68]. The combination of these two joints forms an ideal constant velocity joint. To raise the first gimbal frequency to a value of 1.02/rev, two torsional springs were introduced between the `Hub` and `Mast` nodes;

- `Yoke`: this component denotes the elastic beam that links the hub to the blade. To establish the blade-to-yoke connection, a solitary load path is employed, which involves a revolute hinge;

- `Blade`: this element is simulated as an elastic beam that is joined to the yoke via the pitch-bearing connection. The pitch angle is mandated by the pitch link rod.

3.1.2 Blade-Yoke

The flexible component of the rotor system, which includes the blades and yoke, is modeled using the MBDyn finite volume beam element [15, 42]. This approach allows for a precise representation of the structural dynamics of the blades and yoke, taking into account the deformation and vibration of the components during operation. To ensure accurate results, a total of 12 beam elements are used to model each blade, while each yoke arm is modeled with 5 beam elements. The number of elements was carefully selected to ensure that the mode frequencies of the rotor converge to a stable value, providing reliable predictions of the system's behavior. This approach allows for a comprehensive analysis of the rotor system, taking into account the complex interplay between the various components and their interactions with the environment.

To translate the properties from the CAMRAD-JA model to MBDyn and then to couple the model with the DUST lifting line aerodynamic model, all nodes were placed along the pre-coned feathering axis, rotating each section by the corresponding aerodynamic twist. To accommodate offsets and relative rotations between the neutral, elastic, and feathering axes. a full 6×6 stiffness matrix has been used. In Fig. 3.6 are illustrated the blade main axis. The stiffness and mass distributions of the blade along the span, derived from CAMRAD-JA input, are shown in Fig 3.6. The dotted lines correspond to the beam evaluation section while the red dot corresponds to the pitch-bearing location.

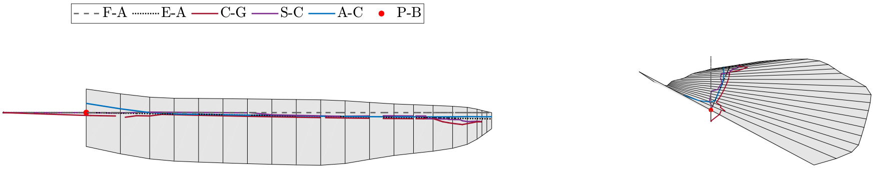

(a) Top view (b) Chord view

Figure 3.6: *ATB blade definition*

3.1.3 Blade aerodynamics

To model the blade aerodynamics, two levels of fidelity were used. The low-fidelity model is based on the 2D strip theory and is available in MBDyn. Four airfoils are placed along the blade with a non-smooth transition, following the distribution presented in Table 3.3, where the blade aerody-

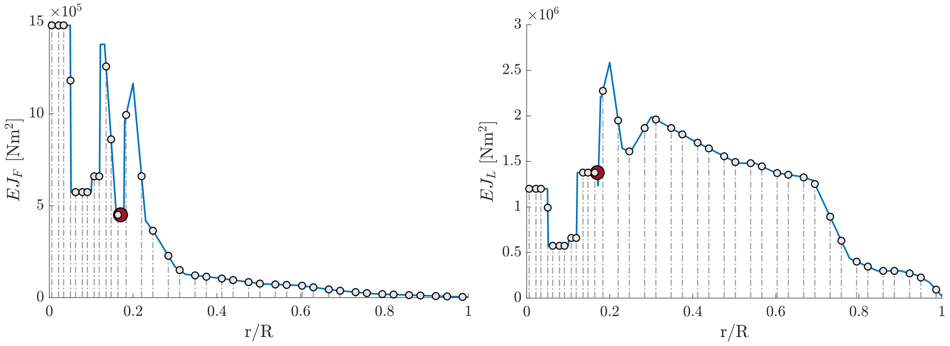

(a) EJ Flap (b) EJ Lag

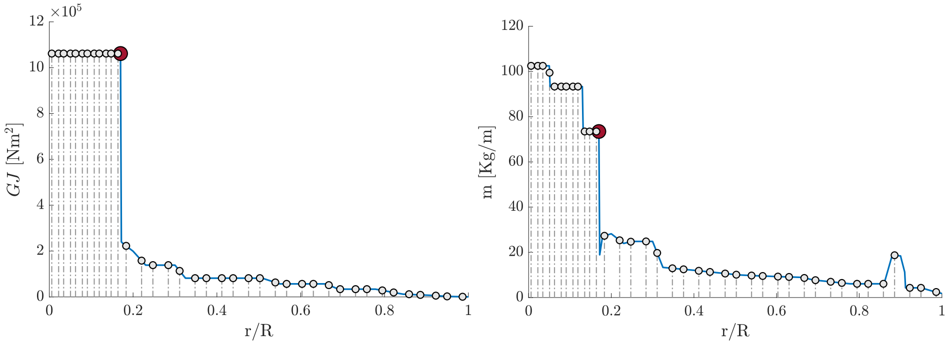

(c) GJ (d) weight

Figure 3.7: *Structural data*

namics was modeled considering the Blade Element/Momentum Theory with a Glauert model [58] for the induced velocity with corrections made according to the original CAMRAD-JA model and reported in Table 3.2:

Table 3.2: *MBDyn inflow parameters*

Parameters	
Hover correction factor	1.2
Forward flight correction factor	2.0
Memory factor	0.9
Tip loss factor	0.995

Table 3.3: *XV-*15 *ATB Blade airfoil distribution [24].*

Airfoil data		
Airfoil	Start [r/R]	End [r/R]
V43030-1p58	0.17	0.20
VR7-3	0.20	0.84
VR8mod	0.84	0.95
VR8	0.95	1

Instead, the DUST mid-fidelity aerodynamic model of each blade is provided by a DUST lifting line component. Lifting line aerodynamic elements are used for the rotor blades because they naturally encompass both compressibility and viscous effects. This simple aerodynamic model gives accurate results on high aspect ratio bodies while being computationally very efficient [63, 75]. 35 aerodynamic elements along the span blade are used for each blade: this number has been determined after a convergence study on hover loads. Each aerodynamic panel can incorporate aerodynamic twist variations and smooth profile transitions. Since in DUST is possible to define a smooth transition between one airfoil and the following, slightly different airfoil distribution is used with respect to the one reported in table 3.3, which is considered more realistic with respect to the actual blade.

Both aerodynamic models incorporate viscous and compressibility effects by means of the aerodynamic airfoil table `.c81`.

3.1.4 Aeroelastic validation

Validation of the dynamic behavior of the isolated rotor in a vacuum is accomplished using the Campbell diagram. This diagram tracks the rotational frequency of each mode shape against the rotor speed. To create each

Campbell diagram, various rotor speeds were considered, and the eigenvalues were calculated using the eigenvalue card available in MBDyn [65]. The outcomes are presented in Figures 3.8(a) and 3.8(b), representing the collective modes and cyclic modes, respectively, for a collective angle of 12°. Figures 3.9(a) and 3.9(b) display identical outcomes, but for a collective angle of 40°. These two collective angles were chosen because they are representative of the two most different flight conditions in which the rotor must operate, namely helicopter and airplane mode. The collective modes involve all blades moving simultaneously in the same direction, while the cyclic modes involve the blades moving anti-symmetrically. The flap mode refers to a beam-bending mode in which the eigenvector's predominant component is out of plane. In contrast, the lag mode has the predominant component of the eigenvector in the in-plane direction. Finally, the torsion mode is defined as the mode with the dominant component of the eigenvector in the blade axis's rotation.

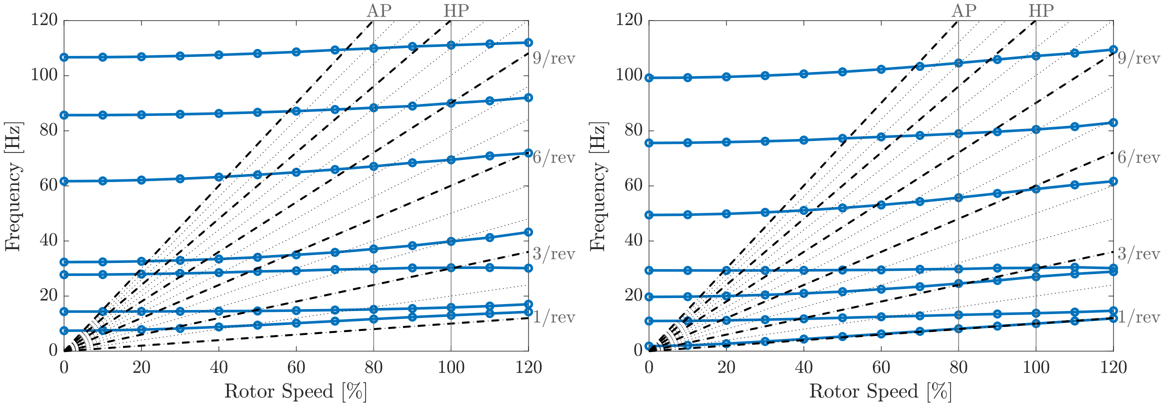

(a) Collective Modes.

(b) Cyclic modes.

Figure 3.8: *Rotor Campbell diagram in vacuum at collective pitch of* 12°.

Tables 3.4 and 3.5 provides a comprehensive comparison between the CAMRAD-JA and MBDyn models. The results show good agreement in both collective and cyclic modes, with only slight differences between the two models. However, the most notable disparity between the models is observed in the first torsion mode. This difference can be attributed to the fact that the CAMRAD-JA model uses a conventional helicopter-like control chain with a single control path, whereas the MBDyn model incorporates a dual load path to model the control chain. Further analysis of the multibody MBDyn model can be found in [28].

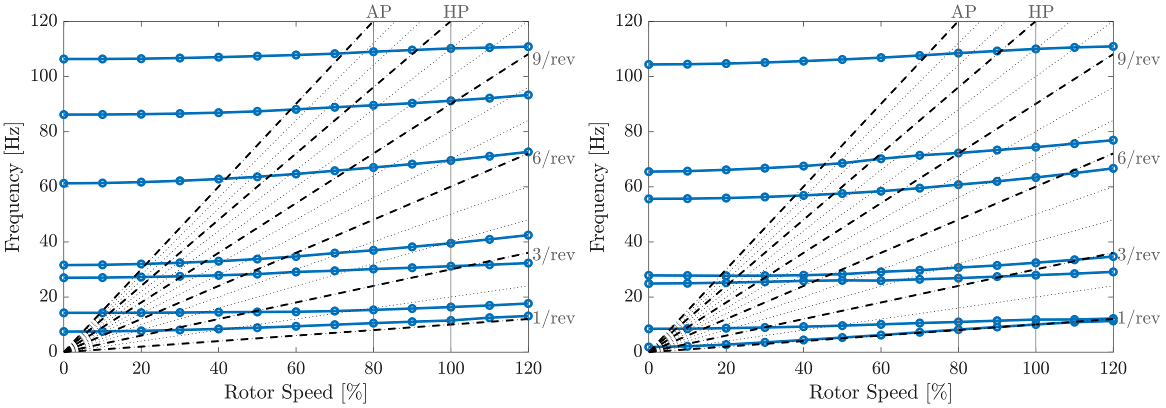

(a) Collective Modes. (b) Cyclic modess.

Figure 3.9: *Rotor Campbell diagram in vacuum at collective pitch of* $40°$.

Table 3.4: *Frequency (Hz) comparison in the non-rotating frame of the first 4 rotor modes in vacuum at* $12°$ *collective in HP mode.*

	CAMRAD-JA			MBDyn		
Mode	Collective	Regressive	Progressive	Collective	Regressive	Progressive
Gimbal	–	0.19	20.22	–	0.15	20.19
First Lag	12.68	3.18	23.22	12.81	3.38	23.43
First Flap	16.03	17.9	37.93	16.24	18.02	38.10
First torsion	30.39	20.85	40.88	30.92	20.23	40.41

Table 3.5: *Frequency (Hz) comparison in the non-rotating frame of the first 4 rotor modes in vacuum at* $40°$ *collective in AP mode.*

	CAMRAD-JA			MBDyn		
Mode	Collective	Regressive	Progressive	Collective	Regressive	Progressive
Gimbal	–	0.24	16.27	–	0.05	16.25
First Lag	10.19	2.42	18.45	10.53	2.83	19.10
First Flap	15.94	22.85	38.88	15.35	22.57	38.83
First Torsion	28.87	20.44	36.47	30.75	18.74	35.72

The proprotor aeroelastic model's predictive capability for rotor performance, loads, and stability in both hover and airplane modes is analyzed in this study. The low-fidelity MBDyn model and mid-fidelity DUST-MBDyn model are used to compare and evaluate the accuracy of the proprotor aeroelastic model. Additionally, the experimental results of OARF are used to validate the accuracy of the model in predicting rotor behavior in hover conditions. To carry out the simulations, a time-marching simulation method is employed with a time step of 120 per rotor revolution. Ten revolutions are taken into account, and the loads and displacement of the last revolution are averaged to obtain the results. The computational time required for simulating the rotor configuration is about 8 minutes for the DUST alone case and 16 minutes for the coupled case, using a workstation with a Dual Intel® Xeon Gold 6230R @2.10GHz processorwith 52 physical cores and 2 threads for each core. In contrast, the MBDyn model, which has a simpler aerodynamic model, can run on a regular laptop computer in about one minute. The numerical results are compared with the experimental run 48 of the OARF test campaign.

The rotor thrust coefficient (C_T/σ) and torque coefficient (C_Q/σ) as a function of the collective angle of the blade, along with the rotor figure of merit (FM), are plotted in Fig. 3.10. The experimental data from OARF [13] are compared with the results obtained using different aerodynamic models, as depicted in Fig. 3.10.

The performance curves obtained with both the DUST alone and the coupled DUST-MBDyn models accurately represent the experimental data across the entire range of blade collective angles tested. The proprotor aeroelastic model correctly captures the rotor stall that begins to occur for a collective angle greater than $15°$. However, the MBDyn alone model does not accurately capture hover performance. Specifically, the slope of the $C_T/\sigma - \theta_{075}$ curve is steeper compared to the experimental results and the DUST one, and no stall is predicted. Additionally, MBDyn overestimates the torque in the polar curve, and this prediction is further amplified when comparing the figure of merit of the rotor.

The wake velocity profile reported in Fig. 3.11 of the coupled model was evaluated for various thrust coefficients, and the obtained data were compared with the results of the experimental analysis. During the experiment, a wake rake composed of pitot-static tubes was installed behind the rotor disc plane to measure the slipstream velocities and angles of the rotor in isolation under different operational conditions. The objective of this was to gain insight into the structure of the rotor slipstream and the distribution of the wing download. The measurements taken were able to provide

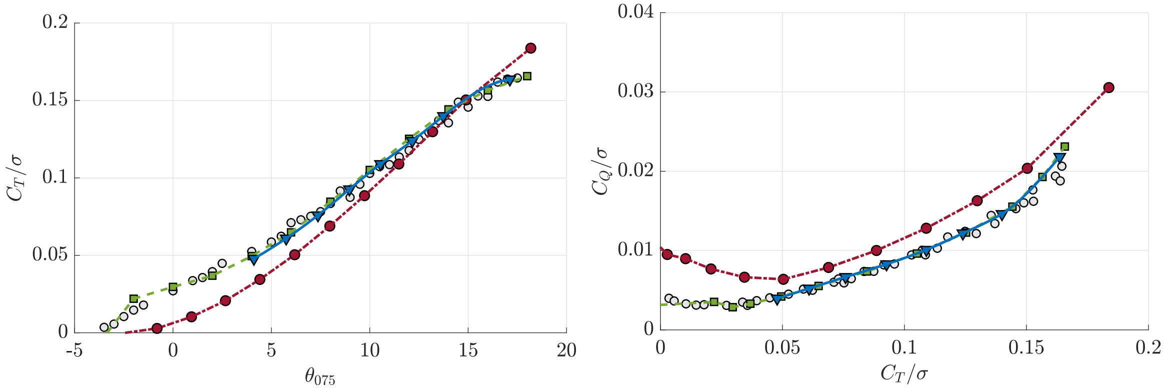

(a) C_T/σ vs θ_{075}.

(b) FM vs C_T/σ.

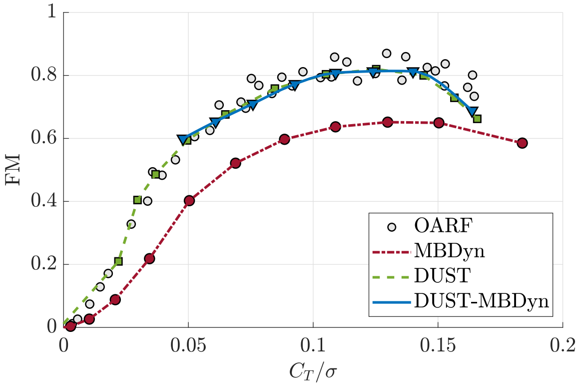

(c) C_Q/σ vs C_T/σ.

Figure 3.10: *ATB proprotor hover aeroelastic performances.*

valuable information that contributed to a better understanding of the flow field. Furthermore, a high degree of correlation was observed between the experimental and simulated data, which can be attributed to the ability of the Vortex Particle Method (VPM) to accurately preserve vorticity.

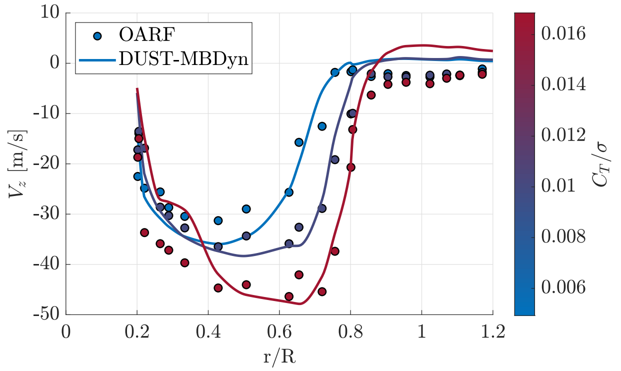

Figure 3.11: *Wake velocity measurements of the DUST-MBDyn model: comparison with experimental results*

This result highlights the usefulness and power of having a tool that allows for the calculation of both aircraft loads and provides insight into the physics of the flow field, a typical output of high-fidelity simulations that would not be achievable with low-fidelity methods.

3.2 Airframe

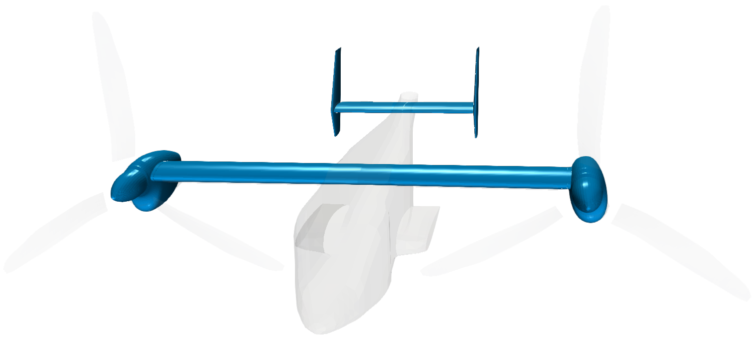

Figure 3.12: *Airframe model.*

This section presents the model implemented for the airframe section, which encompasses the main wing, nacelles, horizontal, and vertical tailplanes, as well as the modeling done for the aileron actuation system. However, unlike the model in Sec. 2.4, the fuselage is not modeled in DUST here. This is because it is not considered an interesting part for subsequent analyses, and also to reduce the numerical cost of the model, given that the focus is always on a preliminary design phase. Then, an aerodynamic validation is shown with respect to a CFD model for the wing-nacelle (wing-pylon) system, essential to understanding whether the presence of the nacelles is captured in the aerodynamic loads of the wing, which are responsible for the maneuver performance of the aircraft.

3.2.1 Multibody model

The airframe multibody model is composed of 14 rigid bodies representing the different parts of the tiltrotor: the fuselage carrying, the horizontal and vertical empennages, and the wing-nacelle system including the ailerons. Each body with the relative mass and inertia property is located in the position of the center of mass of the corresponding component, and inertial data are taken from the Finite Element Model (FEM) model presented in [4]. The nacelle is connected to the wing by deformable joints representing the flexibility of the down-stop attachment. The down-stop stiffness varies as a function of the conversion angle ϕ; it is calculated following the approach presented in [81]. Control surfaces rigid bodies, with associated polar inertia, are attached to the fixed-wing part by a statically determined constraint that is a combination of a spherical and inline joint.

In the absence of detailed data on the aileron actuation mechanism, a generic procedure for the design of an actuation system is used. The constraints given by the known data to be met are the position of the hinge axis placed at 75% of the chord and a max deflection of $47°$. A value of $-25°$ is assumed as the maximum negative deflection. In order to achieve rotation of the hinge with the use of a linear actuator, it is necessary to design a kinematic mechanism that converts the actuation elongation into rotation. The kinematic chain considered has three main points: the hinge point around which the control surface rotates and the two actuator heads, see Fig. 3.13(a). The left actuator head and hinge point are fixed to the ground on the wing and aileron frame respectively. The right head of the actuator, on the other hand, as the actuator extends, slides along a circular trajectory, the red dashed line in Fig. 3.13(a). The radius of this circumference, which represents the rigid connecting rod of the mechanism, has been designed to ensure the accommodation of the system within the wing section. Obviously, the larger its size, the more efficient the system will be since less linear actuation force will be required to ensure the same torque. Two other design parameters are the length of the actuator and the angle between it and the rigid connecting rod with the undeflected aileron. The choice is to consider the connecting rod and actuator perpendicular in the configuration with $\delta_\mathrm{a} = 0°$. Consequently, the length of the actuator is limited by the constraint already mentioned, namely that of placing the whole system inside the wing section. The kinematic operation of the system is shown in Fig. 3.13(b), where it is possible to see the position of the mechanism points for the deflection limits considered. Figure 3.13 shows the kinematic links of the designed mechanism as a function of aileron deflection. Based on the considerations made and the space constraints, an actuator length of $200\,\mathrm{mm}$ and a connecting rod length of $70\,\mathrm{mm}$ have been chosen.

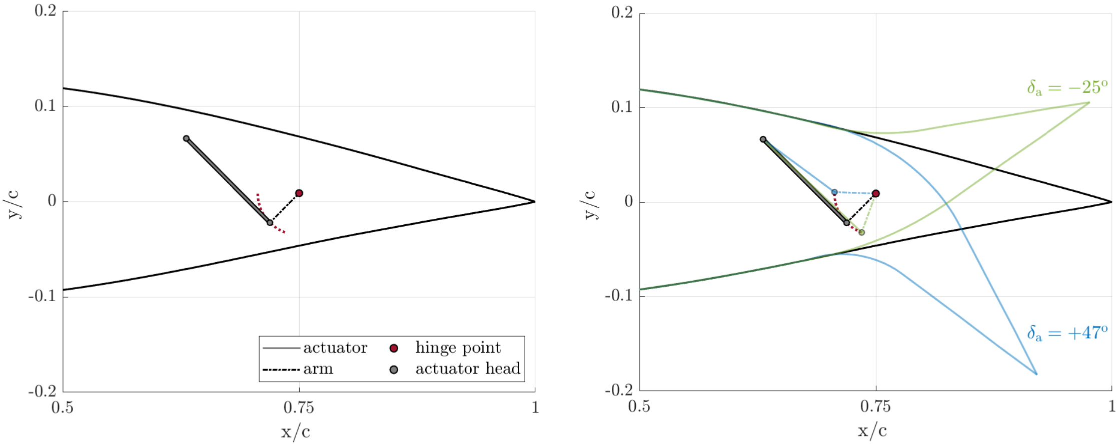

(a) Undeflected configuration.

(b) Deflected configuration.

Figure 3.13: *Aileron actuation system kinematics.*

The actuator elongation, see Fig. 3.14(a), has a fairly linear trend with respect to the deflection obtained in almost all of its operational regions. Nonlinear trends in the relationship are only evident at high-deflection angles. Through a polynomial curve fitting, it is possible to derive a polynomial function describing the kinematic link between the input on the actuator extension and the output on the obtained rotation, see Eq. 3.1.

$$\delta_a = -0.045473 - 1.229078 \cdot \Delta L + 0.000592 \cdot \Delta L^2 + 0.000067 \cdot \Delta L^3 \quad (3.1)$$

On the other hand, concerning the travel arm, defined as the component of the connecting rod length perpendicular to the actuator, there is a nonlinear trend as pointed out in Fig. 3.14(b).

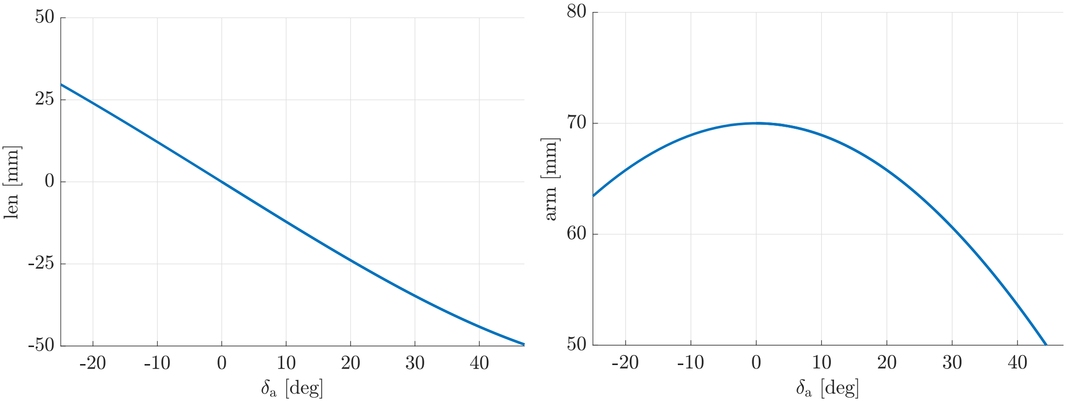

(a) Actuators length.

(b) Travel arm length.

Figure 3.14: *Aileron actuation system kinematics.*

The compliant actuator dynamic is obtained by a compliant dynamic model of the actuator described by Eq. 3.2, where the prescribed motion ΔL_c is first filtered to ΔL_f by a second order low pass Butterworth filter with a cut-off frequency of $7\,\mathrm{Hz}$, that approximates the actual dynamics of the actuator.

$$F_{\text{act}} = -K_a \Delta L_f - C_a \dot{L} \tag{3.2}$$

F_{act} represents the actuation force, $\dot{L}$ is the actuator length variation and K_a and C_a are the equivalent actuator stiffness and damping. The characteristics of the actuators are inspired by data taken from similar aircraft, which mounts 3 equidistant actuators on each control surface with an equivalent static linear stiffness K_a of each actuator equal to $2.8 \times 10^7\,\mathrm{N\,m^{-1}}$. As for the damping C_a, it has been tuned to eliminate high-frequency oscillations. However, in future aeroelastic analyses of the actuators coupled with the dynamics of the control surface and wing, it will be necessary to quantify this value more accurately, which is not deemed necessary for the analyses presented in this study.

From the perspective of multibody modeling, in MBDyn each actuator is modeled with a viscoelastic rod. The rod element represents a force between two nodes that depends on the relative position and velocity of two points, the actuator heads of Fig. 3.13(b). The direction of the force is also based on the relative position of the points defined by the line that passes through them. The actuator elongation is managed by acting on a pre-strain

ϵ_p, consisting of an imposed value of the axial strain that is subtracted from the geometrical strain before being passed to the viscoelastic constitutive law. The input acts on the zero force point ΔL_f through the transfer function that filters the desired set point ΔL_c according to the dynamics of the actuator. Then the rod does dynamic compliance through its stiffness K_a and damping.

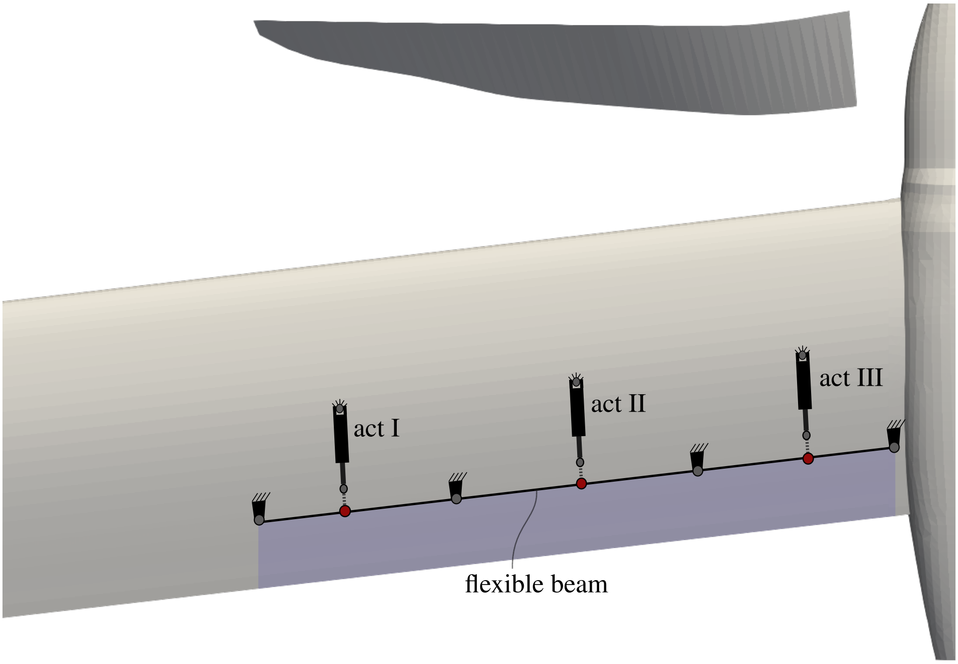

Figure 3.15: *Aileron actuation mechanism scheme, right wing.*

The aileron part, whose mechanism is illustrated in Fig. 3.15, is modeled in MBDyn with the flexible `beam3` element, as done for the rotor blades. The adopted 3 flexible beams are anchored at the main wing component with four spherical hinges that allow for rotation, which is controlled by three actuators mechanism. The elastic properties of the aileron were derived from those obtained during the FORMOSA project (see Sec. **??**) for the Next-Generation Civil Tiltrotor (NGCTR). Since the aircraft have different sizes, in the case of the NGCTR the chord is $1.9\,\mathrm{m}$ compared to the $1.6\,\mathrm{m}$ of the XV-15, according to [74] the elastic properties have been scaled according to the ratio of the areas, while for the torsional stiffness the scaling is proportional to the ratio of the section areas squared. In Tab. 3.6 are reported the stiffness properties of the stick model considered for each aileron. The coordinate x refers to the direction along the chord, y along the span and z upwards.

EA	EJ_{xx}	EJ_{zz}	GJ
N	$\mathrm{N\,m^2}$	$\mathrm{N\,m^2}$	$\mathrm{N\,m^2}$
$8.39 \cdot 10^7$	$1.63 \cdot 10^5$	$1.51 \cdot 10^6$	$2.62 \cdot 10^4$

Table 3.6: *Estimated XV-15 aileron elastic properties.*

3.2.2 Wing-pylon aerodynamics

To assess the capability of DUST to capture the complex three-dimensional aerodynamics due to the presence of the nacelle in the wing tip region, the isolated wing-pylon sub-system of Fig. 3.16 is considered.

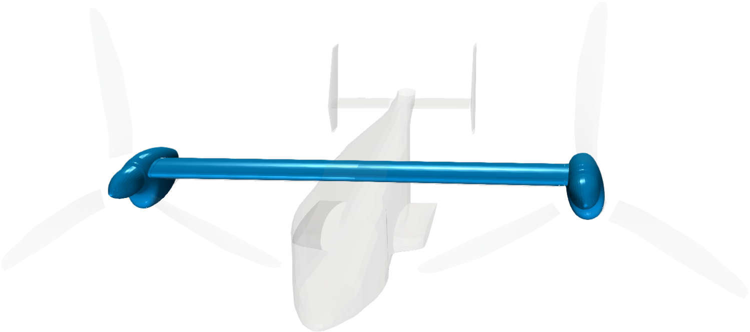

Figure 3.16: *Wing-pylon model.*

The aerodynamic coefficients of the wing-pylon system as a function of the angle of attack are known from [37]. In order to carry out a more complete investigation, a high-fidelity CFD model is built in order to have more comparative results. The numerical model includes the presence of the aileron. The selected CFD solver is SU2 [35], an open-source software suite initiated at the Aerospace Design Laboratory of Stanford University, freely available and licensed under the GNU Lesser General Public License. It uses the finite volume approach to solve partial differential equations (PDE) on unstructured meshes. It employs a vertex-based approach in contrast to a cell-based method, in which the variables are established and stored at the vertices (nodes). This method utilizes a median-dual grid. It solves the Unsteady Reynold-averaged Navier-Stoke (URANS) equations to analyze typical aeronautical problems that involve turbulent flows in the compressible regime. Concerning flux discretization, various techniques are available, notably JST, ROE, AUSM, Lax-Friedrich, and HLLC. Second-order precision is attained using a Monotone Upstream-centered Schemes of Conservation Laws (MUSCL) method with gradient limiting. At each grid node, the gradients of the flow variables are calculated using either the least-squares or Green-Gauss method to determine the gradients at the cell faces. The one equation Spalart-Allmaras (SA) and the two equations Menter Shear Stress Transport (SST) turbulence models are implemented in SU2.

The grid used in this work is a mixed-element grid composed of 19M total elements. The mesh is composed of tetrahedra, prisms, and pyramids around a surface that has been discretized using triangles and quads. For the simulation, the right semi-model was modeled by imposing the symmetry boundary condition on the longitudinal plane. The far-field boundary is located approximately more than 25 body span lengths away from the aircraft, with a boundary layer dimension to allow for $y^+ \approx 1$. The level of the volume grid refinement is managed through two sub-zones, see Fig.3.17, encapsulating wing and nacelle respectively.

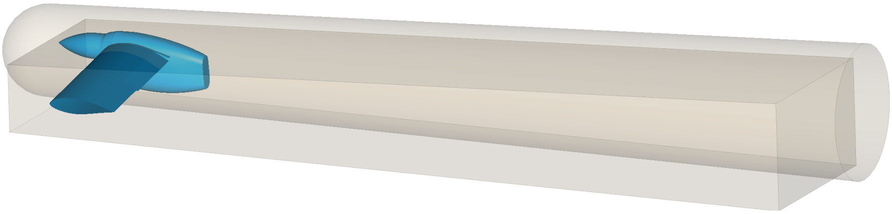

Figure 3.17: *CFD grid refinement zones.*

A JST-centered spatial discretization is used to calculate convective fluxes in the RANS computation. Turbulent variables for the SST models are convected using a first-order scalar upwind method, and the viscous fluxes are calculated using the corrected average-gradient method. Implicit, local time stepping is used to converge the problem to the steady-state solution, and the linear system is solved using the iterative BCGSTAB method with a maximum error tolerance of $\mathcal{O}(10^{-4})$.

The DUST numerical model of the wing-pylon system is modeled as surface panels (SP). Surface panel elements allow to model thick solid bodies, with source and doublet distributions, and following Morino's formulation of the aerodynamic problem a Dirichlet boundary condition for the velocity potential is introduced. Figure 3.19 illustrates the DUST aerodynamic mesh. To model the movable surface of the aileron, the DUST hinge

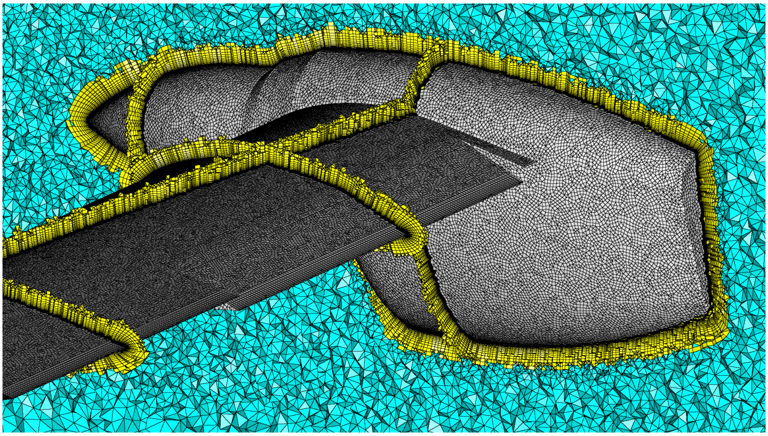

Figure 3.18: *CFD grid detail.*

component [94] is exploited, obtaining a deflected wing region and maintaining the continuity of the mesh. Regarding the mesh discretization in the chord section, a double refinement is employed both in the leading edge and in the hinge axis location, see Fig. 3.20.

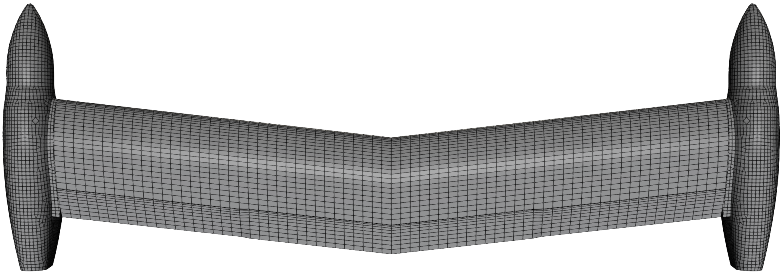

Figure 3.19: *DUST surface mesh for wing-pylon system.*

The wing-pylon aerodynamic system is tested by comparing high-fidelity SU2 results with the DUST mid-fidelity results. Considering the cruise speed condition at Mach=0.4, the aerodynamic coefficients between $-6°$ and +$8°$ degrees of angle of attack (AoA°) are computed, considering three different aileron deflections (δ_a) of $0°$, $10°$, and $20°$.

Figures 3.21(a) and 3.21(b) show the aerodynamic loads in terms of lift coefficient and drag coefficient. In the linear region, the lift coefficient obtained with DUST shows a good agreement with SU2 and experimental data provided by Ferguson [37]. The nonlinear effects on the lift curve related to stall are not captured by DUST, as can be expected considering the

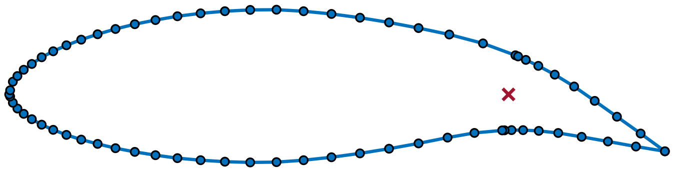

Figure 3.20: *DUST mesh refinement in the chordwise direction; hinge axis (red cross), mesh nodes (blue dot).*

assumptions of the numerical method. The good agreement in the drag coefficient between the SU2 simulations and the experimental data available for δ_a equal to 0° confirms the goodness of the high-fidelity model built to make comparisons with DUST. Since the parasite drag is not modeled by the mid-fidelity solver, there is a discrepancy between DUST and SU2 drag coefficient curves. On the other hand, since the induced drag generated by the wing tip vortices is almost well represented, all the curves show good coherence as a function of the AoA° and δ_a.

In terms of global performance associated with the aileron deflection, it is interesting to analyze the roll moment generated about the longitudinal axis of the aircraft. In Fig. 3.21(c) is reported the moment coefficient around the longitudinal axis considering the right semi-model as a function of the angle of attack for three different aileron deflections. These results confirm a good correlation between SU2 and DUST encouraging the use of the mid-fidelity aerodynamic model to investigate maneuvers.

A more detailed view of the load distribution on the wing-nacelle system is given by the comparison in terms of the pressure coefficient of Fig. 3.22, evaluated at AoA°=0° and δ_a=0°. From Fig. 3.22, it can be seen that in terms of the calculated pressure coefficient, the DUST results are consistent with those obtained with the CFD model. This is valid as long as the angle of incidence is modest and there are no separation zones that are not captured by the DUST aerodynamic model. Moreover, the comparison highlights a good correlation in the wingtip area where the nacelle is installed. Such good correlation is essential when designing the aircraft's control surfaces since these will be positioned near that area. Figure 3.23 shows the pressure coefficient extracted at the six spanwise stations illustrated in Fig. 3.22, whose distances from the longitudinal axis are shown in Table 3.7.

By examining the pressure coefficients at these spanwise stations, a more comprehensive view of the load distribution on the wing-nacelle system can be obtained.

The results of the first 5 stations (from Fig 3.23(a) to Fig 3.23(e))confirm

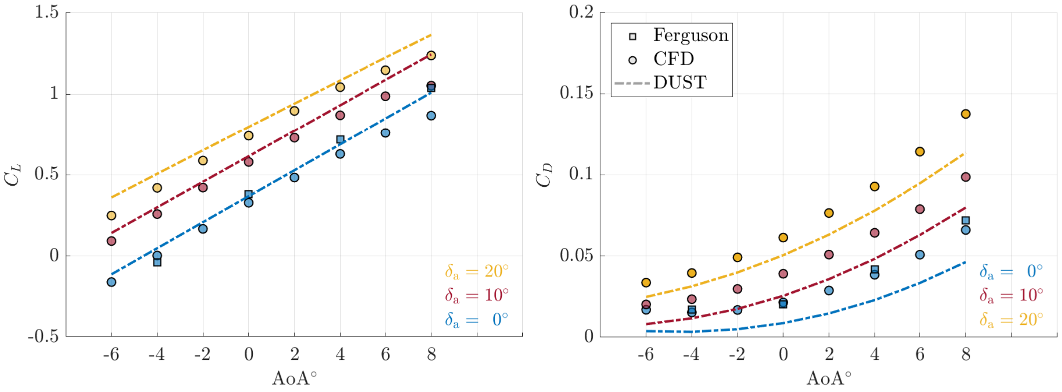

(a) Lift coefficient vs angle of attack.

(b) Drag coefficient vs angle of attack.

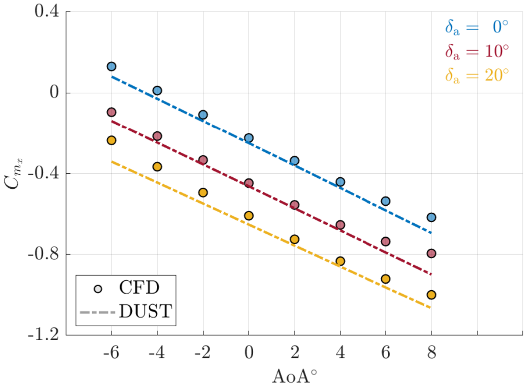

(c) Roll moment coefficient vs angle of attack.

Figure 3.21: *Wing-pylon system aerodynamic performances comparison between SU2 and DUST.*

Table 3.7: *Positions of the pressure probe sections.*

Section	$2y/b$
S1	0.00
S2	0.30
S3	0.50
S4	0.70
S5	0.85
S6	1.00

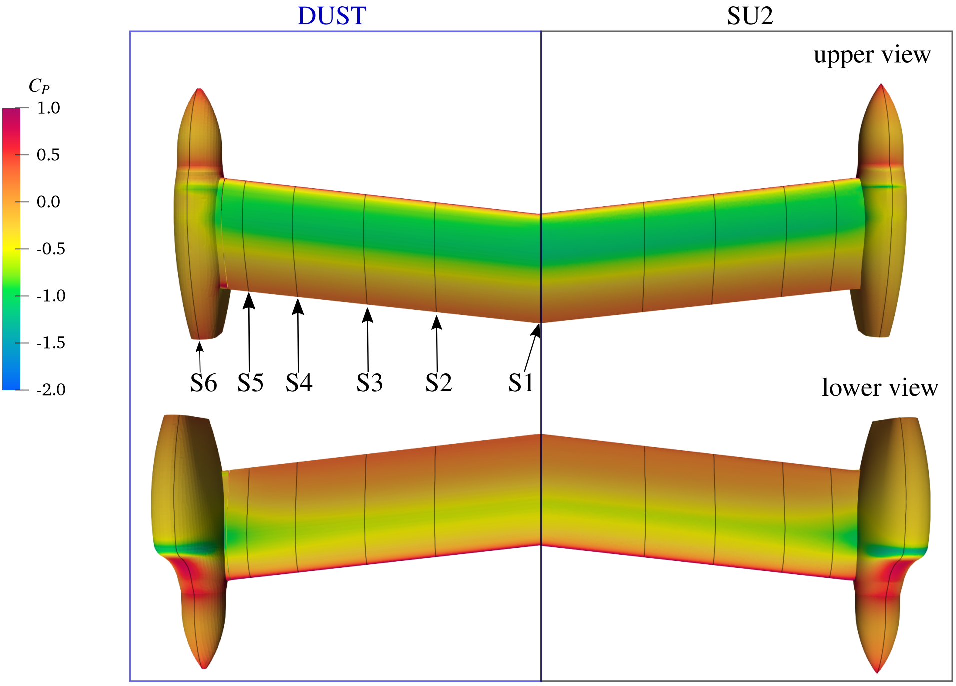

Figure 3.22: *Pressure coefficient comparison between SU2 and DUST.*

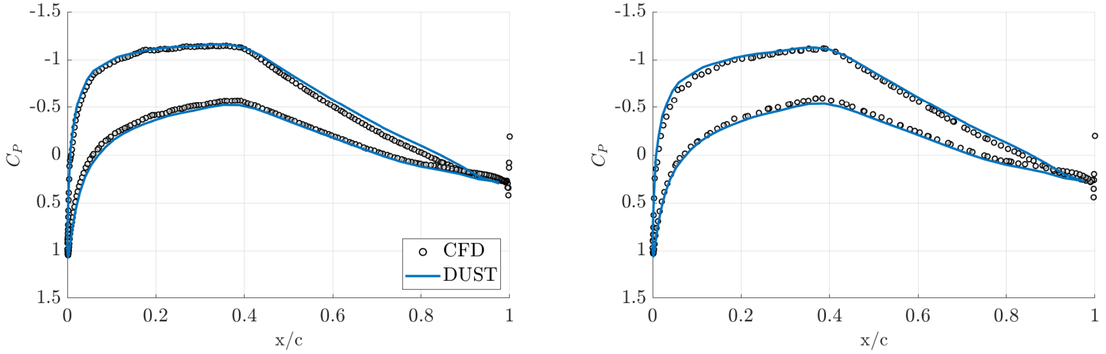

(a) Pressure coefficient at STA 1.

(b) Pressure coefficient at STA 2.

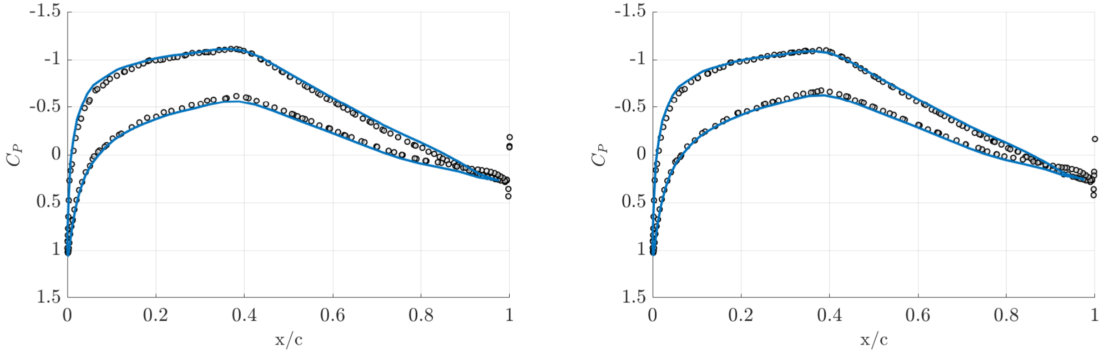

(c) Pressure coefficient at STA 3.

(d) Pressure coefficient at STA 4.

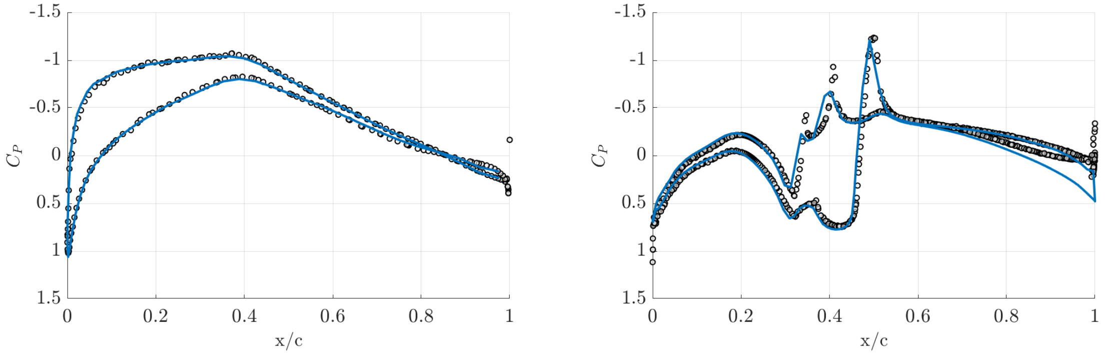

(e) Pressure coefficient at STA 5.

(f) Pressure coefficient at STA 6.

Figure 3.23: *Pressure coefficient distribution at the six span station considered,* $AoA^\circ=0^\circ$ *and* $\delta_a=0^\circ$.

the DUST capability to well capture the effect of the nacelle on the aerodynamic loads of the wing. Moreover, Fig 3.23(f) shows good consistency between the pressure coefficient even on the bluff body of the nacelle. Of course, this does not mean that DUST captures the entire aerodynamic load which is characterized by the presence of large flow separation behind the nacelle body and a consequent viscous contribution in particular on the drag force.

CHAPTER 4

Aeroservoelastic analysis

THIS chapter presents the results of the analyses conducted on the XV-15 tiltrotor model. The aeroservoelastic code DUST-MBDyn is capable of performing various types of analyses, including:

- the aeroservoelastic trim of an aircraft, taking into account both steady and periodic loads (the last essentials for fatigue life and vibratory assessments);
- dynamic loads predictions and performance evaluation during transient maneuvers;
- aeroelastic and aeroservoelastic stability analyses;

In this work, the focus is on the first two items, that is the trim of the vehicle and the response to an aileron roll manoeuvre. The capability of the coupled DUST-MBDyn tool to the study of the whirl flutter phenomenon was recently presented in Ref. [26]. Different levels of accuracy of the tiltrotor are used, to highlight the impact of the interactional aerodynamics.

For trim analysis, two models are considered: from the point of view of the multi-body structural model, the models are identical while they differ in the aerodynamic part. In particular, MBDyn rotor aerodynamics based on Blade Element Momentum Theory (BEMT) is used for the first model, while DUST is used for the second model, as explained in Sec. 3.1.3. Both models use DUST for the airframe, following the results obtained in Sec. 3.2.2. For the sake of brevity, the first model will be referred to us *model A* while the second *model B*. The purpose of this dual modelling approach is to emphasise the importance of having an aerodynamic model that allows the interactions between the different parts to be included even at a preliminary design stage, especially when dealing with a complex aircraft such as a tiltrotor or, more generally, with a multi-rotor configuration.

In the section devoted to the roll maneuver, three additional models with different levels of detail are considered, to demonstrate the actual capability of the tool to simulate aeroelastic and aeroservoelastic responses to pilot input controls. The presence of the actuation system with its own dynamic compliance is also taken into account, as well as the flexibility of the movable surface. The idea is to show how even during the preliminary design phases, it is possible to have a more accurate numerical model for aerodynamics and aeroelastic loads prediction, to be used for structural design and actuation system selection.

Although the focus here is on a tiltrotor aircraft, the same analysis can be carried out on an aircraft with a generic configuration, including multirotors/multipropellers (eVTOL). Additionally, since all dynamic simulations are non-linears, it is therefore possible to use the tool for the development of aircraft digital twins, aeroelastic flight simulators, and Reduced Order Models (ROMs).

4.1 Trim analysis

For a symmetric flight condition in airplane mode, the trim problem consists in computing the elevator deflection δ_{el}, the aircraft pitch angle θ, and the collective pitch angle θ_{75} such that the tiltrotor reaches the equilibrium condition. Firstly, the isolated rotor is considered and a comparison is made considering the two different aerodynamic models of MBDyn and DUST. The results are compared to the CAMRAD-JA model presented in Ref. [82]. Next, the trim of the complete vehicle is computed considering the DUST aerodynamics for the airframe and the two different aerodynamic models for the rotors.

It is worth noting that the CAMRAD-JA model contains several corrective coefficients to take into account the effects of downwash on the tailplanes due to the rotors and wing wakes, as well as power losses and blade tip loss factors. These terms were estimated by Ferguson, Acree, together with the engineers and technicians from NASA and Bell over 20-30 years of work to develop the XV-15 flight simulator (GTR [46]), for aeroelastic stability analysis ([98], [56]) and rotor loads prediction (OARF [13]). They were determined solely through knowledge of flight data, wind tunnel tests, and high-fidelity models. One of the strengths of introducing the interactional aerodynamic model of DUST is that it does not require such corrective factors in the numerical model, since they are implicitly captured.

4.1.1 Isolated Rotor Trim

When considering the isolated rotor, the trim problem consists in evaluating the collective pitch angle θ_{75} such that the prescribed angular speed remains constant for a desired torque value. The longitudinal cyclic pitch is set to -1.5° in airplane mode flight, according to Ref. [5]. The trim is achieved starting from an initial guess of the collective angle with the nominal rotor speed, and then applying the desired torque at the engine. The desired rotor speed is maintained using an integral controller since the main target is to guarantee a null steady-state error on the rotor speed. 14 conditions at different airspeeds U_{∞} were considered, ranging from 140 knots to 280 knots with an increment of 20 knots from one point to the other at Sea Level Standard (SLS) ISA+0 C conditions. It was decided not to go beyond the maximum speed of 280 knots since this represents the condition where maximum power is reached. Higher speed conditions obtained with descending flight are not considered for the purpose of analyzing the aircraft's response to the maneuver, but are useful for stability investigations to predict whirl-flutter phenomena. The following simulations are carried out with a time-marching analysis using a time step of 120 step per rotor revolution. The simulation ends when the error between the measured angular velocity and the prescribed one taken from the nominal data reported in Table 3.1 is below 0.1%.

Figure 4.1 compares the trim results of the MBDyn rotor (only rotor of *model A*) with those obtained from the coupled DUST-MBDyn model (only rotor of *model B*) and the CAMRAD-JA model (Ref. [5]). The results show a good correlation between the DUST-MBDyn and MBDyn models compared to the CAMRAD-JA reference. The torque, Fig. 4.1(b) shows that the target was met. The thrust shows little difference between the models, although the deviation on the collective pitch angle of the developed models from CAMRAD-JA is within 2°.

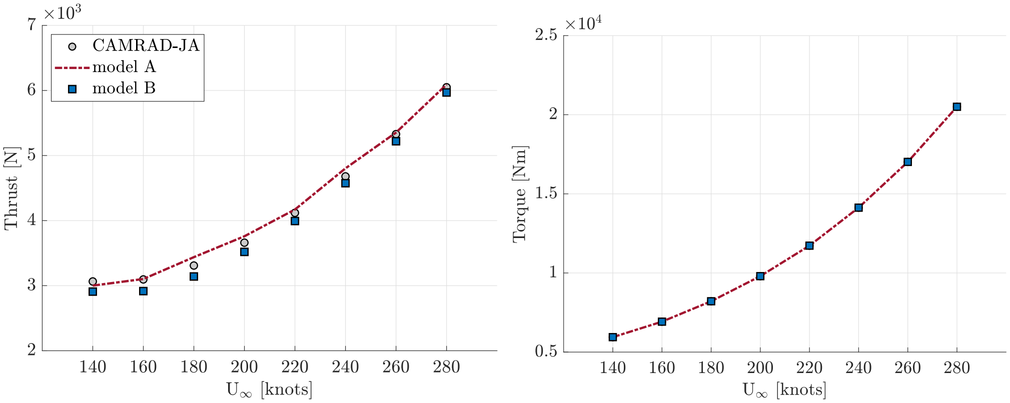

(a) Thrust.

(b) Torque.

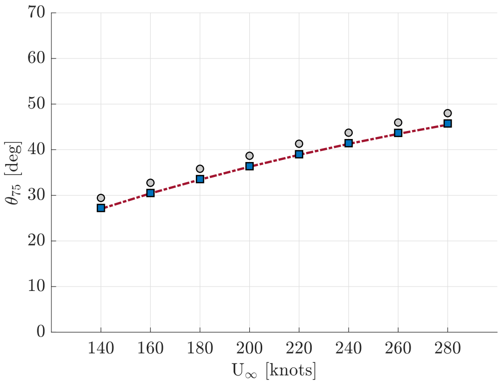

(c) Collective pitch.

Figure 4.1: *Isolated Rotor trim thrust, torque, and collective as function of airspeed.*

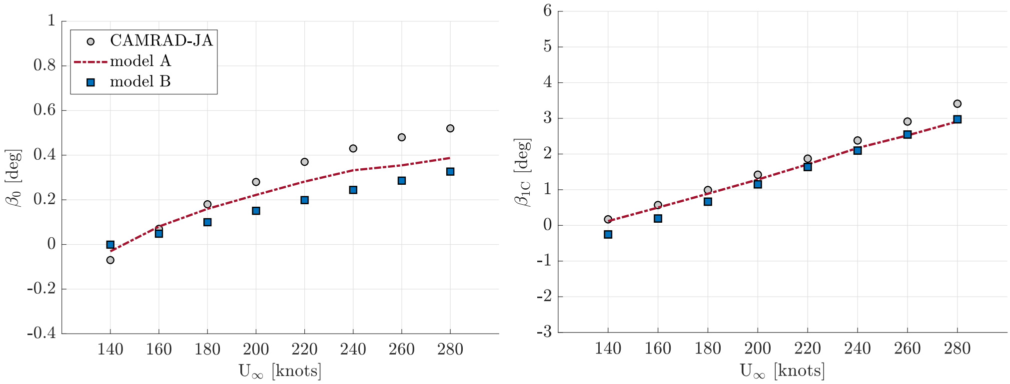

(a) β_0 - Collective Flap Angle.

(b) β_{1C} - Longitudinal cyclic Flap Angle.

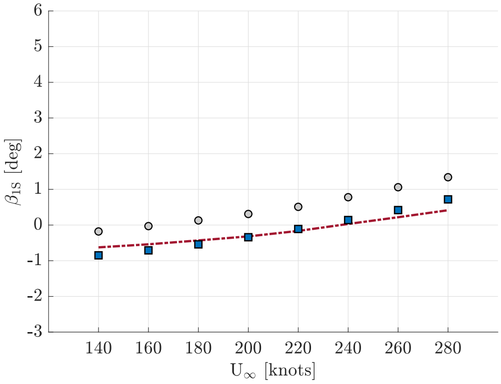

(c) β_{1S} - Lateral cyclic Flap Angle.

Figure 4.2: *Subsystem of XV-15 tiltrotor isolated Rotor flapping angles.*

Figure 4.2 shows the results obtained for collective and cyclic flapping angles. Note that the conditions are not perfectly in axial flow due to the nonzero longitudinal cyclic pitch angle imposed by the FCS. All curves in Fig. 4.2 show a similar trend, with an increment on flapping angles with reference to the flight speed. With regard to the collective component of Fig. 4.2(a), the MBDyn model is more aligned to CAMRAD-JA, which could be explained by the fact that both use the same Glauert inflow model with the same correction factors. The longitudinal flapping component (Fig. 4.2(b)) has a good correlation between the 3 models, while for the lateral component (Fig. 4.2(c)) there is a slight difference between the MBDyn and DUST-MBDyn models compared to CAMRAD-JA. This difference of less than 1°, however, appears to be constant with varying velocity and could therefore be related to some small differences in structural modelling.

Clearly, in the isolated rotor case in AP mode, DUST's ability to model the free wake and capture aerodynamic interactions is of little relevance and may not be the best choice in terms of results and computational cost. These results are intended to show how, for the case of the isolated rotor, the coupled model is aligned to the simpler MBDyn model so as to best highlight and discuss the results of the complete model that follows.

4.1.2 Full-vehicle Trim

The trim of the entire aircraft is now considered. For this purpose, it is necessary to add to the trim variables those relating to the fixed part of the model. For a symmetric flight condition in airplane mode, the trim problem consists of computing the elevator deflection δ_{el}, the aircraft pitch angle θ, and the collective pitch angle θ_0 such that the tiltrotor reaches the equilibrium point. The flight speed and altitude are imposed. However, since the parasite drag is not captured in DUST, the equilibrium condition in the longitudinal direction is not considered at this stage. The collective pitch angle is computed a-priori to maintain a constant rotor speed by imposing a desired torque value, as discussed in the previous section.

The trim problem in the coupled simulation is initialized by setting an initial elevator deflection and pitch angle of the entire aircraft. Then, to automatically find the trim point, a PID regulator is introduced in the simulation with the aim of bringing to zero the vertical reaction force $\mathrm{F_z}$ and the pitching moment $\mathrm{M_y}$ of the total joint located at the center of mass, by computing δ_{E} and θ. Since the objective of the controller is to bring the reaction forces to zero, the most important term in the controller is the integrator $\mathbf{K_I}$:

$$\begin{Bmatrix} \theta \\ \delta_{\mathrm{el}} \end{Bmatrix} = \begin{bmatrix} \mathrm{K}_{\mathrm{I}\theta} & 0 \\ 0 & \mathrm{K}_{\mathrm{I}\delta} \end{bmatrix} \begin{Bmatrix} \int T_z \\ \int M_y \end{Bmatrix} \tag{4.1}$$

To avoid a possible interaction between the controller and the airframe structural dynamics, a Butterworth second-order low-pass filter with a cutting frequency $\omega_{\mathrm{c}} = 1\,\mathrm{Hz}$ is placed between the reaction forces and moments measured at the total joint and the regulator.

The airframe DUST aerodynamic model used to compute the trim curves is composed by the wing-pylon system of section 3.2.2, the horizontal stabilizer and the vertical tail, as shown in Fig. 3.12.

The results for a wind speed of 260 knots, corresponding to the cruise speed U_c, considering the hybrid model with DUST aerodynamics for the airframe and MBDyn aerodynamics for the rotors (*model A*) are shown in Fig. 4.3. Figures 4.3(a) and 4.3(b) show the ground reaction forces evolution varying the pitch attitude and elevator deflection trim parameters, reported respectively in Fig. 4.3(c) and Fig. 4.3(d).

Figure 4.4 shows the resulting airframe trim variables obtained as a function of velocity compared to the CAMRAD-JA model reported by [82]. The dashed red curve refers to the model with hybrid aerodynamics (*model A*), DUST for the airframe and MBDyn for the rotors. The blue square points, on the other hand, refer to the model with full DUST aerodynamics (*model B*).

In terms of trends, both models give similar results as the CAMRAD-JA reference, which is based on data provided by Ferguson in [37]. *Model A* and *model B* provide essentially identical results in terms of airframe trim variables, based on the average load components. At low speeds, on the other hand, there is a marked deviation from the reference model, with noticeable differences on the elevator angle up to $3.5°$. During the analysis, it was observed that the results obtained from the DUST aerodynamic model deviated significantly from the expected values. Upon investigation, it was found that the deviation was caused by the absence of the fuselage in the model. The decision to exclude the fuselage from the model was made based on two primary reasons. Firstly, including the fuselage in the aerodynamic model would increase the computational cost significantly. The fuselage is made up of a large number of panels, and incorporating it would require additional computation time and resources. Secondly, even if the fuselage was included in the model, the solution obtained for the loads would still be approximate and incorrect. This is because the DUST model does not account for the boundary layer and any separation that may occur due to the bluff body shape of the fuselage.

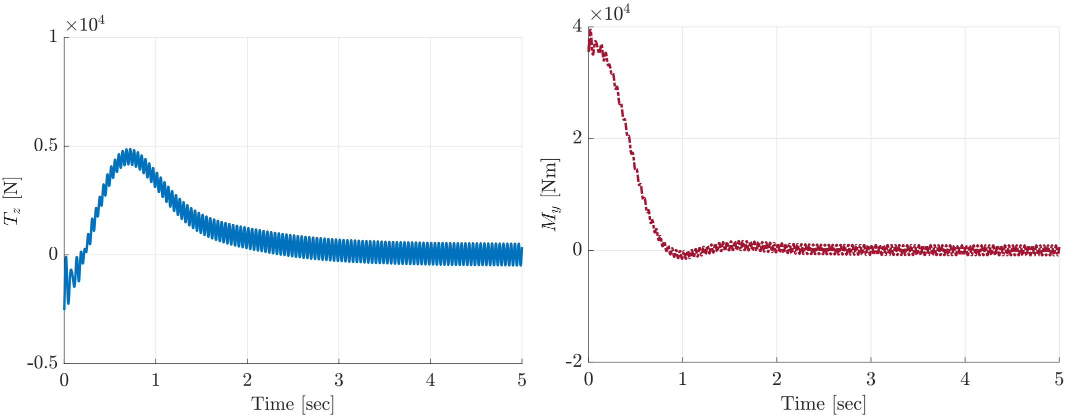

(a) Vertical force reaction.

(b) Pitch moment reaction.

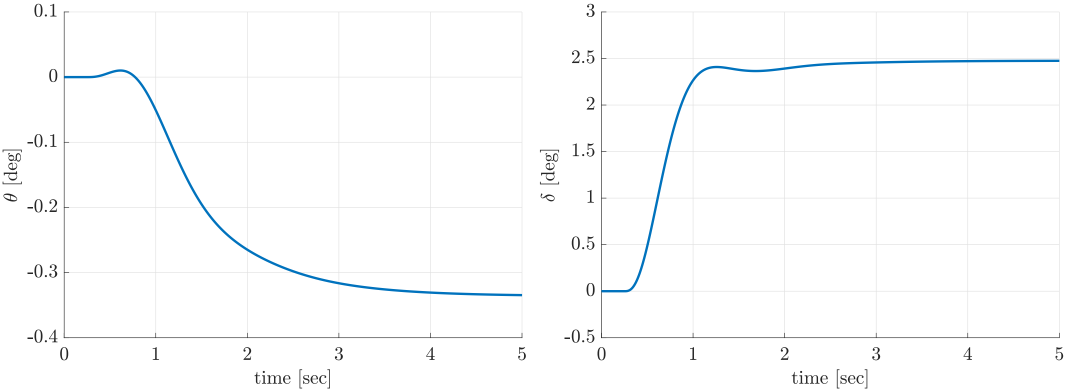

(c) Pitch attitude θ.

(d) Elevator deflection δ.

Figure 4.3: *Airframe Trim variables, wind speed of* 260 *knots.*

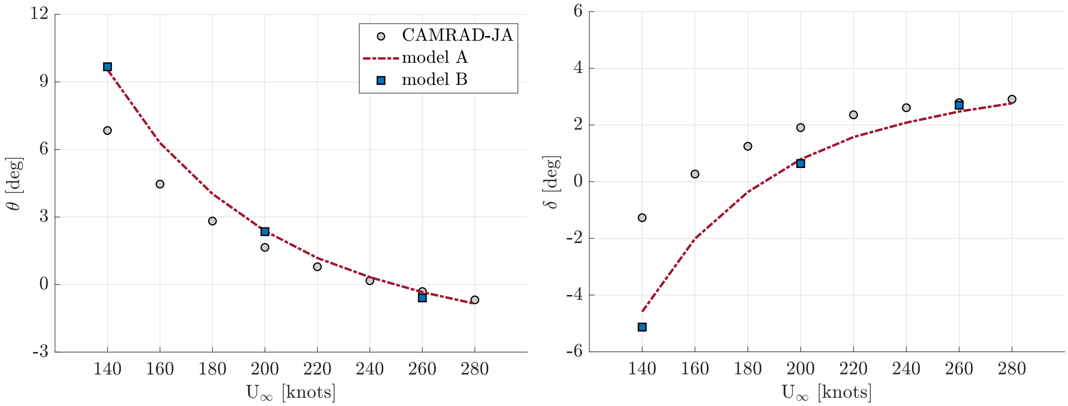

(a) Pitch attitude θ.

(b) Elevator deflection δ.

Figure 4.4: *Airframe Trim variables as function of airspeed.*

In order to verify this hypothesis, an aerobody representing the aerodynamics of the fuselage was introduced into the MBDyn model based on the aerodynamic characteristics reported by Ferguson in [37]. The position of the aerodynamic center of the element is also taken from [37], and it is located about $3.6\,\mathrm{cm}$ back and $0.3\,\mathrm{m}$ below the aerodynamic center of the main wing. In Fig. 4.5, the results obtained with *model A*, which includes the aerodynamics of the fuselage, are shown for three characteristic speeds, namely U_{min}, U_a, and U_c corresponding to 140 knots, 200 knots,

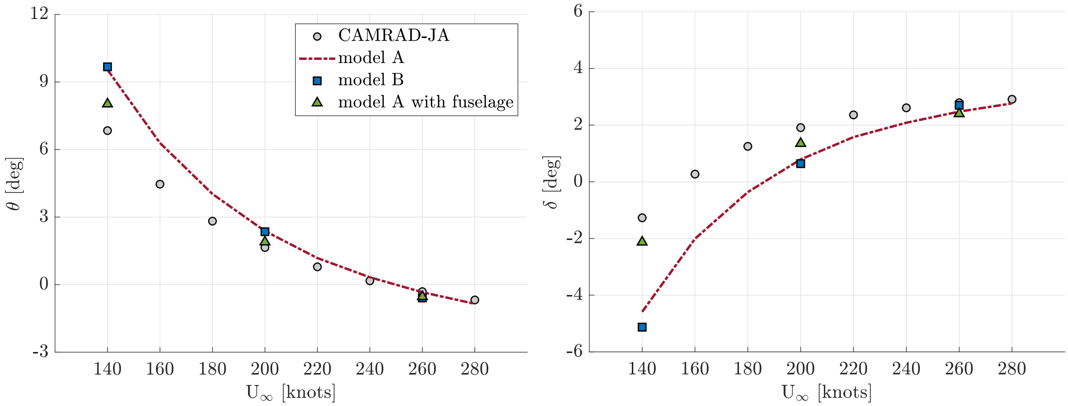

(a) Pitch attitude θ.

(b) Elevator deflection δ.

Figure 4.5: *Airframe Trim variables as function of airspeed considering the introduction of the fuselage aerodynamics in MBDyn model.*

and 240 knots, respectively. It is clear that the contribution of the fuselage compensates for the difference compared to the trim results obtained from CAMRAD-JA, especially at low speeds. At high speeds, the contribution of the fuselage to the pitch moment becomes negligible, as the angle of incidence is reduced. In the context of future work, a possible strategy could be to obtain the aerodynamic tables of the fuselage through CFD simulations for different angles of attack and introduce the fuselage aerodynamics into the model by utilizing the aerobody of MBDyn.

The inclusion of the horizontal force equilibrium in the trim procedure could be obtained by adding the parasite drag due to the wing and the empennages. Indeed, the parasite drag could be approximated as a constant force in airplane mode (for small angle of attacks) and its contribution evaluated a priori by CFD analyses or wind tunnel data if available. In this way, it should be possible to add to the trim problem the longitudinal equilibrium equation, as done for the fuselage $\mathrm{M_y}$.

As already highlighted, there are no significant differences between *model A* and *model B* on the trim curves. Indeed, the pitch attitude and the elevator angle in trim condition depend only on the average load components. These results are not affected by the presence of the rotor wake, which is instead responsible for the generation of periodic loads on the aircraft. The correct evaluation of periodic loads allows us to determine the vibratory level of the aircraft as well as provides the information for fatigue load design.

In order to highlight the differences between the two models, the aerodynamic loads on the wing and horizontal tail plane along a complete revolution of the rotor at trim condition are now considered. The cruise speed U_∞ corresponding to $260\,\mathrm{knots}$ is selected, as this is the speed at which the aircraft operates for most of the time and is subsequently used for the simulation of the roll maneuver. Figure 4.6 shows a comparison of the sectional normal force on the right wing during a proprotor revolution for the two different models, *model A* Fig. 4.6(a) and *model B* Fig. 4.6(b). It should be noted that in both figures, the vertical axis represents the non-dimensional spanwise coordinate as $\mathrm{2y/b}$, where b is the total span of the aircraft as reported in Table 2.7. Similar results for the right horizontal tailplane are shown in Fig. 4.7. The overall span of the tailplane is indicated by $\mathrm{b_t}$.

In *model A*, the load on both the wing and tail remains constant throughout the rotation of the rotor. This is due to the absence of the wake of the rotor. However, in *model B*, periodic loads can be observed function on the azimuth ψ. These loads are caused by the interaction of the rotor's wake with the wing and the empennages. Moreover, in *model B*, it is possible to observe three distinct regions where the wake of each of the three blades of

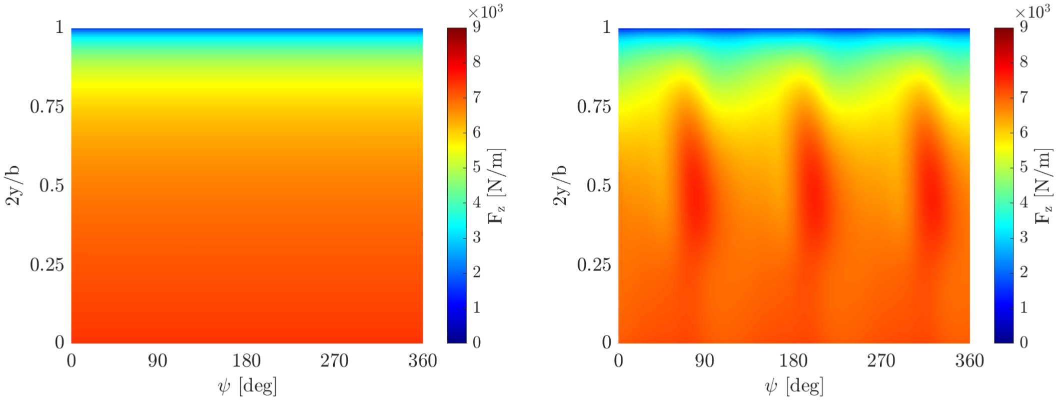

(a) *Model A*. (b) *Model B*.

Figure 4.6: *Comparison of the contours of the sectional normal force on the right wing during a proprotor revolution with the two different aerodynamic models,* U_∞ = 260 knots.

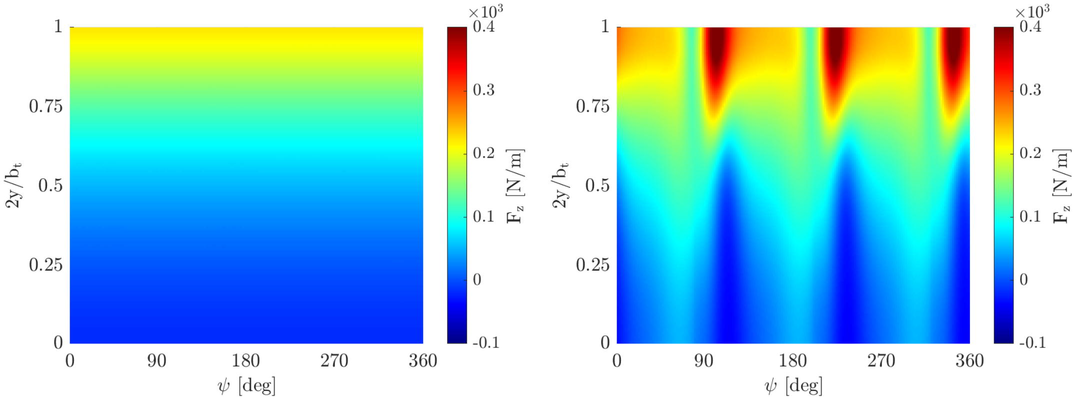

(a) *Model A*. (b) *Model B*.

Figure 4.7: *Comparison of the contours of the sectional normal force on the right horizontal tail during a proprotor revolution for the two different aerodynamic models,* U_∞ = 260 knots.

the rotor passes. As a result, the loads on the wing and on the empennages of *model B* are not constant but rather exhibit periodic variations as the rotor rotates. Considering the first peak, the wing sees it around $\psi = 80°$ while the horizontal tail plane, being further back, sees it at approximately $\psi = 100°$. In order to relate this result to the physics of the wake calculated by DUST, Fig. 4.8 shows the position of the vortical particles and their interaction with the wing and the empennages for $\psi = 80°$ and $\psi = 100°$, respectively shown in Fig. 4.8(a) and Fig. 4.8(b). At $\psi = 80°$, the wake of the third blade impacts on the wing and modifies its load, while the horizontal tail plane remains unaffected. However, as the wake proceds downstream ($\psi = 80°$), the particles released by the first blade impact the horizontal tail plane and is partially channeled between the horizontal tail and the vertical plane. This creates a higher velocity region on the back and therefore a decrease in pressure, which is responsible for the increase in the sectional load in that area, as seen in Fig. 4.9(b).

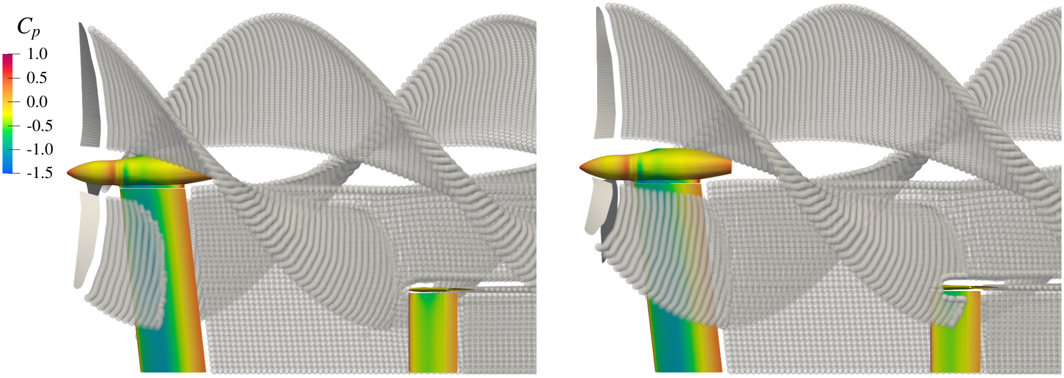

(a) $\psi = 80°$.

(b) $\psi = 100°$.

Figure 4.8: *Comparison of wake structure for different rotor azimuth ψ, U_∞ =* 260 knots.

In order to quantify the variation of these oscillations around the mean value, sectional loads along the spanwise for the wing and horizontal tail are shown in Figure 4.9. The variation of the load around the mean value (solid blue line) for *model B* is represented by the shaded blue region. For the main wing, the difference between the mean value of the two models is quite small and the area of greatest variation in periodic load is around $2y/b = 0.5$, area where the most intense vortices released by the rotor pass through. The results shown in Fig. 4.9(b) for the tail section reveal a noticeable discrepancy in the mean values obtained with the two models. Specifically, the *model B* displays an higher mean load on the entire horizontal tail plane, indicating that the rotor wake during this flight phase is improving its effectiveness in terms of lift. In this case, the wake from the main rotor is impacting the horizontal tail, increasing its lift, which ultimately results in a higher mean load. However, it should be noted that the trim elevator deflection between the two models is slightly different and *model B* has a smaller value of about $0.25°$, which contributes to the identified increase in the averaged load. Regarding the amplitudes of the periodic load variation, the entire surface appears to be affected. In particular, the greatest interaction seems to be in the area at the tip of the tailplane, where there is the attachment between the horizontal and vertical tail plane, in accordance with Fig. 4.8(b). Instead, the variation is lower around $2y/b = 0.65$. This is due to the fact that when the rotor wake impacts the tail plane in the tip region, the load increases in that area while decreasing in the region near the root. This is evident from Fig. 4.7(b). In the region around $2y/b = 0.65$, the load is less sensitive to the wake passage. In other words, it is as if the center of the bundle of curves describing the sectional load in the spanwise direction is located in that region.

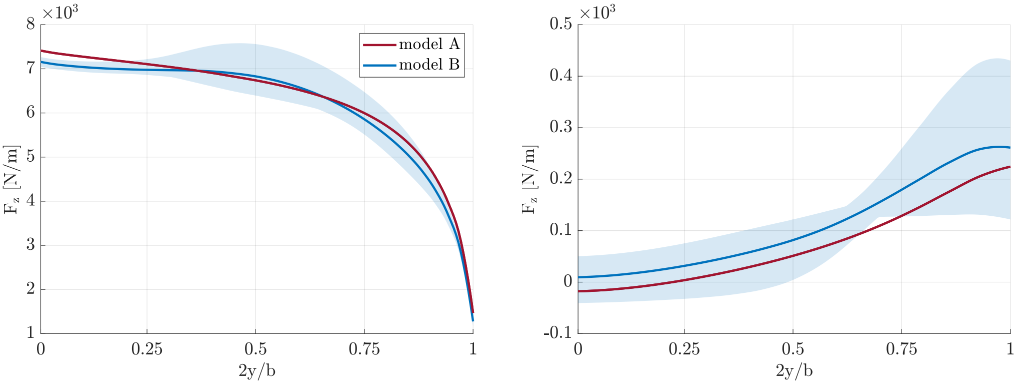

(a) Right wing. (b) Right horizontal tail.

Figure 4.9: *Comparison of the sectional normal force,* U_∞ = 260 knots.

Regarding the rotor parameters, in Fig. 4.10 are reported the thrust and the corresponding trim collective angles with reference to airspeed, as in the case of the isolated proprotor. From the point of view of the overall load and thus the collective pitch angle found, there are no particular deviations from what was obtained in the isolated rotor case reported in Fig. 4.1.

Figure 4.11 depicts a comparison of the contours of the blade non-dimensional normal force ($\mathrm{M^2C_n}$) over a complete rotor revolution. The

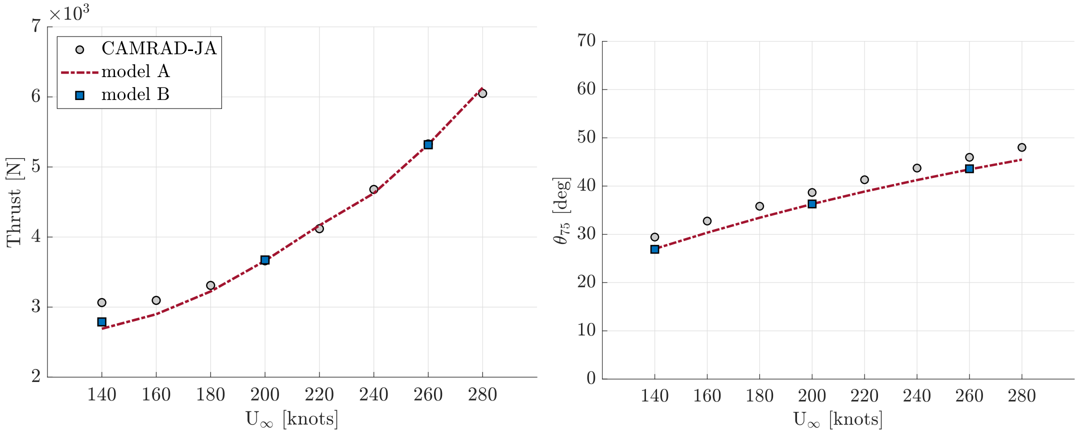

(a) Thrust.

(b) Collective pitch.

Figure 4.10: *Rotor trim thrust and collective as function of airspeed.*

primary purpose of this visualization is to provide an in-depth understanding of the impact of the various aerodynamic fidelity levels utilized. The load distribution clearly illustrates how the DUST model is adept at capturing the aerodynamic interaction on the rotor arising from the wing positioned at $\psi = 270°$. The wing's position leads to an asymmetry in the aerodynamic load that is transmitted to the dynamic behavior of the structure, resulting in a component of cyclic flapping and pitching. This is an important factor to consider when considering the system's stability and overall performance, especially in cases where high levels of accuracy are required. The cyclic flapping component can significantly affect the tiltrotor performance, including maneuverability, stability, and vibration levels. Therefore, understanding this phenomenon and accurately modeling it is critical for designing safe and efficient rotorcraft.

Figure 4.12 shows the rotor pitch angle (4.12(a)) and the flapping angle (4.12(b)) comparison between *model A* and *model B* along one complete rotor revolution at the trim point. In general, *model B* shows larger amplitudes on both pitch and flapping cyclic components with a slight phase offset due to the wing interactions on the disk loads, as highlighted by Fig. 4.11(b). However, although the aerodynamic loads are very different as found in 4.11(b), the dynamic behavior of the rotor is not as different since it is more influenced by the dynamics of the system.

In order to identify the relevant loads during the design phase, three monitor points illustrated in Fig. 4.13 are considered, where internal forces and moments are computed. P_1 and P_2 are located at the root of the wing

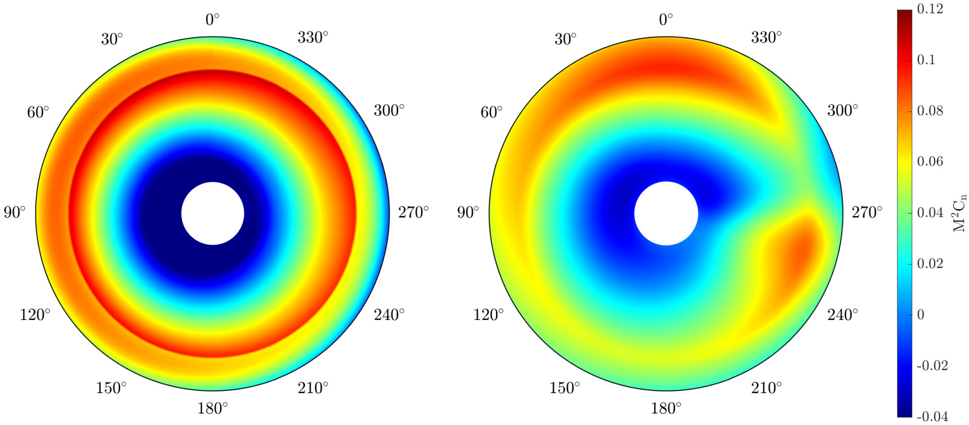

(a) *Model A* (MBDyn).

(b) *Model B* (DUST).

Figure 4.11: *Comparison of the contours of the non-dimensional normal force* $\mathrm{M}^2\mathrm{C}_\mathrm{n}$ *on the proprotor blade (right rotor),* $U_\infty = 260\,\mathrm{knots}$.

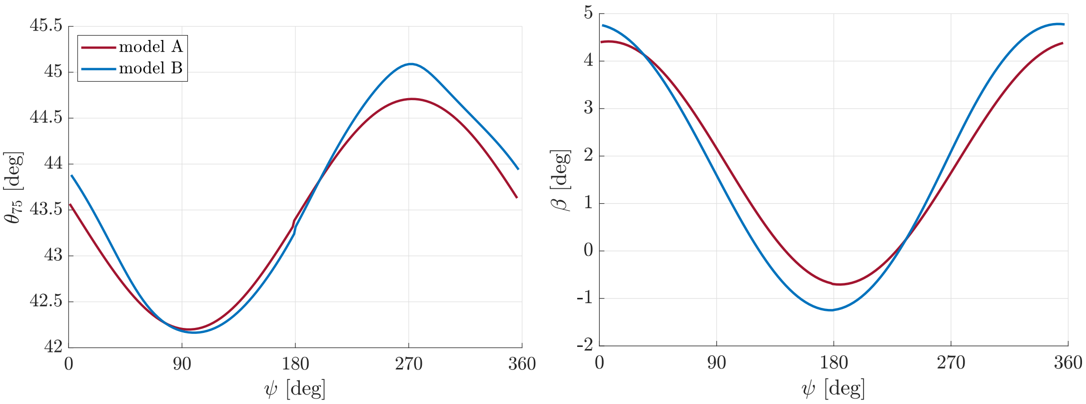

(a) Pitching angle.

(b) Flapping angle.

Figure 4.12: *Comparison of rotor angles* θ_{75} *and* β *for the two different aerodynamic models,* $U_\infty = 260\,\mathrm{knots}$.

and the horizontal tail plane respectively. P_3 represents the point located at the root of the blade for the evaluation of the blade loads in a rotating reference frame.

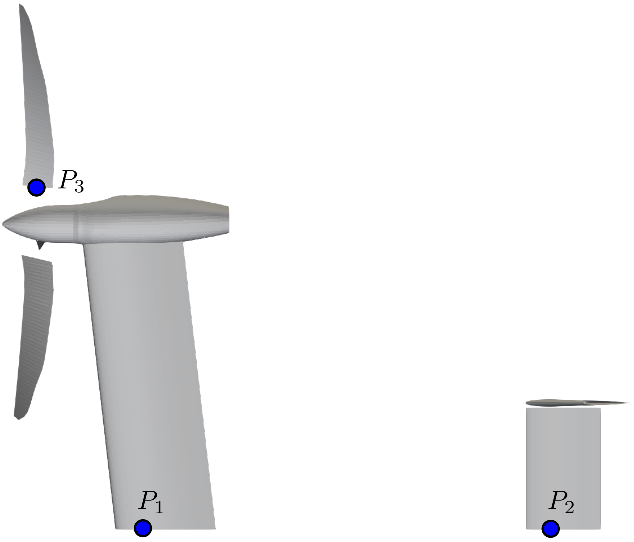

Figure 4.13: *Three monitor points considered on the right half model; upper view.*

The first set of loads depicts the out-of-plane bending moment at the root of the wing (P_1) and the in-plane chordwise shear associated to the thrust generated by the rotor. Similarly, for the third monitor point P_2, the out-of-plane bending moment is evaluated. This load, mainly generated by the aerodynamic force acting on the tail planes, is subjected to the evolution of the wake of the main wing and rotors. Finally, on P_3 are evaluated the critical loads for the rotor system, namely the flapping and lagging bending moments transmitted from the blade to the yoke, critical for the rotor structural integrity and performance, as they are responsible for transmitting the power from the engine to the rotor blades.

Figures 4.14(a) and 4.14(b) show respectively the chordwise shear and the bending moment evaluated during one rotor revolution at P_1. The load oscillations evaluated with the *model B* are significant, particularly with variations of approximately $18\,\mathrm{kN\,m}$ for the bending moment and around $1.2\,\mathrm{kN}$ for the shear. The average load, on the other hand, is very similar between the two models.

By analyzing the bending moment in the monitor point P_2, it can be seen that the average value obtained with the two models is markedly different.

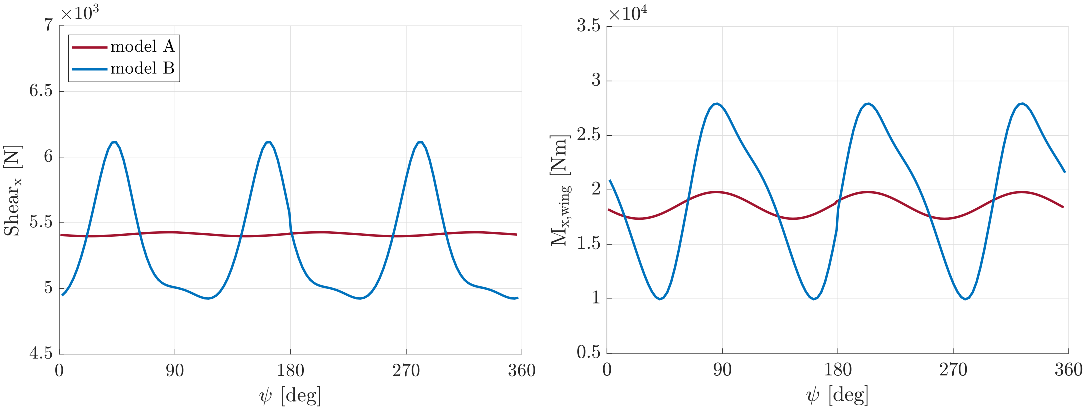

(a) Chordwise shear. (b) Right wing bending moment.

Figure 4.14: *Comparison of loads trasmitted to the airframe part at* P_1 *for the two different aerodynamic models,* U_∞ = 260 knots.

model B shows a value twice higher when compared with *model A*, due to the different spanwise load distribution as shown by Fig. 4.9(b). In addition, *model B* allows to capture the interactional loads associated with the evolution of the wake impacting the tail. Figure 4.15(b) clearly identifies the correspondence of these oscillations with rotor multiples n/rev, with nonnegligible amplitudes up to the harmonic corresponding to $12/rev$.

Similar considerations can be made on the rotor loads. Figure 4.16(a) shows the bending moments measured on the yoke for both *model A* and *model B*. In particular, $\mathrm{M}_{\mathrm{z,yoke}}$ and $\mathrm{M}_{\mathrm{y,yoke}}$ respectively indicate the components of the lagwise and flapwise bending moments. In order to capture the differences between the two models, Fig. 4.16(b) shows the Fourier transform (FFT) of the signals in Fig. 4.16(a) over a complete rotor revolution.

From the spectrum, it is possible to notice how the addition of aerodynamic interactions in the numerical model allows capturing higher harmonics in the signals, thus obtaining a more comprehensive model. For instance, considering the bending moment component associated with the flapping dynamics ($\mathrm{M}_{\mathrm{y,yoke}}$), the *model B* shows a non-negligible term at $3/rev$, whose amplitude is more than one third of that of the first harmonic $1/rev$. Taking these quantities into account, it becomes evident that neglecting the aerodynamic interaction between the wing and the rotor can lead to a loss of information regarding the periodic loads that can create vibration phenomena, and different fatigue life of the structural components. These load oscillations can have a significant impact on the structural

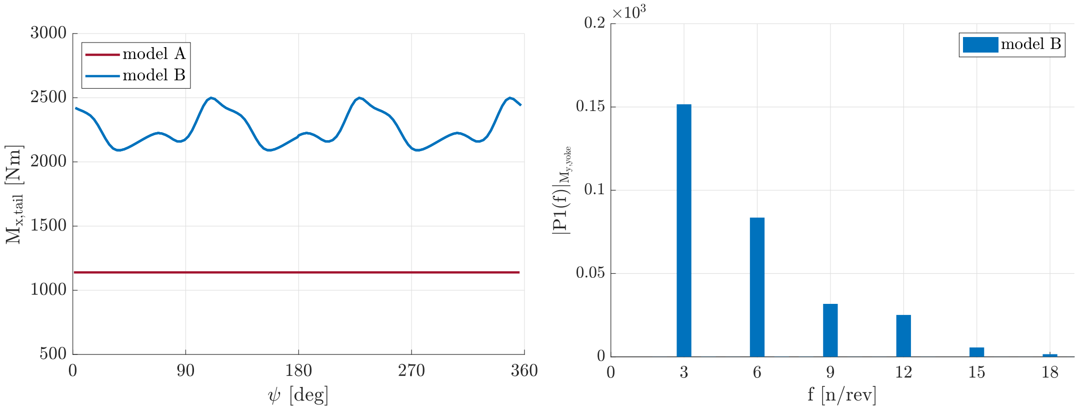

(a) Loads history.

(b) FFT.

Figure 4.15: *Comparison of out-of-plane bending moment trasmitted to the horizontal tail root at P_2 for the two different aerodynamic models, U_∞ = 260 knots.*

integrity of the rotorcraft and can lead to premature component failures. Therefore, it is essential to consider the aerodynamic interaction between the wing and the rotor during the design phase to ensure that the rotorcraft structural integrity and optimal performance are achieved. Furthermore, the possibility of having a numerical model that includes multiple harmonics associated with aerodynamic loads allow us for the construction of accurate reduced order models including different aerodynamic states without a priori approximations. In this regard, mid-fidelity aeroelastic models could be used for the development of flight simulators, as well as for control system design.

4.2 Roll maneuver

Starting from the trim condition identified in Sec. 4.1, it is possible to simulate different maneuver conditions. In the present work, the aileron maneuver is considered to study the aircraft response to roll dynamics. Clearly, in the same way, it is possible to reproduce different maneuvers for the study of performance, such as a pull-up or a lateral-directional maneuver. Thanks to the flexibility of MBDyn to manage the multibody model inputs in various ways, it is possible to exploit this type of modeling to reproduce loading and handling required procedures according to regulations in the verification and sizing phase of an aircraft. The primary objective of this work is not to validate or verify the considered XV-15 tiltrotor model. Instead, the aim is to showcase the type of data that can be obtained with a

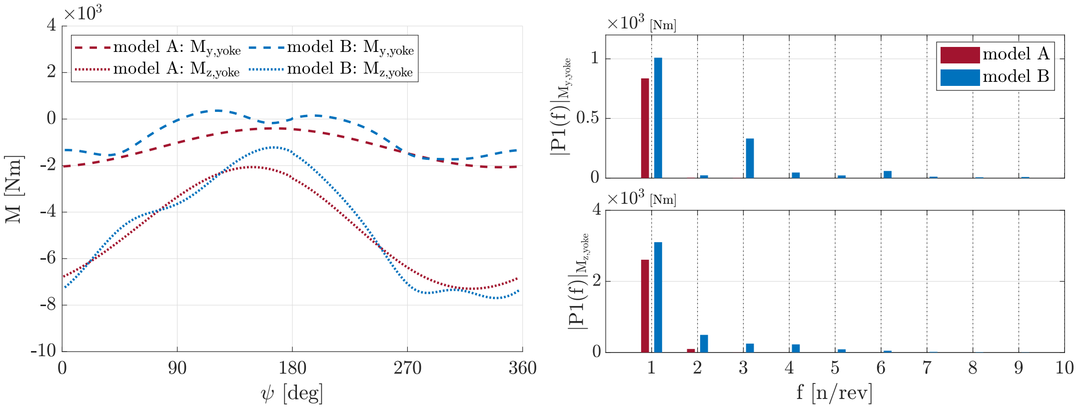

(a) Loads history.

(b) FFT.

Figure 4.16: *Comparison of bending moment loads acting on rotor yoke at P_3 for the two different aerodynamic models,* $U_\infty = 260$ knots.

coupled DUST-MBDyn model. Therefore, various models have been taken into consideration to demonstrate the diverse levels of detail that can be incorporated into a comprehensive model and how performance and loads change when increasing the level of detail of the DUST-MBDyn models. When considering different models, it becomes easier to illustrate the range of features that can be captured in a tiltrotor, such as the impact of different aspects on the maneuver performance and on the involved loads. In particular, by exploiting the incremental configurations in terms of model complexity reported in Tab. 4.1, the following aspects are intended to be highlighted:

- Impact of rotor dynamics:
  comparison between configurations I and II. Configuration I does not involve rotor rotation and the associated rotor dynamics, although rotor mass and inertia properties are taken into account. Configuration II corresponds to *model A* in Sec. 4.1 where the rotor dynamics are considered, while the aerodynamics exploit the simple MBDyn model based on BEMT.

- Impact of rotor aerodynamics interaction:
  comparison between configurations II and III. Configuration III, corresponding to *model B* of Sec. 4.1, replaces MBDyn aerodynamics with DUST aerodynamics, thus introducing the component of interactional aerodynamics in the model through the rotor wake.

configuration	omega [RPM]	gimbal	rotor wake	elastic ailerons
I	0	lock	NO	NO
II (*model A*)	480	unlock	NO	NO
III (*model B*)	480	unlock	YES	NO
IV	480	unlock	YES	YES

Table 4.1: *Model configurations used for the roll maneuver simulation.*

- Impact of aileron elasticity:
  comparison between configurations III and IV. Configuration IV includes the aileron elasticity added by flexible beams of the movables, as presented in Sec. 3.2.1.

The maneuver considered consists of deflecting the ailerons at $\pm 10°$ starting from a trimmed condition in steady level flight at the cruise speed $U_c = 260\,\mathrm{knots}$ with the aircraft free to rotate around its longitudinal axis. The maneuver target is assumed to be reaching a bank angle of $30°$. From the viewpoint of the simulation procedure, once the trim conditions have been identified following Sec. 4.1, a new simulation is started by imposing the trim values as initial conditions. Once the transient aerodynamic effects caused by the initial start-up are exhausted (a time of $0.5\,\mathrm{s}$ corresponding to 4 rotor revolutions is considered in the present work), the aircraft is released to roll rotation and the aileron command is imposed. In order to control the deflection of each aileron, an elongation of the rods is imposed through the kinematic relationship obtained in 3.14, which is subsequently filtered to reproduce the dynamic response of the system. As described in 3.2.1, the servo-valve dynamics consists of a second-order Butterworth filter with a cut-off frequency of $7\,\mathrm{Hz}$. The value of this frequency is based on typical actuator values, but in the case of a more general analysis, it can be an additional design parameter. Figure 4.17(a) shows the step input (ΔL_c) and the filtered input (ΔL_f) on the right wing actuators. The resulting deflection of the rigth aileron is reported in Fig. 4.17(b).

Since the kinematic relationship between the actuator elongation and the control surface deflection of the mechanism is linear for deflections ranging between $\pm 10°$, see Fig. 3.14(a), the control input for the left aileron is analogous but with opposite sign. In other words, the left wing actuators elongate by the same amount as the right ones are shortened.

In the simulations, the aircraft rolls about the longitudinal axis, positive starboard (right) wing up. Yaw rotation is about the vertical axis, positive nose left while pitch rotation is about the axis normal to the longitudinal plane of symmetry, positive nose up.

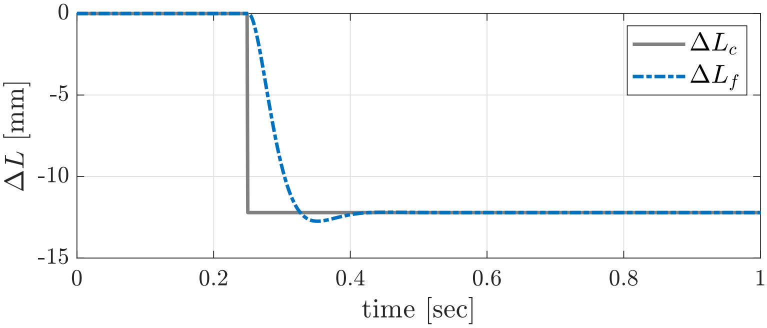

(a) Input: actuators elongation ΔL.

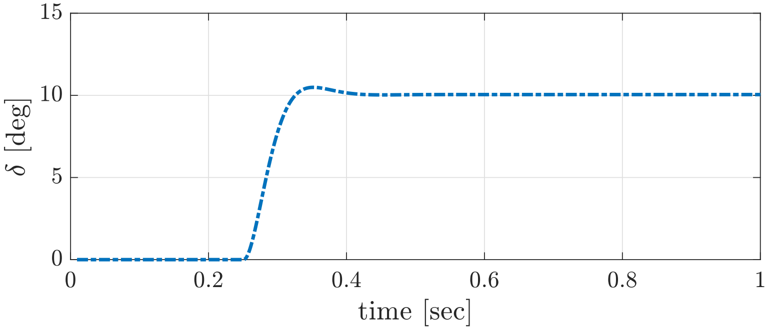

(b) Output: aileron deflection.

Figure 4.17: *Filtered input actuators length and the relative obtained aileron deflection.*

4.2.1 Impact of rotor dynamics

To highlight the impact of rotor dynamics in the numerical model, a comparison between the results of configuration I and II is here proposed. From the perspective of the airframe, the two configurations coincide in both the MBDyn structural part and the DUST aerodynamic part. However, they differ on rotors modeling: configuration I only includes the concentrated masses of the blades without any rotation of the mechanism, while configuration II corresponds to *model A* presented in Sec. 4.1.2, where rotors are modeled with flexible blades and simplified aerodynamics based on BEMT.

Figure 4.18(a) shows the comparison of the bank angle ϕ evolution during the simulated roll maneuver for the two aircraft configurations tested. In particular, the figure clearly shows that the introduction of the rotor component in the model changes the slope of the bank angle curve and influences the roll maneuver performance, by reducing the time-to-bank. Specifically, the time-to-bank is reduced by 7% for configuration II when considering a target bank angle of $30°$. This is confirmed by the comparison of roll rate ($\dot{\phi}$) evolution as a function of the bank angle presented in Fig. 4.18(b). This result is related to the dynamics of the two rotors. The right rotor flap downward due to the smaller velocity (and reduced lift) of the outer blade. The left rotor flap upward (same mechanism but mirrored). The side forces of the rotors create a roll moment opposite to the control moment generated by the aileron, reducing the roll rate.

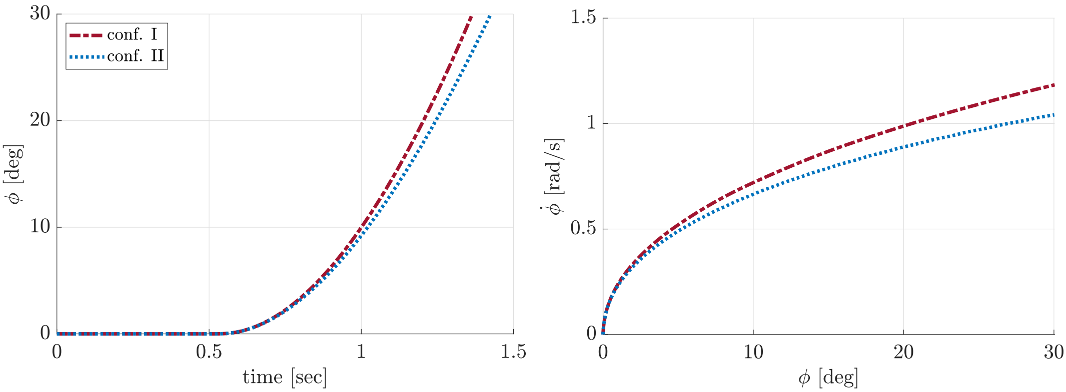

(a) Bank angle ϕ.

(b) Roll rate p.

Figure 4.18: *Comparison of computed bank angle evolution (a), and roll rate evolution (b) for configurations I and II.*

The condition of a steady level turn requires even control of the aircraft around the yaw axis. In this work we have untethered the aircraft with respect to the longitudinal axis only, but we can evaluate what happens around the yaw axis by means of the moment constraint around the vertical axis. Figure 4.19 shows the measured yaw moment reaction at the ground joint, located at the center of mass with corresponding forces breakdown related to the wing-pylon, rotors, and tail components. Since the yaw motion is constrained during the simulation, the purpose of these results is to estimate the impact of the different vehicle components on the reaction moment measured about the yaw axis.

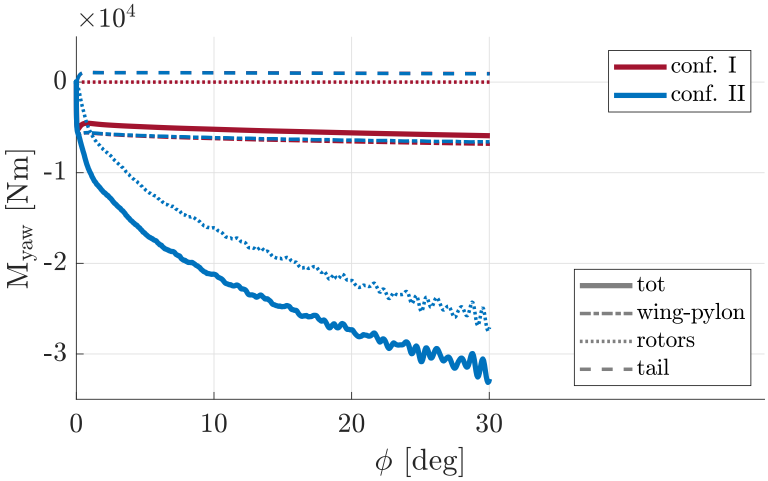

Figure 4.19: *Comparison of measured yaw moment reaction force for configurations I and II.*

The main contribution is related to the adverse yaw moment introduced by the rotors. The wing-pylon system also introduces a negative component on the yaw moment, which, however, unlike rotors, is quite stable during maneuvering. The tail, on the other hand, turns out to be the only component that generates an adverse yaw, the budget of which on the total, however, is very small. This result shows how important it is to consider the rotor system when evaluating yaw moment since the relative budget is the largest.

The dynamic behavior due to the rotor, introduced with configuration II, enables the activation of cyclic components that induce a tilt of the rotor. This tilt is brought about by the reference velocity component associated with the roll rate in the plane of the rotor disk. The speed component associated with the roll motion changes the angle of the rotors with respect to the relative flow, resulting in them moving further away from the axial flow condition as the roll rate increases.

In Fig. 4.20, the components of relative velocity seen by the outer blade of the right and left rotor are depicted. For the right rotor, the rolling motion reduces the velocity and therefore the relative angle of incidence of the blade at $\psi = 90°$. When the blade is instead at $\psi = 270°$, i.e. in front of the wing, the opposite effect occurs, namely that the roll motion increases the angle of attack. This imbalance has the effect of generating an asymmetric load on the rotor disc and therefore introduces flapping. However, in global terms, a global reduction on thrust of the right rotor can be expected due to the roll motion since the contribution to the blade at $\psi = 90°$ is greater, given that the distance from the longitudinal axis is greater and therefore also the velocity contribution associated with the roll rate. As regards the left rotor, the opposite holds true. Eqs. 4.2 and 4.3 report the relationships obtained for the angle of incidence for the right and left rotors, respectively $\alpha_{75,r}$ and $\alpha_{75,l}$, for the blade at $\psi = 90°$.

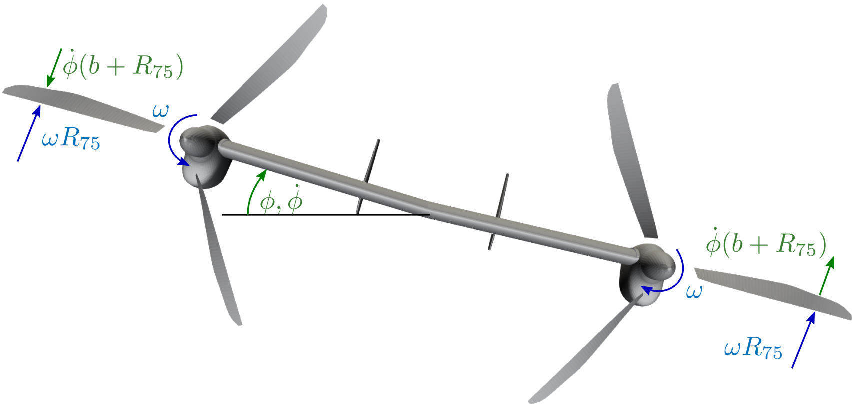

Figure 4.20: *Velocity components acting on rotors during roll; front view.*

$$\alpha_{75,r} = \theta_{75} - \tan^{-1}\left(\frac{U_\infty}{\omega R_{75} - \dot{\phi}(b + R_{75})}\right) \tag{4.2}$$

$$\alpha_{75,l} = \theta_{75} - \tan^{-1}\left(\frac{U_\infty}{\omega R_{75} + \dot{\phi}(b + R_{75})}\right) \tag{4.3}$$

The trends of the angle of attacks as a function of the roll rate evaluated by the simulation, are depicted in Fig. 4.21(a). These trends are confirmed by the measured thrust of the two rotors during the maneuver, see Fig. 4.21(b).

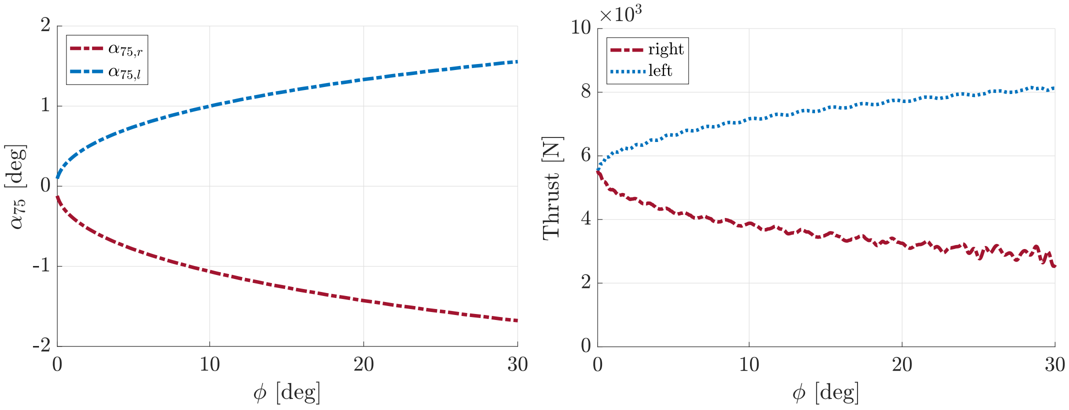

(a) α - Computed Angle of attack. (b) Thrust.

Figure 4.21: *Angle of attack (a) and thrust of the two rotors (b) for configurations II.*

As evidence of this, it is possible to observe in Fig. 4.21(b) the variations in the thrust force of the left and right rotors during the roll maneuver, with greater thrust being generated by the left rotor and lower thrust by the right rotor. The different thrust force on the two rotors results in the insurgence of an adverse yaw moment on the aircraft. This contribution for model I is zero since the rotors are not modeled.

The load generated by the right rotor also shows greater oscillations as the maneuver progresses, with the appearance of higher frequency modes associated with rotors dynamics. This is linked to the behavior of the rotor mechanisms, and in particular to the angles of the gimbal joint that allow the rotor disk to tilt along the mast axis. In Fig. 4.22, the two gimbal angles ϕ_G and θ_G for the left and right rotors are shown as a function of the bank angle. If the left rotor shows a reduction in the amplitudes of both angles as ϕ increases, in the case of the right rotor these amplitudes increase more and more, introducing growing cyclic components.

As for the curves related to the wing-pylon system and the tail system, the models provide identical results since the aerodynamic and structural model is the same, and even though the rotor is present in configuration II, it does not generate a wake and therefore does not create differences related to aerodynamic interactions.

Regarding the contribution of the wing-nacelle, as expected, this creates an adverse yaw in response to a positive roll because the roll rate creates an additional relative velocity component between the body and the wind. Specifically, during the maneuver, the right wing moves upward, creating

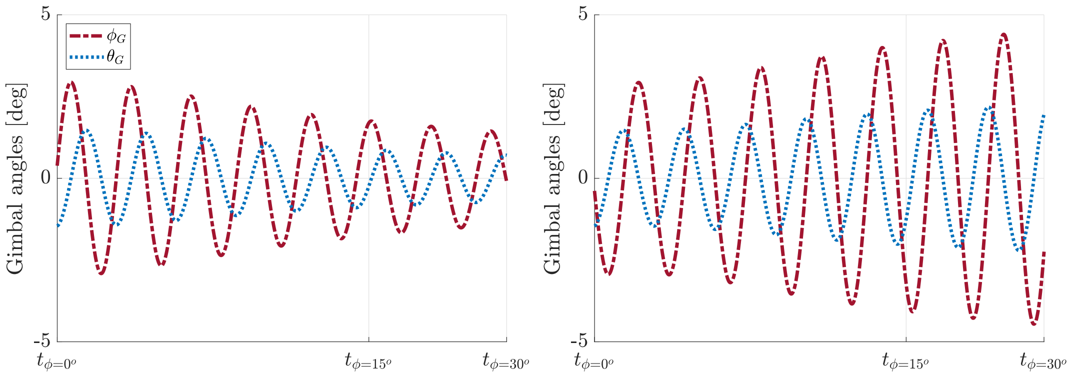

(a) Left rotor.

(b) Right rotor.

Figure 4.22: *Comparison of gimbal angles for left rotor (a) and right rotor (b) for configurations II.*

a downward component of velocity that reduces the effective angle of incidence and causes the lift vector to tilt backward. The opposite is true for the left side. This creates a negative yawing moment. Instead, the tailplanes part introduces a component of proverse yaw into the system, which is still relatively small compared to other contributions.

Regarding the linear forces transmitted to the actuators during the maneuver, the two configurations return the same results having the same numerical model for the airframe part (and no rotor wake). In addition, the load on each actuator of each semi-span wing is the same since the aileron is considered rigid and therefore the loads are equally distributed on the three actuators. As convention adopted, positive force corresponds to actuator traction while negative force corresponds to compression.

During the maneuver, the force on the actuators slightly changes due to the fact that with a non-constant roll rate, the dynamic pressure changes as well, and for the case of the right wing, it creates a component of downward velocity that increases with the roll rate, reducing the effective angle of incidence and decreasing the suction near the wing trailing edge and therefore the hinge moment required by the actuation system. Opposite conditions are obtained to the left wing.

4.2.2 Impact of rotor aerodynamic interaction

Now consider Configuration III which replaces the MBDyn rotor aerodynamics of configuration II with DUST, thus introducing the presence of the free wake of the two rotors in the model. The model coincides with *model*

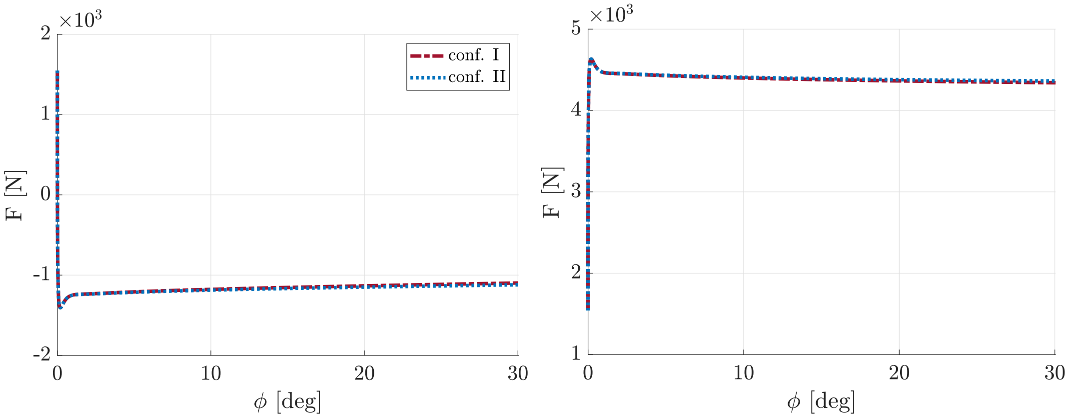

(a) Left aileron.

(b) Right aileron.

Figure 4.23: *Comparison of computed linear force on each actuator considering left aileron (a) and right aileron (b) for configurations I and II.*

B used in Sec. 4.1.

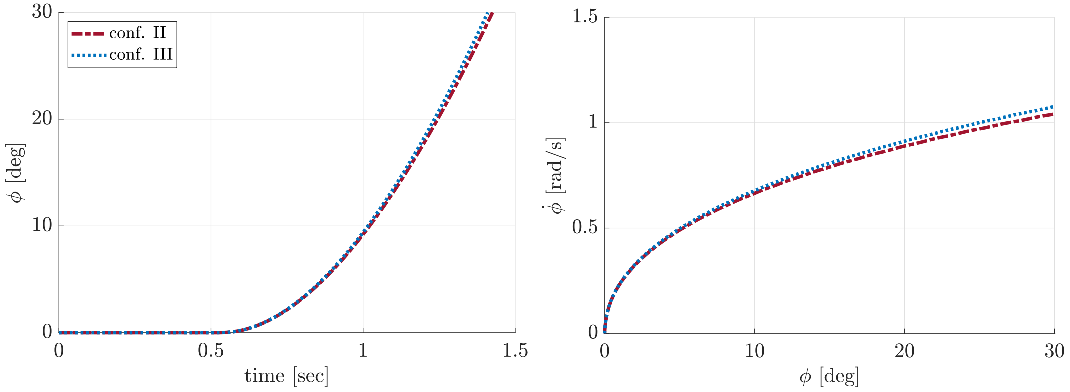

(a) Bank angle ϕ.

(b) Roll rate p.

Figure 4.24: *Comparison of computed bank angle evolution (a), and roll rate evolution (b) for configurations II and III.*

From a performance point of view, see Fig. 4.24, the introduction of aerodynamic interaction due to rotor wake results in a reduction of the time to bank 30° of less 2%. A greater impact is instead seen on the rotor loads and the resulting yaw moment transmitted to the structure. In Fig. 4.25 it is possible to note how in configuration III the rotors create reduced adverse yaw moments, but greater oscillations due to the aerodynamic interactions on the total thrust, as discussed in Sec 4.1.2. The thrust history during the roll maneuver is shown in Fig. 4.26.

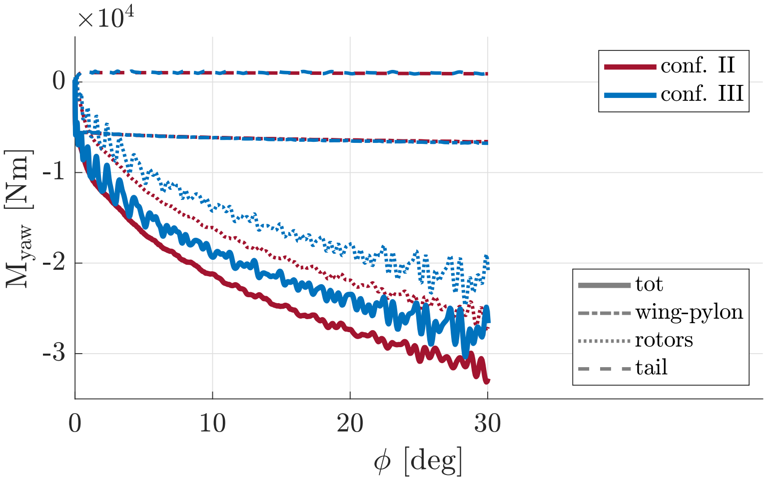

Figure 4.25: *Comparison of measured yaw moment raction force for configurations II and III.*

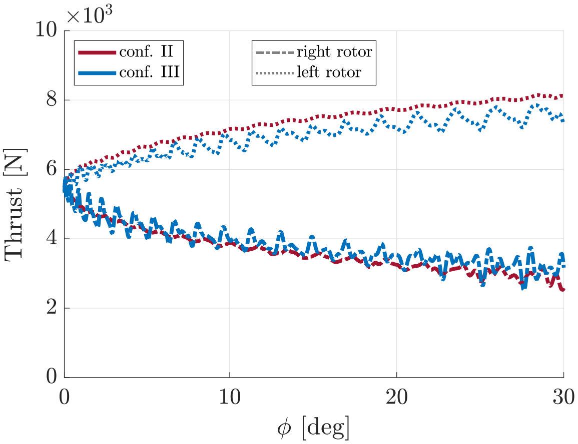

Figure 4.26: *Evolution during the maneuver of the measured thrust for the two proprotors, configurations II and III.*

To better understand the behavior of the rotor during the maneuver, Fig. 4.27 shows the pitch and flapping angles of the right rotor over one full revolution during the initial maneuver phase and at a bank angle around $\phi = 15°$. By observing the flapping angle in Fig. 4.27(b), it is evident by both configurations that its amplitude increases during the maneuver in accordance with what was previously noted about gimbal angles for configuration II in Fig. 4.22. The evolution of the pitch angle, on the other hand, shows multiple high-frequency harmonics, which are more noticeable in Configuration III. In particular, the super-harmonic activated during the maneuver turns out to be corresponding to the second torsional mode of the blade around the $9/rev$. So, the aerodynamics forces in DUST provide less damping in the blade pitch motion than the ones generated by the BEMT.

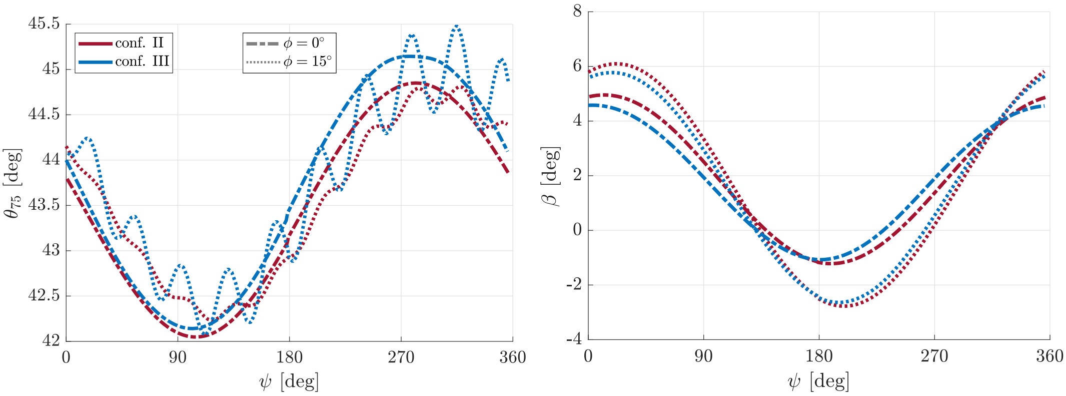

(a) Pitching angle.

(b) Flapping angle.

Figure 4.27: *Comparison of right rotor angles θ_{75} and β for configuration II and III, at different maneuver phase, $\phi = 0°$ and $\phi = 15°$.*

The actuation force measured on each actuator, see Fig. 4.28(a), considering only the right half-wing, generally results in similar values between configurations II and III. Configuration III shows evident oscillations corresponding to the frequency of the $3/rev$ caused by the wake of the 3 blades passing over the wing surface. In Fig.4.28(b), a zoom during the initial phases of the maneuver is shown.

4.2.3 Impact of aileron elasticity

Finally, as a last step, the flexibility of the aileron is considered, modeled as reported in Sec. 3.2.1 and illustrated in Fig. 3.15. With a rigid component, the repartition of the aerodynamic loads on the 3 actuators remains the same. This is no longer valid when introducing the flexibility of the structure modifying the load sharing among the 3 actuators.

Considering the right wing, in the rigid case of configuration III, the maximum actuation force in steady state condition was about $4900\,\mathrm{N}$ and

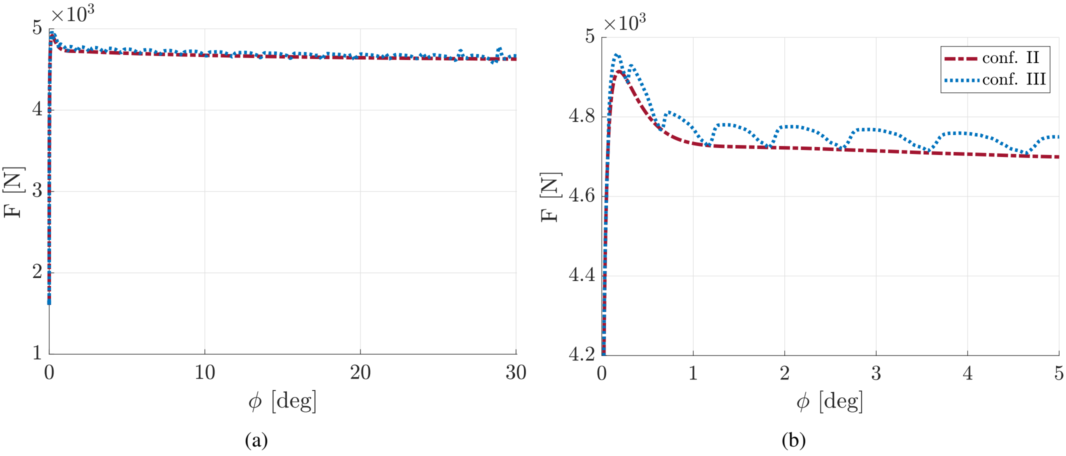

Figure 4.28: *Comparison of computed linear force on each actuator considering right aileron during the maneuver (a) and details during the first phase (b) for configurations II and III.*

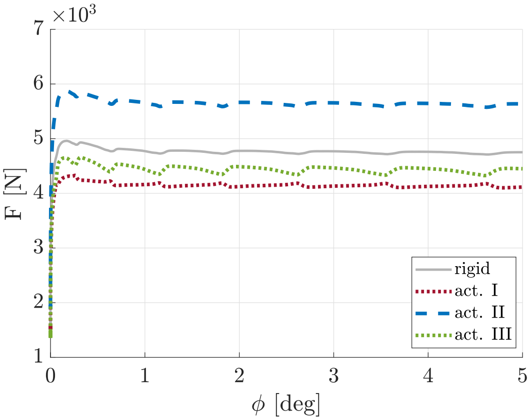

Figure 4.29: *Computed linear force on each actuator considering flexible right aileron during the first phase of the maneuver.*

the same for all actuators. Configuration IV, instead, shows a maximum force of about 5900 N on the centered actuator, (act. II). Fig. 4.29 shows the force values measured on the right aileron actuators during the intial phase of maneuvering. Compared with the rigid case, the center actuator shows an increase in load of about 17%. In contrast, the outer actuators show a force reduction of about 7% and 13%. Although the mean force on the actuators is similar to the value obtained with the rigid model, there is always an actuator with a load greater than the mean value. A sizing based on a rigid model does not turn out to be conservative. From the perspective of the overall aircraft performance, i.e. bank angle, roll rate, and yaw moment, the results are essentially identical to those of configuration III.

This result confirms the importance of using a numerical model as realistic as possible even during the preliminary design phase where the project requires an initial choice of the actuation system. In this way, it is possible to simultaneously carry out analysis dedicated to the study of aircraft performance, analysis about the actuation system, and general analysis of stability and aeroelastic loads.

CHAPTER 5

FORMOSA project

In this final chapter, the application of the coupled code developed in this work is presented in the context of a funded European project. The EU-funded FORMOSA project (`https://cordis.europa.eu/project/id/885971`) aims at developing innovative wing control surfaces concepts for the Next-Generation Civil Tiltrotor (NGCTR) tiltrotor aircraft demonstrator, developed within the EU Clean Sky 2 program. It is a new helicopter–fixed-wing hybrid vehicle designed to meet the increasing demands of aerial mobility and maneuverability in densely populated urban areas. Its configuration will be superior to current architectures for this type of aircraft. In particular, the project addressed in the framework of CleanSky 2 Fast Rotorcraft (FRC) IADP, is dedicated to the design, construction and flying of an innovative Civil Tiltrotor technology demonstrator, the configuration of which will go beyond current architectures for this type of aircraft. Indeed, demonstration activities planned in this framework will be aimed to show significant improvement with respect to current tiltrotors' state of the art. This novel tiltrotor configuration will host a peculiar wing that includes several movable surfaces controlled by complex kinematics mechanisms that will be flight tested in the framework of Clean Sky 2.

The actual NGCTR wing design was conceived to assign a specific function for each movable surface. An inner large flap was conceived for download reduction while an external flaperon was conceived for roll control as well as for download reduction. The design of the future NGCTR encourages an innovative solution for the wing movable surfaces able to incorporate multiple functions including download alleviation, flap, and aileron.

This work proposes a new methodology for the preliminary design and optimization of the flaperon control surface of the NGCTR, through the developed coupled aeroelastic tool. An optimization procedure, based on a Design of Experiment (DoE) approach, is then exploited to define the best configuration to improve the roll performance, trying to reduce the complexity of the actuation system. Finally, the results of these analyses are used as input for the preliminary sizing of the actuation system.

5.1 NGCTR numerical model

The numerical model of the NGCTR tiltrotor is built considering the full-scale dimensions and components of the aircraft. The model shown in Fig. 5.1 includes the fuselage, the wing equipped with control surfaces and the two proprotors with the corresponding nacelles.

Multibody model

The multibody model is composed of 25 rigid bodies representing the different parts of the tiltrotor. Each body with the relative mass and inertia property is located in the position of the center of mass of the corresponding component. The dynamic model includes:

- the wing, modeled as a rigid body, including flaperon and the fuel tank system;
- the fuselage and the empennages, modeled as rigid bodies;
- the pylon/nacelle system, attached to the wing-tip; its tilting with respect to the wing can be driven to model the tiltrotor in airplane mode (APMODE), helicopter mode (HEMODE) or in any intermediate configuration;

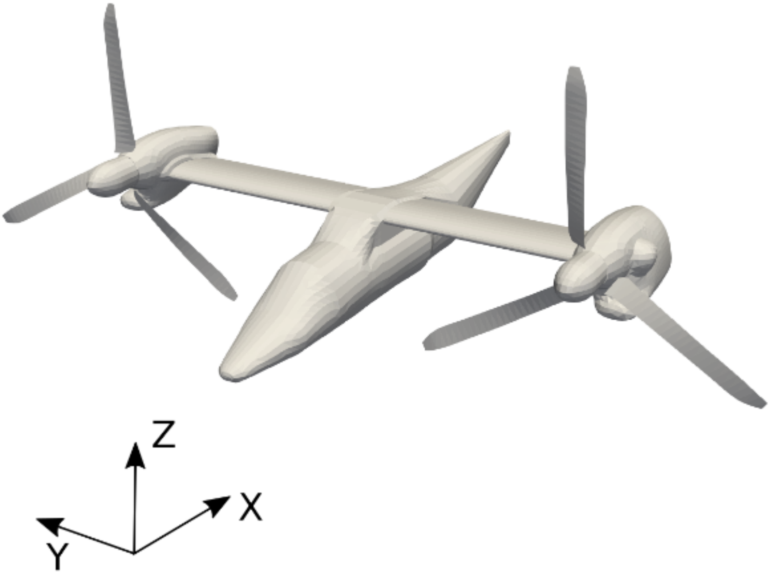

Figure 5.1: *NGCTR full span model.*

- the rotor with the exact kinematics of the blade pitching mechanism, where each blade is condensed in a rigid body. The multibody MBDyn model of a similar control chain is presented in Sec. 3.1;

At the first stage, a preliminary model of the overall tiltrotor is used to perform different simulations by changing the combination of the design variables on the flaperon. The control surface is modeled as a rigid body connected to the fixed wing by two joints. The first joint is a spherical hinge while the second is an inline joint. The flaperon deflection is obtained by imposing a prescribed rotation on the second joint. The combination of the two joints, together with the prescribed motion, makes the constraint statically determined. The line connecting the two joints identifies the hinge axis of rotation of the movable surface. In the final phase, after identifying the optimal geometric configuration, the complete kinematic chain of the control surface is introduced into the model. In this way, it is possible to carry out an inverse dynamics study to evaluate the control loads required by the actuators, useful to perform their preliminary sizing.

Aerodynamic model

The aerodynamic model uses different types of aerodynamic elements: lifting lines (LL) for each proprotor blade and surface panels (SP) for all the other aerodynamic components. Table 5.1 summarizes the details of the DUST mesh used for the trade-off study and the one used for the final simulations.

Table 5.1: *DUST aerodynamic mesh details.*

		Elements number	
Component	Element	Trade-off	Refined
Blade	LL	25×6	25×6
Wing	SP	560×2	5340×2
Fuselage	SP	2002	2002
Nacelle-hub	SP	1402×2	1402×2
Total		6076	15636

The trade-off coarse mesh is selected to guarantee convergence on the roll performance reducing the calculation times. In this way, it is possible to carry out many simulations that represented the data to proceed with a Design of Experiment (DOE) approach.

In Fig. 5.2 is reported a comparison of the lift distribution along with the right-wing between the CFD data provided by Leonardo Helicopter (LH) and the DUST simulation results. It is considered the isolated airframe model at Mach number 0.2 and with an angle of attack equal to $4°$. In particular, the blue line is obtained with the coarse mesh used for the trade-off study while the green line is obtained with the final refined mesh. The load distribution is rescaled to have the resultant of the lift force equal to 1.

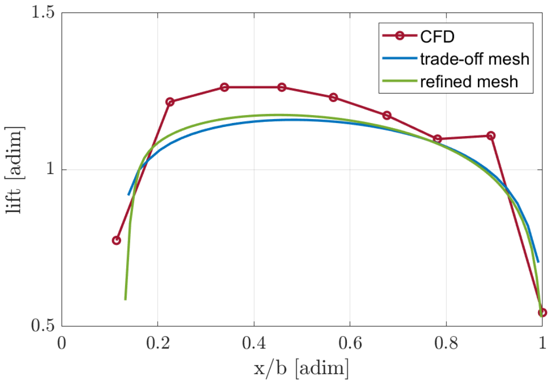

Figure 5.2: *Comparison of adimensional lift distribution on the right-wing.*

From these results, it must be remarked that the main differences in load distribution are in the proximity of the wingtips, specifically in the junction regions with the fuselage (left) and with the nacelle (right). Since the aerodynamic method implemented in DUST is based on an inviscid potential theory, it is not possible to capture phenomena related to the separation that will be present in the nacelle area. Additionally, it must be noted that the lift force distribution estimated by DUST is slightly lower than the one provided by LH. This is also related to the end-plate effects due to the nacelles, not being totally captured by DUST, which reduces the tip vortex formation leading to greater lift forces with less lifting area.

Table 5.2 reports the integral on the area below the three curves obtained, and the related percentage differences concerning the reference CFD data.

Table 5.2: *Lift distribution integral and percentage difference comparison.*

	Integral	Difference w.r.t. CFD [%]
CFD	1.00	0
Trade-off mesh	0.924	-7.6
Refined mesh	0.937	-6.3

It must be remarked that the mesh convergence in terms of span load distribution is also satisfied by the coarse trade-off mesh.

The computation times between trade-off mesh and refined mesh are roughly doubled, while for the time to bank the differences are in the range of 2 percent. In particular, considering a workstation equipped with an Intel® Core™ i9-9980XE processor running on a base frequency of 3.00 GHz, with 18 physical cores and 2 threads for each core, the simulation times were about $11\,\mathrm{h}$ for the coarse mesh and about $25\,\mathrm{h}$ for the refined one.

For this reason, during the preliminary design phase, the effort required by the refined mesh is not justified since the design requirement is about the manoeuvring performance, which is directly linked to the load distribution along the span, well captured even by the coarse mesh.

5.2 Flaperon sizing procedure

The sizing procedure and the design approach rely on the following key points:

- use of reliable multibody simulation tools to fully characterize the proposed concepts, their actuation systems, and the loads required during the deployment of the movable surface, in agreement with the general aircraft behavior and control; the multibody analyses will also consider the failure of one or more actuators and the possible consequences on the aerodynamic loads and on tiltrotor performance (redundancy study);

- application of a multidisciplinary methodology, coupling the multibody simulation with a fast aerodynamic tool able to capture the rotor-airframe interference during the critical maneuvers, at the preliminary design phase: the proposed approach will be useful for the correct choice of the best concept;
- design of the actuation system able to generate the control forces required for the correct deployment of the innovative movable surface, considering the possible failure modes, and the actuators integration with the aircraft power transmission and management;
- the selection of the optimized solution through a Design of Experiments approach (DoE), together with a Response Surface Methodology (RSM);

Optimization procedure

The optimization aims to identify the best geometric configuration of the flaperon using as few simulations as possible to reduce the computational cost and therefore the design time. A Design of Experiments (DoE) approach is selected to evaluate the impact of the different geometrical input parameters on a subset of performance output. The conceptual workflow is reported in Fig. 5.3.

The main geometrical design variables used for the definition of the different model configurations, illustrated in Fig. 5.4, are the flaperon span (b_f), the flaperon inboard location (in_f), and the chordwise hinge axis location (c_f).

The Latin Hypercube Sampling (LHS) is used to partition the design domain and to identify the initial set of configurations to analyze through the coupled simulations. The LHS is more efficient and less time consuming than other methods, and offers a not negligible practical advantage over them: it is able to identify a user-defined number of points to be analyzed that does not depend either on the number of variables or on the number of levels.

Through a trade-off study phase, different combinations of these parameters were investigated to understand the impact on the required performance. During this phase, the aerodynamic trade-off mesh was used (see table 5.1).

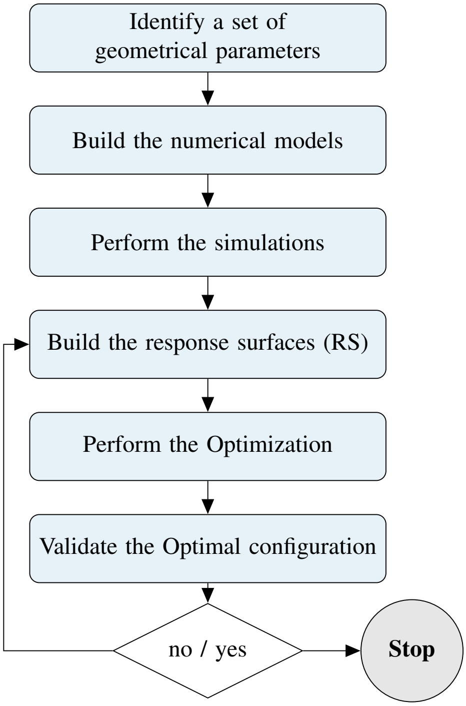

Figure 5.3: *Workflow of the optimization design procedure.*

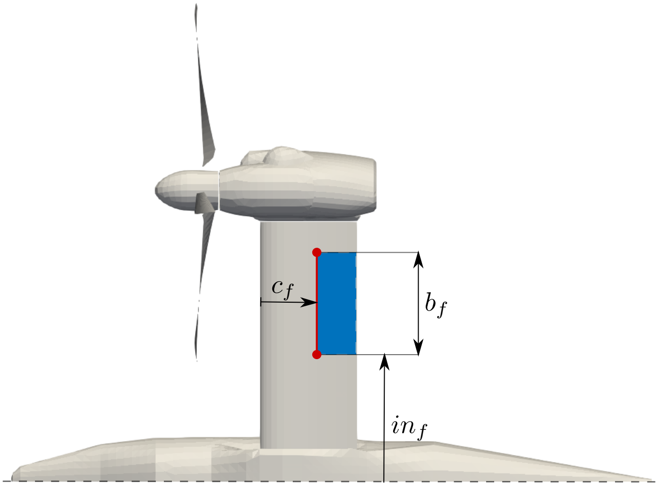

Figure 5.4: *Geometrical flaperon parameters used for the design optimization; the red line represents the hinge axis and the red dots the two joints.*

The simulations procedure foresees the flaperon's deflection according to a step function from $0°$ to $20°$, with the aircraft trimmed in airplane mode at Mach 0.2. The movables are deflected after $0.4\,\mathrm{s}$, to let any initial aerodynamic transient vanish. At the same time, the roll degree of freedom of the entire model, initially constrained, is released, and the aircraft starts to roll around the longitudinal axis, assuming positive starboard (right) wing up. The yaw rotation about the vertical body axis is considered positive nose left while the pitch rotation is about the axis perpendicular to the longitudinal plane of symmetry, positive nose up.

To perform the optimization, a single objective function together with a set of constraint functions are defined and the corresponding response surfaces are built. The objective function is related to a performance index that is assumed as the necessary hinge moment requested to actuate and deflect the flaperon. The solver tries to identify the solution that minimizes it. The main non-linear constraint function is related to the effectiveness of the movables to take the vehicle to a prescribed bank angle ($\phi = 45°$) in a prescribed time (t_b).

In general, for the optimization problem the Δt_b reduction, with reference to the baseline configuration, is defined with an imposed boundary as $-35\% < \Delta t_b < -25\%$.

The other constraint is of geometric type and it is imposed by setting the sum of in_f and b_f less than the aircraft semi-span and greater than a minimum value related to the definition of the clearance span region for the design. Once the response surfaces are available, a single-objective genetic algorithm is adopted to solve the optimization problem.

The response surfaces consist in an interpolation/approximation procedure. The procedure adopted is characterized on a Radial Basis Function (RBF) based on a scalar radius

$$\phi(r) = e^{-r^2/(2\kappa^2)} \tag{5.1}$$

where κ is a constant adjustable parameter whose optimal value is somewhat close to the average distance between the interpolation nodes.

The generic response surface $f(x)$ is obtained by the evaluation of the coefficients a_0, a_1, and λ_i to fit the values at the interpolation nodes x_i.

$$f(x) = a_0 + a_1 x + \sum_{i=1}^{n} \lambda_i \phi(|x - x_i|) \tag{5.2}$$

The goal is to fit the points representing the results coming from the multibody-aerodynamic analyses to obtain an analytical formulation of the objective and constraint functions used by the optimization procedure. The response surfaces can be exploited by the optimization algorithm to estimate the value of the function at any query point.

5.3 Trade-off and optimization results

In this subsection the results of the optimization phase and of the design procedure are reported. Note that the numerical values are dimensionless with respect to the corresponding baseline reference configuration indicated with the subscript ref, since they are linked to a real vehicle managed by Leonardo Helicopter. Working with a function of three parameters a response volume is obtained. To give a visual representation it is possible to freeze one specific parameter and show the parametric surface. In Fig. 5.5(a) and 5.5(b) each surface corresponds to a different (fixed) value of in_f, giving an analytical description of the time to bank t_b and of the hinge moment h_m as a function of the two parameters b_f and c_f. The black dots are the values obtained from the coupled simulations.

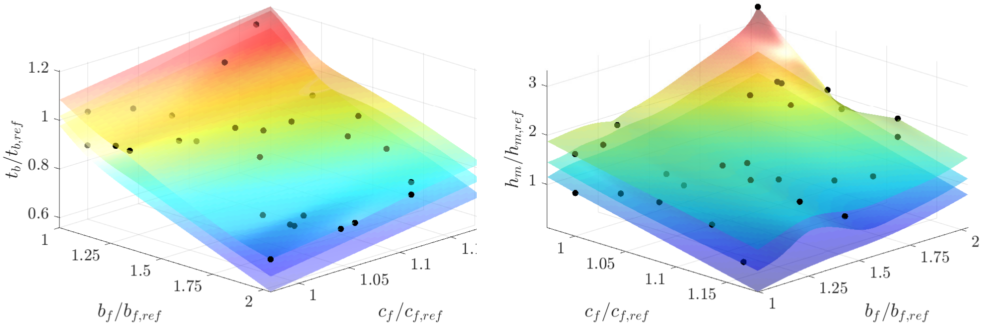

(a) Time to bank.

(b) Hinge moment.

Figure 5.5: *Response surfaces for time to bank and hinge moment at $\phi = 45°$, with reference to b_f and c_f, and different values of in_f.*

In Fig. 5.6(a),5.6(b) are shown some 2D plots obtained by the response surfaces. In particular, in Fig. 5.6(a) are depicted two curves corresponding to the time to bank values with reference to the flaperon span considering two sets of values for the chord and for a fixed value of the $in_f/in_{f,ref}$ equal to 0.51. It is clear that lower t_b values are obtained when increasing both the flaperon span and the chord size. Consider that a reduction of the index $c_f/c_{f,ref}$ represents an increase in the flaperon chord dimension and in the the hinge moment, as reported in Fig. 5.6(b).

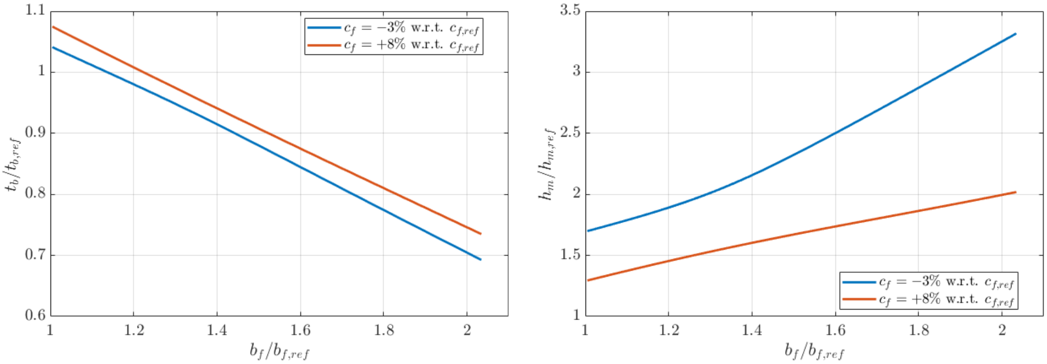

(a) Time to bank. (b) Hinge moment.

Figure 5.6: *2D Representation of RS: time to bank and hinge moment vs flaperon span for fixed values of in_f and two values for c_f.*

The volume described by the response surfaces is the domain within the optimizer that will search the optimal configuration of the three parameters b_f, c_f and in_f such that the time constraint is satisfied and the hinge moment minimized. A single-objective genetic algorithm is adopted to solve the optimization problem, considering a maximum number of generations of 100 and a cross-over fraction of 0.2.

The results obtained from the optimization algorithm are reported in Table 5.3. From the response surfaces, it is evident that is necessary to maximize the flaperon span to reduce the time to bank, while the chord must be contained to minimize the hinge moment.

Table 5.3: *Optimisation results.*

Optimal geometry	
$b_f/b_{f,ref}$	1.948
$c_f/c_{f,ref}$	1.056
$in_f/in_{f,ref}$	0.548
Performance	
Δt_b	-25 %
Δh_m	+60.4 %

The new solution satisfy the desired roll performance requirement, reducing the time to bank when compared to the baseline solution. As expected, a higher flaperon span is needed, while the chord is slightly reduced. The optimized configuration shows an increment of about 60% compared to the baseline solution, due to the improvement on the vehicle performance.

Based on the geometry of the movable surface obtained from optimization, within the context of the FORMOSA project, the corresponding actuation system was designed. Details regarding the entire work have been presented in [91] at the 78^{th} International Annual Forum Vertical Flight Society. In addition, in [93] presented at the 20^{th} Australian International Aerospace Congress, the CFD analysis carried out for the evaluation of the download prediction in helicopter mode for the sizing of the flap movable are reported.

Conclusions and further developments

The purpose of the work was to develop a numerical environment capable of preliminary simulations of complex aircraft such as tiltrotors. This development led to the creation of an aeroservoelastic code useful for preliminary design by engineers and researchers, providing a good compromise in terms of result accuracy and required computation times. In this way, it is possible to set up different analyses, from optimization-based design to aeroelastic simulations aimed at characterizing the system. All of this was done with an open-source approach in order to provide the research community with an accessible and usable tool that can be developed in the future to enhance its capabilities for upcoming studies.

The first part of the work presented the newly developed numerical tool for aeroelastic analysis, achieved through the integration of mid-fidelity aerodynamic software DUST with the multibody dynamics description provided by MBDyn. The benefits and challenges of this technique for rotary wing vehicle simulation were demonstrated, along with a thorough explanation of the resulting solver. Specific emphasis was given to the mathematical formulation of the solvers and their coupling implementation, as well as the significance of movable surface deflection in maneuvering and control studies crucial for novel air vehicle design. By utilizing a multibody structural model in combination with mid-fidelity numerical software, the method allowed for accurate assessment of aerodynamic interaction effects inherent in rotary-wing aircraft while maintaining a cost-effective approach when compared to traditional and more sophisticated CSD/CFD tools. The coupled code was validated with several benchmark cases provided in the literature. Validation tests revealed that providing a more precise explanation of aerodynamics is crucial for replicating the dynamic performance of a wedged wing during a flutter state.

In the second part of the work, the focus was on the aerodynamic solver DUST. Through four cases, the solver's ability to capture the typical aerodynamic loads and interactions typical of a vertical takeoff vehicle was demonstrated and verified through comparisons with numerical and experimental literature data. In general, the results of DUST simulations showed the capability to obtain a degree of accuracy in terms of rotor aerodynamic performance similar to the high-fidelity CFD approach, but at a much lower computational cost. Furthermore, the strength of the DUST approach based on the description of the free wake, has been demonstrated to be the ability to capture the physics of the flow field around the aircraft, a fundamental factor for understanding and investigating different designs in the preliminary phase. This result further highlighted the potential of the implemented approach for the design and investigation of rotorcraft configurations.

The third part of the work was devoted to the presentation of the XV-15 tiltrotor equipped with Advanced Technology Blades (ATB) numerical model, where each subcomponent was thoroughly validated against the available results and, from these, they were extended to allow validation with other analytical tools. The model was built using the new numerical DUST-MBDyn environment to obtain a complete XV-15 aeroservoelastic model of the tiltrotor. The model was divided into two parts: the rotor component and the airframe model, which includes the wing, nacelles, and empennages. The rotor component is validated both from the structural and aerodynamic point of view against literature data, while the airframe model is constructed using a parallel high-fidelity aerodynamic model due to the lack of detailed literature data. This allows for the demonstration of the accuracy of the aerodynamic results on the wing-nacelle system, and some comparisons are made. Globally, a good correlation was reached in the analysis of the entire system. As highlighted in the hover aeroelastic comparison, the simple 2D aerodynamic MBDyn aerodynamic model is inadequate to match the experimental results; however, this limitation can be easily overcome by coupling the MBDyn's structural part to the Vortex Particle aerodynamics of DUST: the coupled model indeed showed a great correlation concerning the experimental results in terms of rotor performance and wake measurement.

The last part was dedicated to the analyses carried out with the tiltrotor model. This part aims to provide an idea of the possible simulations and the results that can be obtained. To this end, two analyses were described:

in the first, the complete aircraft trim was found in steady-level flight with a simple integral control; in the second, the roll maneuver of the aircraft was simulated. In order to highlight the advantages of a more complete and realistic modeling, different hybrid models with different levels of complexity were used.

Recapping the fundamental questions behind the research work outlined in the *Introduction*, some conclusions can be drawn as valuable lessons learned.

1. Understanding Applicability Limits of the Proposed Approach:
   From the presented studies aimed at validating and testing the capabilities of DUST's mid-fidelity aerodynamics, a strong aptitude for capturing the primary phenomena related to transient interactional aerodynamics characteristic of VTOL aircraft has emerged. However, it has become evident that certain phenomena dominated by viscosity and turbulent effects cannot be described adequately. It is important to remember, therefore, that addressing the entire flight envelope solely with mid-fidelity aerodynamics is not feasible; the use of a high-fidelity method (RANS, URANS, . . .) is necessary for specific conditions, such as predicting wing downwash during hover flight.

2. Exploring Modeling Flexibility and Complexity:
   In terms of modeling flexibility, the tool has proven highly robust and sufficiently versatile to explore various configurations. Equally significant is the relative ease of modeling, which spares the user from excessive effort and difficulties in constructing the model.

3. Examining the Impact of Enhanced Modeling on Preliminary Design:
   Through the incorporation of different hybrid fidelity models in this study, it has been demonstrated that even in the early stages of design, considering aerodynamic interaction, component flexibility, and, in general, a more comprehensive model is crucial. This approach yields a more accurate estimation of aircraft performance and a conservative dimensioning of the vehicle components.

The following main aspects and peculiarities of the developed approach should be listed:

- Good compromise in terms of accuracy and computational cost;

- Unsteady 3D aerodynamics description including aerodynamic interactions in both loads and flowfield description with the possibility to investigate the physics related to the aircraft design;

- Possibility to create complex numerical models with different levels of complexity to highlight the impact of the different components on performance, stability and loads;
- Possibility to perform different analyses in the same environment: trim, maneuver, stability (comprehensive analysis);
- Capability to evaluate steady and unsteady periodic loads, useful for vibratory and fatigue life analysis;
- Capability to evaluate the dynamics of the systems including the impact of the elasticity of the components (as done for the aileron in this work).

This work has introduced a new perspective to the scientific and industrial community, revealing that coupled simulations with a mid-fidelity aerodynamic solver can achieve accurate reliable predictions with substantially less computational effort than conventional, higher-fidelity CSD tools. The developed numerical environment is useful in various branches of a typical aeronautical project, where different tools are often used instead. For example, this approach can allow for the conduct of studies typical of flight mechanics, considering a good aerodynamic description, typical instead of pure aerodynamic design analysis. This breakthrough presents an opportunity for performing the numerous aeroelastic analyses required during the preliminary design phase of innovative rotary-wing vehicles (eVTOL), as well as in other fields, such as wind energy and turbomachinery applications. Furthermore, the first steps in using DUST for aeroacoustic analyses have been taken, and future development will involve expanding the current aerosevoelastic analyses to incorporate aeroacoustics, a crucial aspect for the design of the new generation vertical take-off machines.

List of Figures

List of Tables

Bibliography

[1] Accident occured to the augusta westland aw609 aircraft registration marks n609ag. Technical report, ANSV, 2015.

[2] Maya Abou-Zeid, Arun Prakash Akkinepally, and Christelle Al Haddad. Contributors. In Constantinos Antoniou, Dimitrios Efthymiou, and Emmanouil Chaniotakis, editors, *Demand for Emerging Transportation Systems*, pages xiii–xiv. Elsevier, 2020.

[3] C. W. Acree. An improved camrad model for aeroelastic stability analysis of the xv-15 with advanced technology blades. Number 4448, Mountain View, CA, March 1993.

[4] C. W. Acree, R. J. Peyran, and Wayne Johnson. Rotor design options for improving tiltrotor whirl-flutter stability margins. *Journal of the American Helicopter Society*, 46(2):87–95, April 2001. doi:10.4050/JAHS.56.022004.

[5] CW Acree Jr. An improved camrad model for aeroelastic stability analysis of the xv-15 with advanced technology blades. 1993.

[6] Adam Jonas. Flying Cars: Investment Implications of Autonomous Urban Air Mobility. Tech. rep. Morgan Stanley research, 2018.

[7] ARM Altmikus, S Wagner, Ph Beaumier, and G Servera. A comparison- weak versus strong modular coupling for trimmed aeroelastic rotor simulations. In *AHS International, 58 th Annual Forum Proceedings-*, volume 1, pages 697–710, 2002.

[8] Eduardo Alvarez and Andrew Ning. Development of a vortex particle code for the modeling of wake interaction in distributed propulsion. In *AIAA Applied Aerodynamics Conference, Atlanta, GA*, 06 2018.

[9] EJ Alvarez and A Ning. Modeling multirotor aerodynamic interactions through the vortex particle method. In *Proceedings of the 54th AIAA Aviation Forum*, Dallas, TX, USA, 17–19 June 2019.

[10] EJ Alvarez and A Ning. High-fidelity modeling of multirotor aerodynamic interactions for aircraft design. *AIAA Journal*, 58(10):4385–4400, 2020.

[11] W. Arrington, M. Kumpel, and R. Marr. Xv-15 tilt rotor research aircraft flight test data report. Contractor Report 177406, NASA, 1985.

[12] S.M. Barkai, O. Rand, R.J. Peyran, and R.M. Carlson. Modeling and analysis of tilt-rotor aeromechanical phenomena. *Mathematical and Computer Modelling*, 27(12):17–43, 1998.

[13] K. Bartie, H. Alexander, M. McVeigh, S. Lamon, and H. Bishop. Hover performance tests of baseline metal and advanced technology blade (atb) rotor systems for the XV-15 tilt rotor aircraft. Contractor Report 177436, NASA Ames Research Center, 1986.

[14] Lorenzo Battisti, Luca Zanne, Marco Raciti Castelli, Alessandro Bianchini, and Alessandra Brighenti. A generalized method to extend airfoil polars over the full range of angles of attack. *Renewable Energy*, 155:862–875, 2020.

[15] Olivier A. Bauchau, Peter Betsch, Alberto Cardona, Johannes Gerstmayr, Ben Jonker, Pierangelo Masarati, and Valentin Sonneville. Validation of flexible multibody dynamics beam formulations using benchmark problems. *Multibody System Dynamics*, 37(1):29–48, 2016. doi:10.1007/s11044-016-9514-y.

[16] Olivier A. Bauchau and N. K. Kang. A multibody formulation for helicopter structural dynamic analysis. *Journal of the American Helicopter Society*, 38(2):3–14, April 1993.

[17] Tom Berger. Handling qualities requirements and control design for high-speed rotorcraft fixed wing system identification, flight control design, and handling qualities analysis view project f-16 vista system identification-stitched model development view project. *Journal of the American Helicopter Society*, 2019.

[18] Mark D Betzina. Rotor performance of an isolated full-scale xv-15 tiltrotor in helicopter mode. Technical report, NATIONAL AERONAUTICS AND SPACE ADMINISTRATION MOFFETT FIELD CA ROTORCRAFT, 2002.

[19] M Biava. *RANS computations of rotor/fuselage unsteady interactional aerodynamics*. PhD thesis, Politecnico di Milano, 2007.

[20] M Biava, M Woodgate, and GN Barakos. Fully implicit discrete-adjoint methods for rotorcraft applications. *AIAA Journal*, 54(2):735–749, 2016.

[21] J.M. Bilger, R.L. Marr, and A. Zahedi. Results of structural dynamic testing of the XV-15 tilt rotor research aircraft. *Journal of the American Helicopter Society*, 27(2):58–65, 1982. doi:10.4050/JAHS.27.58.

[22] R Boisard and J W Lim. Aerodynamic analysis of rotor/propeller wakes interactions on high speed compound helicopter. In *Proceedings of the 47th European Rotorcraft Forum*, Virtual Event, September 7-9 2021.

[23] Hans-Joachim Bungartz, Florian Lindner, Bernhard Gatzhammer, Miriam Mehl, Klaudius Scheufele, Alexander Shukaev, and Benjamin Uekermann. preCICE – a fully parallel library for multi-physics surface coupling. *Computers and Fluids*, 141:250–258, 2016. Advances in Fluid-Structure Interaction.

[24] Jr. C. W. Acree. An improved CAMRAD model for aeroelastic stability analysis of the XV-15 with advanced technology blades. TM 4448, NASA, 1993.

[25] L Cambier, S Heib, and S Plot. The onera elsa cfd software: input from research and feedback from industry. *Mechanics and Industry*, TP 2013-437, 2013.

[26] Alessandro Cocco. Comprehensive mid-fidelity simulation environment for aeroelastic stability analysis of tiltrotors with pilot-in-the-loop. 2023.

[27] Alessandro Cocco, Andrea Colli, Alberto Savino, Pierangelo Masarati, Alex Zanotti, et al. A non-linear unsteady vortex lattice method for aeroelastic rotor loads evaluation. In *48th European Rotorcraft Forum (ERF 2022)*, pages 1–8, 2022.

[28] Alessandro Cocco, Alberto Savino, and Pierangelo Masarati. Flexible multibody model of a complete tiltrotor for aeroservoelastic analysis. In *International Design Engineering Technical Conferences and Computers and Information in Engineering Conference*, volume 86304, page V009T09A026. American Society of Mechanical Engineers, 2022.

[29] Georges-Henri Cottet, Petros D Koumoutsakos, D Petros, et al. *Vortex methods: theory and practice*. Cambridge University Press, 2000.

[30] Roy R. Craig, Jr. and Mervyn C. C. Bampton. Coupling of substructures for dynamic analysis. *AIAA Journal*, 6(7):1313–1319, July 1968. doi:10.2514/3.4741.

[31] Anubhav Datta, Jayanarayanan Sitaraman, Inderjit Chopra, and James D. Baeder. CFD/CSD prediction of rotor vibratory loads in high-speed flight. *Journal of Aircraft*, 43(6):1698–1709, November-December 2006. doi:10.2514/1.18915.

[32] J Decours, P Beaumier, W Khier, T Kneisch, M Valentini, and L Vigevano. Experimental validation of tilt-rotor aerodynamic predictions. In *Proceedings of the 40th European Rotorcraft Forum*, Southampton, UK, 2–5 September 2014.

[33] Mark Drela. Xfoil: An analysis and design system for low reynolds number airfoils. In Thomas J. Mueller, editor, *Low Reynolds Number Aerodynamics*, pages 1–12, Berlin, Heidelberg, 1989. Springer Berlin Heidelberg.

[34] Giovanni Droandi, Alex Zanotti, and Giuseppe Gibertini. Aerodynamic interaction between rotor and tilting wing in hovering flight condition. *Journal of the American helicopter Society*, 60(4):1–20, 2015.

[35] Thomas D Economon, Francisco Palacios, Sean R Copeland, Trent W Lukaczyk, and Juan J Alonso. Su2: An open-source suite for multiphysics simulation and design. *Aiaa Journal*, 54(3):828–846, 2016.

[36] S. W. Ferguson, W. F. Clement, W. B. Cleveland, and D. L. Key. Assessment of simulation fidelity using measurements of piloting technique in flight. In *American Helicopter Society 40th Annual Forum*, pages 67–92, Arlington, VA, USA, May 16–18 1984.

[37] Samuel W. Ferguson. A mathematical model for real time flight simulation of a generic tilt-rotor aircraft. CR 166536, NASA, 1988.

[38] Samuel W. Ferguson. Development and validation of a simulation for a generic tilt-rotor aircraft. CR 166537, NASA, 1989.

[39] David B. Signor Fort F. Felker, Mark D. Betzina. Performance and loads data from a hover test of a full-scale xv-15 rotor. Technical report, NASA Ames Research Center, Moffett Field California, 1985.

[40] Malcolm Foster. Evolution of tiltrotor aircraft. In *Evolution of Tiltrotor Aircraft*. American Institute of Aeronautics and Astronautics (AIAA), 7 2003.

[41] S Gallay and E Laurendeau. Nonlinear generalized lifting-line coupling algorithms for pre/-poststall flows. *AIAA Journal*, 53(7):1784–1792, 2015.

[42] Gian Luca Ghiringhelli, Pierangelo Masarati, and Paolo Mantegazza. A multi-body implementation of finite volume C^0 beams. *AIAA Journal*, 38(1):131–138, January 2000. doi:10.2514/2.933.

[43] Gian Luca Ghiringhelli, Pierangelo Masarati, Paolo Mantegazza, and Mark W. Nixon. Multi-body analysis of a tiltrotor configuration. *Nonlinear Dynamics*, 19(4):333–357, August 1999. doi:10.1023/A:1008386219934.

[44] Martin Goland. The flutter of a uniform cantilever wing. *Journal of Applied Mechanics-Transactions of the Asme*, 12(4):A197–A208, 1945.

[45] Tongqing GUO, Daixiao LU, Zhiliang LU, Di ZHOU, Binbin LYU, and Jiangpeng WU. Cfd/csd-based flutter prediction method for experimental models in a transonic wind tunnel with porous wall. *Chinese Journal of Aeronautics*, 33(12):3100–3111, 2020.

[46] G. D. Hanson and S. W. Ferguson. Generic tilt-rotor simulation (GTRSIM) user's and programmer's guide. Technical Report CR-166535, NASA, 09 1988.

[47] FD Harris. Technical note: Twin rotor hover performance. *Journal of the American Helicopter Society*, 44(1):34–37, 1999.

[48] John R Hooker, Andrew Wick, Starr R Ginn, Jimmy Walker, and Benjamin T Schiltgen. Overview of low speed wind tunnel testing conducted on a wingtip mounted propeller for the workshop for integrated propeller prediction. In *AIAA AVIATION 2020 FORUM*, page 2673, 2020.

[49] Yingbo Hua and Tapan K Sarkar. Matrix pencil method for estimating parameters of exponentially damped/undamped sinusoids in noise. *IEEE Transactions on Acoustics, Speech, and Signal Processing*, 38(5):814–824, 1990.

[50] Feilin Jia, John Moore, and Qiqi Wang. Assessment of detached eddy simulation and sliding mesh interface in predicting tiltrotor performance in helicopter and airplane modes. In *AIAA AVIATION 2021 FORUM*, page 2601, 2021.

[51] A Jimenez Garcia and GN Barakos. Cfd simulations on the erica tiltrotor using hmb2. In *Proceedings of the 54th AIAA Aerospace Sciences Meeting*, San Diego, CA, USA, 4–8 January 2016.

[52] Wayne Johnson. *CAMRAD II, COMPREHENSIVE ANALYTICAL MODEL OF ROTORCRAFT AERODYNAMICS AND DYNAMICS, Volume I: Theory*. Johnson Aeronautics, 1992.

[53] Joseph Katz and Allen Plotkin. *Low-speed aerodynamics*, volume 13. Cambridge university press, 2001.

[54] W. Khier, M. Dietz, T. Schwarz, and S. Wagner. Trimmed cfd simulation of a complete helicopter configuration. In *High Performance Computing in Science and Engineering*, pages 487–501, 2007.

[55] N Kroll, B Eisfeld, and HM Bleecke. The navier-stokes code flower. *Notes on Numerical Fluid Mechanics*, 71:58–71, 1999.

[56] Wolf R Krüger. Multibody analysis of whirl flutter stability on a tiltrotor wind tunnel model. *Proc. IMechE, Part K: J. of Multi-body Dynamics*, 230(2):121–133, 2016. doi:10.1177/1464419315582128.

[57] Ulrich Küttler and Wolfgang A Wall. Fixed-point fluid-structure interaction solvers with dynamic relaxation. *Computational mechanics*, 43(1):61–72, 2008.

[58] J. Gordon Leishman. *Principles of Helicopter Aerodynamics*. Cambridge University Press, Cambridge, UK, 2nd edition, 2006.

[59] L. Leone, P. Civiletti, P. Costa, and J. Feenstra. Tiltrotor aerodynamic and structural design of the leonardo 609 aircraft. *American Institute of Aeronautics and Astronautics*, 35(3):1–40, 2020.

[60] J. W. Lim. Fundamental investigation of proprotor and wing interactions in tiltrotor aircraft. In *75th Annual Vertical Flight Society Forum and Technology Display, Philadelphia, Pennsylvania, USA*, 2019.

[61] Keith Lindsay and Robert Krasny. A particle method and adaptive treecode for vortex sheet motion in three-dimensional flow. *Journal of Computational Physics*, 172(2):879–907, 2001.

[62] Yang Lu, Taoyong Su, Renliang Chen, Pan Li, and Yu Wang. A method for optimizing the aerodynamic layout of a helicopter that reduces the effects of aerodynamic interaction. *Aerospace Science and Technology*, 88:73 – 83, 2019.

[63] Davide ma, Matteo Tugnoli, Federico Fonte, Alex Zanotti, Monica Syal, Giovanni Droandi, et al. Mid-fidelity analysis of unsteady interactional aerodynamics of complex vtol configurations. In *45th European Rotorcraft Forum (ERF 2019)*, pages 100–110, 2019.

[64] M. Maisel. NASA/Army XV-15 tilt-rotor research aircraft familiarization document. TM X-62,407, NASA, January 1975.

[65] P. Masarati. Direct eigenanalysis of constrained system dynamics. *Proc. IMechE Part K: J. Multi-body Dynamics*, 223(4):335–342, 2009. doi:10.1243/14644193JMBD211.

[66] P. Masarati and M. Morandini. Intrinsic deformable joints. *Multibody System Dynamics*, 23(4):361–386, 2010. doi:10.1007/s11044-010-9194-y.

[67] P. Masarati and J. Sitaraman. Tightly coupled CFD/multibody analysis of NREL unsteady aerodynamic experiment phase VI rotor. In *49th AIAA Aerospace Sciences Meeting*, Orlando, Florida, January 4–7 2011.

[68] Pierangelo Masarati and Marco Morandini. An ideal homokinetic joint formulation for general-purpose multibody real-time simulation. *Multibody System Dynamics*, 20(3):251–270, October 2008. doi:10.1007/s11044-008-9112-8.

[69] Pierangelo Masarati, Marco Morandini, and Paolo Mantegazza. An Efficient Formulation for General-Purpose Multibody/Multiphysics Analysis. *Journal of Computational and Nonlinear Dynamics*, 9(4), 07 2014.

[70] S. Massey, A. Kreshock, and M. Sekula. Coupled cfd/csd analysis of rotor blade structural loads with experimental validation. In *31st AIAA Applied Aerodynamics Conference*, San Diego, CA, USA, June 24–27 2013.

[71] M. Mattaboni, P. Masarati, G. Quaranta, and P. Mantegazza. Multibody simulation of integrated tiltrotor flight mechanics, aeroelasticity and control. *J. of Guidance, Control, and Dynamics*, 35(5):1391–1405, September/October 2012. doi:10.2514/1.57309.

[72] Michael A McVeigh, William K Grauer, and David J Paisley. Rotor/airframe interactions on tiltrotor aircraft. *Journal of the American Helicopter Society*, 35(3):43–51, 1990.

[73] R. Meakin. Unsteady simulation of the viscous flow about a v-22 rotor and wing in hover. In *AIAA Atmospheric Flight Mechanics Conference Proceedings*, Baltimore, MD, USA, August 7–10 1995.

[74] Thomas Henry Gordon Megson. *Aircraft structures for engineering students*, chapter 20. Butterworth-Heinemann, 2016.

[75] D Montagnani, M Tugnoli, A Zanotti, M Syal, G Droandi, et al. Analysis of the interactional aerodynamics of the vahana evtol using a medium fidelity open source tool. In *VFS Aeromechanics for Advanced Vertical Flight Technical Meeting*, pages 1–16, 2020.

[76] Marco Morandini and Pierangelo Masarati. Implementation and validation of a 4-node shell finite element. In *ASME IDETC/CIE 2014*, Buffalo, NY, August 17–20 2014. DETC2014-34473.

[77] L. Morino and C.-C. Kuot. Subsonic potential aerodynamics for complex configurations: A general theory. *AIAA Journal*, 12(2):191–197, 1974. doi:10.2514/3.49191.

[78] Luigi Morino and Ching-Chiang Kuot. Subsonic potential aerodynamics for complex configurations: a general theory. *AIAA Journal*, 12(2):191–197, 1974.

[79] Joseba Murua, Rafael Palacios, and J Michael R Graham. Assessment of wake-tail interference effects on the dynamics of flexible aircraft. *AIAA Journal*, 50(7):1575–1585, 2012.

[80] Vincenzo Muscarello, Francesca Colombo, Giuseppe Quaranta, and Pierangelo Masarati. Aeroelastic rotorcraft–pilot couplings in tiltrotor aircraft. *Journal of Guidance, Control, and Dynamics*, 42(3):524–537, 2019.

[81] Vincenzo Muscarello, Francesca Colombo, Giuseppe Quaranta, and Pierangelo Masarati. Aeroelastic rotorcraft-pilot couplings in tiltrotor aircraft. *J. of Guidance, Control, and Dynamics*, 42(3):524–537, 2019. doi:10.2514/1.G003922.

[82] Vincenzo Muscarello and Giuseppe Quaranta. Structural coupling and whirl-flutter stability with pilot-in-the-loop. *Journal of the American Helicopter Society*, 66(3):1–16, 2021.

[83] Mayuresh J Patil, Dewey H Hodges, and Carlos ES Cesnik. Nonlinear aeroelastic analysis of complete aircraft in subsonic flow. *Journal of Aircraft*, 37(5):753–760, 2000.

[84] Stanley T Piszkin and ES Levinsky. Nonlinear lifting line theory for predicting stalling instabilities on wings of moderate aspect ratio. Technical report, GENERAL DYNAMICS SAN DIEGO CA CONVAIR DIV, 1976.

[85] Mark A Potsdam and Roger C Strawn. Cfd simulations of tiltrotor configurations in hover. *Journal of the American Helicopter Society*, 50(1):82–94, 2005.

[86] Mark A Potsdam and Roger C Strawn. CFD simulations of tiltrotor configurations in hover. *Journal of the American Helicopter Society*, 50(1):82–94, 2005.

[87] Giuseppe Quaranta, Pierangelo Masarati, Massimiliano Lanz, Gian Luca Ghiringhelli, Paolo Mantegazza, and Mark W. Nixon. Dynamic stability of soft-in-plane tiltrotors by parallel multibody analysis. In *26th European Rotorcraft Forum*, pages 60.1–9, The Hague, The Netherlands, 26–29 September 2000.

[88] M Ramasamy. Hover performance measurements toward understanding aerodynamic interference in coaxial, tandem, and tilt rotors. *Journal of the American Helicopter Society*, 60(3):1–17, 2015.

[89] Thomas CS Rendall and Christian B Allen. Unified fluid–structure interpolation and mesh motion using radial basis functions. *International journal for numerical methods in engineering*, 74(10):1519–1559, 2008.

[90] Harold Rosenstein and Ross Clark. Aerodynamic development of the v-22 tilt rotor. In *Aircraft Systems, Design and Technology Meeting*, page 2678, 1986.

[91] A Savino, A Cocco, A Zanoni, A De Gaspari, A Zanotti, J Cardoso, D Carvalhais, V Muscarello, et al. Design and optimization of innovative tiltrotor wing control surfaces through coupled multibody-mid-fidelity aerodynamics simulations. In *78th International Annual Forum Vertical Flight Society*, pages 1–15, 2022.

[92] A. Savino, A. Cocco, A. Zanoni, A. Zanotti, and V Muscarello. A coupled multibody-mid fidelity aerodynamic tool for the simulation of tiltrotor manoeuvres. In *47th European Rotorcraft Forum*, Virtual Event, 2021.

[93] Alberto Savino, João Cardoso, Matteo Pecoraro, Vincenzo Muscarello, et al. Development of innovative movable surfaces for the next-generation civil tiltrotor aircraft. In *20th Australian International Aerospace Congress*, pages 1–6, 2023.

[94] Alberto Savino, Alessandro Cocco, Alex Zanotti, Matteo Tugnoli, Pierangelo Masarati, and Vincenzo Muscarello. Coupling mid-fidelity aerodynamics and multibody dynamics for the aeroelastic analysis of rotary-wing vehicles. *Energies*, 14(21):6979, 2021.

[95] Jayanarayanan Sitaraman and Beatrice Roget. Prediction of helicopter maneuver loads using a fluid-structure analysis. *Journal of Aircraft*, 46(5):1770–1784, 2009.

[96] J.W. Smith, M.J.and Lim, J.D. van der Wall, B.G.and Baeder, R.T. Biedron, D.D. Boyd, B. Jayaraman, S.N. Jung, and B.Y. Min. The HART II international workshop: An assessment of the state of the art in CFD/CSD prediction. *Ceas Aeronautical Journal*, 4, 2013.

[97] J Tan, T Zhou, J Sun, and GN Barakos. Numerical investigation of the aerodynamic interaction between a tiltrotor and a tandem rotor during shipboard operations. *Aerospace Science and Technology*, 87:62–72, 2019.

[98] ES Taylor and KA Browne. Vibration isolation of aircraft power plants. *Journal of the Aeronautical Sciences*, 6(2):43–49, 1938.

[99] Steven Tran and Joon Lim. Interactional structural loads of the XV-15 rotor in airplane mode. In *45th European Rotorcraft Forum, Warsaw, Poland*, 2019.

[100] Steven Tran, Joon Lim, Gerardo Nunez, Andrew Wissink, and Graham Bowen-Davies. CFD calculations of the XV-15 tiltrotor during transition. In *Proceedings of the American Helicopter Society 75th Annual Forum*, Philadelphia, PA, USA, May 2019.

[101] Steven A Tran and Joon W. Lim. Investigation of the interactional aerodynamics of the XV-15 tiltrotor aircraft. In *76th Annual Vertical Flight Society Forum and Technology Display*, 2020.

[102] Matteo Tugnoli, Davide Montagnani, Monica Syal, Giovanni Droandi, and Alex Zanotti. Mid-fidelity approach to aerodynamic simulations of unconventional vtol aircraft configurations. *Aerospace Science and Technology*, 115:106804, 2021.

[103] Matteo Tugnoli, Davide Montagnani, Monica Syal, Giovanni Droandi, and Alex Zanotti. Mid-fidelity approach to aerodynamic simulations of unconventional vtol aircraft configurations. *Aerospace Science and Technology*, 115:106804, 2021.

[104] L A Viterna and D C Janetzke. Theoretical and experimental power from large horizontal-axis wind turbines. Technical report, Washington Procurement Operations Office, Washington, DC (United States), September 1982.

[105] Zhicun Wang, PC Chen, DD Liu, DT Mook, and MJ Patil. Time domain nonlinear aeroelastic analysis for hale wings. In *47th AIAA/ASME/ASCE/AHS/ASC Structures, Structural Dynamics, and Materials Conference 14th AIAA/ASME/AHS Adaptive Structures Conference 7th*, page 1640, 2006.

[106] M Wentrup, J Yin, P Kunze, T Streit, JH Wendisch, T Schwarz, JP Pinacho, Kicker K, and R Fukari. An overview of dlr compound rotorcraft aerodynamics and aeroacoustics activities within the cleansky2 nacor project. In *Proceedings of 74th AHS Annual Forum & Technology Display*, Phoenix, AZ, USA, 14–17 May 2018.

[107] Gregoire Stephane Winckelmans. *Topics in vortex methods for the computation of three-and two-dimensional incompressible unsteady flows*. PhD thesis, California Institute of Technology, 1989.

[108] A. Wissink, M. Potsdam, V. Sankaran, J. Sitaraman, Z. Yang, and D. Mavriplis. Unsteady simulation of the viscous flow about a v-22 rotor and wing in hover. In *American Helicopter Society 66th Annual Forum Proceedings*, Phoenix, AZ, USA, May 11–13 2010.

[109] TL Wood and MA Peryea. Reduction of tiltrotor download. *Journal of the American Helicopter Society*, 40(3):42–51, 1995.

[110] Hyeonsoo Yeo, Mark Potsdam, and A. Ormiston Robert. Rotor Aeroelastic Stability Analysis Using Coupled Computational Fluid Dynamics/Computational Structural Dynamics. *Journal of the American Helicopter Society*, 56(4), 2011.

[111] Hyeonsoo Yeo, Mark Potsdam, Biel Ortun, and Khiem Van Truong. High-Fidelity Structural Loads Analysis of the ONERA 7A Rotor. *Journal of Aircraft*, 54(5), 2017.

[112] J Yin and SR Ahmed. Helicopter main-rotor/tail-rotor interaction. *Journal of the American Helicopter Society*, 4:293–302, 2000.

[113] Alex Zanotti. Experimental study of the aerodynamic interaction between side-by-side propellers in evtol airplane mode through stereoscopic particle image velocimetry. *Aerospace*, 8(9):239, 2021.

[114] Alex Zanotti and Davide Algarotti. Aerodynamic interaction between tandem overlapping propellers in evtol airplane mode flight condition. *Aerospace Science and Technology*, 124:107518, 2022.

[115] Alex Zanotti, Alberto Savino, Michele Palazzi, Matteo Tugnoli, and Vincenzo Muscarello. Assessment of a mid-fidelity numerical approach for the investigation of tiltrotor aerodynamics. *Applied Sciences*, 11(8):3385, 2021.

[116] Beckett Yx Zhou, Myles Morelli, Nicolas R Gauger, and Alberto Guardone. Simulation and sensitivity analysis of a wing-tip mounted propeller configuration from the workshop for integrated propeller prediction (wipp). In *AIAA AVIATION 2020 FORUM*, page 2683, 2020.

[117] W Zhou, Z Ning, H Li, and H Hu. An experimental investigation on rotor-to-rotor interactions of small uav propellers. In *Proceedings of the 35th AIAA Applied Aerodynamics Conference*, Denver, USA, 5–8 June 2017.